

Structure analysis of basic Co-rich decagonal Al-Co-Ni

A dissertation submitted to
ETH ZURICH

for the degree of
Doctor of Science

presented by
Angelica Strutz
M.Sc. Mat. Eng.
Born 21 October 1976
Citizen of Israel

Accepted on the recommendation of
Prof. Dr. Walter Steurer, ETH Zurich, examiner
Prof. Dr. Uwe Grimm, Open University, UK, co-examiner
Asst. Prof. Dr. Cesar Pay Gómez, Uppsala University, Sweden, co-examiner

*"God could cause us considerable
embarrassment by revealing all secrets
of nature to us: we should not know what
to do for sheer apathy and boredom."
— Goethe (Johann Wolfgang von; 1749-1832)*

to my parents

Contents

Abstract	ii
Zusammenfassung	iii
1 Introduction	1
2 Experimental	6
2.1 System Al-Co-Ni	6
2.2 Sample Preparation and Analysis	8
2.3 Single-Crystal X-Ray Diffraction Data Analysis	10
3 Structure Determination of Quasicrystals	15
3.1 Periodicity in Higher-Dimensional Space	18
3.2 From Quasiperiodic Tiling to Higher-Dimensional Modeling	22
3.3 Patterson Technique, <i>Ab Initio</i> Phasing Methods and MEM	30
3.4 The Pseudo-Approximant Method	31
3.5 Theoretical Simplified Superstructure Model	36
4 Average Structure of basic Co-Rich Decagonal Al_{72.5}Co_{18.5}Ni₉	40
4.1 Structure Determination Using <i>Ab Initio</i> Phasing Methods (Article I) . . .	40
4.2 Supplement - Article I	47
4.3 Basic Co-Rich Decagonal Al-Co-Ni: Average Structure (Article II)	54
4.4 Supplement - Article II	64
5 Superstructure of basic Co-Rich Decagonal Al_{72.5}Co_{18.5}Ni₉	71
5.1 Basic Co-Rich Decagonal Al-Co-Ni: Superstructure (Article III)	71
5.2 Supplement - Article III	84
6 Concluding Remarks	102
Bibliography	104
Appendix	109
Acknowledgements	115

Abstract

This thesis presents a thorough structure analysis of the four-layer superstructure of decagonal Co-rich Al-Co-Ni. Due to its ten-fold non-crystallographic symmetry, this analysis was performed with a higher-dimensional approach. For the first time, a five-dimensional superstructure model for a four-layer decagonal quasicrystal was proposed and validated by refinement. In this work, it was proven that the W-phase is a rational $\langle 3/2, 2/1 \rangle$ -approximant of the investigated superstructure. Comparison of the actual W-phase approximant with the generated $\langle 3/2, 2/1 \rangle$ -approximant shows good agreement. In addition, the cluster structures in the W-phase approximant are similar to those observed in the quasicrystal.

Understanding the formation, stability and physical properties of quasicrystals requires knowledge of their structures. However, the structures of only a handful of them have yet been determined due to the intricate complexity of quasicrystal structure analysis. Al-Co-Ni is an excellent model system for structural investigations of decagonal quasicrystals. It not only has a broad stability range, but it also shows complex ordering phenomena as a function of the Co/Ni ratio and/or temperature.

In the course of the current work, single crystals of the Co-rich decagonal $\text{Al}_{72.5}\text{Co}_{18.5}\text{Ni}_9$ phase were successfully grown. The X-ray diffraction pattern of this phase shows sharp Bragg peaks also in the intermediate layers. This structural modification has an $\approx 8 \text{ \AA}$ periodicity along the ten-fold axis, i.e. a four-layer superstructure. The availability of high-quality single crystals provided a unique opportunity to carry out a full structure analysis and to understand the superstructure ordering. Moreover, understanding this complex structure sheds light on short-range order in related quasicrystal phases.

Initially, a five-dimensional structure model of the two-layer average structure was constructed. It was refined in the non-centrosymmetric five-dimensional space group $P\bar{1}0m2$ with 112 parameters, resulting in values of $wR = 0.123$ and $R = 0.156$ for 957 unique reflections. Based on this structure model, the four-layer superstructure model was derived using the non-centrosymmetric five-dimensional space group $P\bar{1}02c$ complemented with additional constraints resulting from normal mode analysis. The refinement with 250 parameters resulted in values of $wR = 0.039$ and $R = 0.186$ for 1222 unique reflections. By introducing appropriate linear phason strains a W-phase $\langle 3/2, 2/1 \rangle$ -approximant was reproduced. The close relationship between the structures of the W-phase and the investigated quasicrystal has two important aspects. Firstly, it proves the physical validity of the proposed structure model. Secondly, it justifies the use of the W-phase for the derivation of structural principles underlying the formation of Al-based decagonal quasicrystals.

Zusammenfassung

Diese Doktorarbeit präsentiert eine vollständige Strukturanalyse der vierschichtigen Überstruktur von dekadonalem Co-reichem Al-Co-Ni. Aufgrund der zehnzähligen, nicht-kristallographischen Symmetrie wurde ein höherdimensionaler Analyseansatz verwendet. Zum ersten Mal wurde ein fünfdimensionales Überstruktur-Modell eines vierschichtigen dekadonalen Quasikristalls entworfen und durch Strukturverfeinerung bestätigt. Die vorliegende Arbeit beweist, dass die W-Phase ein $\langle 3/2, 2/1 \rangle$ -Approximant der untersuchten Überstruktur ist. Der Vergleich der echten W-Phase mit dem generierten $\langle 3/2, 2/1 \rangle$ -Approximanten zeigt gute Übereinstimmung. Zudem gleichen die Cluster-Strukturen des W-Phase Approximanten denjenigen des Quasikristalls.

Wissen über die Struktur von Quasikristallen ist unerlässlich für ein tieferes Verständnis ihrer Entstehung, Stabilität und physikalischen Eigenschaften. Aufgrund der komplexen und anspruchsvollen Strukturanalyse konnten jedoch bislang nur einige wenige dieser Strukturen bestimmt werden. Das System Al-Co-Ni eignet sich hervorragend für Untersuchungen von dekadonalen Quasikristallen. Es weist einen grossen Stabilitätsbereich auf und zeigt komplexe Ordnungseffekte als Funktion des Co/Ni-Verhältnisses und/oder der Temperatur.

Für die vorliegende Arbeit wurden Einkristalle der Co-reichen dekadonalen Phase mit der Zusammensetzung $\text{Al}_{72.5}\text{Co}_{18.5}\text{Ni}_9$ gezüchtet. Beugungsexperimente an Einkristallen dieser Phase zeigen auch in den Zwischenschichten Bragg-Reflexe. Diese Strukturmodifikation besitzt eine ≈ 8 Å-Periodizität entlang der zehnzähligen Drehachse, d.h. eine vierschichtige Überstruktur. Die Verfügbarkeit von hochqualitativen Einkristallen bot die Gelegenheit, eine vollständige Strukturanalyse durchzuführen und die Ordnung innerhalb der Überstruktur zu verstehen. Darüber hinaus liefert das Verständnis dieser komplexen Struktur wichtige Hinweise für Nahordnungen in verwandten quasikristallinen Phasen.

Zunächst wurde ein fünfdimensionales Modell einer zweischichtigen Basisstruktur erstellt. Es wurde in der nicht-zentrosymmetrischen fünfdimensionalen Raumgruppe $P\bar{1}\bar{0}m2$ verfeinert (112 Parameter, $wR = 0.123$, $R = 0.156$, 957 Reflexe). Ausgehend von diesem Strukturmodell wurde die Überstruktur in der Raumgruppe $P\bar{1}02c$ basierend auf Moden-Analysen gelöst und verfeinert (250 Parameter, $wR = 0.039$, $R = 0.186$, 1222 Reflexe). Durch die Anwendung geeigneter linearer Phasonverzerrungen wurde daraus ein W-Phase $\langle 3/2, 2/1 \rangle$ -Approximant erzeugt. Zwei Aspekte der engen Strukturverwandtschaft von W-Phase und dem untersuchten Quasikristall sind besonders wichtig. Erstens wird die physikalische Gültigkeit des vorgeschlagenen Strukturmodells bestätigt. Zweitens rechtfertigt dies die Verwendung der W-Phase für die Ableitung von Strukturprinzipien, die der Entstehung von Al-basierten Quasikristallen zugrunde liegen.

Chapter 1

Introduction

The foundations of the field of crystallography were revolutionized in 1912 by Max von Laue. Soon after he conducted the first diffraction experiment, William Henry Bragg and his son William Lawrence Bragg introduced X-ray analysis of crystal structures. It became clear that X-rays were a form of electromagnetic radiation of short wavelength. Due to interference within a crystal, the scattering of X-rays in reciprocal space is confined to distinct points with characteristic intensities. W. L. Bragg was the first to explain this phenomenon and in honor of this achievement these point-like diffraction spots were named *Bragg peaks*.

The following decades brought significant progress and in the 1970s the field of crystallography seemed to be almost complete and fully understood. Lattice periodicity was considered an essential property of a crystal and hence for observation of sharp Bragg diffraction spots in reciprocal space. However, in addition to a perfect periodicity, one should consider *discreteness* resulting from the requirement for a minimal distance between atoms. This requirement restricts the possible rotational symmetry of a crystal to two-, three-, four- and six-fold. As this restriction also applies to reciprocal space, classical crystallography predicted only diffraction patterns with two-, three-, four- and six-fold symmetry. Considering all possible periodic arrangements in three-dimensional space, Fedorov, Schönflies and Barlow classified 230 crystallographic space groups.

Dan Shechtman's discovery on 1982 April 12th of an icosahedral phase in a rapidly solidified Al-Mn alloy [SBG84] was a sensation and triggered a drastic change in attitude concerning the structure of solids. A remarkable peculiarity of the newly discovered phase was its diffraction pattern. It showed sharp Bragg diffraction spots together with non-crystallographic symmetry, namely icosahedral point symmetry. The term "quasicrystal", coined by Dov Levine and Paul Steinhardt [LS84], accounted for the lack of translational symmetry in three-dimensional space exhibited by this new phase. At this point, it became obvious that the existing requirement for lattice periodicity was too strict. From a more generalized perspective, a crystal is defined by its spectral properties in the reciprocal

space. Namely, a Fourier spectrum of an ideal crystal is *essentially discrete*, see also definition of aperiodic crystals by *IUCr Ad-interim Commission on Aperiodic Crystals*.

Since this pioneering discovery almost three decades ago the field of quasicrystals has attracted a wide range of research by mathematicians, physicists and material scientists. The discovery of the first quasicrystal triggered a series of discoveries during which a large assortment of quasicrystals has been found. In the beginning only very small metastable quasicrystals were obtained. Nowadays several stable quasicrystals of various sizes and chemical compositions with different morphologies are known [SD08]. In addition to the three-dimensional icosahedral quasicrystals, that is to say those with three quasiperiodic directions, two-dimensional quasicrystals have also been discovered. Two-dimensional quasicrystals belong to the axial type, having two quasiperiodic directions and one periodic direction which is parallel to a five-, eight-, ten- or twelve-fold axis. Two-dimensional quasicrystals with a ten-fold axis, named decagonal quasicrystals, were first identified in a rapidly solidified Al-Mn alloy by Chattopadhyay [CRST85]. Independently, Bendersky [B85] came to a similar conclusion and established the Laue symmetry as $10/mmm$.

Recently it was reported that quasicrystal structures are not limited to intermetallic systems. They were also discovered in soft matter, namely superamolecular structures of organic dendrimers [ZULPDH08] and tri-block copolymers [HDT07]. Later, it was shown that micrometre-sized colloidal spheres could be arranged into quasicrystalline arrays by using intense laser beams that create quasi-periodic optical standing-wave patterns [MRHB08], and that colloidal inorganic nanoparticles can self-assemble into binary aperiodic superlattices [TSBCM09]. Moreover the existence of natural quasicrystals in a mineral was reported [BS09].

This new class of material does not only show unusual symmetries, but also very peculiar physical properties. Experimental results demonstrate that quasicrystals do not display the properties of their constituent elements. Despite being intermetallic compounds, they show anomalously high resistivity, which decreases with increasing temperature. For metals this is a very surprising behavior; one would normally expect this only in semiconductors. In addition, quasicrystals behave more like heat insulators at sufficiently low temperatures. Measurements of the electron transport properties show that decagonal quasicrystals show normal metallic behavior along their periodic direction and abnormal metallic behavior along the two quasiperiodic directions, thus they are strongly anisotropic. Similar measurements reveal that icosahedral quasicrystals exhibit abnormal behavior in all three quasiperiodic directions. This special behavior of electronic transport in quasicrystals as a function of temperature must be related to structural properties. In fact, for several quasicrystalline phases the calculated electronic density of states (DOS) exhibits a pseudogap at the Fermi level. This gives additional explanation and validity to the earlier reports regarding the strange electronic properties of quasicrystals. Additionally, at higher temperatures quasicrystals show improved plasticity and stronger magnetic

properties than conventional crystals. Due to their hardness and deformation resistance their main commercial application could be in high-strength surface coatings. However until now, no extensive technological application for quasicrystals have been found. One of the major reasons for this is because of the difficulty producing quasicrystalline materials on an industrial scale. Nevertheless on a small scale many stable quasicrystals of good quality have been found and their physical properties have been rigorously studied. For example, they serve as model structures for applications in phononics and photonics [LAB05, FLFS07, BLVA08].

Most quasicrystals have intimately connected crystalline phases with closely related composition and atomic structure. These crystalline phases are named "approximants", because the arrangement of atoms within their unit cells is a close approximation of the local atomic structures of their related quasicrystals. In other words, quasicrystals and their related approximants contain the same kind of clusters. The similarity of both corresponding structures depends on the size of the common fragment in both structures. Experience shows that quasicrystals and their approximants exhibit similarly anomalous physical properties related to electronic transport. Although there are similarities between quasicrystals and their approximants, the latter possess three-dimensional periodicity. Hence, large approximants serve as model systems to study physical properties of quasicrystals. In fact, without using approximants it is questionable whether theoretical studies of the physical properties of quasicrystals would be possible at all. The reason is that the Bloch theorem is not applicable in a three-dimensional quasiperiodic systems, on one hand. On other hand, a higher-dimensional representation of the interatomic forces is not straightforward. Furthermore, the study of approximants provides invaluable information for structure determination of quasicrystalline structures, as well as hints about the formation and stability of the related quasicrystals, and serves as a good indicator for the existence of a related quasicrystalline phase in a particular system.

An additional unique physical property of quasicrystals is a type of defects named *phasons*. Phasons are excitations along internal space which result in atomic rearrangements in external space. Hence they are strictly related to the higher-dimensional description of quasiperiodic systems. The term "phason" is derived from the phase change of the waves describing the position of atoms in a quasicrystal. In the current work they are of interest for two reasons. Firstly, the presence of random phasons affects the number of observed weak reflections. In a perfect quasicrystal many very weak reflections and a few very strong ones are present. Unfortunately, we cannot produce a "perfect quasicrystal", therefore, in comparison to theoretical predictions, we observe fewer weak reflections due to the presence of random phasons. Secondly, by introducing appropriate linear phason strains, a quasiperiodic structure may be transformed into its rational approximant as will be discussed in Chapter 3.

One of the most investigated systems is decagonal Al-Co-Ni. It serves as a perfect playground for structural investigation, since it has a wide variety of structural modifications. The different modifications have been quite extensively studied by high-resolution electron microscopy (HRTEM), only a few of them have been examined by X-ray diffraction. HRTEM images give 'easy' access to local structural information such as clusters and their ordering (tiling decoration). Consequently, there already exists a qualitative picture of some of the ordering phenomena as far as they are observable in structures projected along the ten-fold axis. The major shortcoming of HRTEM is that only projected information can be obtained. Since the ordering phenomena in the quasiperiodic atomic layers are intimately connected with those along the periodic direction, diffraction data are crucial for a full picture.

Most of the structural modifications in the decagonal Al-Co-Ni system show a periodicity of ≈ 8 Å (i.e. four-layer). So far however, only data related to ≈ 4 Å (i.e. two-layer) periodicity has been used. The reason is that the reciprocal space layers related to the two-fold superstructure along the ten-fold axis, i.e. four-layer periodicity, show only diffuse intensities in all cases except basic Co-rich phase. In addition, in this system a W-phase approximant with ternary composition and a periodicity of $8.158(1)$ Å has been reported [HON01, HOSS01]. A closer look at the behavior of a quasicrystal on an atomic scale may help us to answer several fundamental questions. Firstly, how are these special solid-state systems stabilized? Secondly, why are the physical properties of quasicrystals so unique?

The goal of the present research was to synthesize a single-crystal of the decagonal Al-Co-Ni Co-rich phase and to determine its structure. Single-crystals that show sharp Bragg peaks in all reciprocal layers, related to a complex quasicrystal superstructure with four atomic layers along the decagonal axis, have been successfully prepared. Chapter 2 focuses on the experimental details of the sample preparation, and X-ray data collection and analysis.

Several methods have been applied for the structure determination and these are discussed in Chapter 3, along with the basic concepts for the higher-dimensional approach. Initially, the Patterson method was used which has the advantage that it only requires experimentally obtained intensities as an input. One can check relatively easily the quality of the experimental data after integration and in addition, get an initial idea about the quasicrystal structure in higher-dimensional space. However, the complete deconvolution of the Patterson function of a quasicrystal is very cumbersome so that it is practically impossible to obtain a detailed structure solution. Two different algorithms, Low Density Elimination (LDE) and Charge Flipping (CF) have been applied for *ab initio* phasing of the experimentally obtained amplitudes. Both methods gave an average structure solu-

tion, however, both failed in the determination of the superstructure. Additionally, two different methods for approximant generation from the quasicrystal structure are introduced and complemented by an example. In the final section, a simplified superstructure model is presented and possible methods for its solution are discussed.

Chapters 4 and 5 contain the core of the results. Chapter 4 presents the average structure solution whilst in Chapter 5 a full structure analysis of the four-layer superstructure is discussed. As a final result, a model for the superstructure has been proposed and validated based on X-ray single-crystal data. In addition, it was shown that the W-phase approximant can be derived from a parent quasicrystal structure through a geometrical transformation. The structures of both the existing and generated approximants are very similar. Moreover, they consist of similar building units "clusters" and possess similar structural modulations that lead to the superstructure formation. Chapter 6 contains concluding remarks.

Chapter 2

Experimental

The focus of this chapter is on the experimental work. After a short introduction into the system Al-Co-Ni, a detailed description of the sample synthesis will be presented. The last section concentrates on single-crystal X-ray diffraction data analysis.

2.1 System Al-Co-Ni

The majority of the quasicrystals discovered so far are aluminium-based ternary alloys. The discovery of thermodynamically stable decagonal Al-Co-Ni by Tsai *et al.* in 1989 was the trigger for a massive investigation of the Al-Co-Ni phase diagram [TIM89]. Since then, the system Al-Co-Ni has become one of the most crucial structures investigated. Later Kek found that the stability region of the decagonal Al-Co-Ni phase is $\text{Al}_{74}\text{Co}_{26}$ - $\text{Al}_{69}\text{Ni}_{31}$ which he named 'D-(Al-Co-Ni)' [K91]. Several structural modifications were found within D-(Al-Co-Ni) region during the last twenty years [EIST92, ETYST94, GU94, GH96a, GH96b, GH98, GD04, RBNGSL98]. They are characterized by differences in their diffraction patterns, for example the presence or absence of satellite reflections and different periodicities along the ten-fold axis. The known structural modifications are shown in Fig. 2.1: basic Ni-rich (b-Ni) decagonal phase; basic Co-rich (b-Co); 5f - pentagonal phase with HT and LT modifications; S1 - superstructure type I with only first-order superstructure reflections; I - superstructure type-I (S1+ S2); II - superstructure type-II [EIST92, ETYST94, RBNL95]. On the Ni-richer side the diffraction patterns include main reflections only that results in a period of ≈ 4 Å along the ten-fold axis. Therefore this decagonal quasicrystal modification is named basic Ni-rich decagonal phase. On the Co-richer side most of the diffraction patterns include satellite reflections, which indicates the presence of various structural modifications. In addition, they show diffuse intermediate layers implying disorder related to the ≈ 8 Å period. The intensity of the diffuse reflections is enhanced with increasing Co content and the basic Co-rich phase is a special case as it has a period of ≈ 8 Å that corresponds to a well-ordered superstructure along the ten-fold axis.

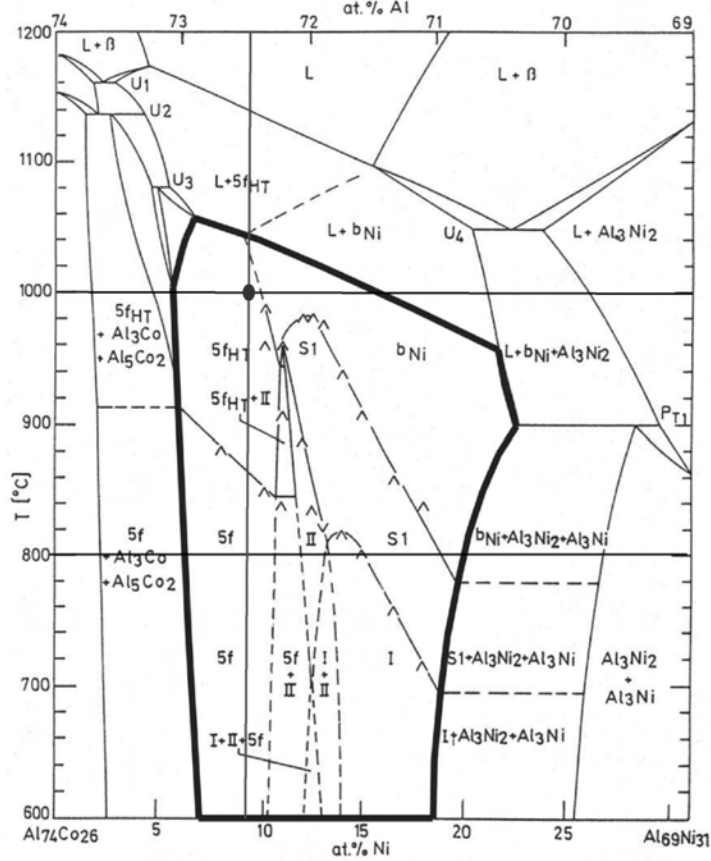


Figure 2.1: Temperature against composition section along the composition line $\text{Al}_{74}\text{Co}_{26}$ - $\text{Al}_{69}\text{Ni}_{31}$ showing the variety of structural modifications within the decagonal phase stability region [RBNGSL98]. The investigated sample with the composition of the $\text{Al}_{72.5}\text{Co}_{18.5}\text{Ni}_9$ is marked. For definition of the phases see text.

Thus it is evident that in the decagonal Al-Co-Ni phase a variety of polymorphism is present. These structural modifications, such as a different period along the ten-fold axis, different structure arrangements and varying sizes of clusters, result from compositional variations and/or changes in thermodynamical processes. It is interesting to mention that the main composition variations occur between the two transition metals (TM), namely Co and Ni, where the Al content is approximately 70 at% for all the modifications. Though Ni and Co are nearest neighbors in the periodic table and differ only by one d -electron, the structures vary significantly when changing the Co/Ni ratio. In the framework of the current research, due to experimental limitations, Co and Ni cannot be distinguished and the Al-Co-Ni system is treated as a binary Al-TM system. Moreover, an approximant structure, the W-phase, has been reported for this system [HON01]. This is the only stable ternary high rational approximant that has been found in the Al-Co-Ni system and it has a chemical composition that is very close to the quasicrystal structure studied here.

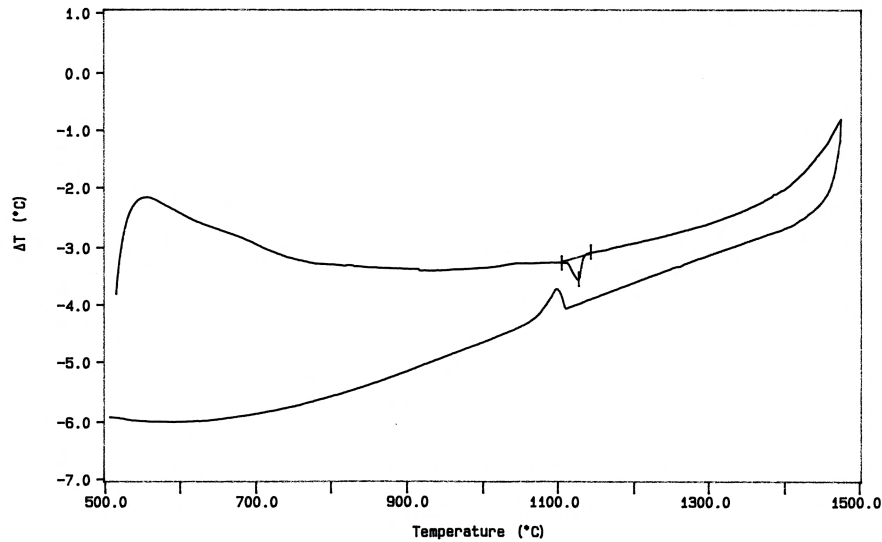


Figure 2.2: DTA analysis showing heating and cooling plots for an as-cast sample (8.34 mg) carried in the temperature range 500 °C-1500 °C with a cooling rate of 10 °C/min. A phase transition from a 5f - pentagonal solid solution to its partially melting state is indicated by an exothermic peak.

2.2 Sample Preparation and Analysis

For sample preparation, compacts with composition $\text{Al}_{72.5}\text{Co}_{18.5}\text{Ni}_9$, weighing 1g each, were pressed from pulverized Al (Heraeus 99.95 wt.%), Co (Alfa Aesar 99.8 wt.%) and Ni (Heraeus 99.99 wt.%) in an argon atmosphere (Mbraun glove box 150 B-G, PanGas Ar 99.998 %). Pre-alloys were prepared by melting the compacts in an arc furnace (DE-GUSSA VOLi O) with a non-consumable tungsten electrode under Ti-gettered argon.

The as-cast samples were analyzed by differential thermal analysis (DTA) (Perkin Elmer DTA 7) using Al_2O_3 crucibles under high-purity argon. Fig. 2.2 shows the DTA analysis of an 8.34 mg sample carried in the temperature range 500 °C - 1500 °C using a cooling rate of 10 °C/min. A phase transition from a 5f - pentagonal solid solution to its partially melting state is indicated by an exothermic peak. This analysis helps to plan the sample preparation.

Quasicrystal growth and annealing was performed in a high-vacuum resistance furnace (PVA MOV 64). Therein, an as-cast sample was heated in an Al_2O_3 crucible to 1350 °C (i.e. above melting temperature), held at this temperature for 20 min, then cooled to 1000 °C with a cooling rate of 0.24 °C/min before subsequent annealing for 48 hours at this temperature. Eventually, the sample was quenched by jetting cold argon into the sample chamber.

A sample that contains single-crystals of the decagonal quasicrystal can be identified by using an optical microscope. Decagonal phase single-crystals are normally characterized by boundary plane facets showing a distinct decagonal morphology. However, in the resulting sample, the decagonal phase often coexists in equilibrium with a second phase.

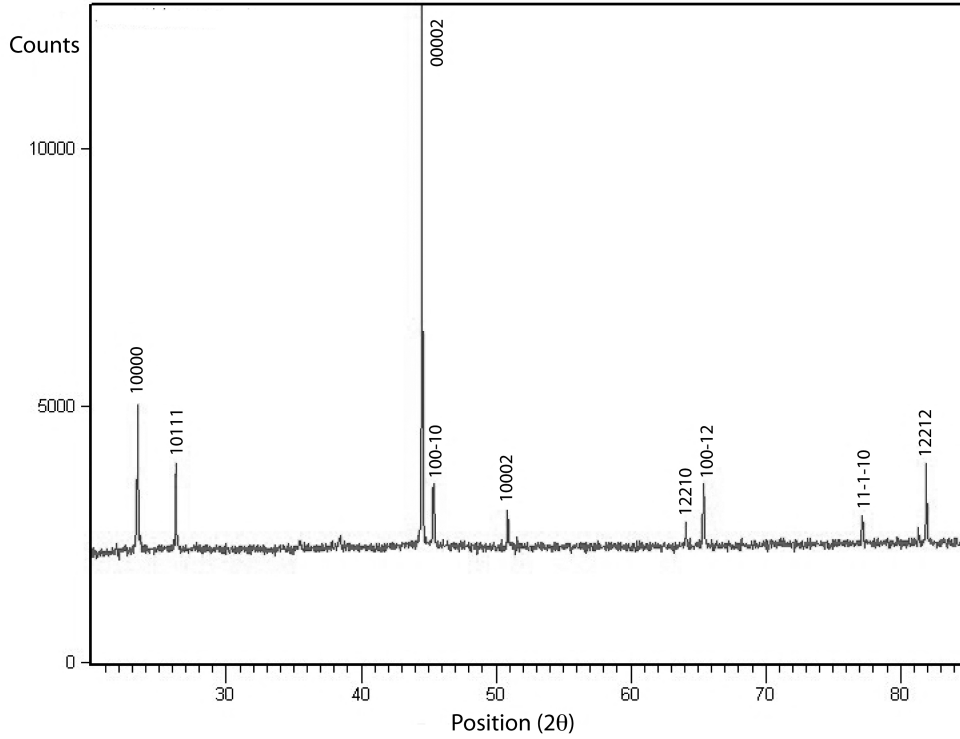


Figure 2.3: XRD intensities of decagonal $\text{Al}_{72.5}\text{Co}_{18.5}\text{Ni}_9$. Indexing refers to the average structure.

The easiest way to detect the additional phase is by analyzing the powder patterns and by observation using scanning electron microscopy (SEM) images.

The powder sample was examined by X-ray powder diffraction (XRPD) (PANalytical X'Pert Pro diffractometer, standard θ - 2θ Bragg-Brentano geometry, $\text{Cu K}\alpha 1$, $10^\circ \leq 2\theta \leq 100^\circ$, 0.02° step width). The XRD pattern, presented in Fig. 2.3, shows that only the decagonal phase is present. The satellite reflections are too weak to be observed in such an experiment. The diffraction peaks were indexed by comparison to the calculated diffraction pattern of the Al-Co-Ni basic structure.

For the SEM analysis, several sample fragments were embedded in epoxy powder (SpeciFast, Struers) pressed under a force of 15 kN at a temperature of 180°C for 5 min. The resulting sample was then polished with a $1\ \mu\text{m}$ diamond suspension, and finally subjected to electropolishing. SEM was performed in back-scattering mode at 30 kV with the resulting imaging, as presented in Fig. 2.4, showing that a homogeneous alloy was obtained. The composition of the sample carried out by the energy dispersive X-ray spectroscopy (EDX) analysis with 15-30 kV accelerating voltage on a LEO 1530 analyzer and using the VOYAGER software. The final composition has been determined to be $\text{Al}_{72.5}\text{Co}_{18.5}\text{Ni}_9$.

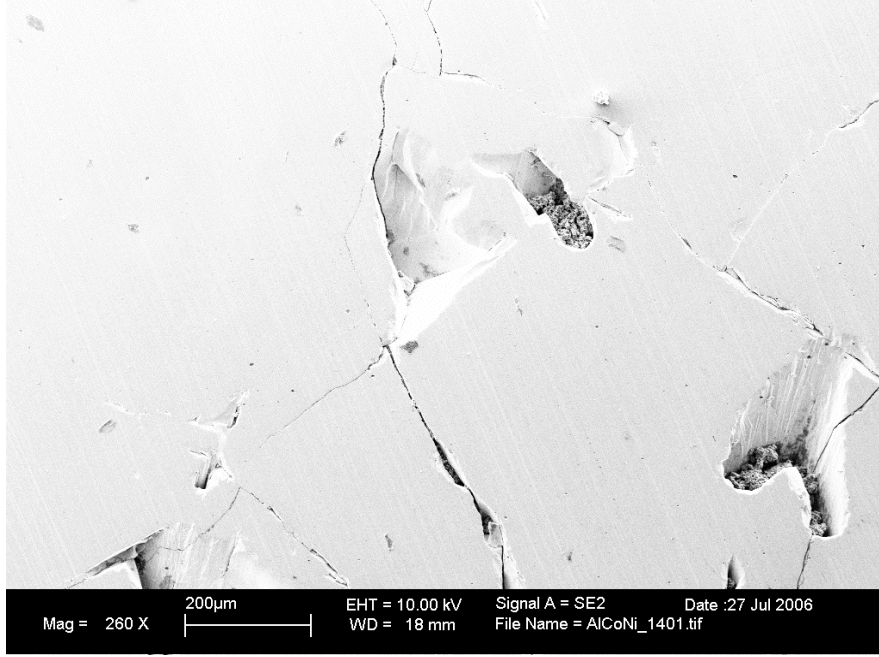


Figure 2.4: Scanning electron microscopy (SEM) image of decagonal $\text{Al}_{72.5}\text{Co}_{18.5}\text{Ni}_9$ obtained in back-scattering mode at 30 kV.

2.3 Single-Crystal X-Ray Diffraction Data Analysis

Single-crystal X-ray diffraction data were collected at SNBL/ESRF Grenoble using a marresearch 345 imaging-plate (IP) scanner (180 frames with an oscillation angle of $\phi = 1^\circ$ each, wavelength $\lambda = 0.72326 \text{ \AA}$). Two data sets were collected, *data set 1* with an exposure time of 4 sec/frame to prevent saturation of strong reflections, and *data set 2* with 100 sec/frame in order to collect weak superstructure reflections. The reciprocal space sections $h_1h_2h_3h_4h_5$ with $h_5 = 0, 1, 2, 3$ as well as $h_1h_2h_2h_1h_5$ and $h_1h_2\bar{h}_2\bar{h}_1h_5$ are shown in Fig. 2.5. Long exposure times during the X-ray experiment increases the quality of the counting statistics, since the background becomes smoother. Hence, to collect reliable information for the weak reflections, it was essential to increase the exposure time. Since the strongest reflections of these two synchrotron data sets are still oversaturated, an *in-house* data set (*data set 3*) was also collected employing a four-cycle diffractometer equipped with a charge-coupled device (CCD) detector (Oxford Diffraction Xcalibur, $7.5^\circ \leq 2\theta \leq 55.5^\circ$, 180 frames with $\phi = 1^\circ$ each, exposure time 10 sec/frame, 50 kV, 40 mA, graphite monochromatized MoK_α radiation). Comparison between reciprocal space sections reconstructed from the data sets that were collected at SNBL/ESRF Grenoble (Fig. 2.5) and by the *in-house* diffractometer (Fig. 1 in Article I) show that the latter have much lower resolution, mainly due to the divergence of the X-ray beam. For the two data sets collected at SNBL/ESRF Grenoble a needle-shape sample of $\approx 30 \mu\text{m}$ and for the *in-house* data set a needle-shape sample of $\approx 70 \mu\text{m}$ were used. In all three X-Ray diffraction data sets the intensities were corrected for Lorentz and polarization factors.

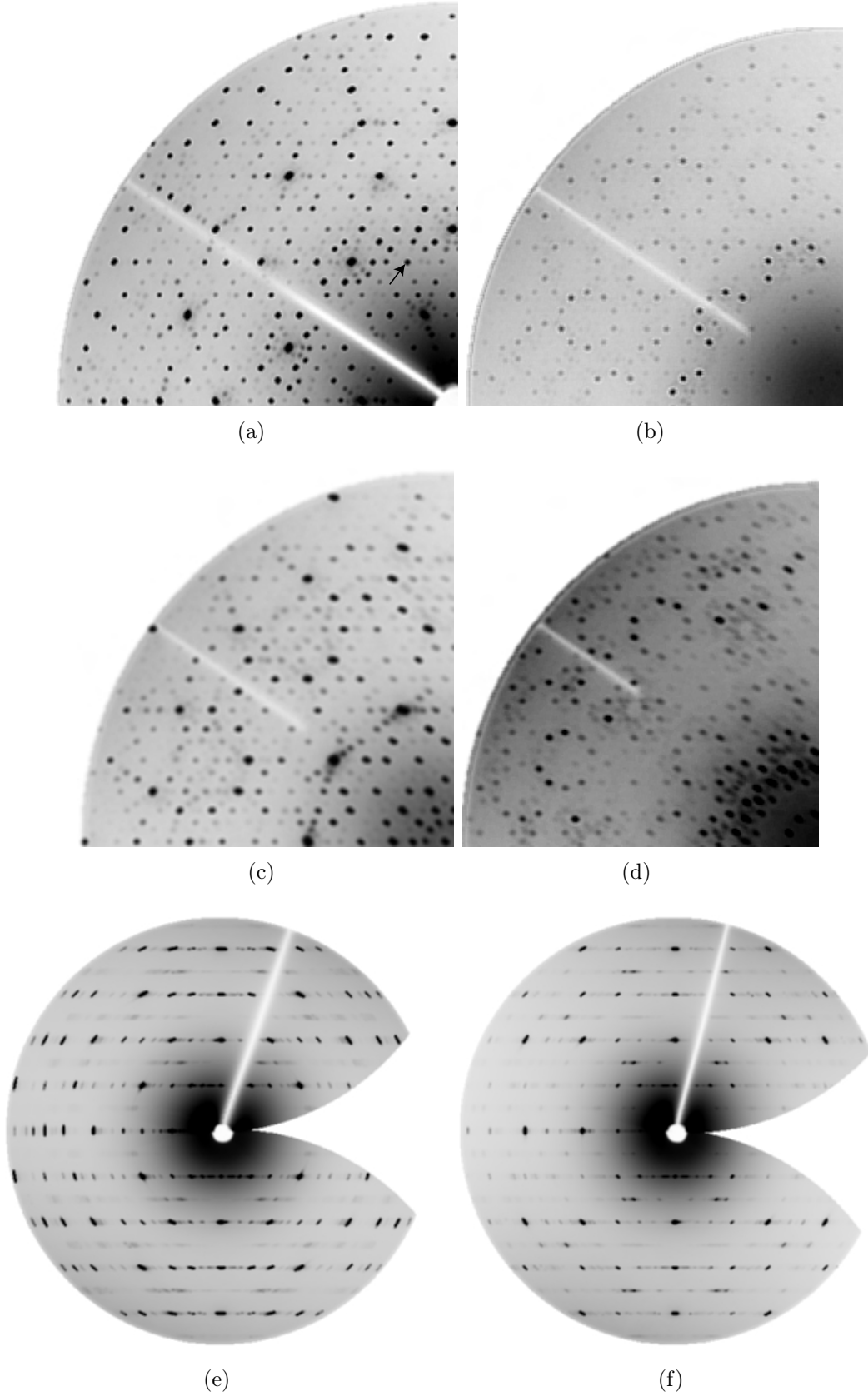


Figure 2.5: Reciprocal space sections of decagonal $\text{Al}_{72.5}\text{Co}_{18.5}\text{Ni}_9$ reconstructed from 180 IP-scanner frames each: $h_1h_2h_3h_4h_5$ with (a) $h_5=0$, (b) $h_5=1$, (c) $h_5=2$, (d) $h_5=3$ (h_5 referring to the four-layer $8.144(2)$ Å period), (e) $h_1h_2\bar{h}_2\bar{h}_1h_5$ and (f) $h_1h_2h_2h_1h_5$. The main ($h_5=2n$) and satellite ($h_5=2n+1$) reflections are shown in sections (a, c) and (b, d), respectively. 10000 reflection (Yamamoto setting[Y96]) is marked by an arrow in (a).

In the case of periodic crystals, the direct lattice and unit cell can be uniquely derived from the experimentally accessible reciprocal lattice. For quasicrystals, the relation between the direct and the reciprocal space is not so evident. Moreover, the presence of superstructure reflections might introduce additional complexity in the reciprocal space analysis. In fact, for decagonal quasicrystals the diffraction pattern of a superstructure will generally appear only rotated and scaled with respect to the average structure.

In contrast to incommensurately modulated crystals, quasicrystals cannot be described in terms of a modulation of a basic structure or by two or more substructures. The fundamental reason for this is that the underlying structure of quasicrystals is itself quasiperiodic. The ideal Penrose tiling serves as a basic model for the description of the underlying quasiperiodic order. In this tiling each vertex is decorated by an atom or an atomic cluster. Because quasicrystals lack a basic periodic structure, their diffraction patterns cannot be characterized by having subsets of "main" and "satellite" reflections in the same meaning as for incommensurately modulated crystals. However, similar terminology is used for quasicrystal structures. Their "main reflections" have relatively strong intensities and can be indexed based on a \mathbb{Z} - module of rank five. All additional reflections have much weaker intensities and appear due to some structural modulations in an underlying quasiperiodic crystal.

In the case of our decagonal quasicrystal, all reflections in the even layers ($h_5=2n$) can be indexed with the basis of the Ni-rich decagonal phase. In contrast, for indexing all reflections in the odd layers ($h_5=2n + 1$) a superstructure basis had to be applied. These bases are related to each other by a roto-scaling operation: rotation by $\pi/10$ and scaling by a factor of $2\cos \pi/10=1.90211$. Hence, all reflections in the even layers are main reflections and all reflections in the odd layers are satellite reflections (see Fig. 2.5). Since the reciprocal space of the decagonal phase is invariant under a scaling by τ^n , no unique setting notation exists. However, the important settings for decagonal quasicrystals are those defined by Steurer and Yamamoto (see [S04] and [Y96] respectively). They are related to each other by a scaling matrix, for more details see [Y96].

Within the Ni-basic basis, the index of the strongest reflection in the zero layer is 13420 in the Yamamoto setting (02210 in the Steurer setting) that is used throughout this thesis (see Fig. 2.5(a)).

A data reduction performed using the software package CrysAlis (Oxford Diffraction). According to the observed Laue symmetry $10/mmm$, *data set 1* has 39,315 reflections merged into 1,405 unique reflections with $R_{int}=0.174$, *data set 2* has 41,810 reflections was merged into 1,434 unique reflections with $R_{int}=0.163$ and *data set 3* has 899,034 reflections merged into 1,764 unique reflections with $R_{int}=0.098$.

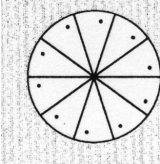
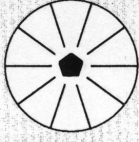
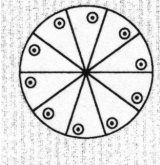
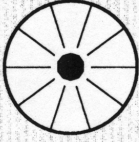
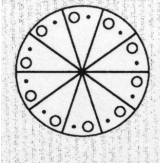

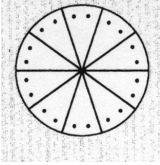
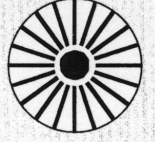
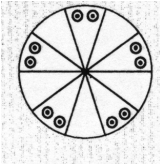

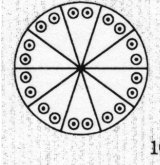
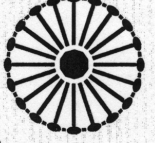
Quasicrystals can be seen as real space projections of crystals in a higher-dimensional space. Accordingly, the number of required dimensions necessary to describe a quasicrystal depends on its symmetry. Decagonal quasicrystals with five-fold or ten-fold rotational axes

require a five-dimensional space description and their symmetry can be described by five-dimensional decagonal space groups. Relevant five-dimensional decagonal space groups should fulfill the condition that their five-dimensional point groups are isomorphous to the three-dimensional point group describing the diffraction symmetries. Hence, there are only 34 relevant decagonal non-equivalent space groups [Y96], whereas the five-dimensional decagonal lattices are all primitive ones. Tab. 2.1 summarizes the possible pentagonal and decagonal point groups.

Essential information about possible space groups can already be obtained from diffraction experiments. Moreover, it is "more natural" to provide formulations of the space groups in the language of reciprocal space, since it is more accessible to experiments than real space. Possible space groups can be determined based on the point group of the Fourier spectrum (Laue group) and the extinction conditions present. In this state, however, the space group determination is not unique, since the Fourier spectrum is always centrosymmetric according to Friedel's law.

As for three-dimensional crystals, extinction conditions can be classified into two types. The first type comprises general extinctions; they uniquely define the Bravais type of the underlying lattice, such as primitive, body-centered or face-centered and concern all reflections. The other type comprises special extinctions; they are related to the presence of glide planes or screw axes and concern only a special series of reflections. Thus the extinction rules carry information about the non-primitive translations and can be expressed as rules on the allowed values for the $h_1h_2h_3h_4h_5$ indices, which is in analogy to classical crystals. However, in contrary to classical crystals, the choice of the coordinate system for quasicrystals is not unique and one should know in which coordinate system the determined extinction conditions were defined.

Table 2.1: Decagonal point and space groups constructed by analogy with trigonal and hexagonal point groups as given in [TTT94].

Three-dimensional point group	k	Five-dimensional space group	Extinction condition
  10	10	$P10$ $P10_j$	No condition $0000h_5: jh_5 = 10n$
  10/m	20	$P\frac{10}{m}$ $P\frac{10_5}{m}$	No condition $0000h_5: h_5 = 2n$
  10 2 2	20	$P1022$ $P10_j22$	No condition $0000h_5: jh_5 = 10n$
  10mm	20	$P10mm$ $P10cc$ $P10_5mc$ $P10_5cm$	No condition $h_1h_2h_2h_1h_5: h_5 = 2n$ $h_1h_2\bar{h}_2\bar{h}_1h_5: h_5 = 2n$ $h_1h_2\bar{h}_2\bar{h}_1h_5: h_5 = 2n$ $h_1h_2h_2h_1h_5: h_5 = 2n$
  $\bar{1}0m2$	20	$P\bar{1}0m2$ $P\bar{1}0c2$ $P\bar{1}02m$ $P\bar{1}02c$	No condition $h_1h_2h_2h_1h_5: h_5 = 2n$ No condition $h_1h_2\bar{h}_2\bar{h}_1h_5: h_5 = 2n$
  10/mmm	40	$P\frac{10}{m}\frac{2}{m}\frac{2}{m}$ $P\frac{10}{m}\frac{2}{c}\frac{2}{c}$ $P\frac{10_5}{m}\frac{2}{m}\frac{2}{c}$ $P\frac{10_5}{m}\frac{2}{c}\frac{2}{m}$	No condition $h_1h_2h_2h_1h_5: h_5 = 2n$ $h_1h_2\bar{h}_2\bar{h}_1h_5: h_5 = 2n$ $h_1h_2\bar{h}_2\bar{h}_1h_5: h_5 = 2n$ $h_1h_2h_2h_1h_5: h_5 = 2n$

Chapter 3

Structure Determination of Quasicrystals

The main goal of a structure analysis is to determine atomic positions and their occupancies. These positions are based on the electron density distribution calculated from the diffraction data while taking into account chemical and physical properties. However, a reconstruction of a crystal structure from an X-ray diffraction experiment is not a straightforward process since the experimentally accessible information is incomplete.

In a single-crystal X-ray experiment, the positions and intensities of the Bragg peaks are measured. The former carry information about the lattice whilst the latter convey incomplete information on the structure factors which describe the electron distribution in the unit cell. Structure factors are complex numbers; only their real parts, the amplitudes (square root of intensities), are measured while the imaginary parts, the phases, are missing. The missing information has to be obtained indirectly. Once it is done in a satisfactory way, a Fourier transform can be used to convert the reciprocal-space diffraction pattern into a real-space object, the crystal structure.

Structure analysis is one of the most intriguing questions in the field of quasicrystals. A lack of periodicity in three-dimensional space makes the structure determination process a less intuitive and challenging task. On top of this, the quality of X-ray data for a single-crystal of decagonal quasicrystal suffers from several offsets. The X-ray diffraction data sets of the decagonal quasicrystals consist of few strong and many weak reflections. However in comparison to an ideal quasicrystal, the total number of observed weak reflections is still relatively low because of the presence of random phason fluctuations. The occurrence of superstructure reflections can impose additional challenges on the process of structure determination.

Various experimental methods have been used to determine the structure of quasicrystals as well as to investigate their physical properties directly [SD09]. Methods such as high-resolution transmission electron microscopy (HRTEM), selected area electron diffraction (SAED) and high-angle annular detector dark-field scanning transmis-

sion electron microscopy (HAADF-STEM) have been employed. The electron microscopy methods, however, provide only local information average averaged over the sample thickness. Whereas, X-ray diffraction provides global information taken modulo the higher-dimensional unit cell. Still, none of the previously mentioned methods can distinguish between non-centrosymmetric and centrosymmetric space groups. This only becomes possible applying convergent beam electron diffraction (CBED).

In the past, two different competing approaches have been developed. One, higher-dimensional method, relies on numerical structure refinement by applying Patterson, Fourier and MEM analysis to the intensities obtained by X-ray experiments. As a result, the structure in higher-dimensional space is obtained. That is to say, the location of the occupation domains in the higher-dimensional unit cell is determined. By applying the section method (which will be discussed further), the coordinates of individual atoms in external space are obtained. The drawback of this approach is that only approximate higher-dimensional structure solution can be obtained. Consequently, it can lead to unreasonable solutions in physical space.

The other, three-dimensional method, is based on tiling and decoration. One starts with two or more elementary cells (tiles) which fill the space quasiperiodically. These tiles are then decorated with atoms or with atomic clusters using appropriate matching rules and assuming a reasonable atomic packing. Also, a higher-dimensional approach is applied here, but this time only the coordinates of the tile vertices are determined and not those of individual atoms. As a result, a variety of structure models for quasicrystals have been proposed. Most of them are based on different types of tilings [SD09] including ideal quasiperiodic tilings, random tilings and glass models.

Meanwhile it became clear that to tackle structure determination of quasicrystals it is important to use all available methods to take into account as much information as possible. Furthermore, it is evident that the refinement process is a necessary step in a quantitative structure analysis and should be performed to confirm and improve a structure model. A possible description of the structure determination process is presented in Fig. 3.1.

In the current work several methods have been applied to determine the structure of decagonal $\text{Al}_{72.5}\text{Co}_{18.5}\text{Ni}_9$. The focus of this section is on the basic concepts required for the structure analysis of quasicrystals. Firstly, the mathematical background required for a higher-dimensional approach will be given. Then the different tiling methods will be discussed. Finally an overview of the crystallographic methods that were used for structure analysis will be presented.

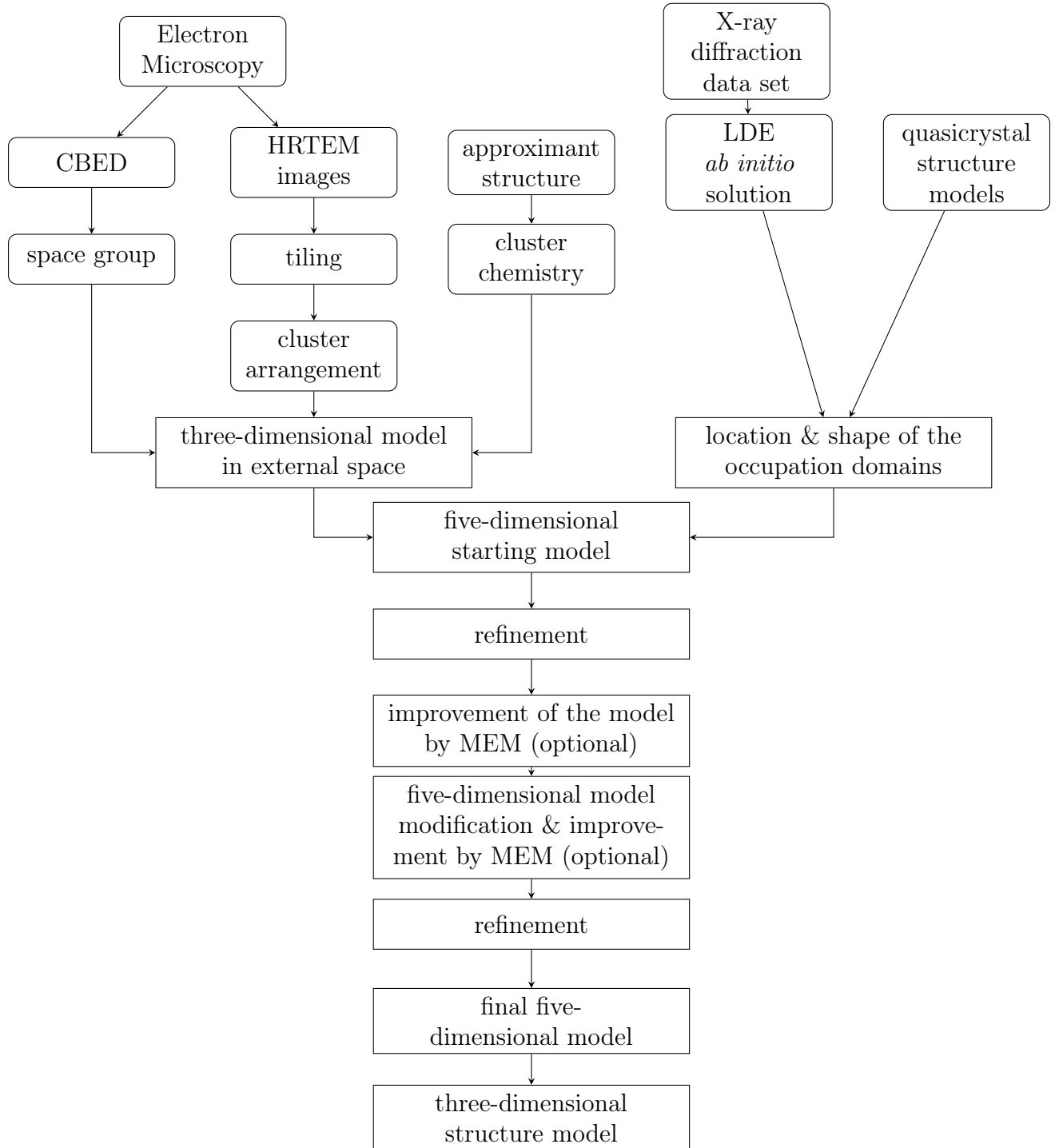


Figure 3.1: Flowchart for decagonal quasicrystal structure analysis.

3.1 Periodicity in Higher-Dimensional Space

One of the most important developments in the 1980s was the application of higher-dimensional crystallography to real structures. Efforts were made to extend the theory of the basic 230 crystallographic space groups. The most comprehensive studies on crystallography in four-dimensional space were carried out by H. Brown, R. Bülow, J. Neubüser, H. Wondratschek, and H. Zassenhaus [NWB71, BNW71, WBN71, BBNWZ78]. Furthermore, a study of N -dimensional crystallography was published by Schwarzenberger [S80].

The first extension of classical three-dimensional crystallography accounted for incommensurably modulated structures [dW74, JJ77, dW77, JJ79, JJ80], and later work also included quasicrystals [B86, J86, CGM88a, CGM88b]. Nowadays, non-crystallographic point groups are included in the International Tables for Crystallography - Volume A [ITCA].

In the framework of the higher-dimensional approach (with dimensions >3) fictitious additional dimensions are used. The higher-dimensional (nD) space is split into two subspaces, orthonormal to each other. These are the three-dimensional (3D) external space and the $(n-3)$ -dimensional internal space. This introduces additional degrees of freedom that allows to describe quasicrystals as periodic structures. Hence, this approach enables the classification of higher-dimensional space groups and the formulation of the extinction conditions observed in the diffraction patterns. This significantly simplifies structure analysis and structure description. Moreover the generalization of three-dimensional crystallography to higher dimensions allows well-developed powerful mathematical techniques from standard crystal structure analysis to be applied to quasicrystal structure analysis. These techniques include Patterson method, Fourier method, Maximum Entropy Method (MEM) and Least Square method. All of these methods are implemented in the software QUASI07_08 by Akiji Yamamoto [Y96, Y08].

A hint for applying a higher-dimensional approach to quasicrystal analysis came from the analysis of diffraction patterns. It was clear that three integer indices (Miller hkl indices) are insufficient to index all Bragg peaks in diffraction patterns that do not obey classical crystallographic symmetries. That is to say, in the framework of higher-dimensional crystallography, diffraction spots in external space are considered a projection of the higher-dimensional reciprocal lattice and their intensities are interpreted as Fourier spectra of a higher-dimensional crystal.

It is important to mention that while the higher-dimensional approach proved to be an excellent mathematical tool, its application is not straightforward. Therefore there is always a tendency to seek a simpler way to tackle and visualize quasicrystal structures. An alternative more general physical space approach has been established by Rokhsar, Wright, and Mermin [RWM88a, RWM88a] with later contributions by Rabson, Ho, Dräger, and Lifshitz [L95]. They showed that the Fourier space approach for the conventional symme-

try classification of crystals can be reformulated by abandoning the traditional reliance on periodicity. As a result, a unified method in three dimensions has been proposed for the treatment of aperiodic crystals - modulated crystals, composite crystals and quasicrystals. The method does not rely on projecting higher-dimensional crystallographic space groups, but on three-dimensional Fourier space. In the framework of this approach the extinction conditions can be expressed by simple phase relationships. This approach allows the computation of all crystallographic or quasicrystallographic space groups in three-dimensional space.

In the particular case of decagonal quasicrystals, diffraction patterns possess a ten-fold axis. Thus, for indexing all Bragg peaks, five reciprocal basis vectors are needed. Hence, any scattering vector \mathbf{H} can be written as a linear combination as follows:

$$\mathbf{H} = \sum_{j=1}^5 h_j \mathbf{a}_j^* \text{ with } h_j \in \mathbb{Z} \quad (3.1)$$

where the basis vectors \mathbf{a}^* are given as follows due to orthogonality:

$$\mathbf{a}_j^* = a^*(\cos(2\pi j/5), \sin(2\pi j/5), 0), \text{ where } a^* = \|\mathbf{a}_j^*\| \text{ for } j = 1, \dots, 4$$

$$\text{and along the ten-fold axis } \mathbf{a}_5^* = a_5^*(001). \quad (3.2)$$

The unit vectors that span the reciprocal lattice \mathbf{D}^* in terms of the basis vectors of the corresponding irreducible representations \mathbf{a}_i ($i = 1, \dots, 4$) and \mathbf{a}_5 are given as:

$$\mathbf{d}_j^* = \frac{a^*}{\sqrt{5}}[c_{(j-1)}\mathbf{a}_1 + s_{(j-1)}\mathbf{a}_2] + \frac{a'^*}{\sqrt{5}}[c_{2(j-1)}\mathbf{a}_3 + s_{2(j-1)}\mathbf{a}_4]$$

$$\text{and } \mathbf{d}_5^* = c^*\mathbf{a}_5 = \mathbf{c}^*. \quad (3.3)$$

Expanding or contracting a diffraction pattern of a decagonal quasicrystal by a factor of τ^n ($\tau = 2\cos(\pi/5) = (1 + \sqrt{5})/2$ and $n \in \mathbb{Z}$) yields a diffraction pattern similar to the original. This interesting property shows that inflation/deflation symmetry is present. Therefore the choice of the five reciprocal-basis vectors is not unique, since a^* in external space cannot be uniquely determined. It is possible to obtain equivalent sets of vectors by applying the similarity transformation matrix S on the unit vectors \mathbf{d}_j^* , where S for the decagonal lattice is given by:

$$S = \begin{pmatrix} 0 & 1 & 0 & -1 & 0 \\ 0 & 1 & 1 & -1 & 0 \\ -1 & 1 & 1 & 0 & 0 \\ -1 & 0 & 1 & 0 & 0 \\ 0 & 0 & 0 & 0 & 1 \end{pmatrix}. \quad (3.4)$$

Thus, unit vectors related by $\mathbf{d}_i^{*'} = \sum_{j=1}^m \mathbf{d}_j^* (S^m)_{ji}$ are equivalent. The determinant of S should be ± 1 , since the similarity transformation should preserve the unit cell volume. The resulting vectors $\mathbf{d}_i^{*'}$ are parallel to \mathbf{d}_j^* , but have τ^m times larger external components and τ^{-m} times smaller internal components. In the framework of this work transformations between two bases, the so called Yamamoto basis and Steurer basis are used frequently. These relevant transformations are as follows:

The transformation matrix from the Steurer basis to the Yamamoto basis is:

$$S_{s \rightarrow y} = \begin{pmatrix} 0 & 1 & 0 & -1 & 0 \\ 0 & 1 & 1 & -1 & 0 \\ -1 & 1 & 1 & 0 & 0 \\ -1 & 0 & 1 & 0 & 0 \\ 0 & 0 & 0 & 0 & 1 \end{pmatrix}. \quad (3.5)$$

The transformation matrix from the Yamamoto basis to the Steurer basis is:

$$S_{y \rightarrow s} = \begin{pmatrix} -1 & 1 & 0 & -1 & 0 \\ 0 & 0 & 1 & -1 & 0 \\ -1 & 1 & 0 & 0 & 0 \\ -1 & 0 & 1 & -1 & 0 \\ 0 & 0 & 0 & 0 & 1 \end{pmatrix}. \quad (3.6)$$

The five vectors that span the five-dimensional direct lattice \mathbf{d} are obtained from Eq. 3.3 by using the orthogonal conditions:

$$\mathbf{d}_j = \frac{2a}{\sqrt{5}} [(c_j - 1)\mathbf{a}_1 + s_j\mathbf{a}_2 + (c_{2j} - 1)\mathbf{a}_3 + s_{2j}\mathbf{a}_4] \\ \text{for } j = 1, \dots, 4 \text{ and } \mathbf{d}_5 = c\mathbf{a}_5 = \mathbf{c} \quad (3.7)$$

where $a^* = 1/a$, $c^* = 1/c$ and $c_j = \cos(2\pi j/5)$, $s_j = \sin(2\pi j/5)$, $j = 1, \dots, 4$. The vectors \mathbf{a}_1 , \mathbf{a}_2 and \mathbf{a}_5 are perp-space unit vectors and \mathbf{a}_3 and \mathbf{a}_4 are par-space unit vectors.

The five-dimensional \mathbf{D} lattice can be decomposed into two orthogonal subspaces: the external three-dimensional space V_E (physical space) and the internal two-dimensional space V_I (complementary space). This corresponds to the decomposition of \mathbf{D}^* into V_E^* and V_I^* . Hence, the D-basis is the crystal reference system and the V-basis is a Cartesian orthonormal reference system. In reciprocal space, the \mathbf{D}^* -basis is the reciprocal lattice reference system and its orthogonal reference system is given by the \mathbf{V}^* -basis. The unit vectors of decagonal reciprocal and direct lattices in four-dimensional space as defined in Yamamoto's settings are shown in Fig. 3.2.

The transformation matrix from an average basis to a superstructure basis in reciprocal

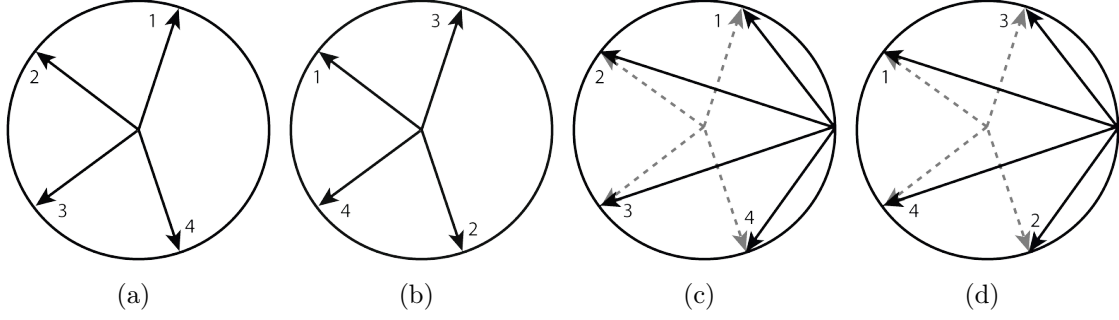


Figure 3.2: The projection of the unit vectors of decagonal reciprocal (a, b) and direct (c, d) lattices in four-dimensional space showing the external components of the unit vectors (a, c) and the internal space components (b, d).

space is:

$$S_{av \rightarrow sup} = \begin{pmatrix} 1 & 0 & 1 & -1 & 0 \\ 0 & 1 & 1 & 0 & 0 \\ -1 & 0 & 2 & 0 & 0 \\ 0 & -1 & 1 & 1 & 0 \\ 0 & 0 & 0 & 0 & 2 \end{pmatrix}. \quad (3.8)$$

Consequently, the transformation matrix from a superstructure basis to an average basis in reciprocal space is:

$$S_{sup \rightarrow av} = \begin{pmatrix} 1 & 0 & 1 & -1 & 0 \\ 0 & 1 & 1 & 0 & 0 \\ -1 & 0 & 2 & 0 & 0 \\ 0 & -1 & 1 & 1 & 0 \\ 0 & 0 & 0 & 0 & 2 \end{pmatrix}^{-1} = 1/5 \begin{pmatrix} 2 & 2 & -3 & 2 & 0 \\ -1 & 4 & -1 & -1 & 0 \\ 1 & 1 & 1 & 1 & 0 \\ -2 & 3 & -2 & -2 & 0 \\ 0 & 0 & 0 & 0 & 5/2 \end{pmatrix}. \quad (3.9)$$

In direct space the transformation matrix for the coordinates (i.e. the location of the occupation domains) is:

$$S_{av \rightarrow sup} = \left[\begin{pmatrix} 1 & 0 & 1 & -1 & 0 \\ 0 & 1 & 1 & 0 & 0 \\ -1 & 0 & 2 & 0 & 0 \\ 0 & -1 & 1 & 1 & 0 \\ 0 & 0 & 0 & 0 & 2 \end{pmatrix}^{-1} \right]^T = 1/5 \begin{pmatrix} 2 & -1 & 1 & -2 & 0 \\ 2 & 4 & 1 & 3 & 0 \\ -3 & -1 & 1 & -2 & 0 \\ 2 & -1 & 1 & -2 & 0 \\ 0 & 0 & 0 & 0 & 5/2 \end{pmatrix} \quad (3.10)$$

In the current work, a decagonal quasicrystal will be analyzed using the higher-dimensional approach. For its periodicity recovery, five-dimensional space is used. The

periodicity of the higher-dimensional lattice \mathbf{D} , allows to determine the higher-dimensional unit cell and its space group. This corresponds to a classical crystal structure which is described by a unit cell and a three-dimensional space group. The lattice with three-dimensional periodicity is decorated with atoms, whereas the higher-dimensional lattice is decorated with hyperatoms, so called occupation domains or atomic surfaces. For axial quasicrystals the occupation domains are two-dimensional objects, extended parallel to the internal space and have no extension along external space.

The Fibonacci Chain is a classical example of a one-dimensional quasicrystal, Fig. 3.3. This example will be given for didactic reasons, since it can be visualized easily. In the framework of this example, external (physical) space is one-dimensional, and a two-dimensional lattice serves as an example of a hyperlattice (higher-dimensional lattice). The two-dimensional lattice is decorated by line segments (occupation domains), as an analogy to hyperatoms. The two-dimensional lattice is defined by external space and an additional space, the so-called internal space (complementary space). In other words, to recover periodicity of the one-dimensional quasiperiodic lattice, it can be lifted to two-dimensional space by adding an additional fictitious dimension.

A one-dimensional quasiperiodic tiling can be created by *section* or *projection methods*. Within the section method, a one-dimensional external space cuts the two-dimensional periodic lattice with an irrational slope, as in Fig. 3.3. As a result, a quasiperiodic pattern of dots is obtained in external space. By changing the slope of external space relative to the higher-dimensional lattice, different one-dimensional structures can be obtained. For example by choosing a rational slope, one obtains so-called rational approximants. An example of $\langle 2,1 \rangle$ -rational approximant is shown by a dashed line.

Within the projection method, a strip ("acceptance domain") with a certain width is defined parallel to external space. All lattice points present in that strip are projected onto external space. The projection results in a dense quasiperiodic set of points and the intensities of the projected points are related to their internal component.

3.2 From Quasiperiodic Tiling to Higher-Dimensional Modeling

A close correspondence between decagonal quasicrystal structures and Penrose tilings was found immediately after the discovery of quasicrystals [LS84]. It served as the main motivation for many scientists as well as artists, designers and others to join this new field. Tiling theory is a field devoted to the general question of how to fill the plane or space without gaps. For more details see [GS85].

In the 1970s Sir Roger Penrose [P74] investigated a type of tiling that can be described as a non-periodic tiling with long-range orientational order and with non-crystallographic

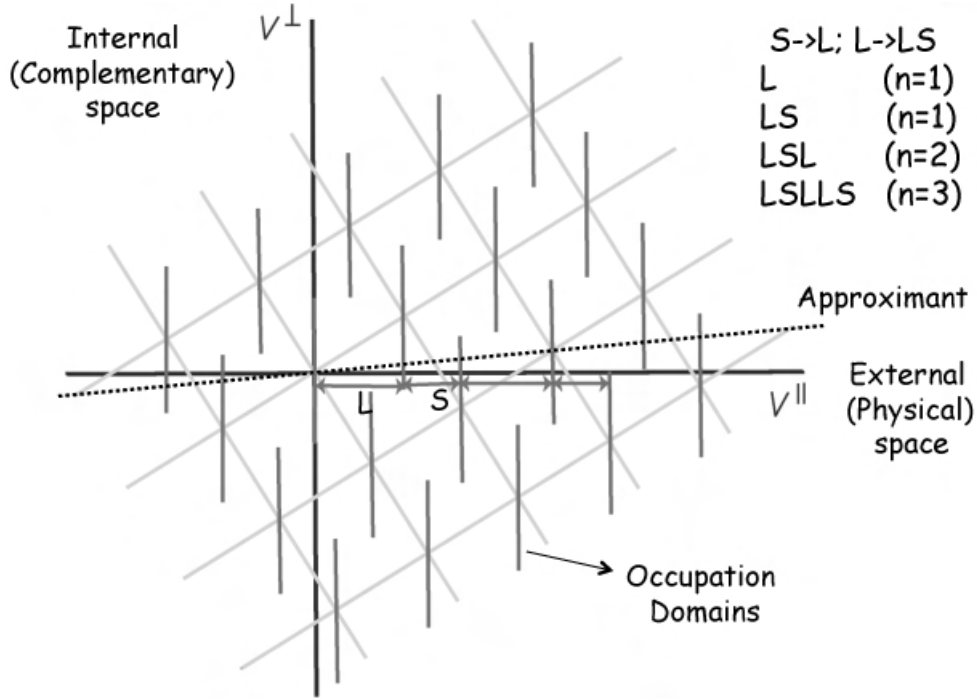


Figure 3.3: Creation of a Fibonacci chain, a one-dimensional quasiperiodic pattern, by an irrational cut of the two-dimensional periodic lattice (the section method). A rational cut, shown by a dashed line, leads to a $\langle 2,1 \rangle$ -rational approximant (periodic pattern).

rotational symmetry. These tilings belong to the category of aperiodic tilings and are today known as Penrose tilings. An original rhombic Penrose tiling is constructed from two types of rhombi, fat with angles of $2\pi/5$ and $3\pi/5$, and skinny with angles of $\pi/5$ and $4\pi/5$. Their edges are decorated, e.g. with arrows or with color. They may be joined only if their decoration permits, following so-called *matching rules*. Non-congruent Penrose tilings are *locally isomorphic*. That means that every finite pattern of one tiling occurs also in every other tiling. On the other hand, two tilings are considered to be different if there is no distance-preserving affine transformation (Euclidean transformation) which maps one to the other.

The similarity between quasicrystal structures and Penrose tilings has been recognized based on their diffraction patterns. Since both possess, sharp Bragg reflections and non-crystallographic symmetries. These special diffraction patterns of Penrose tiling have been observed already in 1982 by using the optical Fourier transformation, as reported in [M82]. Presence of Bragg peaks implies an underlying long-range order. In both, quasicrystal structures and Penrose tilings, the long-range order is related to inflation / deflation symmetry but not to translation symmetry.

According to a Penrose tiling picture, quasicrystal materials consist of two types of atomic units which are the building blocks intermixed in a particular ratio. This picture is less intuitive than that of classical crystals since the latter require only one type of building units, unit cell, which are energetically favorable. This requirement raises important and

still ongoing discussions concerning the stabilization of quasicrystals.

For a physically meaningful quasilattice construction a minimal interatomic distance should be considered. Hence the set of points that forms a quasiperiodic system should satisfy the *Delauney condition*, an essentially dense point set with a minimum distance r between the points. Essentially dense in the meaning that in a radius R around a point a there is at least one other point b . Based on these considerations, an axial quasicrystal can be viewed as quasiperiodic atomic layers stacked periodically along the third direction (in the following only tilings related to decagonal quasicrystals will be considered). Therefore each quasiperiodic atomic layer of an axial quasicrystal can be described as some two-dimensional tiling decorated with atoms in an appropriate way. Consequently, a Penrose tiling can be viewed as an ideal two-dimensional quasicrystal. An example of a Penrose tiling with vertices decorated by atoms is shown in Fig. 3.6b.

A characteristic property of an ideal Penrose tiling is its *scaling* (inflation or deflation) symmetry. For example, a fat rhombus can be subdivided into two fat rhombi and one skinny rhombus with an edge length scaled by τ ; this process is called *inflation*. As a consequence of this property, the crystal basis cannot be uniquely defined for quasiperiodic structures.

Real quasiperiodic structures may not be obtained by a simple decoration of the vertex model as they require a more general type of tiling for their description. However, the vertex model serves as a preliminary structure model for decagonal quasicrystals. Using the set of fat and skinny rhombi but omitting the matching rules, random tilings can be constructed. The relation between quasicrystal structures and random tilings was first presented by Elser in 1985 [EH85]. Later it was shown by Gummelt [G96] that quasiperiodic tilings can be forced using a single type of decagonal covering with matching rules. Covering means that the tiles are permitted to overlap.

Several methods are known to generate a quasiperiodic tiling: *Inflation/Deflation Method* (IDM), *Dual Method or Generalized Dual Method* (DM/GDM), *Projection Method* (PM) and *Section Method* (SM). A detailed description of these methods is given in a variety of previous works [dB81, KN84, SSL85, E85b, E86, KKL85, DK85, ML83]. Here only a brief overview will be given. In the framework of IDM, a structure consists of a certain rule for a local transformation of structure elements into patches of a new structure which is of the same type as the original one, but scaled. Due to its local criteria, IDM has been used as a model to simulate the growth process of real quasicrystals. It became clear, however, that applicability of IDM for real quasicrystal structures is rather limited. Since, quasicrystals almost never correspond to an ideal tiling; some degree of randomness is always present which can be taken into account by introducing deliberate violations of rules for a local transformation. To reduce the complexity involved, a covering approach has been proposed. This is a more intuitive method, since only one type of covering cluster can be used and the restriction is only on how these clusters overlap. These overlapping

regions represent overlapping area/volume of clusters in the real structures and include shared atoms between two clusters. Tiling models are constructed based on diffraction experiments or on known crystalline structures. Later those models are employed to interpret the high resolution electron microscope (HRTEM) images.

DM/GDM allow to a large variety of quasiperiodic tilings to be obtained without limitation on the rotation symmetry and were reported as the most convenient methods for writing computer algorithms for generating rhombic tilings [WW88].

Neither IDM nor DM/GDM can be used directly in the course of structure determination, hence more relevant methods for the current research are PM and SM. By using SM/PM, not only tilings can be generated but also atomic positions of realistic quasicrystal structures; their point density as well as their diffraction patterns can be calculated. This makes these methods suitable for quantitative structure determination. Here it is of interest to stress a few additional points related to the tilings generated by SM. More detailed information concerning known tilings is given in [Y96] and the references therein.

For generating decagonal quasilattices using SM, the minimum number of required dimensions of the higher-dimensional unit cell is four. Hence the internal space and the occupation domains are two-dimensional. Another point is that tilings obtained by SM can be subdivided into two categories. Namely, tilings that are generated from one occupation domain and tilings that are generated from more than one occupation domain. The latter can be a superstructure of the former. As an example, the pentagonal Penrose tiling generated from one decagonal occupation domain (Fig. 3.4) is a substructure of the rhombic Penrose tiling which is generated from four pentagonal occupation domain (Fig. 3.5). Understanding these relationships is crucial to a determination of the superstructure [YW97a, SYS10].

As was stressed before, the application of local matching rules seems to be not applicable for quasicrystal growth. A more suitable model for that is based on *random tilings*. In the framework of this method, the space is filled with tiles in a quasiperiodic random way. According to the thermodynamic law, minimization of the free energy $F = E - TS$ leads to system stabilization. The configurational entropy (S) increases with randomness and cause to the minimization of the free energy, therefore the random tilings approach is favorable.

As an another example, in Fig. 3.6 four occupation domains have been decorated with two different types of atoms which results in an atomic decoration of the vertices of the rhombic Penrose tiling. The structure model in Fig. 3.6 is an example of a *perfect quasiperiodic model*. Since they are related to a perfect tiling, they cannot account for structural defects. It has to be kept in mind that real quasicrystal structures are more complex, therefore for their description more complex occupation domains should be used, see Fig. 3.7. In this example an occupation domain is subdivided into smaller subdomains. Different chemical elements are assigned to each subdomain, as indicated by

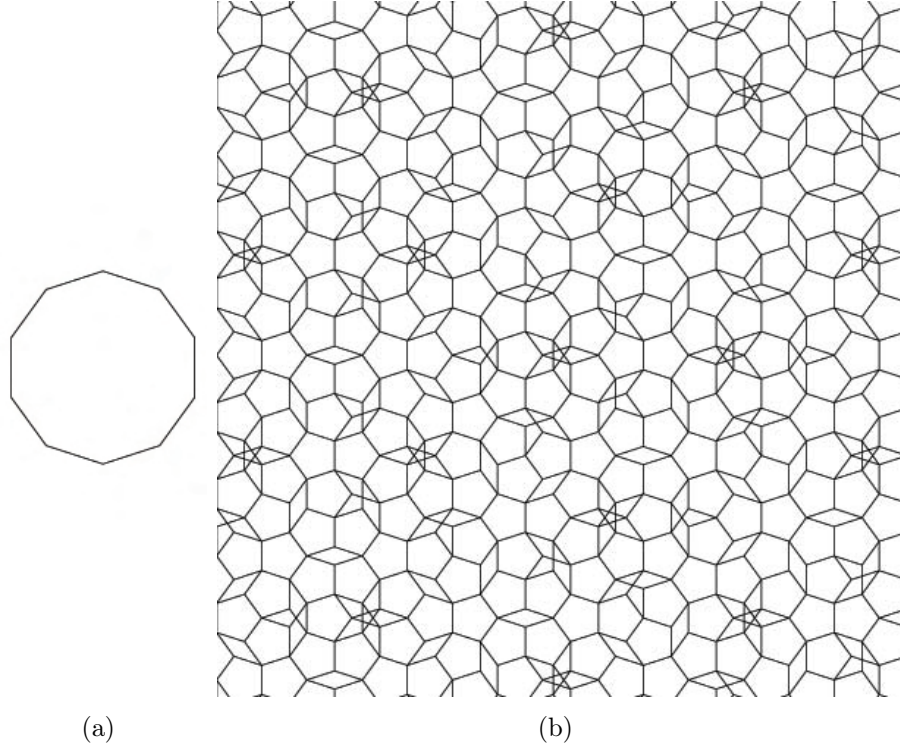


Figure 3.4: (a) Decagonal occupation domain located at $(0,0,0,0,0)$ in the four-dimensional unit cell. (b) Corresponding pentagonal Penrose tiling in external space.

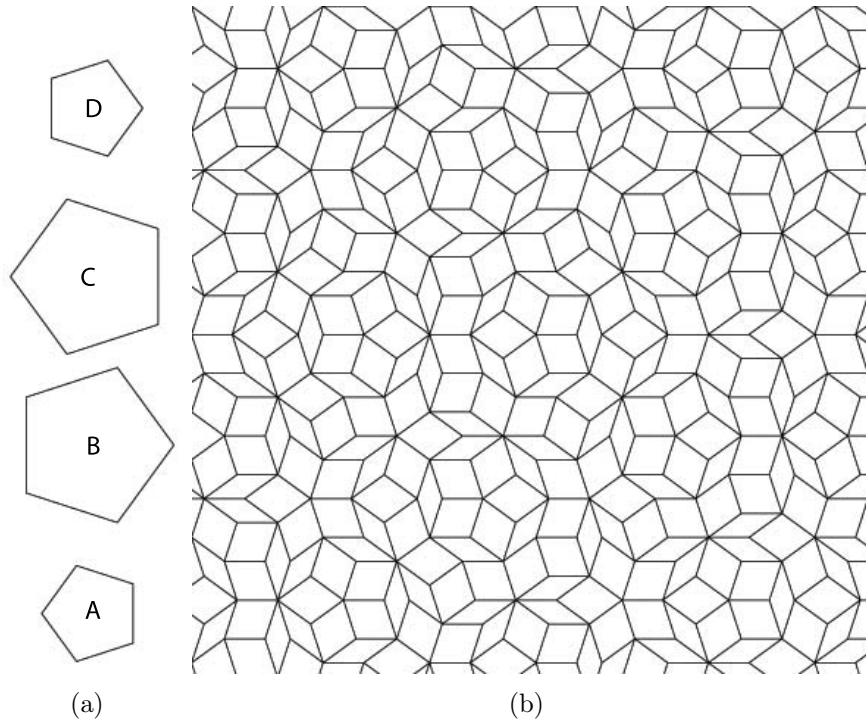


Figure 3.5: (a) Four pentagonal occupation domains located at $(i,i,i,i,0)/5$, $i=1,\dots,4$ in the four-dimensional unit cell. (b) Corresponding rhombic Penrose tiling in external space.

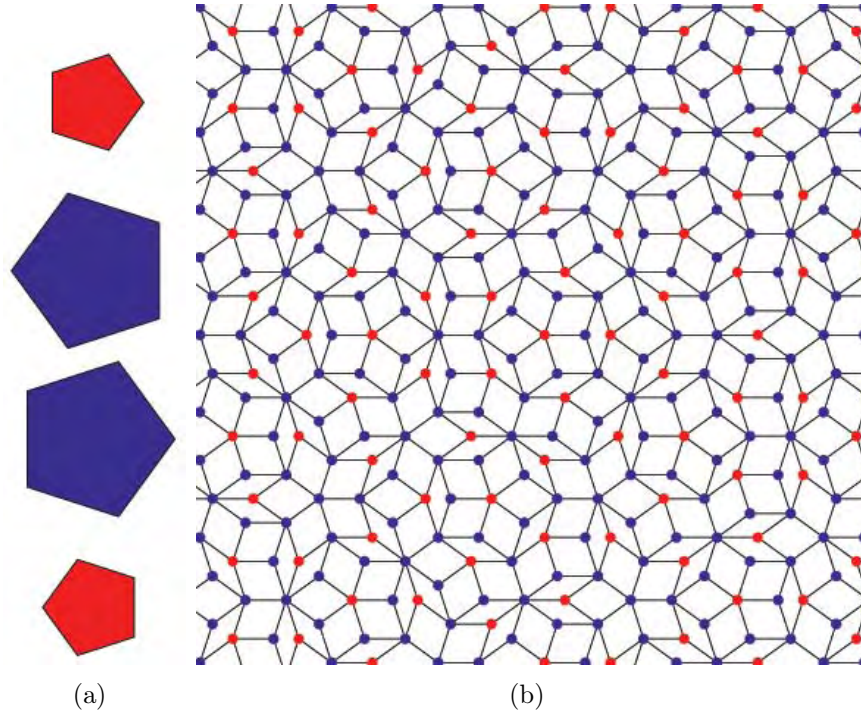


Figure 3.6: (a) Four pentagonal occupation domains occupied by two different types of atoms located at $(i, i, i, i, 0)/5$, $i=1, \dots, 4$ in the four-dimensional unit cell. (b) Corresponding rhombic Penrose lattice with vertex decoration for approximating a quasiperiodic atomic layer.

different colors. The corresponding external space obtained by the irrational cut through the higher-dimensional space is shown in Fig. 3.7b. Atoms in external and internal spaces are indicated by corresponding colors.

The structures of decagonal quasicrystals can be described geometrically as a periodic stacking of quasiperiodic layers. Hence, the additional periodic direction should be taken into account in a structure analysis of real quasicrystals. Moreover, axial quasicrystals can be described as a packing of partially overlapping columnar clusters with an orientation along the periodic axis. Hence the vertices of a tiling should be decorated by atomic clusters instead of single atoms. An example for such a structure is shown in Fig. 3.8. This structure model consists of five occupation domains. They are subdivided into subdomains which are occupied with different chemical elements as indicated by different colors. Occupation domains A-D are located in special positions $(i, i, i, i, x_5)/5$ ($i = 0, 1, 2, 4$; $x_5=5/4, 15/4$) of a five-dimensional unit cell and possess site symmetry $5m$. Occupation domains A and B are located at $x_5=1/4$ and C-E at $x_5=3/4$, where x_5 is an axis along the periodic direction. As a result from an irrational cut through the five-dimensional structure two different layers in external space have been obtained at $x_5=1/4$ and $3/4$ respectively as shown in Fig. 3.8f and g. The tiling was added as a visual guideline. 20 Å clusters are indicated by decagonal cages surrounded by ten pentagonal cages. In this structure model, columnar clusters have an atom in the centre, indicated

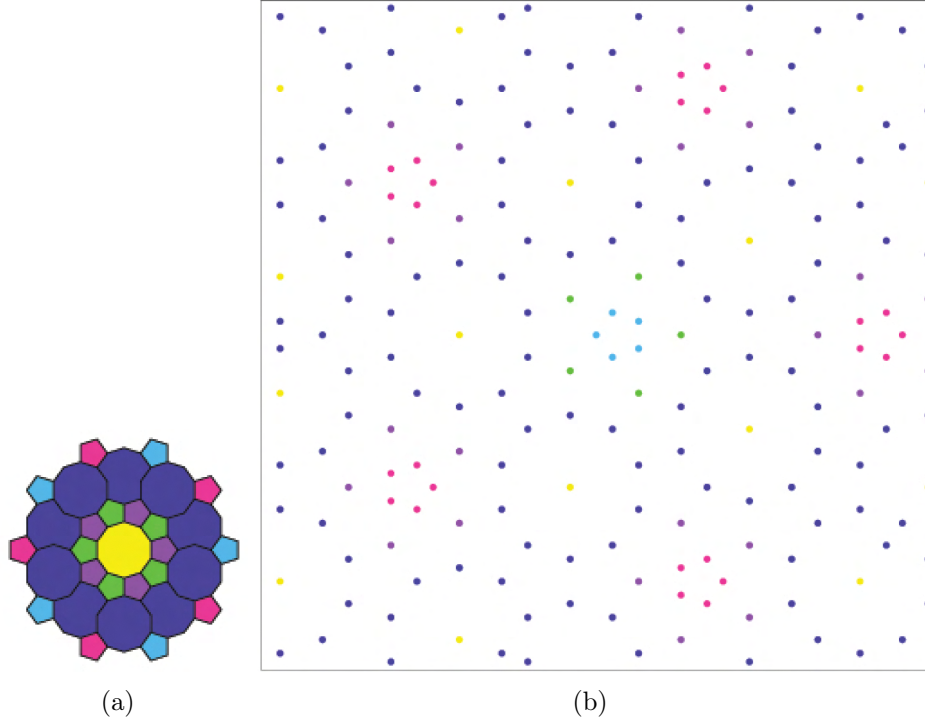


Figure 3.7: Independent occupation domains of the refined model structure of Co-rich decagonal Al-Co-Ni, located at (a) $(0,0,0,0,1/4)$ in a five-dimensional unit cell. (b) External space obtained by an irrational cut through the five-dimensional structure. The atoms derived from the subdomains in (a) are represented by the same color.

by red and generated from a central occupation domain E.

As for any structure refinement, a good starting structure model is needed. Hence, the first questions that must be answered in the process of quasicrystal structure determination are: Where are the occupation domains located? What is the size of the occupation domains? How are the occupation domains shaped?

Originally, HRTEM images show that the structures of decagonal quasicrystals can be visualized as consisting of overlapping clusters; based on this, a higher-dimensional structure model can be introduced. This periodic higher-dimensional model describes the cluster distribution in three-dimensional space.

A frequently used procedure of building a higher-dimensional structure model can be described as follows. Initially, by using HRTEM images cluster centers as well as their distribution and size are identified. In the next step, all cluster centers are connected by an appropriate tiling. This results in a tiling that underlines the distribution of cluster centers. Next, the coordinates of each tiling vertex is lifted to higher-dimensional space. To obtain the initial size and shape of the occupation domain, the higher-dimensional representation is projected onto complementary space. Thus, the shape of the subdomain in the center of the occupation domain for the structure model is derived from the cluster arrangements in HRTEM images; the edge length of the tiling gives us an understanding

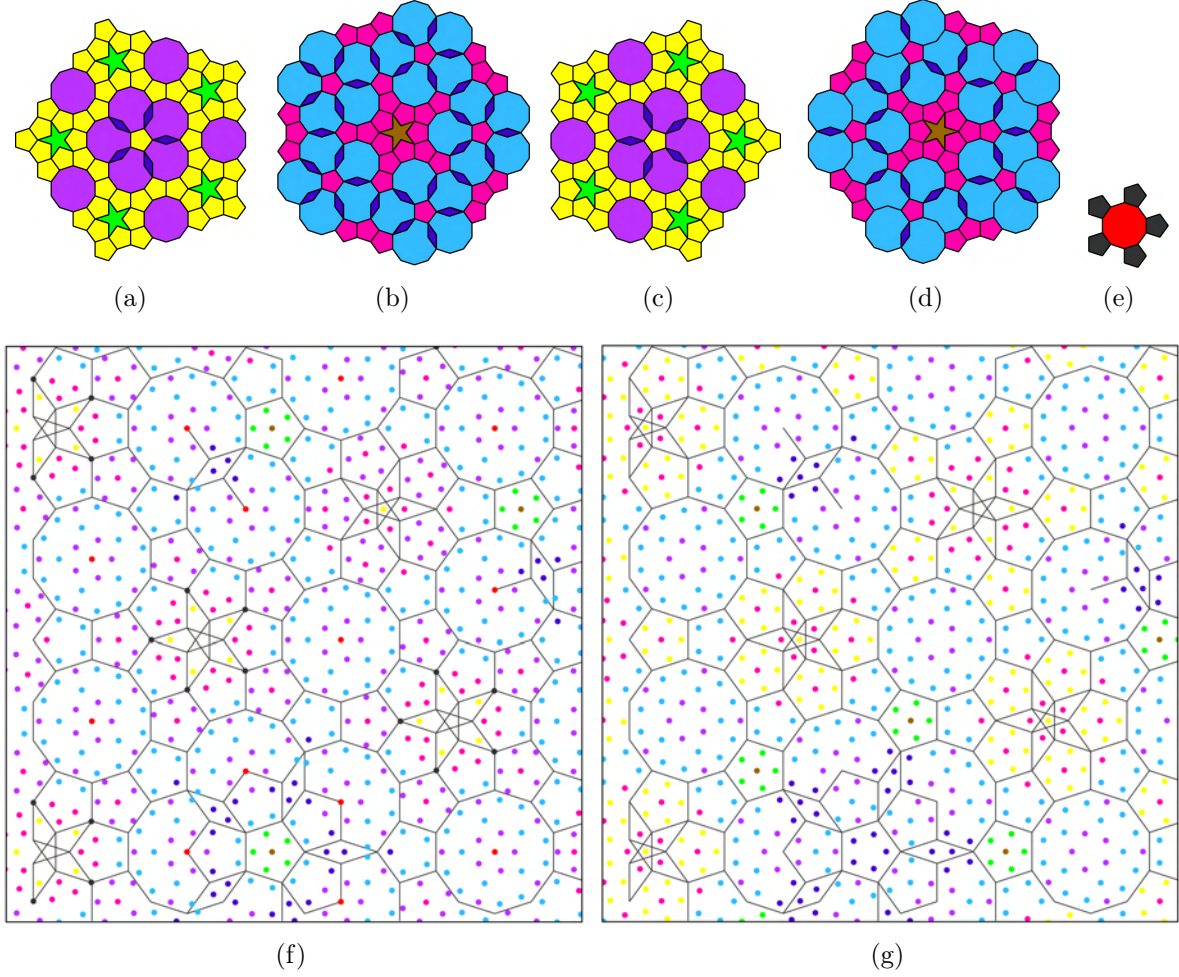


Figure 3.8: Independent occupation domains of the refined model structure of Co-rich decagonal Al-Co-Ni, located at (a) $(1,1,1,1,5/4)/5$, (b) $(2,2,2,2,5/4)/5$, (c) $(4,4,4,4,15/4)/5$, (d) $(3,3,3,3,15/4)/5$, (e) $(0,0,0,0,15/4)/5$ in the five-dimensional unit cell. External space obtained by an irrational cut through a five-dimensional structure at (f) $x_5=3/4$ and (g) $x_5=1/4$. The atoms derived from the subdomains in (a-e) are represented by the same color. The decagonal clusters are on the vertices of a Penrose pentagon tiling.

about the size of the occupation domain.

Model building is one of the most challenging and crucial steps in the structure solution process [Y96]. However, it is important to notice that from HRTEM images only low resolution information in external space is available. How would it be possible to determine a more detailed atomic distribution? In this step it is essential to complement HRTEM information by single-crystal X-ray diffraction data which allows the exact location of the occupation domains to be determined. This can be done by using CF/LDE, since these methods require only the experimentally obtained intensities, but no structural information. In addition, the analysis of the closely related known structures of the quasicrystal and its approximant can give an initial understanding about the chemical distribution within the clusters. In the current quasicrystal structure analysis, the W-phase approximant was found to be a closely related crystal structure. Based on this information, the occupation domains were subdivided into subdomains. The external space component is obtained by applying the section method on a higher-dimensional model. Each subdomain creates atoms with the same local environment in external space. Therefore construction of complicated occupation domains, consisting of several subdomains, is required to mimic the structure in external space, see Fig. 3.7 and Fig. 3.8. Small subdomains (stars and pentagons) accommodate smaller clusters with five-fold symmetry, where decagons accommodate larger clusters with ten-fold symmetry. In this model additional very small subdomains, rhombi, were needed for the construction of the model that preserves the closeness conditions (the occupation domains without voids). The occupation domains should be constructed in such a way that by applying the section method, the observed cluster arrangement is obtained.

3.3 Patterson Technique, *Ab Initio* Phasing Methods and MEM

The Patterson analysis is the most straightforward approach for structure determination since it uses only experimentally obtained reflection intensities and is also suitable for the determination of interatomic distances. In the structure analysis of quasicrystals, Patterson maps give an initial idea about the location of the occupation domains and serve as a good tool for the initial check of data quality. Moreover, in the analysis of the superstructure, difference Patterson maps carry invaluable information.

There are several iterative methods for *ab initio* phasing of structure factors available. Two methods, Charge Flipping (CF) and Low Density Elimination (LDE), were extended to higher-dimensional structure analysis. In the current study both methods have been applied for structure analysis of decagonal $\text{Al}_{72.5}\text{Co}_{18.5}\text{Ni}_9$. The LDE method is implemented in the LODEM code in a program package QUASI07_08_f90 [Y08]. CF

and LDE methods are both implemented in the SUPERFLIP code [OS04, OS05, P04]. These methods can provide approximate structure solution which is reconstructed without *a priori* knowledge of the structure or symmetry. The reconstruction of approximate electron densities from structure factor amplitudes is an iterative process. The iteration is initialized by assigning random phases to the experimentally obtained amplitudes of the structure factors. An electron density distribution function is then calculated by inverse Fourier transform on a discrete grid of points. Then, using CF, all grid points with electron densities below a positive threshold δ are multiplied by -1 (flipped), and new temporary structure factors are calculated by Fourier transform of these modified densities. The phases of these temporary structure factors are combined with the observed amplitudes and as such a new set of structure factors enters the next iteration cycle. This procedure is repeated until a stable solution is found. The LDE method is similar to CF but the threshold δ is set to zero and all the grid points with density below zero are eliminated. Therefore, electron density maps obtained by the LDE method are sharper (contain less noise).

To improve the results after *ab initio* phasing as well as to sharpen the Fourier maps after a refinement process, the Maximum Entropy Method (MEM) applied. Traditionally, MEM is used in data analysis to reconstruct positive distributions such as images and spectra from imperfect data. Within this language, the positive distribution ought to be assigned probabilities that are based on the entropy of that distribution. Therefore the most probable element corresponds to the maximum entropy reconstruction, thereby its selection leads to entropy maximization. Reconstructing the electron density from the imperfect crystallographic data is not a trivial task though, since the resulting electron density is described by a large number of parameters. To reconstruct the electron densities using MEM the QCMEM code in the program package QUASI07_08_f90 has been implemented. It allows the reconstruction of electron densities in arbitrary dimensions. For the calculation we use the Sakata-Sato algorithm, which is an approximate solution of the MEM equation [SS90]. MEM requires the knowledge of the structure factors and quite precise information about the $F(\mathbf{0})$ reflection value. MEM helps to eliminate the noise and to sharpen the peaks on the electron density maps calculated by CF/LDE or after refinement.

3.4 The Pseudo-Approximant Method

Approximants are periodic structures that are built from structural units, clusters, similar to those encountered in quasicrystals. Similar structural fragments in quasicrystals and their approximants can include various numbers of local environments. The closeness of approximants to their quasicrystals is directly proportional to the size of their similar structural fragments. Moreover, approximant structures can be derived from the

quasicrystal structure through geometrical transformations. The point symmetries of the approximants are subgroups of those of their parent quasicrystals [I89]. The Bravais class of the approximant lattice depends directly on the applied geometrical transformation. In the framework of the current work, these relationships between approximants and their parent quasicrystal are of great interest since known approximant structures shed light on the atomic arrangement in the clusters of quasicrystals.

Several methods are known for generating approximant structures from their parent quasicrystal structure two of which we applied. The first approach is applied on a higher-dimensional structure, hence it is called the *higher-dimensional approach*. It obtains a quasilattice of a quasicrystal from a higher-dimensional periodic lattice L [J88]. An approximant structure can be achieved by a deformation of lattice L to lattice \tilde{L} , so the deformed lattice is fully commensurate with the physical space [E85b, H85, I89, N91]. In other words, by introducing appropriate linear phason strains an approximant structure can be created from a higher-dimensional structure of a quasicrystal. This approach has been used to generate the W-phase, a rational $\langle 3/2, 2/1 \rangle$ -approximant, as shown in Article II in Chapter 4.

Here the second approach, the pseudo-approximant method, will be discussed in more details. A pseudo-approximant is a mathematical construct obtained by transformation of the quasicrystal in reciprocal space into that of $\langle p/q, r/s \rangle$ -approximant. Due to that, all Bragg peaks resulting from the quasicrystal structure are shifted to produce an approximant structure and the resulting diffraction pattern depends on the applied transformation matrix. Since these pseudo-approximant structures obey periodicity in three-dimensional space, their structures can be solved with standard crystallographic methods. After refinement, the phases can be combined with the experimentally obtained amplitudes. Next, electron density maps for the parent quasicrystal are generated by the Fourier transform.

As an example, a pseudo-approximant was constructed from a data set calculated from the simplified model of Takakura for a Ni-basic quasicrystal structure [TYSST02]. In this simplified model only the outer shape of the large occupation domains was considered and they were occupied with one type of chemical element, Al, as in Fig. 3.9. Four occupation domains in Fig. 3.9(a-d) were obtained by Fourier transform of the structure factors calculated from the model, whereas the resulting four occupation domains in Fig. 3.9(e-h) were obtained by LDE algorithm. Some differences in the electron density distribution can be observed.

The corresponding external space sections obtained by an irrational cut through the higher-dimensional structure are shown in Fig. 3.10. Comparison of the electron density maps reveals almost no differences in both cases.

A quasicrystal diffraction data set was transformed into a $\langle 3/5 \rangle$ pseudo-approximant. Its space group was identified as $Cmcm$. The resulting indices of the rational approximant are:

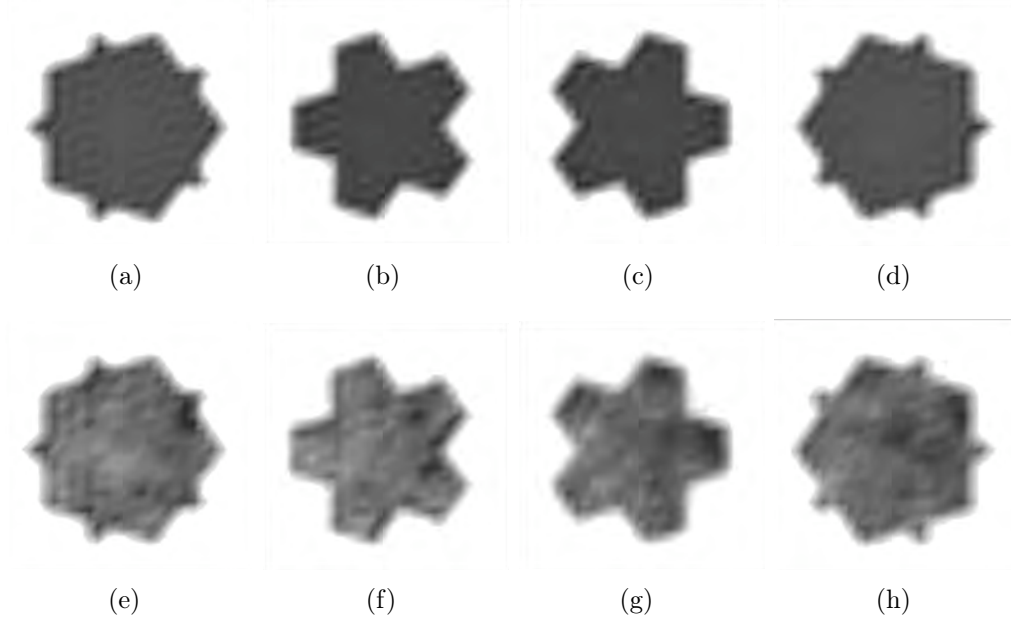


Figure 3.9: Four occupation domains based on Takakura's model occupied by Al are generated from a full data set (a-d) by Fourier transform; (e-h) by applying LDE algorithm.

$$h_1^{app} = -5(h_2 + h_3) + 2(h_1 + h_4), h_2^{app} = 8(h_1 - h_4) + 5(h_2 - h_3), h_3^{app} = h_5 \quad (3.11)$$

while the resulting lattice parameters are $a = 23 \text{ \AA}$, $b = 31 \text{ \AA}$ and $c = 8.44 \text{ \AA}$ as calculated from the relationship:

$$a_1^{app} = 2(3 - \tau)\tau^{3+2}/5a^*, a_2^{app} = 2\sqrt{(3 - \tau)}\tau^{5+1}/5a^*, a_3^{app} = 1/a_5^* \quad (3.12)$$

where a^* and a_5^* are reciprocal lattice parameters in the reciprocal plane and along the periodic direction, respectively.

The transformation of quasicrystal diffraction data to the $3/5$ pseudo-approximant leads to reflection overlaps. It is not clear how to treat this kind of reflection, especially if only experimentally obtained intensities are available. The analysis of the deviation of the summed intensities from the summed structure factors is shown in Fig. 3.11. Weak reflections are strongly overestimated due to summation of the intensities of the overlapping reflections.

Three cases were compared. First, an ideal case was obtained by Fourier transform of the diffraction data using summed structure factors (Fig. 3.12(a)). In the second case electron density maps were calculated by the LDE algorithm from the diffraction data with summed up intensities (Fig. 3.12(b)). In the third case electron maps were calculated by the LDE algorithm from the diffraction data with intensities merged by the refinement

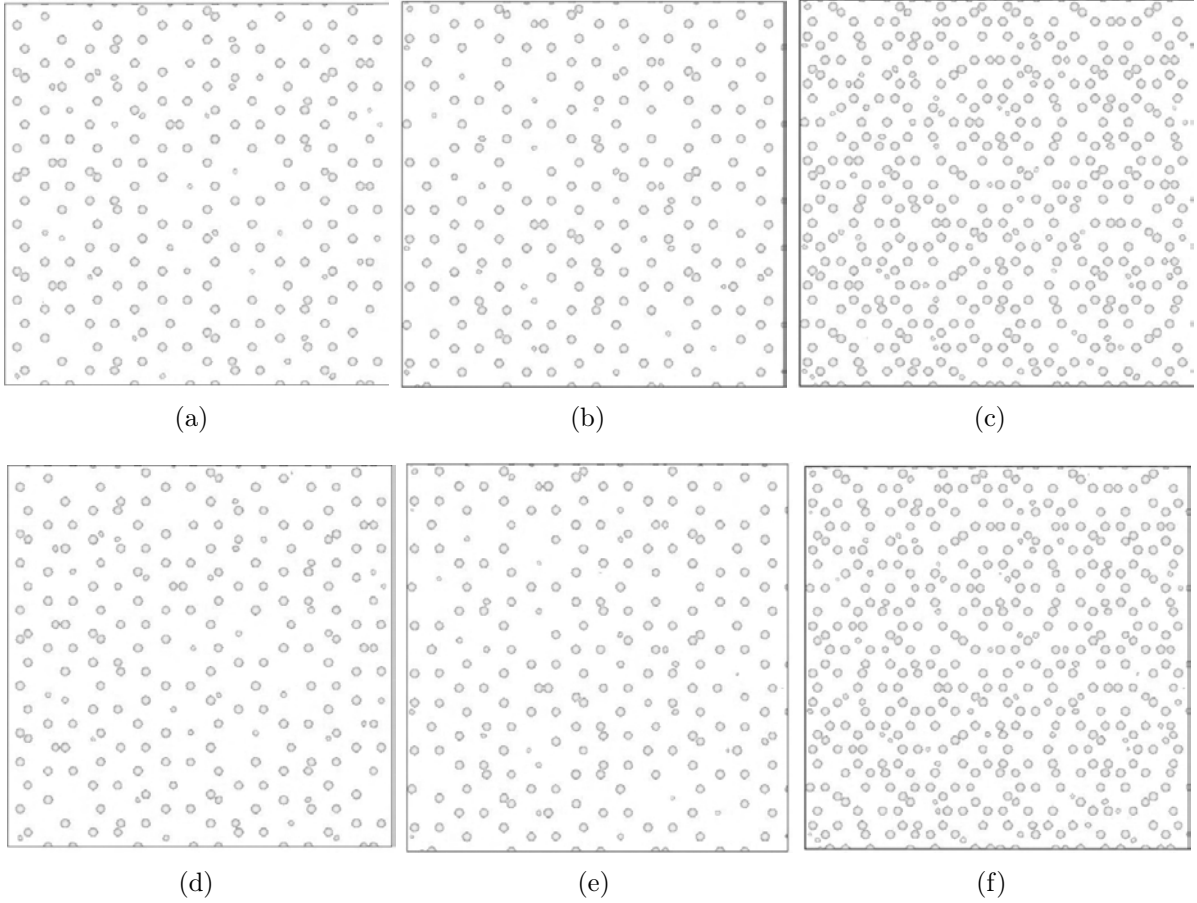


Figure 3.10: $34 \times 34 \text{ \AA}^2$ parallel-space sections (11000) along the periodic direction (x_3) of the five-dimensional electron density distribution function of the decagonal structure based on Takakura's model occupied by Al only at $x_3 = 0.25$ (a, d), $x_3 = 0.75$ (b, e) and the projected structure (c, f). A full data set was analyzed by applying a Fourier transform (a-c) and by applying LDE (d-f). All coordinates are given on the V-basis.

program (Fig. 3.12(c)). In all cases a full data set has been used and the results have been obtained in $P1$. Surprisingly, better electron density maps were obtained in the third case. Averaging in the space group $Cmcm$, applied to the same input data as in the third case, leads to a drastically improved electron density distribution as shown in Fig. 3.12(d). In Fig. 3.12(e) the resulting electron density shown in Fig. 3.12(d) has been improved by MEM. Sharpened peaks and elimination of the weak information were observed.

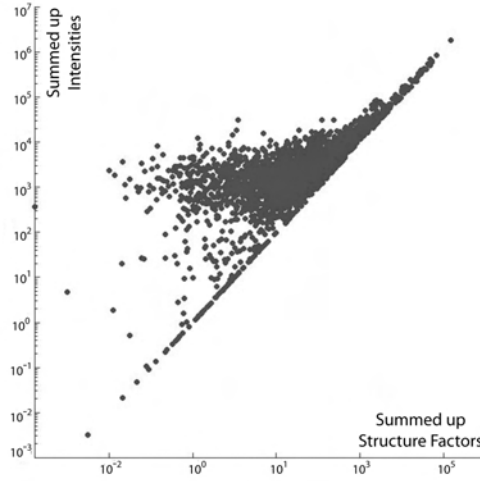


Figure 3.11: Summed up structure factors as a function of summed up intensities on the logarithmic scale.

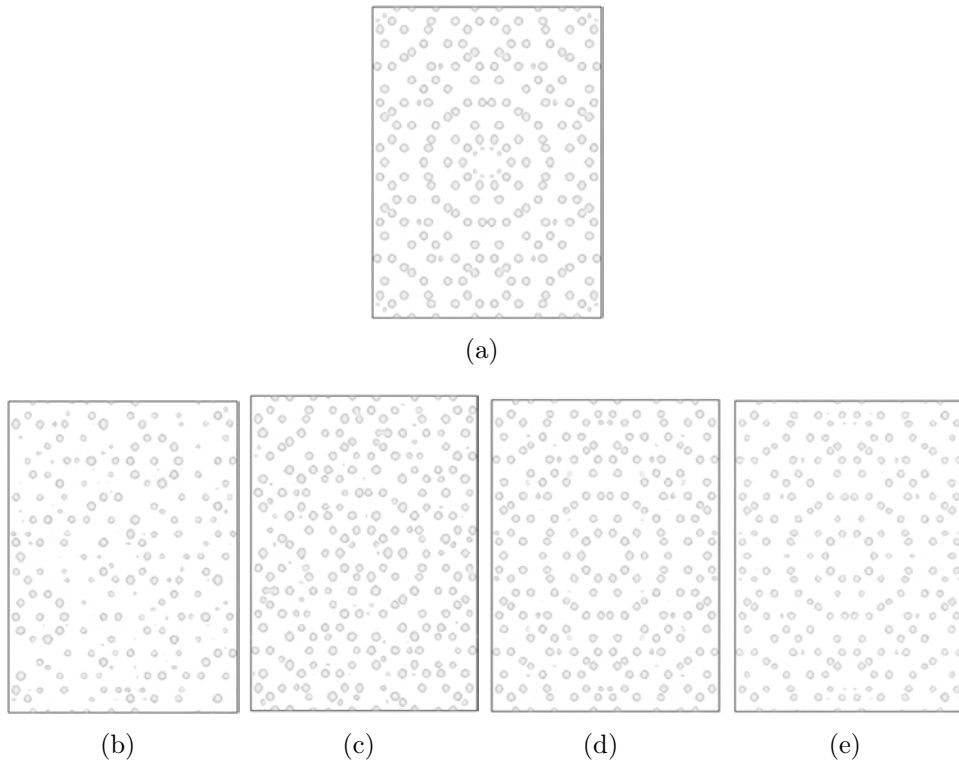


Figure 3.12: Projected structures along the periodic direction of the pseudo-approximant (cross section of $23 \times 31 \text{ \AA}^2$) obtained by (a) Fourier transform using structure factors as an input; (b) and (c) obtained by LDE using intensities as an input. The intensities of the overlapping reflections were summed (b) and merged (c). Results obtained in P1. (d) was obtained by LDE by merging the overlapped reflections and averaging in the space group $Cmcm$. (e) was obtained by MEM using LDE results.

3.5 Theoretical Simplified Superstructure Model

To obtain a better understanding of possible superstructure origins, a simple model of a pentagonal cluster has been constructed as an example. To simulate a superstructure with double periodicity, a cluster model with puckering in some layers has been constructed. The two-layer average structure has a period of $\approx 4 \text{ \AA}$ along the z direction. The stacking consists of alternating flat and puckered layers and to preserve the two-layer average structure, atoms that deviate by $\pm \Delta z$ from their ideal in-plane positions have occupancies of 0.5. This case is illustrated in Fig. 3.13.

To investigate a superstructure with a double periodicity along z , four-layer superstructure models have been constructed as illustrated in Fig. 3.13(b)-(d). Fig. 3.13(b) shows a superstructure model with one Al atom shifted down from the plane $z = 0.25$ and one Al atom shifted up from the plane $z = 0.75$. Both shifts have the same displacement amplitude. Fig. 3.13(c) shows a superstructure model with two Al atoms displaced in the same direction and with the same displacement amplitude out of planes at $z = 0.25, 0.75$. Fig. 3.13(d) shows a superstructure model with two Al atoms displaced in opposite directions with the same displacement amplitude out of planes at $z = 0.25, 0.75$.

Single-crystal X-ray diffraction for the average structure and for the superstructure were calculated and shown in Fig. 3.14 (a) and (b) respectively. Diffraction patterns of the superstructure models show superstructure reflections, which correspond to a doubling of the lattice parameter in the z direction, as expected.

The dependence of the superstructure reflections on various atomic displacements has been analyzed for three superstructure models, Fig. 3.13(b-d). These results are summarized in Fig. 3.15 where the magnitudes of atomic displacements are given as a function of ratio of the superstructure reflections from the total intensity. All three models show similar dependencies. The contribution of superstructure reflections to the intensity is strongly correlated to the magnitude of the atomic displacements. In the real superstructure of decagonal $\text{Al}_{72.5}\text{Co}_{18.5}\text{Ni}_9$ the contribution from the superstructure reflection is 1.4% for the X-ray data sets. To obtain equivalent results from a theoretical model, the atomic displacements should exceed 0.04 \AA .

Accounting only the main reflections, CF and LDE methods gave similar electron density distributions Fig. 3.16(a). In the resulting electron density a discrepancy between the real chemical and the calculated intensity distributions is observed. However, already this *ab initio* structure solution gives one peak with relatively poor intensity. This peak with weak intensity indicates puckering (an atomic shift out of the plane).

The resulting electron density distribution obtained by averaging the best 200 runs of CF/LDE results is shown in Fig. 3.16(b). The calculated result shows a good agreement with the chemical distribution in the model. It is interesting to notice that as a result from the averaging the difference between Al atoms at $z = 0.25$ is eliminated. However,

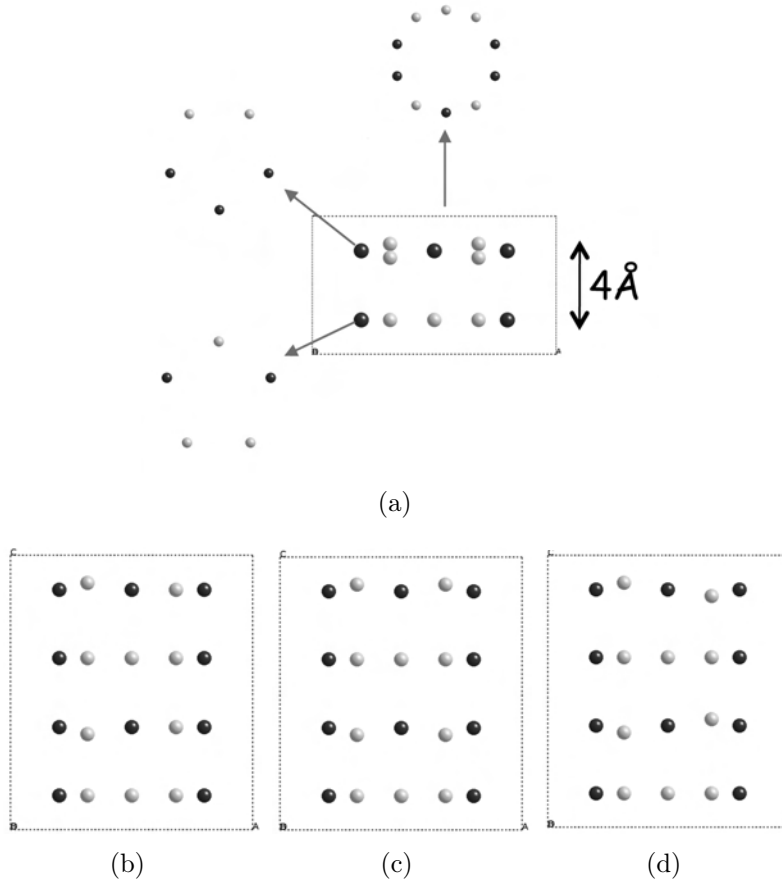


Figure 3.13: (a) Model of an average structure, side view and top view of each layer and their projection. Al and Co atoms are indicated by light and dark gray, respectively. Superstructure models with double periodicity along the z axis with (b) one Al atom displaced from the atomic plane, (c) two Al atoms displaced from the atomic plane in the same direction, and (d) two Al atoms displaced from the atomic plane in opposite directions.

intensity of all the electron density peaks at $z = 0.25$ is lower than at $z = 0$. This observation allows us to conclude that averaging process over several CF/LDE results is less suitable for a superstructure determination.

The resulting electron distribution after MEM is applied to the CF/LDE results without averaging is shown in Fig. 3.17(a). Also here, the resulting density shows only an average structure solution; no indication of puckering is observed.

Fig. 3.17(b) shows the electron density calculated by CF for superstructure reflections only and improved by MEM. This is a surprisingly good result indicating the origin of the superstructure. The resulting electron density calculated by CF only showed similar, though less sharp, electron density distribution.

Both the CF and LDE algorithms yield similar results. However, LDE converged more often than CF. For example for 200 runs, 199 LDE runs converged successfully but only 63 CF runs. Applying MEM to the CF or LDE results sharpens the electron density

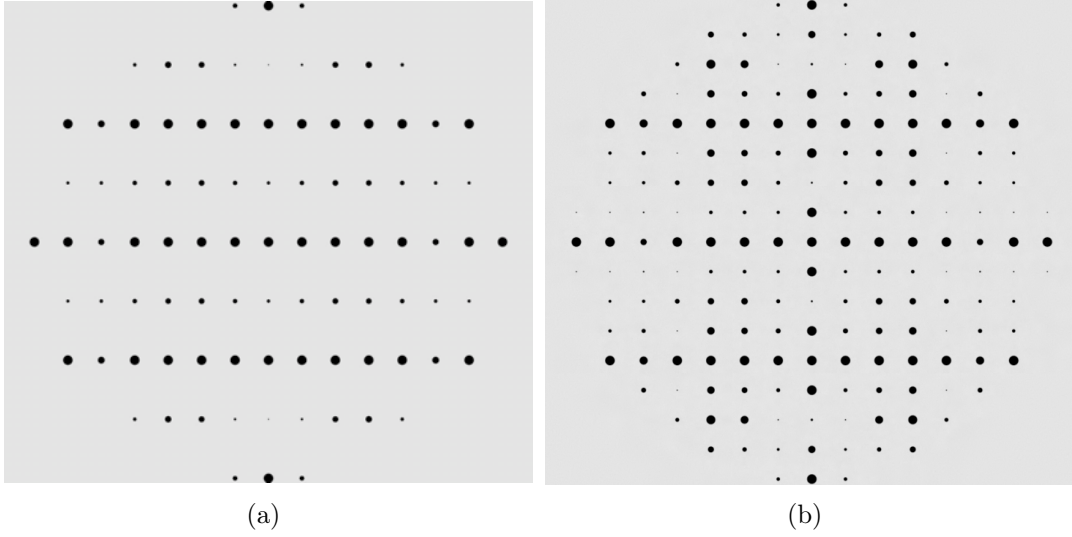


Figure 3.14: X-ray single-crystal diffraction calculated from the theoretical models of (a) an average structure, and (b) a superstructure.

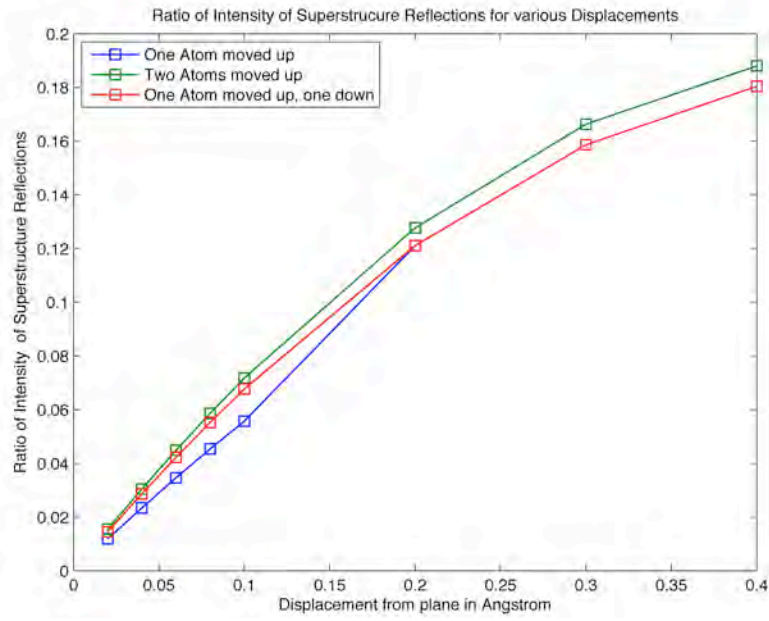


Figure 3.15: Ratio of the superstructure reflections from the total intensity for various displacements (in Å) for three different models.

distribution and eliminates artifacts.

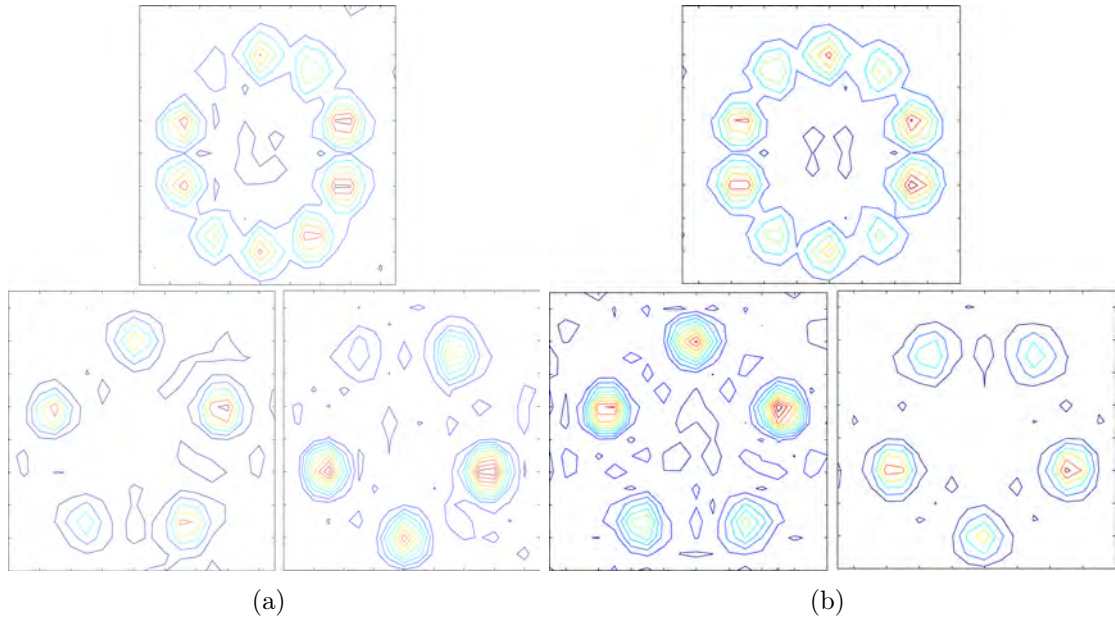


Figure 3.16: $6.8 \times 7.2 \text{ \AA}^2$ (unit cell) electron density distribution sections along the z direction of the model obtained by CF for main reflections (a) with one and (b) with 200 computational runs. The resulting projected structure and the layers at $z = 0$ and $z = 0.25$ are shown for each case.

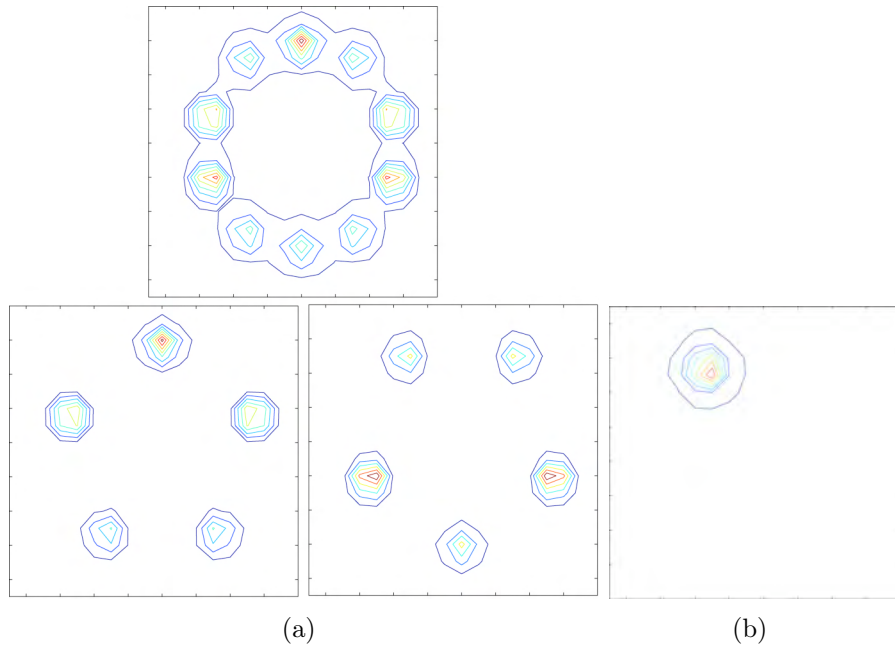


Figure 3.17: $6.8 \times 7.2 \text{ \AA}^2$ (unit cell) electron density distribution for the model given in Fig. 3.13(d): (a) the projected structure and of sections at $z = 0$ and $z = 0.25$ and (b) difference electron density distribution along z direction obtained by CF (see text). In both cases electron density has been improved by MEM.

Chapter 4

Average Structure of basic Co-Rich Decagonal $\text{Al}_{72.5}\text{Co}_{18.5}\text{Ni}_9$

This chapter presents the average structure solution for decagonal $\text{Al}_{72.5}\text{Co}_{18.5}\text{Ni}_9$.

4.1 Structure Determination Using *Ab Initio* Phasing Methods (Article I)

In the first section, the main results are presented in a reprint of the article:

A. Strutz, and W. Steurer, *Structure solution of Co-rich decagonal Al-Co-Ni*, Philosophical Magazine, 87, 2747-2752, (2007).

Additional figures are given in the supplementary section.

Structure solution of Co-rich decagonal Al-Co-Ni

A. STRUTZ and W. STEURER

ETH Zurich, Laboratory of Crystallography, Wolfgang-Pauli-Str. 10, 8093 Zurich, Switzerland

The structure of Co-rich decagonal $\text{Al}_{72.5}\text{Co}_{18.5}\text{Ni}_9$ has been determined by single crystal X-ray diffraction methods. This modification is the only one with four-layer periodicity showing sharp Bragg reflections in all reciprocal space layers. The quasilattice parameters are $a_{1-4} = 4.464(1)\text{\AA}$ and $a_5 = 8.137(3)\text{\AA}$, the Laue group is $10/mmm$. Structure solution was performed by the 5D 'charge-flipping method'. Due to pseudosymmetry only a structure model averaged over a two-layer period (4.068\AA) could be obtained.

Keywords: Co-rich decagonal; Structure solution; Al-Co-Ni; Charge-flipping method

1. Introduction

A huge amount of work has already been invested into the study of decagonal Al-Co-Ni (see [1] and references therein). This phase is an excellent model system for understanding decagonal quasicrystals. It not only has a broad stability range over almost 20 at.%, it also shows complex ordering phenomena as a function of the Co/Ni ratio and/or the temperature. The different modifications have been quite extensively studied by high-resolution electron microscopy (HRTEM) and, only a few of them, by X-ray diffraction. HRTEM images give 'easy' access to local structural information such as clusters and their ordering (tiling decoration). Consequently, there already exists a qualitative picture on some of the ordering phenomena as far as they are observable in structures projected along the tenfold axis. This is the major shortcoming of HRTEM that only projected information can be obtained. Since the ordering phenomena in the quasiperiodic atomic layers are intimately connected with those along the periodic direction, diffraction data are crucial for the full picture. Up to day, however, only data related to $\approx 4\text{\AA}$ (i.e. two-layer) periodicity have been used. The reason for this is that the reciprocal space layers related to the two-fold superstructure along the tenfold axis, i.e. the four-layer periodicity, show just diffuse intensities in almost all cases. We succeeded, however, in growing single crystals of the Co-rich decagonal phase that show sharp Bragg layers only [2].

The present work reports the single crystal X-ray diffraction study on decagonal $\text{Al}_{72.5}\text{Co}_{18.5}\text{Ni}_9$. Besides the solution of the structure of the Co-rich decagonal phase, the

potentialities and limits of a new method for higher-dimensional structure analysis, the 'charge-flipping method', should be tested an iterative algorithm for reconstructions of approximate electron densities from structure factor amplitudes [3-5]. Before, it had been used only once, for the solution of the decagonal phase, with 8-layer periodicity, in the system Al-Ir-Os [6]. For that purpose, the program SUPERFLIP [3] was used.

2. Experimental

For the preparation of the samples, elemental powders of Al (Heraeus 99.95 wt.%), Co (Alfa Aesar 99.8 wt.%) and Ni (Heraeus 99.99 wt.%) were used. Compacts with composition $\text{Al}_{72.5}\text{Co}_{18.5}\text{Ni}_9$, 1g each, were pressed under argon atmosphere (Mbraun glove box 150 B-G, PanGas Ar 99.998). Prealloys were prepared by melting the compacts in an arc furnace (DEGUSSA VOLi O) with non-consumable tungsten electrode under Ti-gettered argon. The as cast sample was analyzed by differential temperature analysis (DTA) (Perkin Elmer DTA 7) using Al_2O_3 crucibles under high purity argon at heating with cooling rates of $10^\circ\text{C}/\text{min}$. Quasicrystal growth and annealing was performed in a high-vacuum resistance furnace (PVA MOV 64). An as cast sample was heated in an Al_2O_3 crucible to 1350°C (i.e. above melting temperature), held at this temperature for 20 min, then cooled to 1000°C with a cooling rate of $0.24^\circ\text{C}/\text{min}$ and subsequently annealed for 48 hours at 1000°C . Eventually, the sample was quenched by jetting cold argon into the sample chamber.

The sample was examined by powder X-Ray diffraction (XRD) (PANalytical X'Pert Pro diffractometer, standard θ - 2θ Bragg-Brentano geometry, $\text{Cu } K_{\alpha 1}$, $10^\circ \leq 2\theta \leq 100^\circ$, 0.02° step width). Scanning electron microscopy (SEM) was performed in back-scattering mode at 30 kV and energy dispersive X-Ray spectroscopy (EDX) analysis was carried out at 15-30 kV accelerating voltage on a LEO 1530 analyzer using the VOYAGER software. Single crystal X-ray data collection was performed on a four-cycle diffractometer equipped with charge-coupled device (CCD) (Oxford Diffraction Xcalibur, $7.5^\circ \leq 2\theta \leq 55.5^\circ$, sample to detector distance 160 mm, 1° φ -scan per frame, exposure time 10 sec per frame, 50 kV, 40 mA, graphite monochromatized $\text{Mo}K_{\alpha}$ radiation).

3. Results and discussion

The first four reciprocal space layers are shown in figure 1. The X-ray diffraction patterns show 10-fold symmetry and reflection planes parallel and perpendicular to it, i.e. Laue group $10/\text{mmm}$. No systematic extinctions are observed. It is remarkable that neither 10_5 -screw axis

nor c -glide plane pseudosymmetry is present. The reflections of the even layers (related to the two-layer average structure) can be indexed on the standard basis [7], i.e. the same basis as the Ni-rich decagonal phase. For indexing both even and odd layers, the reciprocal basis of the superstructure type I has to be used. It can be obtained from the reciprocal standard basis by rotoresizing, i.e. a rotation by $\pi/10$ and a contraction by a factor of $1/\sqrt{3-\tau}$ [8]. This basis is related to $a_{1-4} = 4.694(1) \text{ \AA}$ for the quasilattice parameter, and $a_5 = 8.137(3) \text{ \AA}$ for the periodic direction. For practical purposes (limited computer memory) we used a setting with a being τ^3 times smaller than recommended by [8] (τ is the golden mean $2\cos\pi/5$). In this setting, the indices of the reflection 10000 in the standard setting transform into $0\bar{1}100$ (marked by an arrow in figure 1a). There are only superstructure reflections in the odd layers, and main reflections only in the even layers. The intensities of the superstructure reflections are approximately two to three orders of magnitude weaker than those of the main reflections.

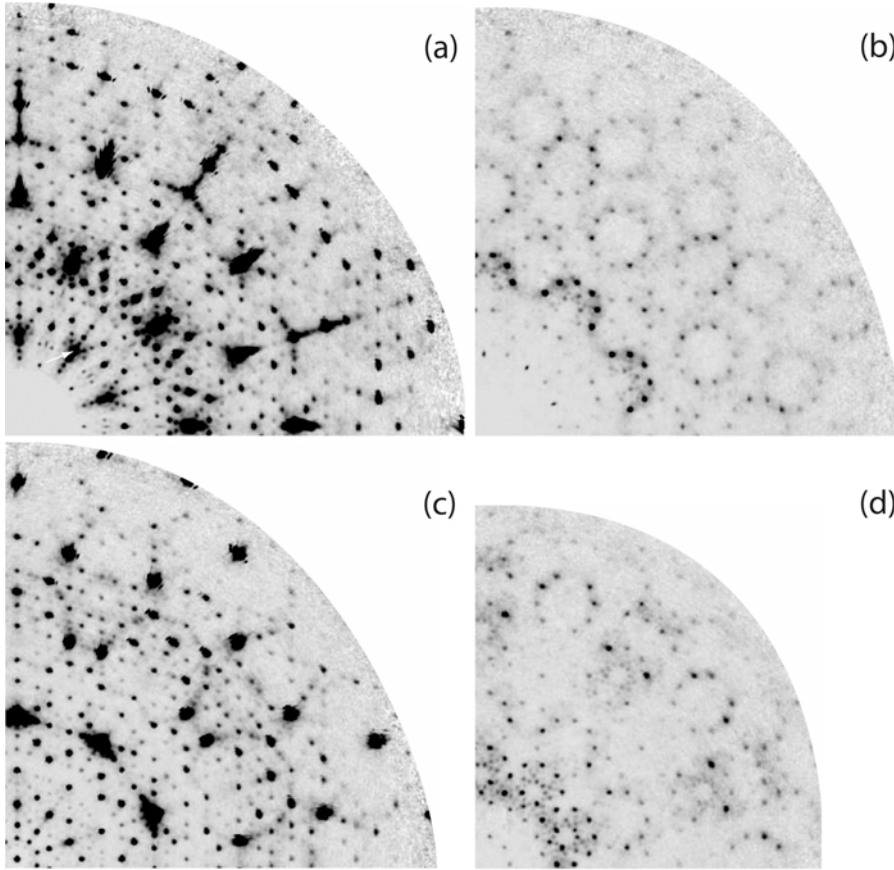


Figure 1. Reciprocal space sections of decagonal $\text{Al}_{72.5}\text{Co}_{18.5}\text{Ni}_9$ reconstructed from 360 CCD frames each: $h_1h_2h_3h_4h_5$ with (a) $h_5=0$, (b) $h_5=1$, (c) $h_5=2$, (d) $h_5=3$ (h_5 referring to the $\approx 8 \text{ \AA}$ period). Since a graphite monochromator was used, second harmonics ($\lambda/2$) reflections of the strongest reflections are visible on the images $h_5=0, 1, 3$.

Along the periodic direction (≈ 8 Å superstructure), there are four quasiperiodic atomic layers, A , B , C , D , at $x_3 = 0, 1/4, 1/2, 3/4$. From the distribution of reflection classes we can draw some conclusions on their symmetry and structure. First, from the respective zero reciprocal-space layers we learn that the projected structure, $(A + B + C + D)$, of the Co-rich phase is of the basic type while that of the type-I is still a five-fold superstructure. Second, from the respective even reciprocal-space layers we can conclude that the two-layer (≈ 4 Å) average structure, containing the averaged layers $(A + C)$ and $(B + D)$, is still of the basic type for the Co-rich phase. Only the full four-layer structure of the Co-rich phase shows the five-fold superstructure features.

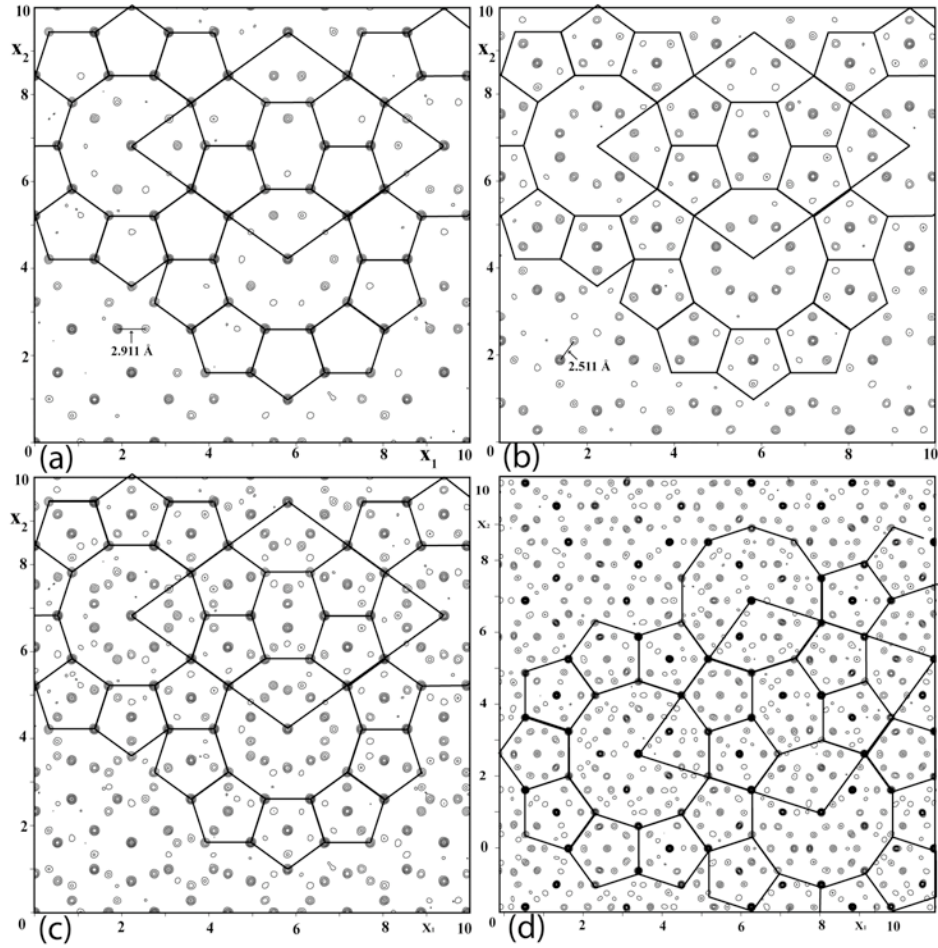


Fig. 2: 44×44 Å² parallel-space (11×300) sections of the 5D Fourier function of decagonal $\text{Al}_{72.5}\text{Co}_{18.5}\text{Ni}_9$ at (a) $x_3 = 0$, (b) $x_3 = 1/4$ and (c) the projected structure. For comparison, the analogous map of decagonal $\text{Al}_{70.6}\text{Co}_{6.7}\text{Ni}_{22.7}$ [10] is shown in (d). Due to its differently oriented basis, the map in (d) is rotated by $\pi/10$ relative to the other ones. Characteristic structure motifs are outlined as guide for the eye. On the axes, a -units are marked.

For the structure analysis, the computer program SUPERFLIP was employed using a data set with 2293 unique reflections. The 5D supercell was divided into $42 \times 42 \times 42 \times 42 \times 84$ voxels, the full data set needed for input was reconstructed based on $10/mmm$ symmetry. The program converged smoothly and quickly with automatic choice of the flip selection threshold δ . The resulting electron density maps of the layers A in $x_3 = 0$ and B in $x_3 = 1/4$ in are shown in figure 2. The quality of the maps corresponds to the quality of an in-house diffraction data set, i.e. the limited number of reflections leads to a significant background so that not all Al atoms are properly resolved or visible, respectively. More disappointing is that the four atomic layers, A , B , C , D are not fully resolved. At least three of the four layers have to be different to produce a four-layer periodicity. SUPERFLIP, however, shows almost the same density for A and C as well as for B and D , respectively. This means, that the weight of the superstructure reflections in the odd layers was too small to be accounted for in the calculations. The result is an average structure with two different, averaged layers, $(A+C)$ and $(B+D)$ (figure 2). Anyway, it gives a first, semi-quantitative, structure model of the different layers of the Co-rich decagonal Al-Co-Ni phase. A comparison with the corresponding maps of decagonal $\text{Al}_{70}\text{Co}_{15}\text{Ni}_{15}$ [7] and $\text{Al}_{70.6}\text{Co}_{6.7}\text{Ni}_{22.7}$ [9], also average structures, shows as most important difference the lack of (pseudo)symmetry relationships between the two layers. The main difference between the projected structures of the basic Co-rich and the Ni-rich phase is in the occurrence of decagonal rings. These are found in the basic Ni-rich structure around large decagons alternating with pentagonal stars (figure 2d). In case of the Co-rich phase, rings of this type are not observed at the corresponding sites (figure 2c). A more detailed discussion is given by Deloudi & Steurer [10].

4. Conclusion

The (partial) structure solution of the Co-rich decagonal phase is an important contribution to the structural database necessary for modeling and understanding formation, stability, structure and ordering of the quasicrystals in the system Al-Co-Ni. In the paper by S. Deloudi [10] at this conference, this structural information is already used for this purpose. The higher-dimensional 'charge-flipping method' seems to be a useful approach for the solution of aperiodic crystal structures. In case of pseudosymmetry, the resulting structure model is averaged with high probability. Further developments of this method may lead to a solution of this problem. Another possibility will be the use of the maximum-entropy method (MEM) [11].

Acknowledgement:

We thank Lukas Palatinus for his strong support concerning SUPERFLIP and gratefully acknowledge financial support under grant SNF 200020-105158.

References

- [1] W. Steurer, Z. Kristallogr. **219** 391 (2004).
- [2] S. Katrych and W. Steurer, Z. Kristallogr. **219** 606 (2004).
- [3] L. Palatinus, Acta Cryst. A **60** 604 (2004).
- [4] G. Oszlányi and A. Süto, Acta Cryst. A **60** 134 (2004).
- [5] G. Oszlányi and A. Süto, Acta Cryst. A **61** 147 (2005).
- [6] S. Katrych, Th. Weber, M. Kobas, L. Massüger, L. Palatinus, G. Chapuis and W. Steurer, J. Alloys Comp. **428** 164 (2007).
- [7] W. Steurer, T. Haibach, B. Zhang, S. Kek and R. Lück, Acta Crystallogr. B **49** 661 (1993).
- [8] T. Haibach, A. Cervellino, M.A. Estermann and W. Steurer, Philos. Mag. A **79** 933 (1999).
- [9] A. Cervellino, T. Haibach and W. Steurer, Acta Crystallogr. B **58** 8 (2002).
- [10] S. Deloudi and W. Steurer, Philos. Mag. (2007) this volume.
- [11] T. Haibach and W. Steurer, Acta Crystallogr. A **52** 277 (1996).

4.2 Supplement - Article I

The average structure solution obtained by the CF algorithm is shown in Fig. 2 of the preceding article. Electron density distribution of the quasiperiodic layers separated by half a period are indicated by black and gray and superimposed for the comparison, Fig. 4.1. The results, obtained using the two different methods CF and LDE, are presented in Fig. 4.1(a, c) and (b, d), respectively, with some of the significant differences indicated by arrows. Electron density distribution of the quasiperiodic layers separated by half a period are indicated by black and gray and superimposed for the comparison. A comparison of the electron density distributions calculated by CF and LDE methods does not reveal which one of the two methods is superior for the current structure investigation. In general, both methods seem to give a useful initial electron density distribution for the average structure with ≈ 4 Å periodicity. In both cases, a comparison between the two layers reveals some differences in the electron density distribution, however, the density in both layers is too low. Hence, this structure solution cannot be plausible and informative enough to find the final differences between these layers that cause the superlattice ordering. At this point we conclude that CF and LDE methods are comparably good and for reasons of convenience the LDE method will be used in the rest of this project.

It is clear that obtaining a superstructure solution using the LDE method alone will be a very challenging task. Furthermore, pseudosymmetry is already present in the average structure; this fact introduces a difficulty in finding the correct intersection at the symmetry centers. Therefore many trials were required to obtain an electron density distribution that is in good agreement with the symmetry elements of the provided space group. Here, we will concentrate only on the average structure taking into account only the main reflections of the *in-house* data set. In the following section a detailed analysis of the shape and location of the occupation domains will be presented. In the first step, only 168 strong reflections with $|F| > 3\sigma_F$ were included. The raw output from LDE is shown in Fig. 4.2(a-c), where three independent occupation domains can be seen. The LDE results improved by the application of MEM are shown in Fig. 4.2(d-f). This last step resolves further details in the occupation domains at $(1,1,1,1/4)/5$, and $(2,2,2,1/4)/5$ (Fig. 4.2(a-b), (d-e)). However, the electron density in the small occupation domain at $(0,0,0,1/4)$ is drastically diminished (Fig. 4.2(c), (f)). The corresponding external space sections obtained by the irrational cut through the five-dimensional structure are presented in Fig. 4.3. A similar analysis has been done with 218 reflections with $|F| > 2\sigma_F$. However, the use of these additional reflections caused only minor changes to the shape of the occupation domain at $(0,0,0,1/4)$. In the external space section, no changes have been observed. The results after including all 1120 reflections are presented in Fig. 4.4 and Fig. 4.5. The main change occurs in the occupation domain at $(2,2,2,1/4)/5$; its shape becomes much sharper. Furthermore, additional details could be resolved in the

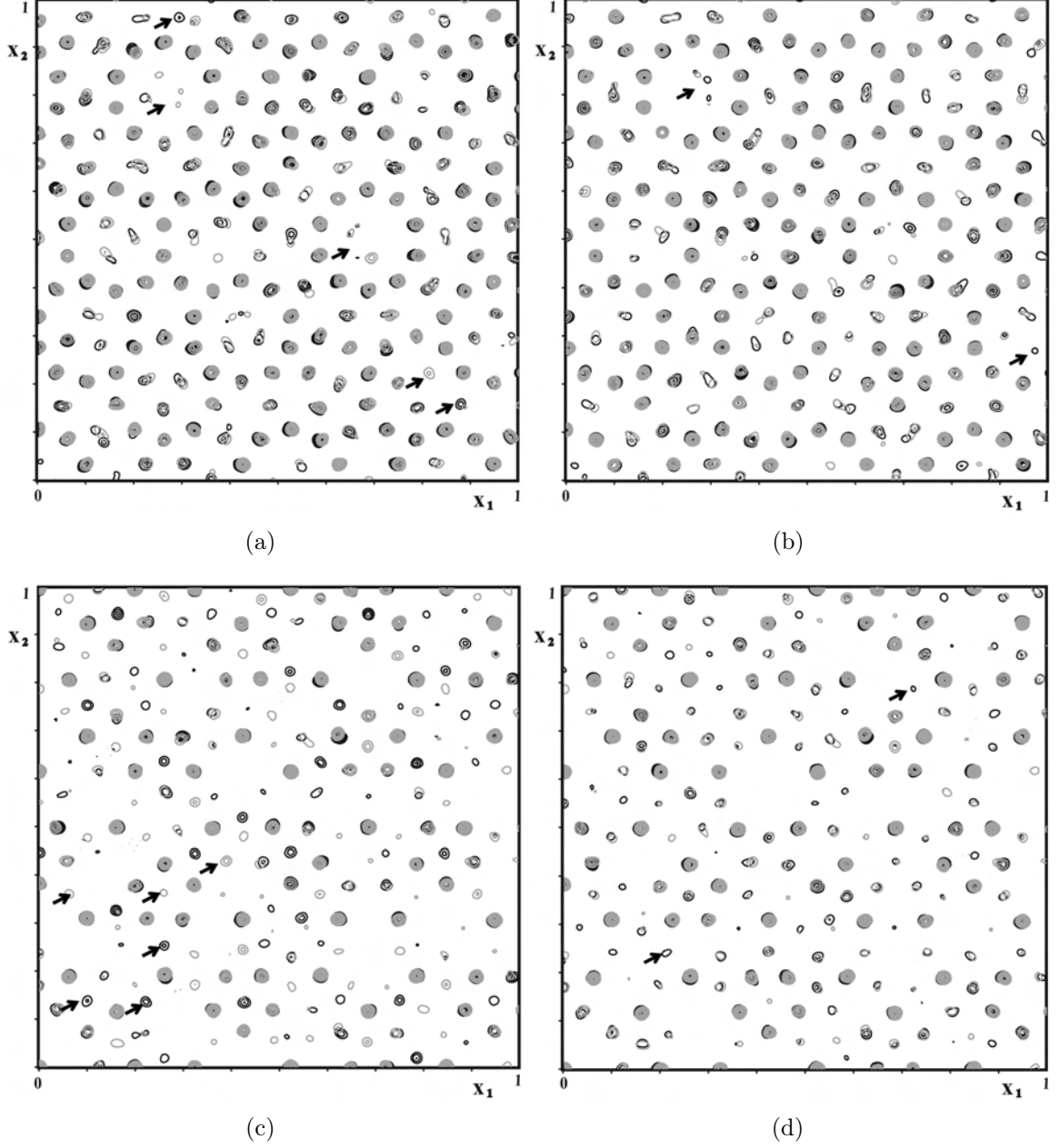


Figure 4.1: Electron density distribution ($40 \times 40 \text{ \AA}^2$) of the quasiperiodic layers at $x_3 = 0$ (black) and $x_3 = 1/2$ (gray) (a, b) and at $x_3 = 1/4$ (black) and $x_3 = 3/4$ (gray) as indicated respectively by black and blue colors (c, d), obtained by CF (a, c) and LDE (b, d) algorithms. Some of the significant differences are indicated by arrows.

external space sections.

1193 unique reflections were used in a combined data set composed of the *in-house* and two synchrotron data sets. The resulting sections of the five-dimensional electron density distribution are shown in Fig. 4.6 and Fig. 4.7.

For the average structure solution, see for comparison the occupation domains obtained using a non-centrosymmetric space group after LDE Fig. 4.12 and refinement Fig. 4.14. For the superstructure solution, see Fig. 5.8. The prominent difference between non- and centrosymmetric cases can be seen in the occupation domain at $(1,1,1,1/4)/5$. This occupation domain is better defined when a non-centrosymmetric space group is used. Hence, a non-centrosymmetric space group results in a better structure solution.

After considering only main reflections, superstructure reflections were included in the analysis. As previously mentioned, the electron density maps obtained directly after the LDE method do not carry sufficient information about the superstructure ordering. For that reason, difference electron density maps were calculated using the CF method and by treating the data as neutron data allowing positive and negative intensities to be obtained. By definition, the difference electron density is the difference between the real and average structures. Hence, the positive peaks correspond to areas with more electron density in the real structure than in the average. Correspondingly, negative peaks correspond to areas with less electron density in the real structure than in the average. The distribution of these difference peaks is shown in Fig. 4.8. According to this result, only two layers show non-zero peaks. Hence, the superstructure originates mainly due to structural modulations in the layers at $x_3=1/4$ and $x_3=3/4$. However, the obtained difference electron density maps do not contain sufficient information to fully elucidate the underlying mechanism of the superstructure formation.

The positions of the atoms defining the cluster were determined from the high electron density peaks. The resulting four-layer cluster with two flat and two puckered layers is shown in Fig. 4.9. Based on the information obtained from the difference electron density and PF maps, the atomic positions that produce the superstructure were identified as indicated by red and green circles. Already from this initial picture we can conclude that the superstructure modulations break the five-fold symmetry in the quasiperiodic layers of the cluster. Whereas, by superimposing these two layers, the five-fold symmetry is recovered. This cluster model is only a rough approximation for the real structure picture it cannot be confirmed without a quantitative structure analysis in five-dimensional space. Nevertheless, it gives us a first idea about the cluster structure in external space.

As a final step to check the correctness of the cluster model, a PF map was calculated, shown in Fig. 4.10, and compared with the PF map obtained from the experimental data. Already this rough approximation shows good agreement with the experimentally obtained PF.

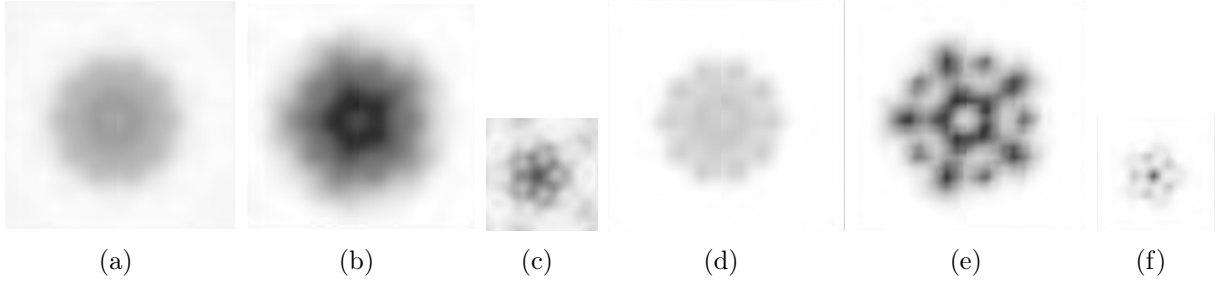


Figure 4.2: Occupation domains at (a) $(1,1,1,1,1/4)/5$, (b) $(2,2,2,2,1/4)/5$ and (c) $(0,0,0,0,1/4)$. Occupation domains at $(3,3,3,3,1/4)/5$ and $(4,4,4,4,1/4)/5$ are obtained by the inversion operation from hyperatoms (b) and (a) respectively. Dark gray corresponds to the TM atom distribution and bright gray to the Al atom distribution. 163 unique reflections with $|F| > 3\sigma_F$ (*in-house* data set) were used in the in the LDE analysis (a-c) and improved by MEM (d-f).

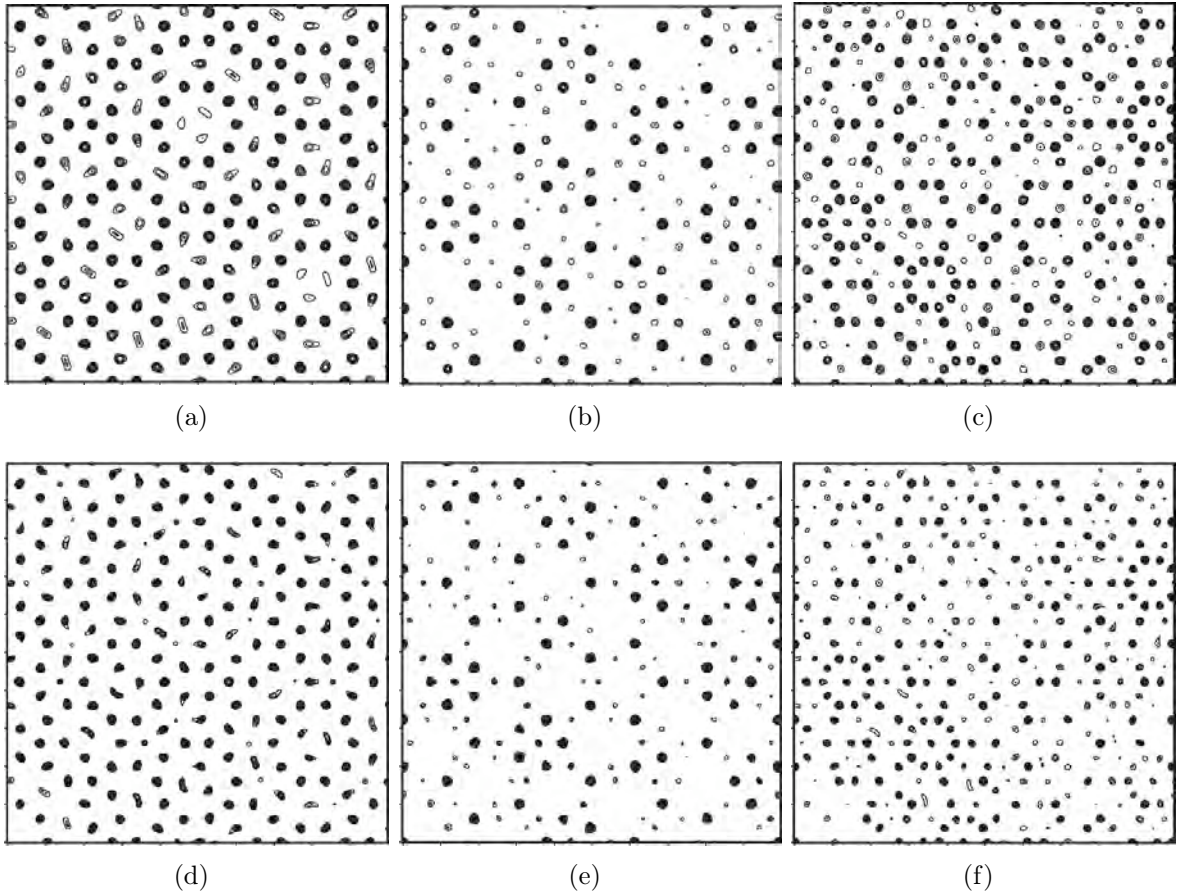


Figure 4.3: Electron density distribution ($40 \times 40 \text{ \AA}^2$) of the quasiperiodic layers at $x_3 = 0$ (a, d), $x_3 = 1/2$ (b, e), and the projected structure (c, f). 163 unique reflections with $|F| > 3\sigma_F$ (*in-house* data set) were used in the in the LDE analysis (a-c) and improved by MEM (d-f).

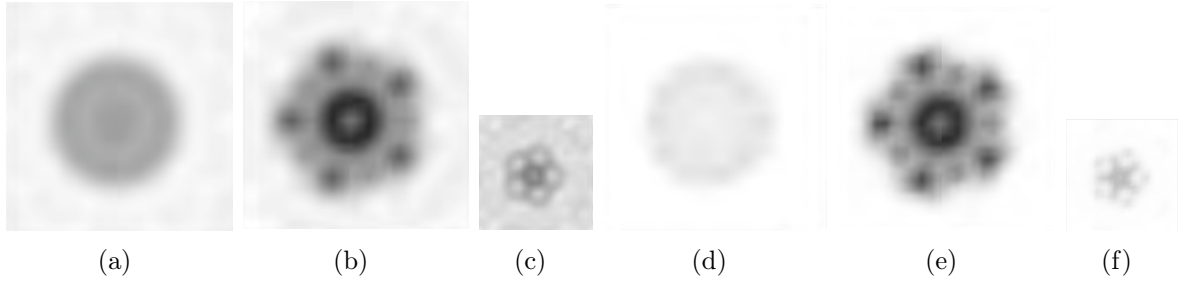


Figure 4.4: Occupation domains at (a) $(1,1,1,1,1/4)/5$, (b) $(2,2,2,2,1/4)/5$ and (c) $(0,0,0,0,1/4)$. Occupation domains at $(3,3,3,3,1/4)/5$ and $(4,4,4,4,1/4)/5$ are obtained by the inversion operation from hyperatoms (b) and (a) respectively. Dark gray corresponds to the TM atom distribution and bright gray to the Al atom distribution. All 1120 unique reflections (*in-house* data set) were used in the in the LDE analysis (a-c) and improved by MEM (d-f).

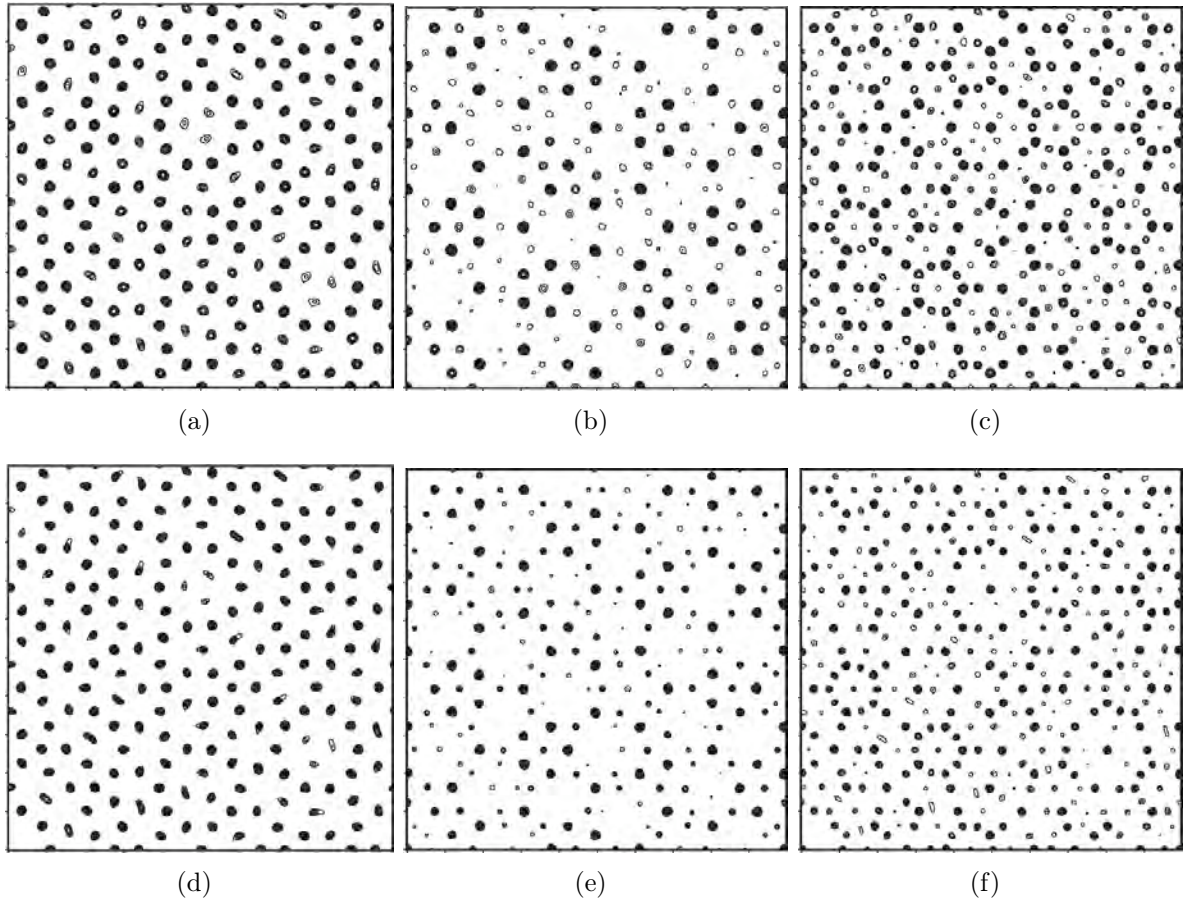


Figure 4.5: Electron density distribution ($40 \times 40 \text{ \AA}^2$) of the quasiperiodic layers at $x_3 = 0$ (a, d), $x_3 = 1/2$ (b, e), and the projected structure (c, f). All 1120 unique reflections (*in-house* data set) were used in the in the LDE analysis (a-c) and improved by MEM (d-f).

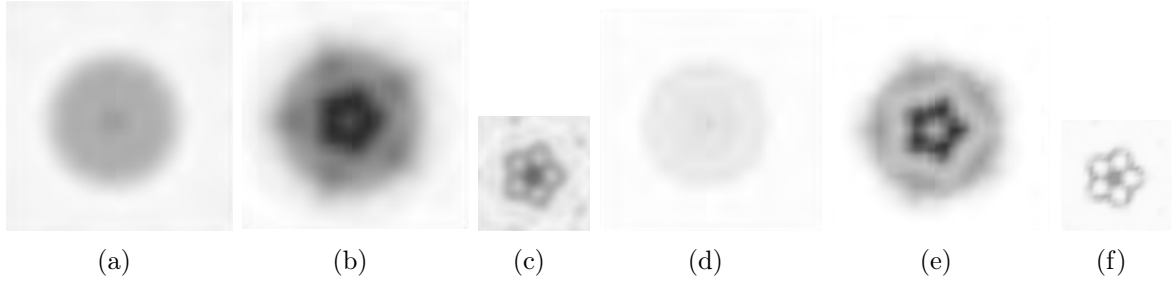


Figure 4.6: Occupation domains at (a) $(1,1,1,1,1/4)/5$, (b) $(2,2,2,2,1/4)/5$ and (c) $(0,0,0,0,1/4)$. Occupation domains at $(3,3,3,3,1/4)/5$ and $(4,4,4,4,1/4)/5$ are obtained by the inversion operation from hyperatoms (b) and (a) respectively. Dark gray corresponds to the TM atom distribution and bright gray to the Al atom distribution. 1193 unique reflections (*in-house* and synchrotron data sets) were used in the in the LDE analysis (a-c) and improved by MEM (d-f).

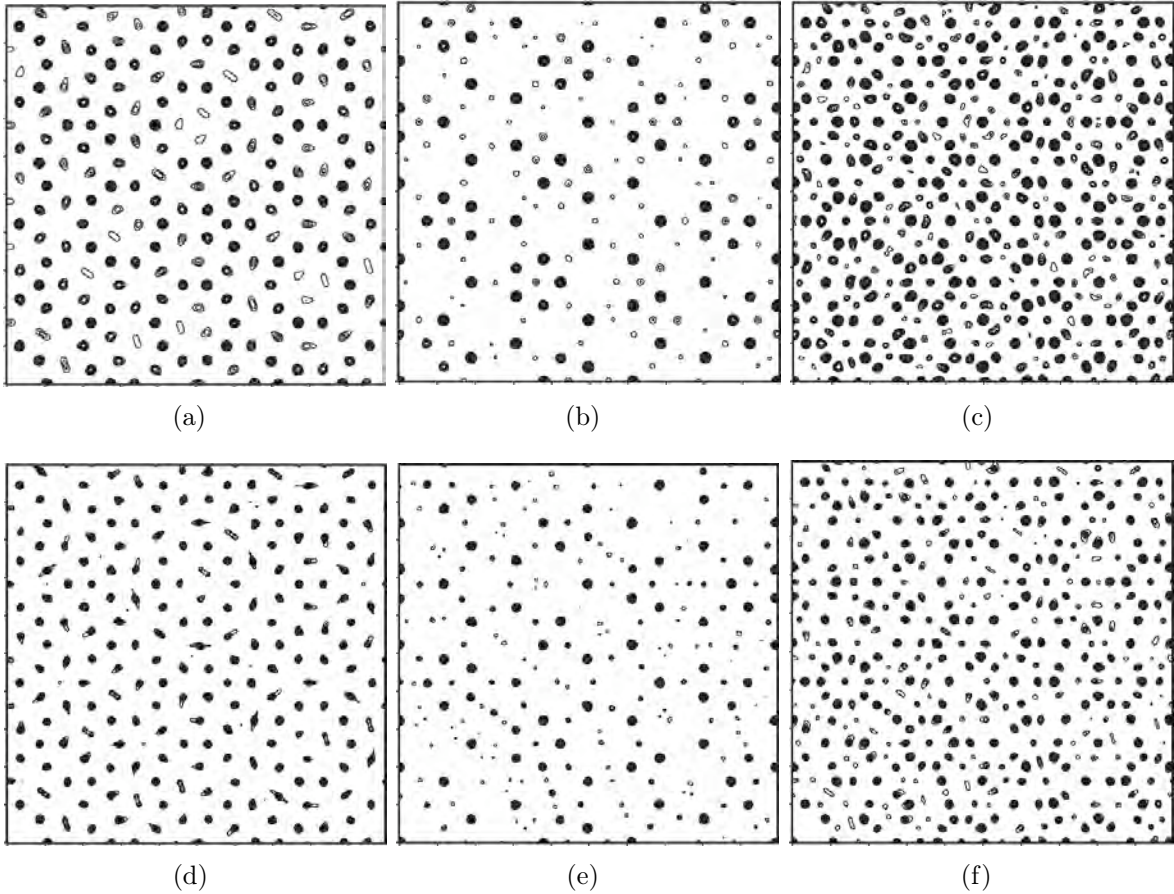


Figure 4.7: Electron density distribution ($40 \times 40 \text{ \AA}^2$) of the quasiperiodic layers at $x_3 = 0$ (a, d), $x_3 = 1/2$ (b, e), and the projected structure (c, f). 1193 unique reflections (*in-house* and synchrotron data sets) were used in the in the LDE analysis (a-c) and improved by MEM (d-f).

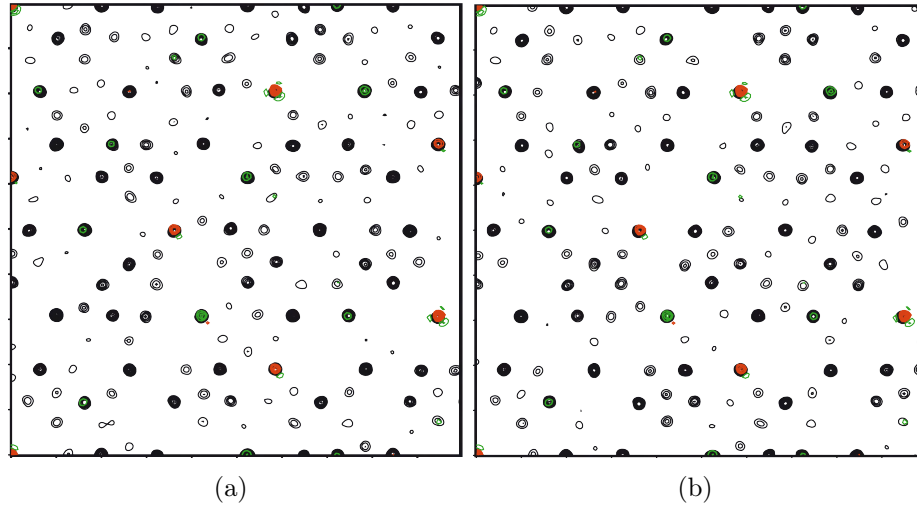


Figure 4.8: Electron density distribution ($40 \times 40 \text{ \AA}^2$) of the quasiperiodic layers at (a) $x_3 = 1/4$ and (b) $x_3 = 3/4$ highlighting the peaks that might contribute to the superstructure modulations as it is results from the difference electron density calculated by the CF.

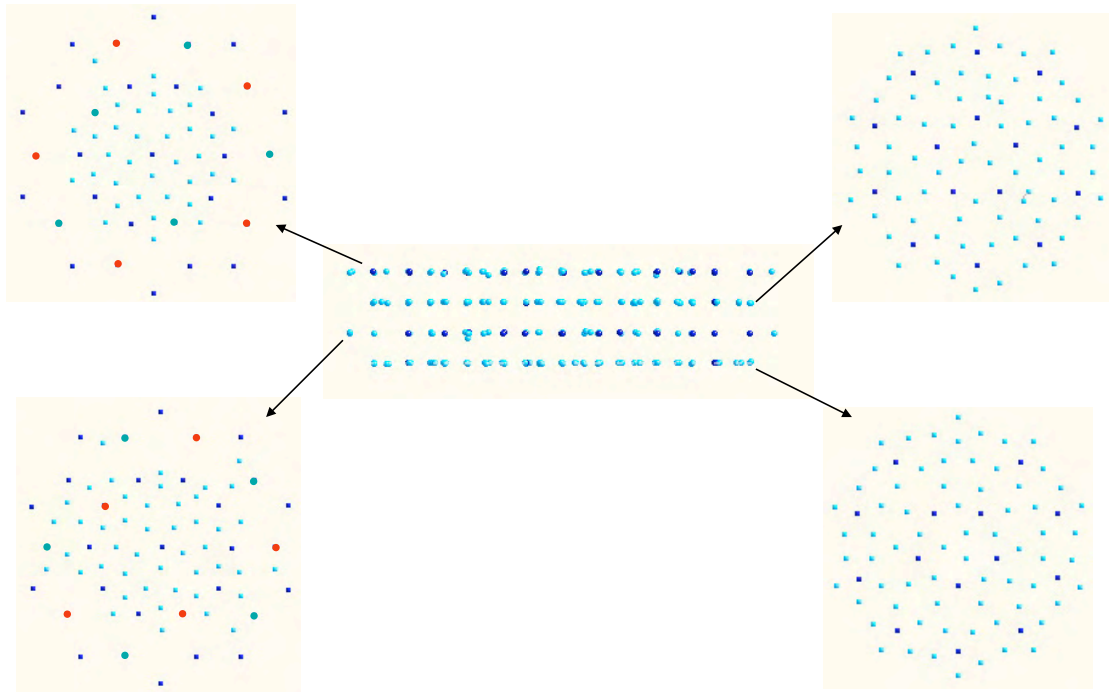


Figure 4.9: Four layers of a 20 \AA cluster model. Atoms that are suspected to produce a superstructure modification are indicated by red and blue circles.

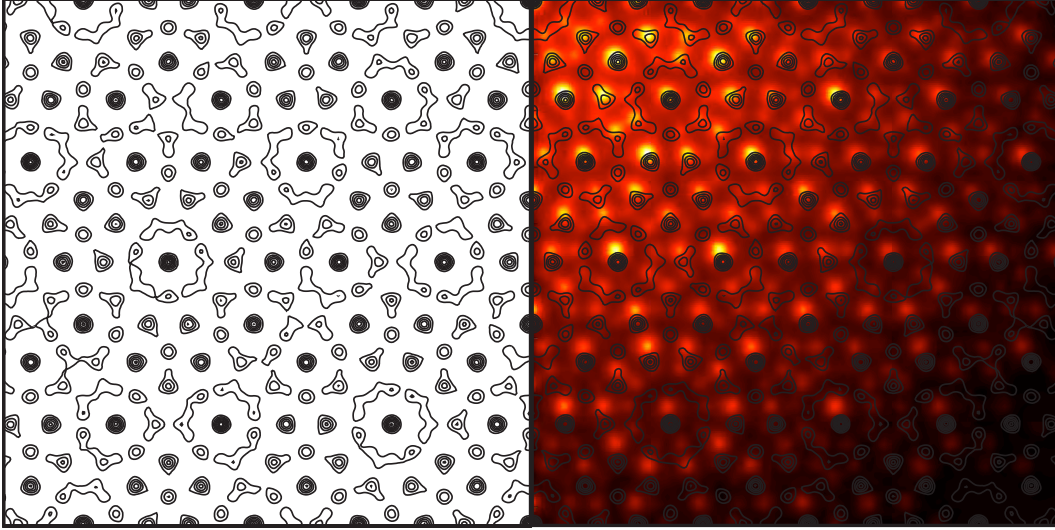


Figure 4.10: On the left hand side, the PF map obtained from the experimental data (black contour map). On the right hand side, this map is superimposed onto the PF map calculated (colored map) from the four-layer 20 Å cluster model shown in Fig. 4.9.

4.3 Basic Co-Rich Decagonal Al-Co-Ni: Average Structure (Article II)

In the structure analysis discussed in this part, only main diffraction peaks have been considered resulting in an average structure solution. The known structure of the W-phase approximant was of great help in understanding the cluster structure of decagonal $\text{Al}_{72.5}\text{Co}_{18.5}\text{Ni}_9$. Moreover, the W-phase possesses an ≈ 8 Å period, hence its structure solution provides a good starting point in the analysis of the full superstructure of the decagonal $\text{Al}_{72.5}\text{Co}_{18.5}\text{Ni}_9$ phase. The structure analysis in the current section was done with FORTRAN coded programs developed by Dr. Akiji Yamamoto and included in the program package QUASI07_08; more details are given in Appendix A and [W97, Y08].

This section contains a reprint of the article:

A. Strutz, A. Yamamoto and W. Steurer, Basic Co-rich decagonal Al-Co-Ni: Average structure, Phys. Rev. B **80**, 184102 (2009).

Additional figures concerning this article are given in the supplement.

Basic Co-rich decagonal Al-Co-Ni. Part I: Average structure

Angelica Strutz,¹ Akiji Yamamoto,² and Walter Steurer^{1,*}

¹*Laboratory of Crystallography, Department of Materials, ETH Zurich, 8093 Zurich, Switzerland[†]*

²*National Institute for Materials Science, Namiki 1, Tsukuba, Ibaraki, 305-0044, Japan[‡]*

(Dated: September 29, 2010)

The two-layer average structure of the high-temperature phase basic Co-rich d(ecagonal)- $\text{Al}_{72.5}\text{Co}_{18.5}\text{Ni}_9$ was determined based on single-crystal X-ray diffraction data. The five-dimensional (5D) structure model was refined in the non-centrosymmetric 5D space group $P\overline{1}0m2$ (112 parameters, $wR = 0.123$ and $R = 0.156$ for 957 reflections). The close relationship of the model structure with that of W-Al-Co-Ni, a $\langle 3/2, 2/1 \rangle$ -approximant, is shown.

PACS numbers: 61.05.cp, 61.44.Br, 61.50Ah, 61.66.Dk

I. INTRODUCTION

Understanding formation, stability and physical properties of quasicrystals requires the knowledge of their structures. Furthermore, some of the structure/property relationships of quasicrystals, which are mostly inter-metallic phases, are not only of interest in their own right, but also, increasingly, for the design of photonic and phononic crystals¹. However, of the more than seventy stable quasicrystals discovered so far, the structures of only a handful of them have been determined yet due to the intricate complexity of quasicrystal structure analysis^{2,3}.

Decagonal quasicrystals, i.e. quasicrystals with decagonal diffraction symmetry, can geometrically be described either as periodic stacking of quasiperiodic atomic layers or as packing of decagonal clusters. From the viewpoint of chemical bonding, however, decagonal quasicrystals are by no means layer structures and the term cluster has to be understood just as a synonym for structural building unit^{4,5}.

The system Al-Co-Ni is an excellent model system for the study of the influence of chemical composition on the formation of different quasicrystal modifications and approximants⁶. As a function of the Co/Ni ratio, different superstructures form either in the quasiperiodic directions or along the periodic tenfold axis⁷. Though Co and Ni are next to each other in the periodic table differing by only one d -electron, the X-ray diffraction patterns of those modifications show significant variations⁸. This indicates significant structural changes accompanying Co/Ni ordering with the variation of their ratio. Indeed, quantum-mechanical model calculations showed local rearrangements of coordination polyhedra depending on the kind of TM atoms present⁹.

Basic Co-rich d(ecagonal)-Al-Co-Ni, stable above approximately 900°, possesses a twofold superstructure along the tenfold axis, doubling the two-layer periodicity present in the basic Ni-rich modification. This kind of superstructure is also present in all other d-Al-Co-Ni modifications as well as in d-Al-Co-Cu. However, only in the basic Co-rich modification it has the long-range correlation needed for single-crystal X-ray structure analy-

sis. In other words, only in basic Co-rich d-Al-Co-Ni the superstructure reflections are sharp Bragg reflections, in all other cases they are diffuse, indicating a correlation length of a few cluster-diameters only⁸.

While all modifications have already been investigated by electron microscopy¹⁰, quantitative single-crystal X-ray diffraction structure analyses have only been performed so far for the basic Ni-rich phase^{11–13} as well as for the average structure of the superstructure of type II¹⁴. In a more qualitative manner, basic Co-rich d-Al-Co-Ni has as well been modeled based on X-ray diffraction data^{15,16}. Electron microscopy can only provide projected structural information, therefore it can be highly valuable for identifying clusters and underlying tilings but it cannot give a full, quantitative picture of the 3D structure. This is the domain of single-crystal X-ray diffraction methods, and this is the goal of our study.

In the following we present the refined 5D model of the average structure of basic Co-rich d-Al_{72.5}Co_{18.5}Ni₉. This represents the first part of the tedious determination of its full structure based on single-crystal X-ray diffraction data. A 5D model¹⁷ of d-Al-Fe-Ni with four-layer periodicity has been used as basis for our 5D starting model. The good fit between observed and calculated X-ray diffraction intensities as well as the convincing agreement with the projected structure of the closely related W-phase, a rational approximant, prove the validity of the proposed structure solution. Since quasicrystals and their structurally closely related approximants consist of the same atomic clusters, the four-layer structure of the W-phase gives valuable information on the twofold superstructure of basic Co-rich d-Al_{72.5}Co_{18.5}Ni₉, which will be presented in a follow-up paper.

II. EXPERIMENTAL

For sample preparation, compacts with composition Al_{72.5}Co_{18.5}Ni₉, 1g each, were pressed from pulverized Al (Heraeus 99.95 wt.%), Co (Alfa Aesar 99.8 wt.%) and Ni (Heraeus 99.99 wt.%) in argon atmosphere (Mbraun glove box 150 B-G, PanGas Ar 99.998). Pre-alloys were prepared by melting the compacts in an arc furnace (DE-

GUSSA VOLi O) with non-consumable tungsten electrode under Ti-gettered argon. The as-cast samples were analyzed by differential temperature analysis (DTA) (Perkin Elmer DTA 7) using Al_2O_3 crucibles under high purity argon (cooling rates of $10^\circ\text{C}/\text{min}$). Quasicrystal growth and annealing was performed in a high-vacuum resistance furnace (PVA MOV 64). Therein, an as cast sample was heated in an Al_2O_3 crucible to 1350°C (i.e. above melting temperature), held at this temperature for 20 min, then cooled to 1000°C with a cooling rate of $0.24^\circ\text{C}/\text{min}$ and subsequently annealed for 48 hours at 1000°C . Eventually, the sample was quenched by jetting cold argon into the sample chamber.

Single crystal X-ray data were collected at SNBL/ESRF Grenoble, using a marresearch 345 imaging-plate scanner (180 frames with an oscillation angle of $\phi = 1^\circ$ each, wavelength $\lambda = 0.72326 \text{ \AA}$). Two data sets were collected, *data set 1* with an exposure time of 4 sec/frame to prevent saturation of strong reflections, *data set 2* with 100 sec/frame in order to detect a sufficient amount of the rather weak superstructure reflections. The reciprocal space layers $h_1h_2h_3h_4h_5$ with $h_5 = 0, 1, 2, 3$ and the reciprocal space sections $h_1h_2h_2h_1h_5$ and $h_1h_2\bar{h}_2\bar{h}_1h_5$, perpendicular to them as well as to each other and containing the tenfold axis, are shown in Fig. 1.

Since the strongest reflections of these two synchrotron data sets are still oversaturated, additionally an in-house data set (*data set 3*) was collected employing a four-cycle diffractometer equipped with a charge-coupled device (CCD) detector (Oxford Diffraction Xcalibur, $7.5^\circ \leq 2\theta \leq 55.5^\circ$, 360 frames with $\phi = 1^\circ$ each, exposure time 10 sec/frame, 50 kV, 40 mA, graphite monochromatized MoK_α radiation).

Data reduction was performed using the software package CrysAlis (Oxford Diffraction). According to the observed Laue symmetry $10/mmm$, *data set 1* with 39,315 reflections was merged into 1,405 unique reflections with $R_{\text{int}} = 0.174$, *data set 2* with 41,810 reflections was merged into 1,434 unique reflections with $R_{\text{int}} = 0.163$ and *data set 3* with 899,034 reflections was merged into 1,764 unique reflections with $R_{\text{int}} = 0.098$. The index of the strongest reflection in the zero layer is 13420 in the Yamamoto setting¹⁸ (02210 in the Steurer setting⁶) that is used throughout the paper (see Fig. 1(a)). The three data sets were scaled to each other using QCDIFF, a refinement program for quasicrystal structures included in the program package QUASI07.08¹⁹.

III. 5D MODEL BUILDING

The reconstructed reciprocal space layers (Fig. 1) show quite different intensity distributions in even and odd layers perpendicular to the tenfold axis. The even layers consist of main reflections only that can be indexed using the basis of the basic Ni-rich phase. These reflections contain the information on the two-layer average

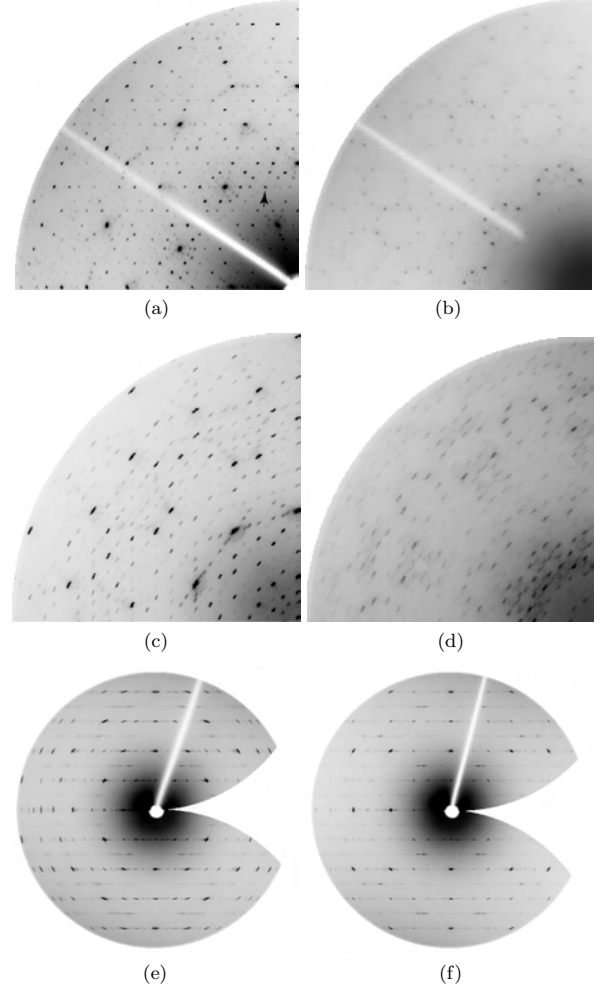


FIG. 1: Reciprocal space sections of decagonal $\text{Al}_{72.5}\text{Co}_{18.5}\text{Ni}_9$ reconstructed from 180 image-plate-scanner frames each: $h_1h_2h_3h_4h_5$ with (a) $h_5 = 0$, (b) $h_5 = 1$, (c) $h_5 = 2$, (d) $h_5 = 3$ (h_5 referring to the four-layer 8.16(4) \AA period), (e) $h_1h_2\bar{h}_2\bar{h}_1h_5$ and (f) $h_1h_2h_2h_1h_5$. The sections in (b) and (d) contain superstructure reflections only. The reflection 10000 (Yamamoto setting¹⁸) is marked by an arrow in (a).

structure. The superstructure reflections, which are only present in the odd layers and result from some modifications of the average structure, cannot be indexed on the same basis. The reciprocal basis of the superstructure of type I^{20} can be used as a common basis for both main and satellite reflections. It can be obtained from that of the basic structure by rotoscaling, i.e. a rotation by $\pi/10$ and scaling by a factor of $1/(2 \cos(\pi/10)) = 0.5257$. In the present analysis of the average structure, however, only the main reflections are included in the refinements.

With the parameters $a_o = 2.745(2) \text{ \AA}$ (defined by the 10000 reflection marked in Fig. 1(a)) and $c_o = 4.072(1)$

Å (along the tenfold axis), we obtain a proper 5D basis (Yamamoto setting²¹) for the main reflections:

$$\mathbf{d}_j^* = \frac{a_o^*}{\sqrt{5}}[c_j\mathbf{a}_1 + s_j\mathbf{a}_2 + c_{2j}\mathbf{a}_3 + s_{2j}\mathbf{a}_4]$$

$$\text{for } j = 1, \dots, 4 \text{ and } \mathbf{d}_5^* = c_o^*\mathbf{a}_5 = \mathbf{c}_o^* \quad (1)$$

and, reciprocal to it

$$\mathbf{d}_j = \frac{2a_o}{\sqrt{5}}[(c_j - 1)\mathbf{a}_1 + s_j\mathbf{a}_2 + (c_{2j} - 1)\mathbf{a}_3 + s_{2j}\mathbf{a}_4]$$

$$\text{for } j = 1, \dots, 4 \text{ and } \mathbf{d}_5 = c_a\mathbf{a}_5 = \mathbf{c}_o \quad (2)$$

where $a_o^* = 1/a_o$, $c_o^* = 1/c_o$, $c_j = \cos(2\pi j/5)$, $s_j = \sin(2\pi j/5)$, $c_{2j} = \cos(4\pi j/5)$ and $s_{2j} = \sin(4\pi j/5)$. The vectors \mathbf{a}_1 , \mathbf{a}_2 and \mathbf{a}_5 are external space unit vectors and \mathbf{a}_3 and \mathbf{a}_4 internal space unit vectors.

A symmetry analysis of the full reflection data set reveals the Laue symmetry $10/mmm$. Neglecting some weaker reflections, one finds an extinction rule for the superstructure, $h_1h_2h_3h_4h_5$ with $h_5 = 2n + 1$ indicating a pseudo 5D c -glide plane for the four-layer superstructure. Considering the pseudosymmetry as true symmetry, possible space groups would either be centrosymmetric $P10_5/mmc$ or non-centrosymmetric $P\bar{1}0_2c$, otherwise $P10/mmm$ or $P\bar{1}0_2m$, respectively.

If we take the pseudosymmetry into account, then the projection of the four-layer superstructure onto the two-layer average structure changes the symmetry from $P10_5/mmc$ to $P10/mmm$, and from $P\bar{1}0_2c$ to $P\bar{1}0_2m$. If we consider the true symmetry of the four-layer structure for the average structure we end up with $P10/mmm$ or $P\bar{1}0_2m$, respectively, as well. For the average structure described by the basis of the basic Ni-rich phase, the mirror plane is rotated by $\pi/10$ relatively to the superstructure basis. Hence the higher dimensional space group is $P\bar{1}0m2$.

The structure of a decagonal quasicrystal can be described as an external space cut of a 5D periodic hypercrystal structure with basis \mathbf{d}_j , $j = 1, \dots, 5$. The structural information is coded in 2D occupation domains (OD), which are parallel to internal space. A starting model for the structure refinements has been obtained by the low-density elimination (LDE) method²². The principle behind this powerful iterative direct-space approach is that all (electron) density values below a given threshold value δ are set to zero. The OD identified in this way are centered at the special positions $(1,1,1,1,5/4)/5$, $(2,2,2,2,5/4)/5$, $(4,4,4,4,15/4)/5$, $(3,3,3,3,15/4)/5$, $(0,0,0,0,1/4)$ and $(0,0,0,0,3/4)$. The two OD at $(0,0,0,0,1/4)$ and $(0,0,0,0,3/4)$ have an external space distance of only 2.04 Å. Consequently, they will generate partially occupied (split) positions with partial occupancies summing up to at most one.

For the structure refinements the obtained density distribution has to be properly parameterized by polygonal

subdomains^{17,18}. Due to the similarity between the observed diffraction patterns of basic Co-rich d-Al-Co-Ni and the simulated diffraction pattern of d-Al-Ni-Fe, this could be done based on Yamamoto's model for d-Al-Fe-Ni¹⁷. For that purpose, five internal space basis vectors are defined

$$\mathbf{v}_j = \frac{2a_o}{\sqrt{5}}[c_{2j}\mathbf{a}_3 + s_{2j}\mathbf{a}_4], \quad j = 1, \dots, 5 \quad (3)$$

with $2a_o/\sqrt{5}=2.43$ Å. Each vector is parallel to one of the center-to-vertex vectors of a reference pentagon. The vector \mathbf{v}_5 is redundant, since it can be expressed as a linear combination of the other four vectors, $\mathbf{v}_5 = -(\mathbf{v}_1 + \mathbf{v}_2 + \mathbf{v}_3 + \mathbf{v}_4)$. The vectors \mathbf{v}_j ($j = 1, \dots, 4$) are equal to the internal space components of the decagonal lattice vectors $\mathbf{d}_j - \mathbf{v}_5$. Note that \mathbf{d}_5 is parallel to the 10-fold axis in external space. By using \mathbf{v}_j as unit vectors, the i th corner vector of an OD is written as $\mathbf{e}_i = (x_1, x_2, x_3, x_4, x_5)$.

The number of atoms per unit cell, a hard constraint for modeling in standard structure analysis, is not available for quasiperiodic structures. Its role is taken over by the point density, i.e. the inverse of the average atomic volume, which can be derived from the mass density of the quasicrystal. This quantity is convenient for checking the quality of a model also during the refinement steps, since the point density can be expressed as the ratio between the total area of the occupation domains times their individual occupancies and the 5D unit cell volume.

Lacking CBED (convergent-beam electron diffraction) information, it was not possible to decide whether or not the average structure has an inversion center. Therefore, five independent OD were used. Since the final distribution of the Al and TM atoms strongly deviates from the centrosymmetric case, we conclude that the 5D space group is $P\bar{1}0m2$ indeed. The point density of the model is $\rho' \approx 0.073$ Å⁻³.

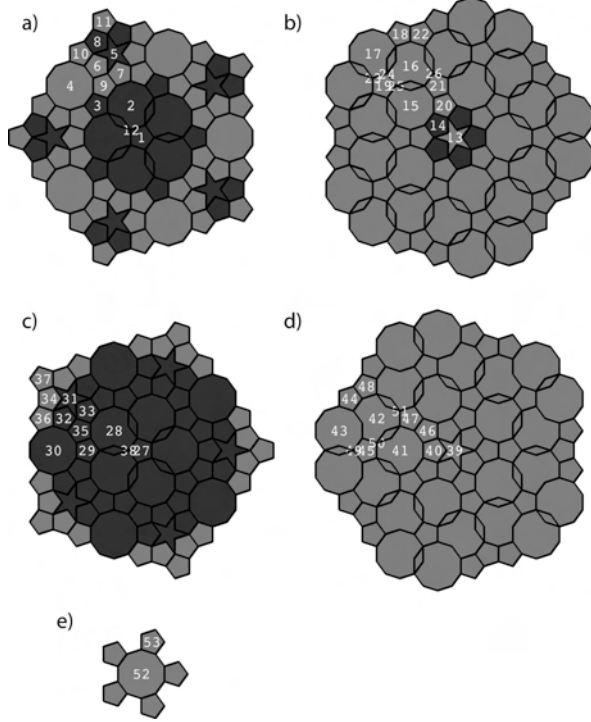
IV. STRUCTURE REFINEMENT

Since it is hardly possible to distinguish between Co and Ni based on X-ray diffraction data, the structure has been refined as a pseudo-binary phase containing just Al and TM atoms. For the latter atomic scattering factors of Co were used. It may be possible to comment on the Co/Ni ordering once the full structure of basic Co-rich decagonal Al-Co-Ni will have been solved by drawing conclusions from the ordering in W-Al-Co-Ni. There, the influence of Co and Ni atoms on their local atomic coordinations has been studied by quantum-mechanical calculations⁹ as well as by neutron diffraction²³.

The final model contains 5 OD subdivided into 53 independent subdomains (Fig. 2) based on the basic polygons listed in Table I. During the refinement process various modifications were required for the subdivision of the OD as well as for the chemical occupancies of the

TABLE I: Basic polygons defining the subdomains partitioning the large OD (Fig. 2). The superscript i refers to the internal space component. $\tau=(1+\sqrt{5})/2$

Polygon	Corner vectors defining the polygonal subdomains		
decagon	$\mathbf{e}_1=(0, \tau^{-4}, -\tau^{-4}, 0, 0)^i$	$\mathbf{e}_2=(-\tau^{-4}, \tau^{-4}, 0, 0, 0)^i$	$\mathbf{e}_3=(-\tau^{-4}, 0, 0, 0, \tau^{-4})^i$
pentagon	$\mathbf{e}_1=\tau^{-5}(0.4, 0.4, -0.6, -0.4, -0.6)^i$	$\mathbf{e}_2=\tau^{-5}(-0.6, 0.4, -0.6, 0.4, 0.4)^i$	$\mathbf{e}_3=\tau^{-5}(-0.6, 0.4, 0.4, -0.6, 0.4)^i$
	$\mathbf{e}_4=\tau^{-5}(0.4, -0.6, 0.4, -0.6, 0.4)^i$	$\mathbf{e}_5=\tau^{-5}(0.4, -0.6, 0.4, 0.4, -0.6)^i$	
star	$\mathbf{e}_1=\tau^{-5}(-0.2, 0.8, -1.2, 0.8, -0.2)^i$	$\mathbf{e}_2=\tau^{-5}(0.43, 0.43, -0.43, 0.0, -0.43)^i$	$\mathbf{e}_3=\tau^{-5}(0.8, -0.2, -0.2, 0.8, -1.2)^i$
rhombus	$\mathbf{e}_1=(\tau^{-5}, -\tau^{-5}, 0, 0, 0)^i$	$\mathbf{e}_2=(2\tau^{-5}, -\tau^{-5}, 0.0, 0.0, -\tau^{-5})^i$	$\mathbf{e}_3=(\tau^{-5}, 0.0, 0.0, 0.0, -\tau^{-5})^i$


 FIG. 2: Independent OD of the refined model structure of Co-rich d-Al-Co-Ni, located at (a) $(1,1,1,1,5/4)/5$, (b) $(2,2,2,2,5/4)/5$, (c) $(4,4,4,4,15/4)/5$, (d) $(3,3,3,3,15/4)/5$, (e) $(0,0,0,0,3/4)$. Dark grey indicates TM atoms (Co or Ni) and light grey Al atoms.

subdomains. The OD in $(0\ 0\ 0\ 0\ 1/4)$ had to be removed because its occupancy refined to zero. The final Al/TM distribution is illustrated in Fig. 2 and Table III.

For each subdomain in the current model, the external space displacements u_1, u_2 from their ideal positions and Al/TM ratio (mixing parameter s_1) were refined. Overall external space atomic displacement parameters (ADP, "Debye-Waller factor"), $B_{||}$ within the quasiperiodic plane and B_{\perp} perpendicular to it, were refined for each OD ($B = 8\pi^2 \langle u^2 \rangle$, with u the displacement amplitude). The refinement of individual ADP from each subdomain was not possible due to the limited number of reflections.

The center of a subdomain is displaced by the internal space vector \mathbf{x}^i relative to the center \mathbf{x}_0 of the OD, hence the actual position of each subdomain is $\mathbf{x}_0 + \mathbf{x}^i$. Taking into consideration symmetry restrictions, we identified for each subdomain possible external space shift vectors, \mathbf{x}_1^e and \mathbf{x}_2^e , defined on the basis

$$\mathbf{u}_j = \frac{2a_o}{\sqrt{5}}[c_j \mathbf{a}_1 + s_j \mathbf{a}_2], \quad (j = 1, \dots, 5), \quad \mathbf{u}_6 = \mathbf{a}_3. \quad (4)$$

The number of shift vectors for the individual subdomains is restricted by site symmetry to maximum two (Table II). In this case the position of a displaced subdomain is given by $\mathbf{x} = \mathbf{x}_0 + \mathbf{x}^i + u_1[\mathbf{x}_1^e/|\mathbf{x}_1^e|] + u_2[\mathbf{x}_2^e/|\mathbf{x}_2^e|]$. The displacements resulting from the refinements are listed in Table III.

The refined parameters for each individual subdomain are summarized in Table III. For each subdomain are given its relative position \mathbf{x}^i , external space displacements u_1, u_2 and partial occupancy factor p . Where all subdomain are fully occupied. $B_{||}$ and B_{\perp} components of the ADP are given for each OD. The estimated standard deviation (esd) for each refined parameter is less or equal 0.01.

Scaling factors and two parameters for the secondary extinction factor were refined as common parameters for all subdomains and individually for each diffraction data set. In addition, a phason displacement parameter ("phason Debye-Waller factor") was refined to $b_i = 0.112(2) \text{ \AA}^2$ for the synchrotron data with weak reflections.

Three penalty functions were included, PF_1 for occupation probabilities, PF_2 for the displacement parameter and PF_3 for the chemical composition. Their weights were chosen to be 0.5, 0.3 and 0.3 respectively. In the framework of the present structure solution the final model was refined with a chemical composition of $\text{Al}_{72.3}\text{TM}_{27.7}$ compared to the actual one of $\text{Al}_{72.5}(\text{Co,Ni})_{27.5}$. The final R-values are $wR = 0.123$ and $R = 0.156$ for 957 unique reflections based on three data sets. The high quality of the fit is reflected in the $F_{\text{obs}}/F_{\text{calc}}$ distribution shown in Fig. 3.

Not all the reflections from the three data sets were included in the refinement process. Our threshold parameters are based on $\sigma|F_o|$, which is $\sigma|F_o| = \sqrt{\sigma(F_o^2)}/2$ for strong reflections and $\sigma|F_o| = \sigma(F_o^2)/2|F_o|$ for weak reflections²⁴. The resulting R-factors of the partial subdomains are:

TABLE II: Symmetry allowed shift vectors of the subdomains shown in Fig. 2. The superscript e indicates that the shifts only have external space components.

subdomain	shift vector \mathbf{x}_1^e	shift vector \mathbf{x}_2^e
#1, #13, #27, #39, #52	-	-
#2, #5, #7, #11, #20, #21, #22, #26	(0, -1, 0, 0, 0, 0) ^e	-
#3, #4, #12, #14, #15, #17, #19, #23, #28, #31, #33, #37, #46, #47, #48, #51	(1, 0, 0, 0, 0, 0) ^e	-
#29, #30, #38, #40, #41, #45, #49	(0, 0, 0, 0, -1, 0) ^e	-
#53	(0, 0, 1, 0, 0, 0) ^e	-
#6, #8, #9, #10, #16, #17, #18, #24, #25	(1, 0, 0, 0, 0, 0) ^e	(0, -1, 0, 0, 0, 0) ^e
#32, #34, #35, #36, #42, #43, #44, #50	(1, 0, 0, 0, 0, 0) ^e	(0, 0, 0, 0, -1, 0) ^e

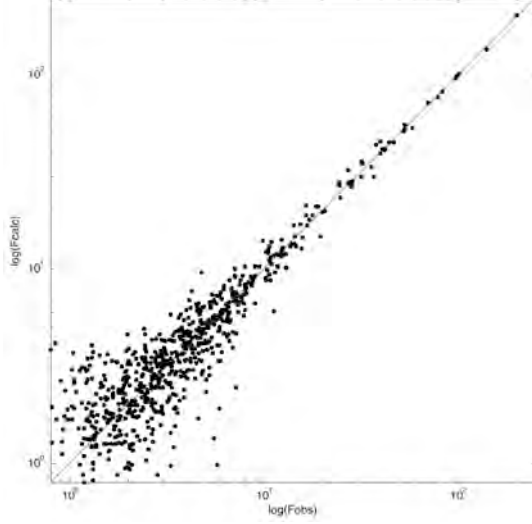


FIG. 3: F_{obs}/F_{calc} plot on a logarithmic scale for the final model of $\text{Al}_{72.5}\text{Co}_{18.5}\text{Ni}_9$ (957 reflections, $wR = 0.123$ and $R = 0.156$).

- $wR = 0.040$ and $R = 0.094$ for *data set 1* with strong reflections ($|F_o| > 3\sigma(|F_o|)$), 177 unique reflections;
- $wR = 0.201$ and $R = 0.241$ for *data set 2* with weak reflections ($|F_o| > 1\sigma(|F_o|)$), 780 unique reflections;
- $wR = 0.057$ and $R = 0.081$ for *data set 3* with strongest reflections ($|F_o| > 10\sigma(|F_o|)$), 85 unique reflections.

The maxima and minima of the residual electron density according to the difference Fourier maps in external space are $\Delta\rho_{max}^e = 1.15 \text{ e}\text{\AA}^{-3}$ and $\Delta\rho_{min}^e = -0.88 \text{ e}\text{\AA}^{-3}$, respectively. The corresponding values for the maxima and the minima of the full electron density are $\rho_{max}^e = 43.54 \text{ e}\text{\AA}^{-3}$ and $\rho_{min}^e = -6.12 \text{ e}\text{\AA}^{-3}$, respectively. Electron density maps calculated by the maximum-entropy method (MEM) fully agree with the structure derived from the 5D model.

V. 3D STRUCTURE MODEL AND THE W-PHASE

A 3D quasiperiodic structure model can be obtained as a particular irrational cut of the 5D hypercrystal structure with 3D external space. In Fig. 4, characteristic sections and a projection of the 3D structure are shown. The underlying tiling with an edge length of $\approx 4.8 \text{ \AA}$ marks the typical columnar clusters with $\approx 20 \text{ \AA}$ diameter (see also Fig. 5). One has to keep in mind that the choice of a fundamental cluster is not unique^{4,5}. In the following, we will use the same kind of cluster that has been frequently employed for the description of the W-phase²⁷ and the different modifications of d-Al-Co-Ni. However, the structure could be equally well described by the alternative generic cluster model²⁸.

In our structure model, only one type of cluster can be identified that is oriented always in the same way as it is the case for the W-phase²⁶, which is a rational approximant. The cluster centers decorate the vertices of a pentagon tiling with $\approx 20 \text{ \AA}$ edge length (Fig. 4(c)). The main difference between the current structure and the model of the d-Al-Co-Ni superstructure of type I (S1)²⁵ is that in the latter the clusters occur in two orientations and do not feature a central atom.

The structures of basic Co-rich d-Al-Co-Ni and the W-phase are built from the same fundamental $\approx 20 \text{ \AA}$ cluster. It consists of a decagon surrounded by ten pentagons. In the layer at $x_3=3/4$, an Al atom is surrounded by five TM atoms followed by a large Al pentagon and subsequently by a 15-gon of five TM and ten Al atoms. The layer at $x_3=1/4$ is rotated by $\pi/5$ relatively to the former and the innermost atomic shell consists of an Al pentagon without a central atom.

These two layers are similar to the layers (A plus A') and B in the W-phase (see Fig. 6). The Al atoms at layer $x_3=3/4$, related to the averaged layers A and A' in the W-phase, exhibit larger displacements from their ideal positions. The maximal shifts we observed for the Al subdomains #44, #46 and #50, reach each $\approx 1 \text{ \AA}$, while those occupied by TM are maximum 0.16 \AA .

Since the W-phase²⁷ (space group of Cm , $a=39.668(3) \text{ \AA}$, $b=8.158(1) \text{ \AA}$, $c=23.392(1) \text{ \AA}$, $\beta = 90.05(1)^\circ$) is a rational approximant, its structure can be directly obtained from the 5D structure of basic Co-rich d-Al_{72.5}Co_{18.5}Ni₉

4.3. BASIC CO-RICH DECAGONAL AL-CO-NI: AVERAGE STRUCTURE (ARTICLE II)

6

TABLE III: Refined parameters: the external space displacements u_1 , u_2 ; $B_{||}$ and B_{\perp} components of the ADP and partial occupancy factors p for TM and Al. esds of refined parameters are less or equal 0.01. Fixed parameters are indicated by *.

subdomain: \mathbf{x}^i	u_1 (Å)	u_2 (Å)	$B_{ }$ (Å ²)	B_{\perp} (Å ²)	$p(\text{TM})$	$p(\text{Al})$
OD1: $\mathbf{x}_0 = (0.2, 0.2, 0.2, 0.2, 0.25)$			0.73	1.27		
1: $(0, 0, 0, 0, 0)^i$	-	-			0.93	0.07
2: $\tau^{-1}(0.4, 0.4, 0.4, -0.6, -0.6, 0)^i$	0.07	-			1.00	0.00
3: $\tau^{-1}(0.8, -0.2, -0.2, -0.2, -0.2, 0)^i$	-0.01	-			0.84	0.16
4: $\tau^{-1}(0.4, -0.6, 0.4, 0.4, -0.6, 0)^i$	0.13	-			0.24	0.76
5: $\tau^{-1}(0.6, -0.4, 0.6, -0.4, -0.4, 0)^i$	0.16	-			1.00	0.00
6: $\tau^{-1}(-0.2, -1.2, 0.8, 0.8, -0.2, 0)^i$	0.01	0.21			0.32	0.68
7: $\tau^{-1}(0.8, 0.8, 0.8, -1.2, -1.2, 0)^i$	0.05	-			0.29	0.71
8: $\tau^{-1}(1.8, -0.2, -0.2, -1.2, -0.2, 0)^i$	-0.10	-0.22			0.75	0.25
9: $\tau^{-1}(0, 0, 1, 0, -1, 0)^i$	0.08	-0.01			0.00	1.00
10: $\tau^{-1}(1, -1, 0, 0, 0, 0)^i$	0.09	0.16			0.00	1.00
11: $\tau^{-1}(1, 0, 1, -1, -1, 0)^i$	0.24	-			0.00	1.00
12: $\tau^{-5}(0.4, -0.6, 0.4, 0.4, -0.6, 0)^i$	0.02	-			1.00	0.00
OD2: $\mathbf{x}_0 = (0.4, 0.4, 0.4, 0.4, 0.25)$			0.88	6.54		
13: $(0, 0, 0, 0, 0, 0)^i$	-	-			0.49	0.51
14: $\tau^{-1}(1.2, 0.2, -0.8, -0.8, 0.2, 0)^i$	0.07	-			0.41	0.59
15: $\tau^{-1}(0.8, -0.2, -0.2, -0.2, -0.2, 0)^i$	0.08	-			0.00*	1.00
16: $\tau^{-1}(-0.2, -1.2, 0.8, 0.8, -0.2, 0)^i$	0.06	0.10			0.00*	1.00*
17: $\tau^{-1}(0.8, -0.2, 0.8, -0.2, -1.2, 0)^i$	0.02	0.21			0.00*	1.00*
18: $\tau^{-1}(0.2, -0.8, 1.2, 0.2, -0.8, 0)^i$	0.10	0.21			0.00*	1.00*
19: $\tau^{-1}(0.4, -0.6, 0.4, 0.4, -0.6, 0)^i$	0.16	-			0.42	0.58
20: $\tau^{-1}(0.4, 0.4, 0.4, -0.6, -0.6, 0)^i$	0.04	-			0.11	0.89
21: $\tau^{-1}(0.2, -0.8, 0.2, 0.2, 0.2, 0)^i$	0.02	-			0.84	0.16
22: $\tau^{-1}(0.4, -1.6, 0.4, 0.4, 0.4, 0)^i$	0.55	-			0.16	0.84
23: $\tau^{-1}(1.8543, 0, 0, 0, 0, 0)^i$	-0.12	-			0.00*	1.00*
24: $\tau^{-1}(0.4584, -0.6876, 0.4521, 0.3124, -0.5416, 0)^i$	-0.21	-0.14			0.00*	1.00*
25: $\tau^{-1}(0.3124, -0.5416, 0.4584, 0.3124, -0.5416, 0)^i$	-0.24	0.24			0.00*	1.00*
26: $\tau^{-1}(0, -1.2362, 0, 0, 0, 0)^i$	-0.57	-			0.00*	1.00*
OD3: $\mathbf{x}_0 = (-0.2, -0.2, -0.2, -0.2, -0.25)$			0.90	0.10		
27: $(0, 0, 0, 0, 0, 0)^i$	-	-			1.00	0.00
28: $\tau^{-1}(-0.4, -0.4, 0.6, 0.6, -0.4, 0)^i$	0.01	-			1.00	0.00
29: $\tau^{-1}(0.2, 0.2, 0.2, 0.2, -0.8, 0)^i$	0.03	-			1.00	0.00
30: $\tau^{-1}(0.6, -0.4, -0.4, 0.6, -0.4, 0)^i$	0.02	-			1.00	0.00
31: $\tau^{-1}(0.4, -0.6, 0.4, 0.4, -0.6, 0)^i$	0.14	-			0.76	0.24
32: $\tau^{-1}(1.2, -0.8, -0.8, 0.2, 0.2, 0)^i$	-0.13	-0.02			1.00	0.00
33: $\tau^{-1}(-0.8, -0.8, 1.2, 1.2, -0.8, 0)^i$	0.12	-			1.00	0.00
34: $\tau^{-1}(0.2, 0.2, 1.2, 0.2, -1.8, 0)^i$	0.00	0.48			1.00	0.00
35: $\tau^{-1}(0, -1, 0, 1, 0, 0)^i$	0.05	-0.01			1.00	0.00
36: $\tau^{-1}(1, 0, 0, 0, -1, 0)^i$	0.26	0.05			0.00	1.00
37: $\tau^{-1}(0, 1, 1, 1, -1, 0)^i$	-0.37	-			0.00	1.00
38: $\tau^{-5}(0.6, -0.4, -0.4, 0.6, -0.4, 0)^i$	-0.08	-			1.00	0.00
OD4: $\mathbf{x}_0 = (-0.4, -0.4, -0.4, -0.4, -0.25)$			2.10	2.04		
39: $(0, 0, 0, 0, 0, 0)^i$	-	-			0.47	0.53
40: $\tau^{-1}(-0.2, 0.8, 0.8, -0.2, -1.2, 0)^i$	-0.04	-			0.00*	1.00*
41: $\tau^{-1}(0.2, 0.2, 0.2, 0.2, -0.8, 0)^i$	0.02	-			0.00*	1.00*
42: $\tau^{-1}(1.2, -0.8, -0.8, 0.2, 0.2, 0)^i$	-0.01	-			0.00*	1.00*
43: $\tau^{-1}(0.2, -0.8, 0.2, 1.2, -0.8, 0)^i$	-0.25	-0.11			0.00*	1.00*
44: $\tau^{-1}(0.8, -1.2, -0.2, 0.8, -0.2, 0)^i$	0.70	0.09			0.00*	1.00*
45: $\tau^{-1}(0.6, -0.4, -0.4, 0.6, -0.4, 0)^i$	-0.09	-			0.10	0.90
46: $\tau^{-1}(-0.4, -0.4, 0.6, 0.6, -0.4, 0)^i$	-0.94	-			0.00*	1.00*
47: $\tau^{-1}(0.8, -0.2, -0.2, -0.2, -0.2, 0)^i$	-0.08	-			0.28	0.72
48: $\tau^{-1}(1.6, -0.4, -0.4, -0.4, -0.4, 0)^i$	0.34	-			0.00*	1.00*
49: $\tau^{-1}(0, 0, 0, 0, -1.8543, 0)^i$	0.65	-			0.00*	1.00*
50: $\tau^{-1}(0, 0.4584, 0, -0.5055, 0.8763, 0)^i$	-0.69	0.03			0.00*	1.00*
51: $\tau^{-1}(1.2362, 0, 0, 0, 0, 0)^i$	0.26	-			0.00*	1.00*
OD5: $\mathbf{x}_0 = (0, 0, 0, 0, -0.25)$			0.40	0.40		
52: $(0, 0, 0, 0, 0, 0)^i$	-	-			0.21	0.79
53: $\tau^{-1}(0.6, -0.4, -0.4, -0.4, 0.6, 0)^i$	0.10	-			0.30	0.70

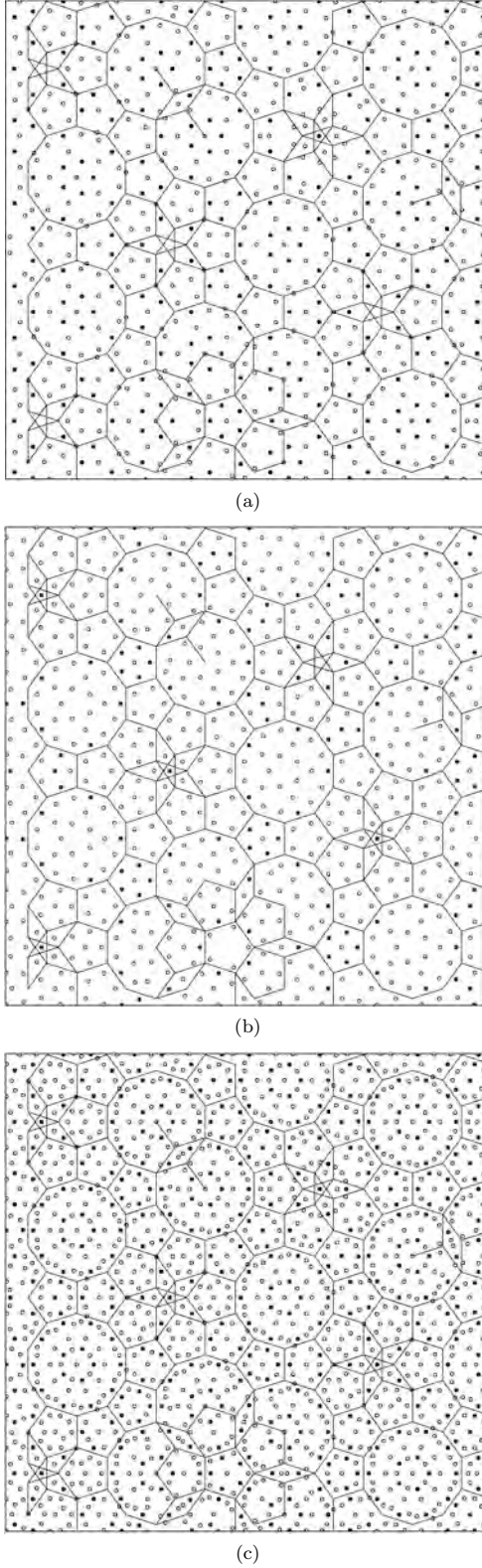


FIG. 4: Atomic layers at (a) $x_3 = 3/4$, (b) $x_3 = 1/4$ and (c) projection along the tenfold axis of the average structure of decagonal $\text{Al}_{72.5}\text{Co}_{18.5}\text{Ni}_9$ ($70 \times 70 \text{ \AA}^2$). White and black circles correspond to Al and TM atoms, respectively. In case of mixed atomic sites, the majority component is indicated.

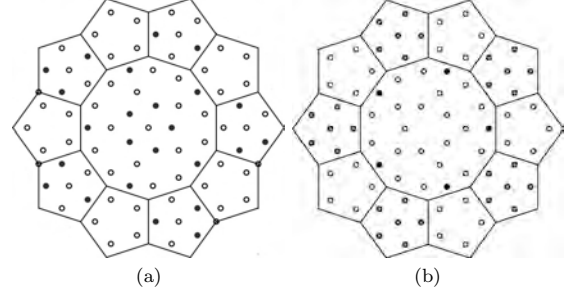


FIG. 5: Atomic layers at (a) $x_3 = 3/4$ and (b) $x_3 = 1/4$ of the $\approx 20 \text{ \AA}$ cluster of the average structure with two layer periodicity. Open and filled circles correspond to Al and TM atoms, respectively, and grey shaded circles indicate mixed occupied positions. The shortest interatomic distances are $\approx 2.5 \text{ \AA}$.

by applying a particular linear phason strain. For this purpose, we have to use the basis of the four-layer superstructure embedding since the W-phase has a four layer structure as well. We have also to take into account, that a rational approximant of the two-layer average structure of the d-phase can only give the two-layer average structure of the W-phase, which has space group Pm and only half the lattice parameter in a -direction.

The 5D unit cell of the superstructure is five times larger than that of the average structure²⁵ (ten times if we consider the doubling of the period along the tenfold axis). Therefore, we first have to transform the basis of the average structure into that of the superstructure. The reciprocal basis vectors of the superstructure, \mathbf{d}_j^* ($j = 1, \dots, 5$), are related to those of the average structure, \mathbf{d}_{0j}^* by $\mathbf{d}_j^* = \sum_j T_{ij} \mathbf{d}_{0j}^*$ with

$$T = \frac{1}{5} \begin{pmatrix} 2 & -1 & 1 & -2 & 0 \\ 2 & 4 & 1 & 3 & 0 \\ -3 & -1 & 1 & -2 & 0 \\ 2 & -1 & 1 & 3 & 0 \\ 0 & 0 & 0 & 0 & 5/2 \end{pmatrix}$$

The resulting quasilattice parameters are $a'_o = 5.221 \text{ \AA}$ and $c'_o = 8.144 \text{ \AA}$ (along the tenfold axis).

The lattice vectors of the approximant can be determined²⁹ to $\mathbf{a}_{app} = \tau^k \mathbf{a}'_o$, $\mathbf{c}_{app} = \tau^{k'} a'_o (\mathbf{a}_1 - \mathbf{a}_4)$ and $\mathbf{b}_{app} = \mathbf{c}'_o$ along tenfold axis of the quasicrystal. Then $a_{app} = |\mathbf{a}_{app}| = \tau^k |\mathbf{a}'_o|$, $c_{app} = |\mathbf{c}_{app}| = 2 \cos(\pi/10) \tau^{k'} |\mathbf{a}'_o|$, where $|\mathbf{a}'_o| = \frac{2}{\sqrt{5}} |\mathbf{a}_o| = 4.670 \text{ \AA}$. Then, we obtain for the lattice parameters of the two-layer average structure of the W-phase $k = 3$ and $k' = 2$, so that $a_{app} = \tau^3 |\mathbf{a}'_o| = 19.782 \text{ \AA}$, $c_{app} = 2 \cos(\pi/10) \tau^2 |\mathbf{a}'_o| = 23.256 \text{ \AA}$.

In other terms, it can be written as:

$$\mathbf{a}_{app} = p \mathbf{a}_0 + q (\mathbf{a}_1 + \mathbf{a}_4) \quad (5)$$

$$\mathbf{c}_{app} = r (\mathbf{a}_1 - \mathbf{a}_4) + s (\mathbf{a}_2 - \mathbf{a}_3) \quad (6)$$

Substituting in eq. (5) the lattice constants of the approximant and of the quasicrystal we obtain $p = 3$ and $q = 2$. And for eq. (6) the parameters result to $r = 2$ and $s = 1$. Hence we have a rational $\langle 3/2, 2/1 \rangle$ -approximant, defined by the ratio of two consecutive Fibonacci numbers. The Fibonacci series is generated by the recursion relation: $F_{k+1} = F_k + F_{k-1}$ where $F_0 = 0$ and $F_1 = 1$. In our case $p = F_{k+1}$, $q = F_k$, $r = F_{k'+1}$ and $s = F_{k'}$.

Based on these results the required phason strain matrix can be calculated to $\mathbf{H} = \mathbf{I} + \mathbf{H}'$ where \mathbf{I} is the unit matrix and the \mathbf{H}' contains coefficients in the bottom-left 2×2 block. For the current case of $\langle F_{k+1}/F_k, F_{k'+1}/F_{k'} \rangle$, the non-vanishing matrix coefficients are $\delta_1 = -(-1/\tau^2)^k = 0.0557 (= \tau(q\tau-p)/(q+p\tau))$ and $\delta_2 = (-1/\tau)(-1/\tau^2)^{k'} = -0.0902 (= (s\tau-r)/(s+r\tau))$.

Taking into consideration the space group of the W-phase we determined the origin of the section with the five-dimensional space to be $(1\ 0\ \bar{1}\ \bar{1}\ 0)^i/2$. The resulting structure of the approximant is shown in Fig. 6. Similar to the average structure of the decagonal $\text{Al}_{72.5}\text{Co}_{18.5}\text{Ni}_9$, the average structure of the W-phase approximant has only two different layers along the b axis. Consequently the layer at $z = 3/4$ is an average of layers A and A' in the real W-phase structure and, consequently, it contains a number of split positions. The translation period along the axes a_{app} and b_{app} of the created approximant are half of the original values in the W-phase. Therefore we have an average structure of the W-phase with the $a_{app}^{av} = 19.884\ \text{\AA}$, $b_{app}^{av} = 4.069\ \text{\AA}$ and $c_{app}^{av} = 23.375\ \text{\AA}$. It is rotated by $\pi/10$ to that of the average structure of the quasicrystal presented in Fig. 4, since they are defined by different bases.

VI. CONCLUSIONS

In this first step of the structure solution of basic Co-rich d- $\text{Al}_{72.5}\text{Co}_{18.5}\text{Ni}_9$, its two-layer average structure could be successfully determined. As could be anticipated from the respective electron micrographs and X-ray diffraction patterns, it is closely related to the d-Al-Co-Ni superstructure of type I (S1) and to the structure of d-Al-Fe-Ni. This allowed to use a modified structure model, originally proposed for d-Al-Fe-Ni¹⁷, as starting model for the refinements.

An important result of this study is that the average structure of the W-phase can be directly obtained as rational approximant of the average structure of basic Co-rich d- $\text{Al}_{72.5}\text{Co}_{18.5}\text{Ni}_9$. This has the consequence that we can use the structure of the W-phase in the 5D embedding to design a starting model for the determination of the full four-layer structure. This first structure solution of the full four-layer structure will enhance our understanding of the complex ordering phenomena in the system Al-Co-Ni.

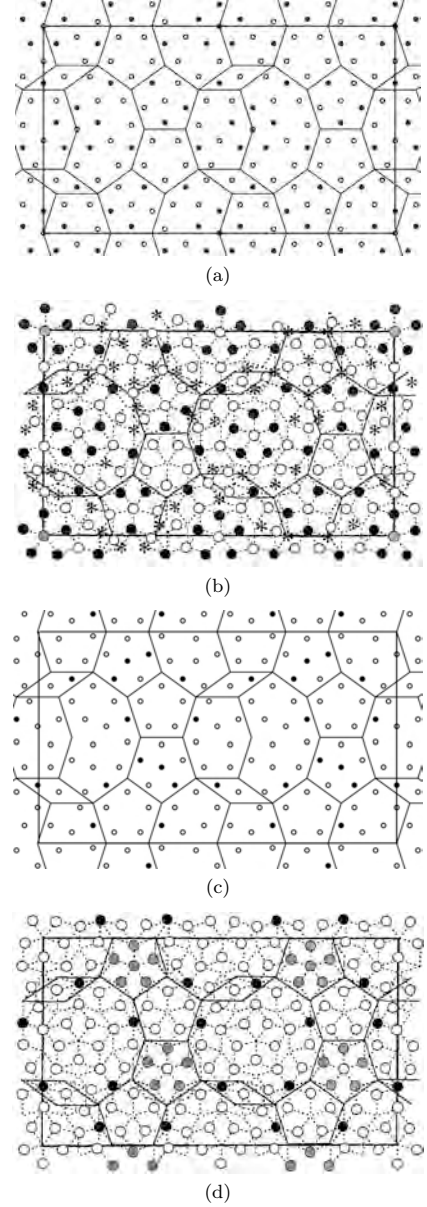


FIG. 6: Layers of the W-phase as derived from basic Co-rich d- $\text{Al}_{72.5}\text{Co}_{18.5}\text{Ni}_9$ (a,c) compared to its actual structure²⁷ (b,d); $x_3 = 3/4$ for (a, b) and $x_3 = 1/4$ for (c,d). The layer in (b) is combined from layers A and A', related by C -centering, of the W-phase. The differences between layers at A and at A' are indicated by asterisks. Wherever atoms are too close to each other in this combined layer, these are partially occupied split positions. White and black circles correspond to Al and TM atoms, respectively, and grey circles indicate mixed occupied positions.

Acknowledgments

We thank Cesar Pay Gomez and Thomas Weber for helpful discussions and gratefully acknowledge financial

support under grant SNF 200020-105158. We also acknowledge support by the staff of the SwissNorwegian beamline (SNBL) at ESRF.

-
- * Electronic address: walter.steurer@mat.ethz.ch
 † Electronic address: angelica.strutz@mat.ethz.ch
 ‡ Electronic address: Yamamoto.Akiji@nims.go.jp
- ¹ W. Steurer, D. Sutter-Widmer, D., J. Phys. D **40** R229-R247 (2007).
 - ² W. Steurer, S. Deloudi, Acta Crystallogr. A **64**, 1 (2008).
 - ³ W. Steurer, J. Non-Cryst. Solids **334**, 137-142 (2004).
 - ⁴ W. Steurer, Philos. Mag. **86**, 1105 (2006).
 - ⁵ C. L. Henley, M. de Boissieu, W. Steurer, Philos. Mag. **86**, 1131 (2006).
 - ⁶ W. Steurer, Z. Kristallogr. **219**, 319 (2004)
 - ⁷ S. Ritsch, C. Beeli, H. U. Nissen, T. Gdecke, M. Scheffer, R. Lck, Philos. Mag. Lett. **78**, 67 (1998).
 - ⁸ S. Katrych, W. Steurer, Z. Kristallogr. **219**, 606 (2004).
 - ⁹ K. H. Hassdenteufel, A. R. Oganov, S. Katrych, W. Steurer, Phys. Rev. B **75**, art. no. 144115 (2007) and references cited therein.
 - ¹⁰ K. Hiraga, Adv. Imag. Electr. Phys. **122**, 1 (2002).
 - ¹¹ H. Takakura, A. Yamamoto, A. P. Tsai, Acta Crystallogr. A **57**, 576 (2001).
 - ¹² A. Cervellino, T. Haibach, W. Steurer, Acta Crystallogr. B **58**, 8 (2002).
 - ¹³ H. Takakura, A. Yamamoto, A. P. Tsai, Ferroelectrics **305**, 257 (2004).
 - ¹⁴ W. Steurer, T. Haibach, B. Zhang, S. Kek, R. Lck, Acta Crystallogr. B **49**, 661 (1993).
 - ¹⁵ A. Yamamoto, K. Kato, T. Shibuya, S. Takeuchi, Phys. Rev. Lett. **65**, 1603 (1990)
 - ¹⁶ A. Strutz, W. Steurer, Philos. Mag. **87**, 2747 (2007).
 - ¹⁷ A. Yamamoto, S. Weber Phys. Rev. Lett. **79**, 861 (1997).
 - ¹⁸ A. Yamamoto, Acta Cryst. A **52**, 509 (1996).
 - ¹⁹ A. Yamamoto, Sci. Technol. Adv. Mater. **9**, 13001 (2008).
 - ²⁰ K. Edagawa, M. Ichihara, K. Suzuki, S. Takeuchi, Philos. Mag. Lett. **66**, 19 (1992).
 - ²¹ A. Yamamoto, K. N. Ishihara, Acta Crystallogr. A **44**, 707 (1988).
 - ²² H. Takakura, A. Yamamoto, M. Shiono, T.J. Sato, A.P. Tsai, J. Alloys Comp. **342**, 72 (2002).
 - ²³ S. Deloudi, Modeling of Quasiperiodic Systems, PhD Thesis ETH No. 18107, (2008).
 - ²⁴ D. Schwarzenbach, Acta Crystallogr. A **45**, 63 (1989).
 - ²⁵ A. Yamamoto, H. Takakura, and E. Abe, Phys. Rev. B **72**, art. no. 144202 (2005).
 - ²⁶ K. Hiraga, T. Ohsuna, W. Sun, K. Sugiyama, Mater. Trans. **42**, 2354 (2001).
 - ²⁷ K. Sugiyama, S. Nishimura, K. Hiraga, J. Alloy. Compd. **342**, 65 (2002).
 - ²⁸ S. Deloudi, W. Steurer, Philos. Mag. **87**, 2727 (2007).
 - ²⁹ K. Niizeki, J. Phys. A: Math Gen **24**, 3641 (1991).

4.4 Supplement - Article II

The atomic structure in external space was generated by an irrational cut through the refined five-dimensional structure. The resulting atomic layers of the refined structure are shown in Fig. 4. The atoms in this structure originate from 53 subdomains as shown in Fig. 2. In Fig. 4.11, the atomic layers are given and their corresponding occupation domains are shown (numbered).

As was previously mentioned, the shapes and positions of the occupation domains were determined using the LDE method. In the initial structure solution, six occupation domains were found as shown in Fig. 4.12. Here we have two small occupation domains at $(0, 0, 0, 0, 1/4)$ and $(0, 0, 0, 0, 3/4)$. These occupation domains create atoms in the centers of the decagonal clusters (indicated by a decagonal cage) in the external space. Electron densities are observed in the centers of the decagonal cages in both layers, Fig. 4.13. Coexistence of these two occupation domains is impossible, since it creates atoms in two atomic layers with unphysically short interatomic distances. The electron density however, in the layer at $x_3 = 1/4$ is significantly lower. This implies that one of the occupation domains has a lower occupancy probability. In the initial structure model, two such occupation domains were constructed and their occupancies were set to 0.5. During the refinement process, the occupation domain at $(0,0,0,0,1/4)$ was eliminated.

The final five occupation domains, improved by MEM, are shown in Fig. 4.14. Their corresponding profiles, plotted on a relative scale, are useful in illustrating the density distribution of each occupation domain. The profiles of the occupation domains at $(-2,-2,-2,15/4)/5$ and $(1,1,1,1,1/4)/5$ are two times larger than the profiles of the occupation domains at $(-1,-1,-1,-1,15/4)/5$ and $(2,2,2,2,1/4)/5$. Hence, the former two are occupied mainly by TM, whereas the latter two are occupied mainly by Al.

The corresponding electron density distribution in external space is shown in Fig. 4.15 as it results from the irrational cut through the refined five-dimensional structure after improvement by MEM. The resulting structure in the external space shows electron densities at the centers of the decagonal clusters only in the layer at $x_3 = 3/4$, as was expected from the refinement. It is important to stress that the information contained in the Fourier or MEM maps is of a more general character, since it is based on experimentally obtained amplitudes.

A comparison of the corresponding layers in Figs. 4.13 and 4.15 reveals that the electron density distribution has been drastically improved in the layer at $x_3 = 1/4$. Whereas, even after the refinement, the electron density in the layer at $x_3 = 3/4$ still contains a lot of so called *split positions*.

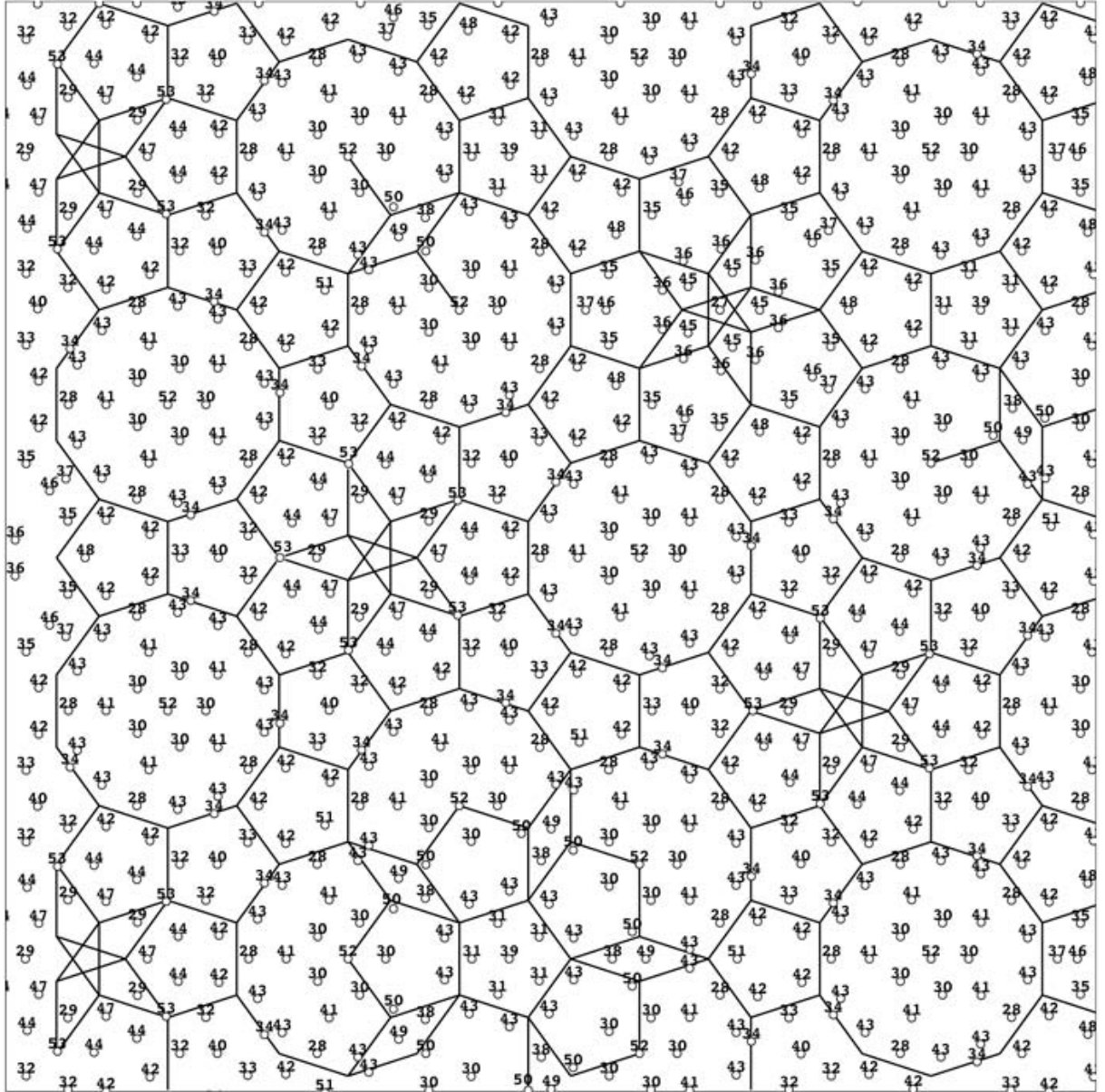
One should keep in mind that this is an average structure solution, therefore each atomic layer is a superposition of two layers in the real four-layer superstructure. Taking into account the structure of the W-phase approximant and the electron distribution in

the layers shown in Fig. 4.15, we can conclude that the layer at $x_3 = 3/4$ is a superposition of two layers that have in-plane displacements and the layer at $x_3 = 1/4$ is a superposition of the two puckered (off-plane displacements) layers.

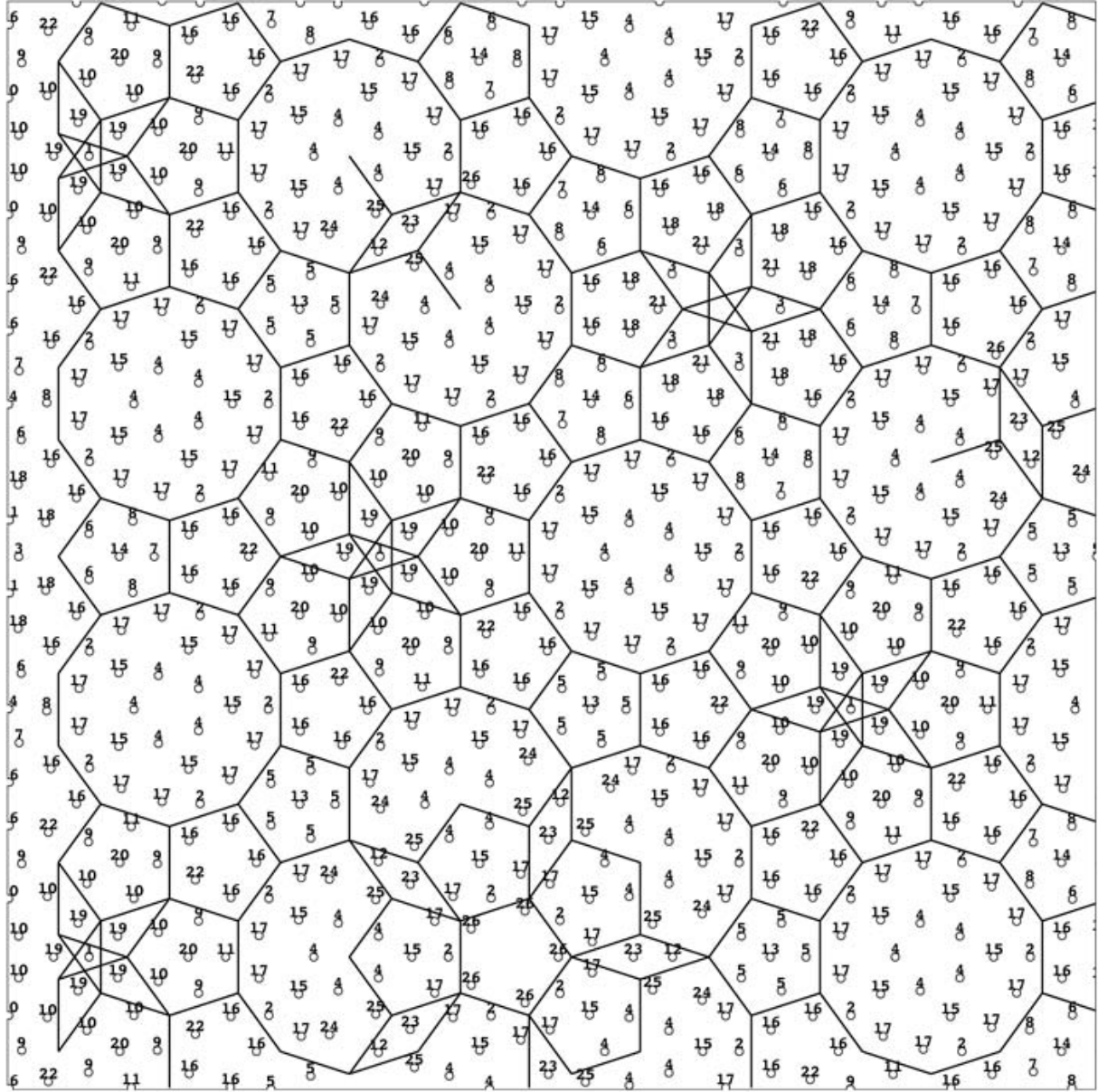
Lets take a closer look at the MEM map corresponding to the layer at $x_3 = 3/4$. The split atomic position in the pentagonal cage, as indicated by an arrow, corresponds to the subdomain #47 (Fig. 4.15(a)). Hence, we expect that in the real, four-layer structure, we will have two different atoms in the two corresponding layers with slightly different positions. A strange electron density distribution is observed inside of the decagonal cage as indicated by a rectangle (Fig. 4.15(a)). The atoms at these positions stem from the outer part of the occupation domain at $(-2,-2,-2,-2,15/4)/5$, namely from subdomain #43, which are normally not clearly defined and result in not clearly defined atomic positions in external space. However, similar shifts are indicated in the W-phase structure, hence we expect to observe these atomic displacements in the real four-layer structure. In some pentagonal and decagonal cages, electron density has very low intensity as indicated by circles. The atoms in the decagonal cages originate again from subdomain #43 and in the pentagonal cages from subdomains #42 and #51. This is a good indication of partially occupied atomic sites which is also in agreement with the structure of the W-phase as shown in Fig. 6(b) in Article II. Moreover, in the present average structure solution, several split atomic positions (atoms which are separated by interatomic distances that are too short) are visible. This is an indication of the presence of phason defects in the system.

The projection of the two layers is given in Fig. 2(c). It is complemented with the projection given in Fig. 4.16, where atoms in different structure layers are indicated. Additionally, two more comparisons were performed. Firstly, a generated $\langle 3/2, 2/1 \rangle$ -approximant W-phase from the refined five-dimensional model of the decagonal $\text{Al}_{72.5}\text{Co}_{18.5}\text{Ni}_9$ is superimposed onto the HAADF-STEM images of the W-phase [HON01] (Fig. 4.17(a)). Secondly, a structure-fragment of the refined decagonal $\text{Al}_{72.5}\text{Co}_{18.5}\text{Ni}_9$ phase is superimposed onto the basic Co-rich structure [HOSS02](Fig. 4.17(b)).

One should keep in mind that this higher-dimensional model is based on an ideal pentagonal Penrose tiling. Hence, it is not taking into account the presence of random phasons. The random phasons are higher-dimensional structural defects which result from various types of defect in the quasiperiodic structures. These include split atomic positions, changes in a position of cluster centers, microdomain structure and others. For the structure description including the random phasons, it would be necessary to use a model based on a random tiling. However, the implementation of such a model is still not clear. To compensate for this, in the current work a phason Debey-Waller factor has been calculated. The random phason factor is a relative property of the quasicrystal structures. To estimate the significance of this parameter, it can be compared with other phason Debey-Waller factors obtained by the refinement of quasicrystal structures.



(a)



(b)

Figure 4.11: $70 \times 70 \text{ \AA}^2$ sections of the atomic layers at (a) $x_3 = 3/4$, (b) $x_3 = 1/4$ of the two-layer average structure decagonal $\text{Al}_{72.5}\text{Co}_{18.5}\text{Ni}_9$ related to Fig. 4 in Article II with an indicated number for each atom.

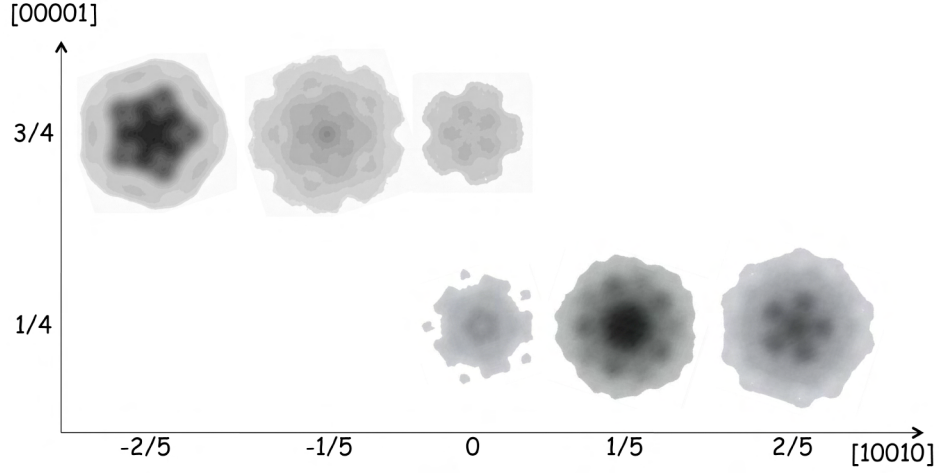


Figure 4.12: Resulting occupation domains of decagonal $\text{Al}_{72.5}\text{Co}_{18.5}\text{Ni}_9$ obtained by LDE at $(0,0,0,0,1/4)$ and $(0,0,0,0,3/4)$. As was reported in Article II, the occupation domain at $(0,0,0,0,3/4)$ has been eliminated during the refinement process. Dark gray indicates TM atoms (Co or Ni) and light gray Al atoms.

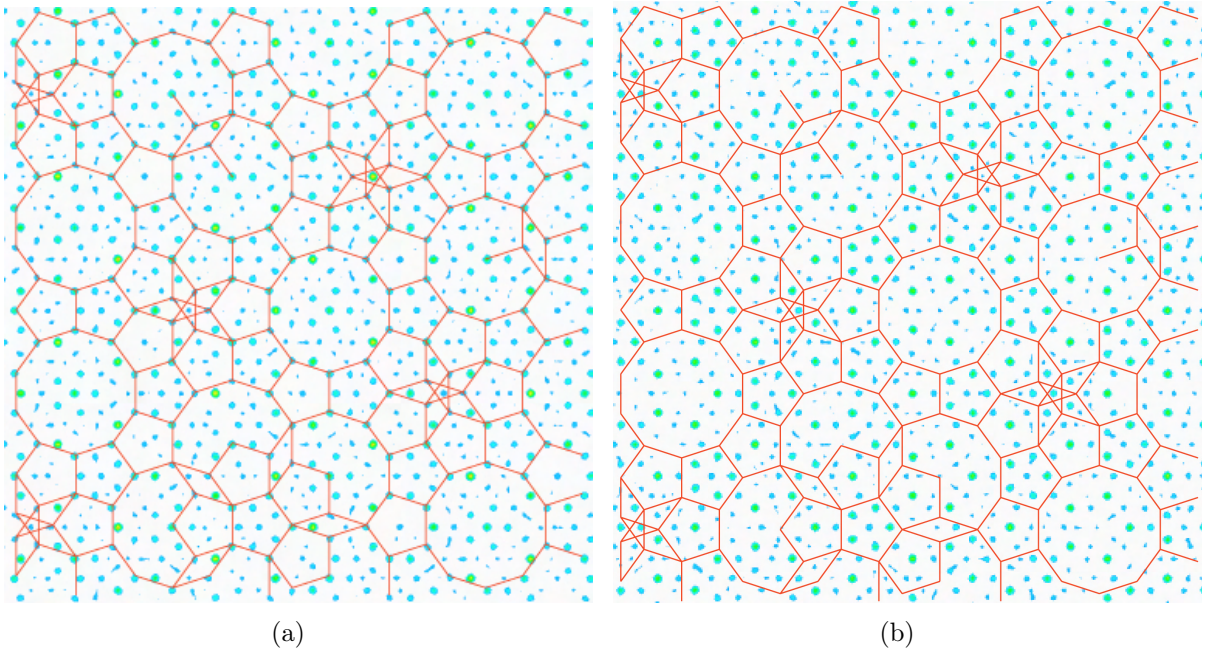


Figure 4.13: Electron density distribution in external space of decagonal $\text{Al}_{72.5}\text{Co}_{18.5}\text{Ni}_9$ ($70 \times 70 \text{ \AA}^2$) calculated by LDE at (a) $x_3 = 3/4$, (b) $x_3 = 1/4$.

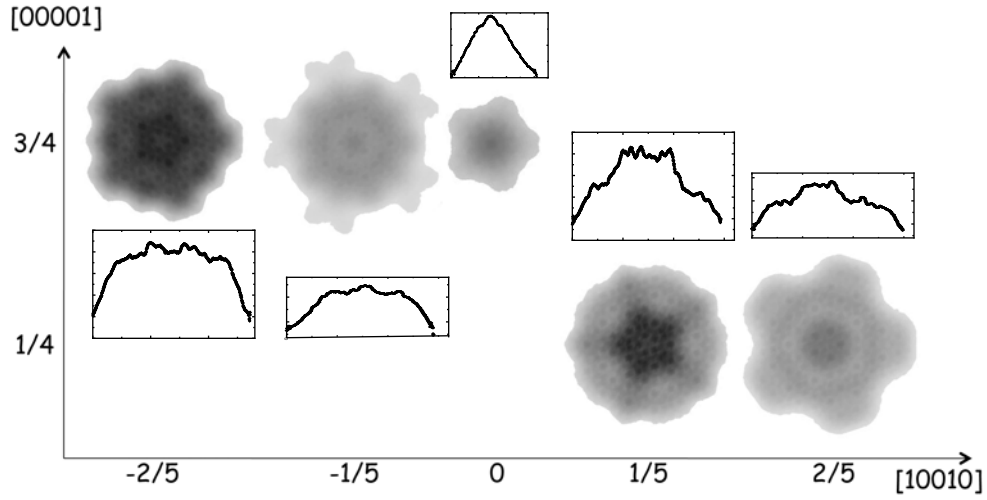


Figure 4.14: Occupation domains resulting from the refinement and after MEM with the corresponding profiles of the density distribution at (a, c) $((1,1,1,1/4)/5$, (b, d) $(2,2,2,2,1/4)/5$, (e, g) $(-2,-2,-2,-2,15/4)/5$, (f, h) $(-1,-1,-1,-1,15/4)/5$, (i, j) $(0,0,0,0,1/4)$. Dark gray indicates TM atoms (Co or Ni) and light gray Al atoms.

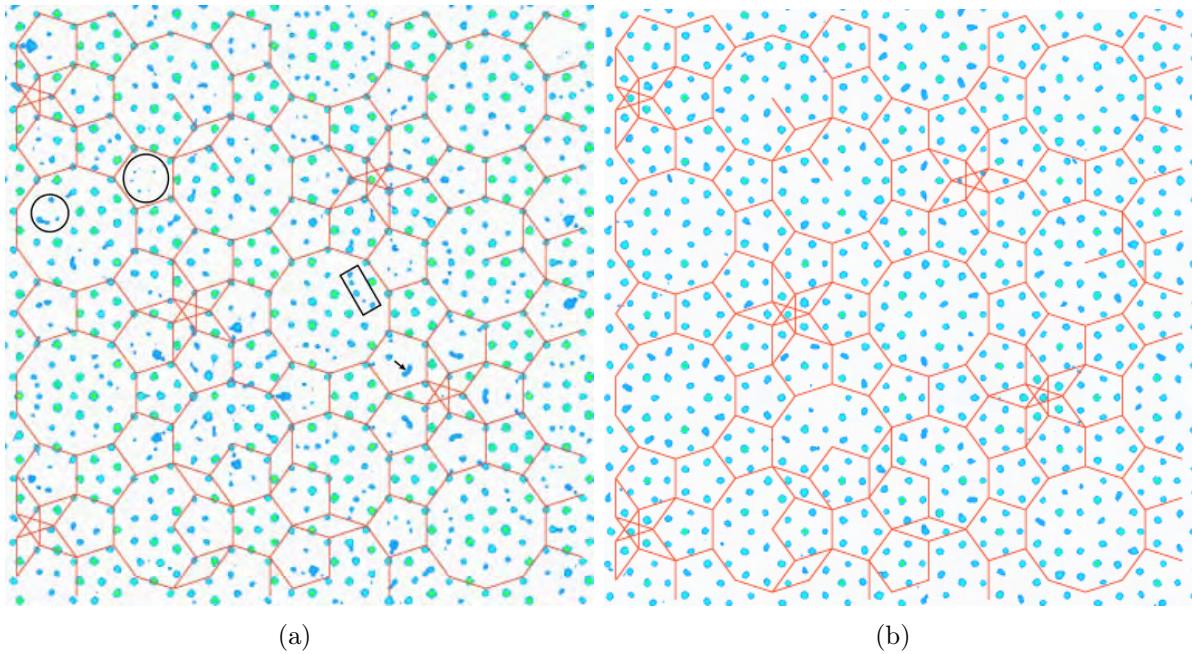


Figure 4.15: Electron density distribution in external space after refinement and MEM calculations at (a) $x_3 = 3/4$, (b) $x_3 = 1/4$.

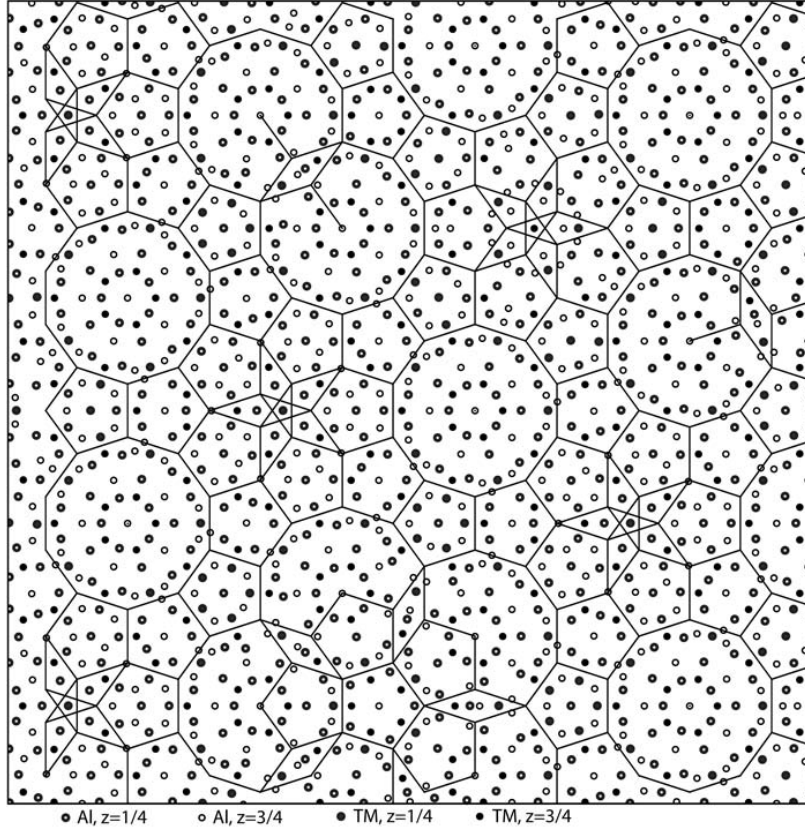


Figure 4.16: Two projected layers along the ten-fold axis of the average structure of decagonal $\text{Al}_{72.5}\text{Co}_{18.5}\text{Ni}_9$ ($70 \times 70 \text{ \AA}^2$).

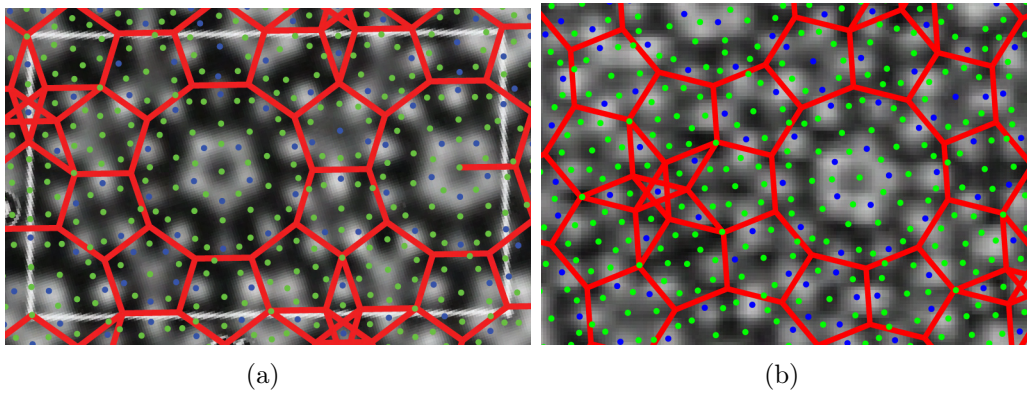


Figure 4.17: A structure-fragment of refined decagonal $\text{Al}_{72.5}\text{Co}_{18.5}\text{Ni}_9$ in comparison with HAADF-STEM images of (a) the W-phase, taken with the incident beam parallel to b -axis [HON01] and (b) the basic Co-rich structure, taken with the incident beam parallel to the periodic axis [HOSS02]. Al and TM atoms are indicated respectively by green and blue circles.

Chapter 5

Superstructure of basic Co-Rich Decagonal $\text{Al}_{72.5}\text{Co}_{18.5}\text{Ni}_9$

5.1 Basic Co-Rich Decagonal Al-Co-Ni: Superstructure (Article III)

The first higher-dimensional refinement of a quasicrystal superstructure has been performed. As a result, a five-dimensional model is proposed. The three-dimensional model shows good agreement with its closely related W-phase approximant. Both structures have four-atomic layers which are stacked as an alternation of flat and puckered layers. A comparison of the corresponding layers in these structures reveals remarkable similarities of the atomic arrangements within their clusters. Moreover, both structures show similar structural modulations that lead to a superstructure formation. The current section contains a reprint of the article:

A. Strutz, A. Yamamoto and W. Steurer, Basic Co-rich decagonal Al-Co-Ni: Superstructure, *submitted to* Phys. Rev. B (2010).

Additional figures concerning this article are given in the supplementary section.

Basic Co-rich decagonal Al-Co-Ni: Superstructure

Angelica Strutz

*Laboratory of Crystallography, Department of Materials,
ETH Zurich, 8093 Zurich, Switzerland**

Akiji Yamamoto

*National Institute for Materials Science,
Namiki 1, Tsukuba, Ibaraki, 305-0044, Japan†*

Walter Steurer^{1‡}

(Dated: July 14, 2010)

Abstract

The four-layer superstructure of basic Co-rich decagonal $\text{Al}_{72.5}\text{Co}_{18.5}\text{Ni}_9$ was determined by single-crystal X-ray diffraction. Based on our previous work [A. Strutz, A. Yamamoto and W. Steurer, Phys. Rev. B **80**, 184102 (2009)], a superstructure model was derived with five-dimensional (5D) non-centrosymmetric space group symmetry $P\overline{1}02c$ with some additional constraints resulting from normal mode analysis. The 5D structure model was refined with 250 parameters, resulting in values of $wR = 0.039$ and $R = 0.186$ for 1222 unique reflections. Its close relationship with the structure of W-Al-Co-Ni, a $\langle 3/2, 2/1 \rangle$ -approximant, proves the physical validity of our structure model and justifies the use of the W-phase for the derivation of structural principles underlying the formation of Al-based decagonal quasicrystals.

PACS numbers: 61.05.cp, 61.44.Br, 61.50.Ah, 61.66.Dk

*Electronic address: angelica.strutz@mat.ethz.ch

†Electronic address: Yamamoto.Akiji@nims.go.jp

‡Electronic address: steurer@mat.ethz.ch

I. INTRODUCTION

This is part II of our structure analysis of basic Co-rich decagonal $\text{Al}_{72.5}\text{Co}_{18.5}\text{Ni}_9$ (d-Al-Co-Ni). In part I [1], we described the determination of the two-layer average structure, while here in part II we present the solution of the actual four-layer superstructure. This is the first determination of such a superstructure, which is quite common in aluminum-based decagonal quasicrystals. In the system Al-Co-Ni, the lateral correlation length of the superstructure decreases with decreasing Co/Ni ratio by approximately two orders of magnitude while it remains constantly large along the periodic direction. Basic Co-rich d-Al-Co-Ni is the only decagonal quasicrystal modification that has sharp superstructure reflections related to the four-layer periodicity, allowing a quantitative structure analysis. All others show only diffuse scattering phenomena which get weaker and less peaked and structured with increasing Ni content, being no more observable at all in case of basic Ni-rich d-Al_{70.2}Co_{5.4}Ni_{24.4} [2–4].

The formation of a twofold superstructure along the periodic direction stabilizes all low-temperature modifications of d-Al-Co-Ni and all their approximants with the exception of the Ni-rich ones [2]. At high temperatures, the entropic contribution, mainly by Co/Ni disorder and vacancy formation, is sufficient for the stabilization of these phases and all superstructures disappear. In order to better understand formation, stability and physical properties of d-Al-Co-Ni full structural information, not only averaged one, is required. More than 500 papers on these phases and structurally related d-Al-Co-Cu and d-Al-Fe-Ni testify the broad interest in these model systems justifying the tedious determination of the superstructure.

One of the main results of the determination of the average structure in part I was that it allows the direct derivation of the two layer average structure of the W-phase, a high rational approximant of d-Al-Co-Ni, by a 5D shear operation. And one of the goals of the determination of the superstructure of d-Al-Co-Ni was to find out whether this is also true for the full four-layer structure of the W-phase. In this case, the W-phase can be employed as a periodic model system, suitable for quantum-mechanical calculations, for all modifications of d-Al-Co-Ni as well as d-Al-Co-Cu and d-Al-Fe-Ni. Furthermore, its fundamental building clusters can be used for modeling the structures of all modifications of these decagonal phases. That this works has already been demonstrated [5].

For the experimental details concerning the single-crystal X-ray diffraction data collection and reduction see part I. There, we already pointed out that the $h_5 = 2n$ reciprocal space layers, containing main reflections only, resemble those of the basic Ni-rich phase, while those with $h_5 = 2n + 1$, containing superstructure reflections only, can be only indexed employing the superstructure basis. Depending on the value of $m = (\sum_{i=1}^4 h_i) \bmod 5$, we can distinguish between main reflections ($m = 0$) and superstructure reflections of first (S1, $|m| = 1$) and second order (S2, $|m| = 2$). The intensities of S1 reflections are systematically stronger than those of S2 reflections as it is usually the case for first and second order satellites.

The superstructure basis is identical to that of the superstructure of type I [6], which is related to that of the basic structure by roto-scaling, i.e. a rotation by $\pi/10$ and scaling by a factor of $1/(2 \cos(\pi/10)) = 0.5257$. This leads to the quasilattice parameter $a_s = 5.221(4)$ Å and the period $c_s = 8.144(2)$ Å along the tenfold axis. According to the determinant of the transformation matrix [7], basic Co-rich d-Al-Co-Ni is a fivefold superstructure (regarding the volume of the 5D unit cell) of the basic Ni-rich modification in the quasiperiodic directions and a twofold one along the tenfold axis. Both types of superstructures have been analyzed in the work presented here.

II. 5D STRUCTURE MODEL BUILDING

For d-Al-Ni-Fe, a similar peculiar distribution of main and superstructure reflections as in our case has been observed and qualitatively explained by a 5D structure model with color symmetry [8]. Unfortunately, this approach is not applicable to our case since it lacks the necessary degrees of freedom for the description of puckered quasiperiodic atomic layers. We need these degrees of freedom because we know from the structure of the W-phase that at least two of the four quasiperiodic layers have to be puckered. We also know from the diffraction pattern that the superstructure reflections do not systematically decay with increasing values of h_5 , indicating that the atomic displacements along the tenfold axis strongly contribute to the intensities of the superstructure reflections.

A hard constraint for our superstructure model is set by symmetry. According to the superspace group $P\overline{1}02c$, the OD in the layers separated by one half of the translation period are related by the c -glide operation cutting them into halves (OD transformed by the

c -glide operation will be marked by primed symbols); OD A and A' as well as B and B' are, additionally, related by reflection on the mirror plane perpendicular to the tenfold direction and halfway between them (note: $\overline{10} = 5/m$).

Another hard constraint is that the projection of the actual four-layer structure onto the two-layer period has to reproduce exactly the average structure determined in part I. This means that we can neither change the general shapes of the five occupation domains (OD) A, B, C, D, and E (see part I and Fig. EPAPS-1 [11]) nor those of their small subdomains. If we denote the OD of the average structure by the subscript $_{AS}$, we get the following conditions: $A_{AS}=A+A'$, $B_{AS}=B+B'$, $C_{AS}=C+C'$, $D_{AS}=D+D'$, $E_{AS}=E+E'$. This means that in projection the point symmetry of all OD has to be $\overline{10}m2$. At contrast, in the actual superstructure the fivefold symmetry of the OD is broken and the point symmetry is reduced to m for OD C, D, C' and D', which are located within mirror planes and are generating flat atomic layers, and that of OD A, A', B and B', generating puckered atomic layers, is even lowered to 1.

The relationships between the symmetry of the average structure and that of the superstructure, together with the above mentioned peculiar reciprocal space distribution of main (even) and superstructure reflections (odd reciprocal space layers), put strong constraints on the allowed shifts and chemical occupancies of the subdomains. Unfortunately, because of the very limited number of observable superstructure reflections, not all remaining allowed parameters can be refined. Therefore, starting from the average structure described in part I, we constrain in our superstructure model the relevant parameters in the form of shift and substitutional modes obtained from a symmetry-based normal mode analysis. Four different shift modes and two substitutional modes, symmetric and antisymmetric ones, were selected and used simultaneously in the refinements.

The shift modes are realized by different combinations of the external space shifts u_1 , u_2 and u_3 for each subdomain. Shifts u_3 , i.e. along the periodic axis $[0\ 0\ 0\ 0\ 0\ \pm 1]$ are only allowed for OD A and B, which generate the puckered atomic layers. For these OD, two different shift modes were used as shown in Fig. 1(a,b). Empty circles and crossed circles identify subdomains with displacement vectors $[0\ 0\ 0\ 0\ 0\ +1]$ (up) and $[0\ 0\ 0\ 0\ 0\ -1]$ (down), respectively. For these OD, the reflection conditions do not allow displacements parallel to the quasiperiodic layers. The maximal amplitude of $\approx 0.5\ \text{\AA}$ was observed for the subdomains 47, 52-55. These subdomains are fully occupied by Al.

At contrast, OD C and D, located within mirror planes and generating the flat atomic layers, have displacements within the quasiperiodic layers only. The two different shift modes employed are shown in Fig. 1(c,d), with external space shift directions indicated by arrows. Atoms originating from the outermost subdomains 168, 169, 184, 185, 200, 201, 210 - 213 experience large shifts exceeding 1 Å. Therefore their total occupancies were set to one half. In the external space, these atoms are located in the decagonal cages of the 20 Å clusters. The comparison with the 20 Å clusters in the W-phase reveals similar atomic relaxations in the quasiperiodic flat layers, mainly due to the presence of vacancies.

The two substitutional modes are of the same type as shown in Fig. 1(a,b), but only apply to OD C and D. The symbols mark now plus and minus deviation of the Al/TM occupancy from equal distribution. The variations in the Al/TM occupancies, in most of the cases, are coupled with the displacements parallel to the quasiperiodic layers. Analysis of the changes in R-factors during the refinement shows that the importance of the substitutional modes in the superstructure formation is less significant in comparison with puckering or with displacements parallel to the quasiperiodic layers. The maximal amplitude of the total substitutional modes of $\approx 50\%$ was observed for the subdomains 160, 161, 190 - 193 related by a fivefold symmetry.

III. STRUCTURE REFINEMENT

All structure refinements have been performed using the program package QUASI07_08 [9]. In the first step, one scale factor and two parameters for secondary extinction correction as well as all average structure parameters [1] were refined against the full data set. These parameters include: for each OD the overall external[13] space atomic displacement parameters (ADP), B_{\parallel} within the quasiperiodic plane and B_{\perp} perpendicular to it ($B = 8\pi^2 \langle u^2 \rangle$, with u the displacement amplitude); for each subdomain the external space shifts u_1, u_2 from the ideal positions as defined by the coordinates of the respective OD and the Al/TM site occupancy (mixing parameter s_1). The limited number of reflections does not allow to refine individual ADP for each subdomain.

In the next step, the superstructure parameters were successively refined in addition. As in the superstructure the fivefold symmetry of the OD is broken, the number of symmetrically independent subdomains is drastically increased from 53 in the average structure to 275.

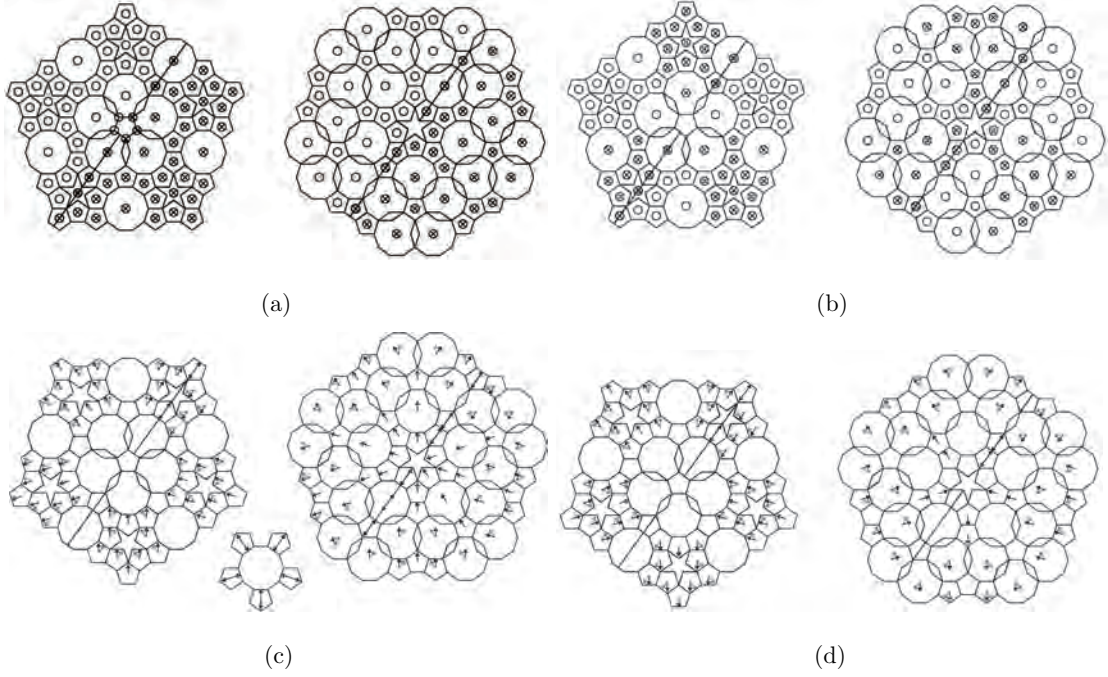


FIG. 1: Different shift modes generating the superstructure. (a,b) Atoms in the puckered layer at $x_3=1/8$ can be displaced along the periodic direction. Empty (crossed) circles mark shifts into the $[00100]$, up ($[00\bar{1}00]$, down) direction. (c,d) Atoms in the flat layer at $x_3=3/8$ can have shifts only within the quasiperiodic layer. Note: although the arrows are plotted in the respective subdomains they denote shifts that are only in external space.

This is more than just $5 \times 53 = 265$, because the subdomains cut by the c -glide plane have to be split into two parts. In order to keep the number of parameters as small as possible, all shifts less than their standard deviations were reset to zero and fixed in the further refinement steps.

In addition, a phason displacement parameter was refined to $b^i = 0.684(2) \text{ \AA}^2$. A penalty function was included in order to constrain the chemical composition, which then was refined to $\text{Al}_{72.3}\text{TM}_{27.7}$ compared to the actual one of $\text{Al}_{72.5}\text{TM}_{27.5}$. Since the standard deviations of our data were calculated from averaging up to 40 symmetrically equivalent reflections, they are systematically underestimated with regard to systematic errors (weak intensity data integration, for instance). For the minimization of the weighted reliability factor, wR , we used weights directly proportional to the standard deviations [10], consequently.

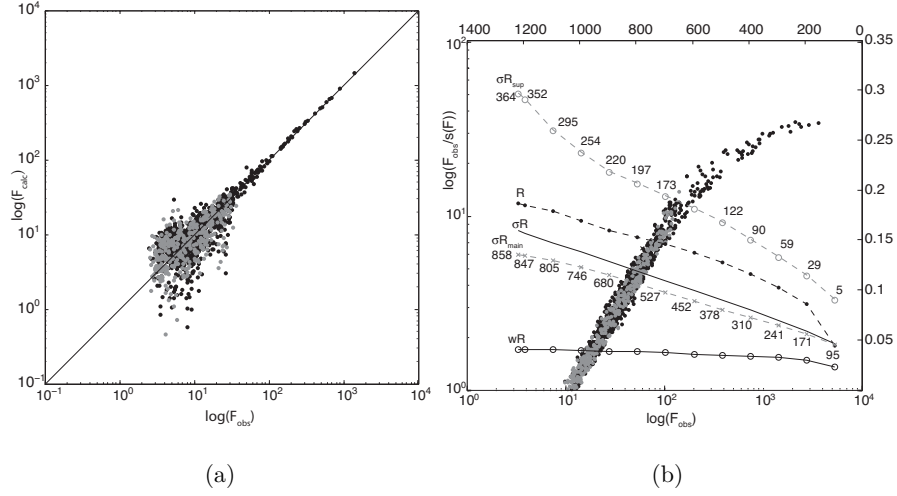


FIG. 2: (a) F_{obs}/F_{calc} plot for the final model of $\text{Al}_{72.5}\text{Co}_{18.5}\text{Ni}_9$. The 858 main and 364 superstructure reflections are marked as black and gray dots, respectively. (b) Distribution of F_{obs}/σ_F on a double-logarithmic scale for main and superstructure reflections (black and gray dots, respectively). Weighted, unweighted and expected R -factors (right scale) as a function of the N strongest reflections (top scale). The expected R -factors, σR , are given as function of the N strongest reflections with N given at the respective data points.

The refinement of the 250 parameters (therefrom 117 superstructure parameters) against the 1222 unique reflections with $|F_o| > 1\sigma(|F_o|)$ converged to $wR = 0.039$ and $R = 0.186$. The reliability factors for the 858 main reflections amount to $wR = 0.034$, $R = 0.150$, those for the 364 satellite reflections to $wR = 0.405$ and $R = 0.364$. For a list of the resulting refined parameters see Table EPAPS-1 [11].

The quality of the least-squares fit is reflected in the F_{obs}/F_{calc} distribution shown in Fig. 2(a). It clearly shows that the fit of the weak superstructure reflections is of the same quality as that of the main reflections. The rather high R -factor for the superstructure reflections can be attributed mainly to their weak intensities leading to large standard deviations and problems for intensity integration. Multiple diffraction effects may also contribute. The internal R -factors, resulting from the averaging of symmetrically equivalent reflections, indicate the range where the refinement R -factors are expected to be. In our case, R_{int} values of 0.422 and 0.591 have been obtained for superstructure reflections of type S1 and S2, respectively.

The distribution of F_{obs}/σ_F for main (black dots) and superstructure (gray dots) reflections (Fig. 2(b)) shows perfect coincidence. This means, that statistical and systematic errors are equally distributed for both reflection classes. In the same figure, the dependence of reliability factors on the number of reflections used for their calculation is shown in comparison with the expected R -factor, $\sigma R = \sum \sigma_F / \sum |F_{obs}|$. This reliability factor corresponds to the unweighted R -factor if $\Delta = |F_{obs}| - |F_{dc}| = \sigma_F$. Usually, due to systematic errors, Δ is significantly larger. The expected R -factors are: for all reflections $\sigma R = 0.159$, for main reflections $\sigma R_{main} = 0.135$ and for superstructure reflections $\sigma R_{sup} = 0.296$.

The maxima and minima of the residual electron density according to the difference Fourier maps in external space are $\Delta\rho_{max}^e = 0.86 \text{ e}\text{\AA}^{-3}$ and $\Delta\rho_{min}^e = -0.87 \text{ e}\text{\AA}^{-3}$, respectively. The corresponding values for the maxima and the minima of the full electron density are $\rho_{max}^e = 43.54 \text{ e}\text{\AA}^{-3}$ and $\rho_{min}^e = -6.12 \text{ e}\text{\AA}^{-3}$, respectively. Electron density maps calculated by the maximum-entropy method (MEM) agree with the structure derived from the 5D model.

IV. 3D STRUCTURE MODEL AND THE W-PHASE

A 3D structure model in physical space can be obtained by a proper irrational cut of the refined 5D structure model. Three successive atomic layers are shown in Fig. 3. The most prominent difference between the superstructure and average structure is the presence of puckered layers (at $x_3 = 1/8$ and $5/8$) in the former. The maximum puckering amplitudes amount to $\pm 0.5 \text{ \AA}$, comparable to those in the W-phase. In the flat layers (at $x_3 = 3/8$ and $7/8$), the shifts for some atoms reach values of up to 1.4 \AA . There are no too short distances resulting between fully occupied atomic positions, only between half-occupied atomic split sites.

To check the physical relevance of the obtained structure model, we generated its $\langle 3/2, 2/1 \rangle$ -approximant with lattice parameters $a_{app}^{av} = 19.884 \text{ \AA}$, $b_{app}^{av} = 8.1425 \text{ \AA}$ and $c_{app}^{av} = 23.375 \text{ \AA}$ as described in part I. Fig. 4 shows a comparison of three different layers of the W-phase constructed from the 5D model of the QC with the actual experimentally obtained structure [12]. With the exception of a few atomic sites, the agreement is surprisingly good. Surprisingly, because a really existing approximant (W-phase) needs not to be a perfect rational approximant. To summarize, the four-layer superstructure is mainly caused by a puckering of every other layer and a relaxation of the flat layers in between. These building

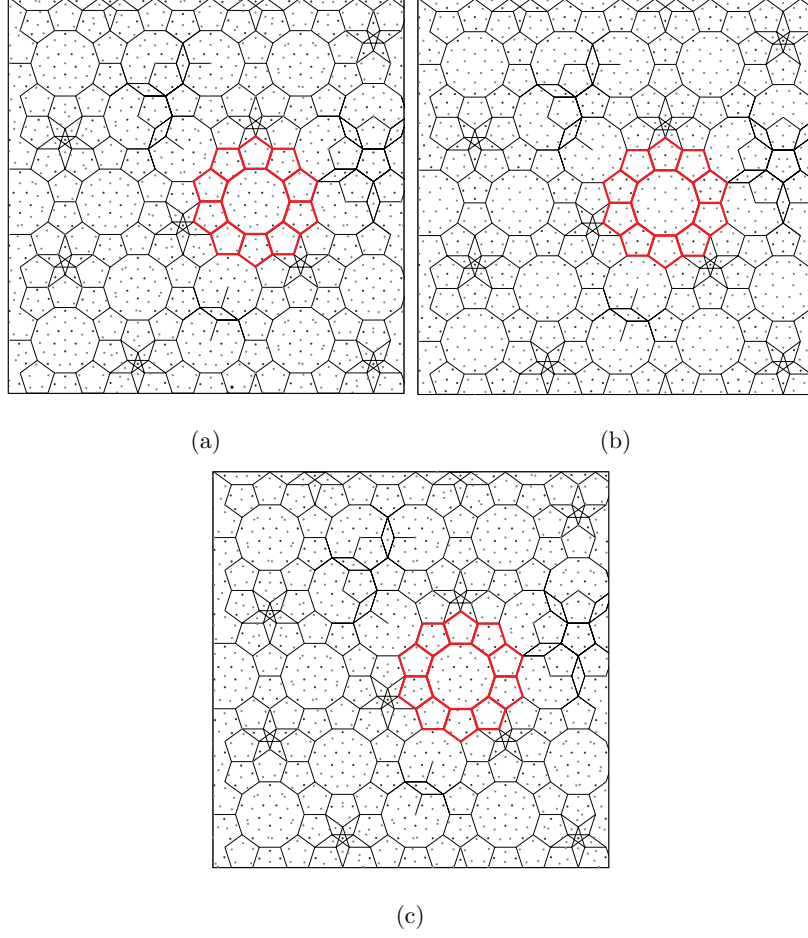


FIG. 3: $70 \times 70 \text{ \AA}^2$ sections of the atomic layers at (a) $x_3 = -1/8$ (flat), (b) $x_3 = 1/8$ (puckered) and (c) $x_3 = 3/8$ (flat) of the four-layer superstructure of decagonal $\text{Al}_{72.5}\text{Co}_{18.5}\text{Ni}_9$. The two flat layers, located on mirror planes, are related by a c -glide plane in the 5D structure. White and black circles correspond to Al and TM atoms, respectively. The thick (online red) outlined $\approx 20 \text{ \AA}$ cluster can be compared with Fig. 5 in part I. There, the average structure layer at $x_3 = 3/4$ (part I Fig. 5(a)) corresponds to the superposition of the superstructure layers at (a) $x_3 = 3/8$ and (c) $x_3 = 7/8$, and that at $x_3 = 1/4$ (part I Fig. 5(b)) to the superposition of the superstructure layers at (b) $x_3 = 1/8$ and $x_3 = 5/8$. The structures are related by a $\pi/10$ rotation around $[00100]$.

principles are also found in the other approximants in the system Al-Co-Ni [2].

V. CONCLUSIONS

Since real quasicrystals are never strictly quasiperiodically ordered, diffraction experiments can only give a kind of globally averaged 5D structure model. In our case of a tenfold superstructure, the limited observable diffraction data set limits the complexity and information content of the resulting structure model. Therefore, we see as the main result of this first quantitative structure analysis of the four-layer superstructure of d-Al-Co-Ni that the W-phase is a good rational approximant, indeed. This gives the clue for the modeling of all the different modifications of aluminum-based decagonal phases with four-layer period, since the clusters identified in the W-phase can be used as fundamental clusters for this purpose [5]. Furthermore, the results of the first-principles calculations performed for the W-phase can be transferred to some extent to the decagonal phase [12]. Then, the ordering phenomena as a function of the Co/Ni ratio can be related to the TM atomic environments that significantly differ in the case of Ni and Co atoms, respectively.

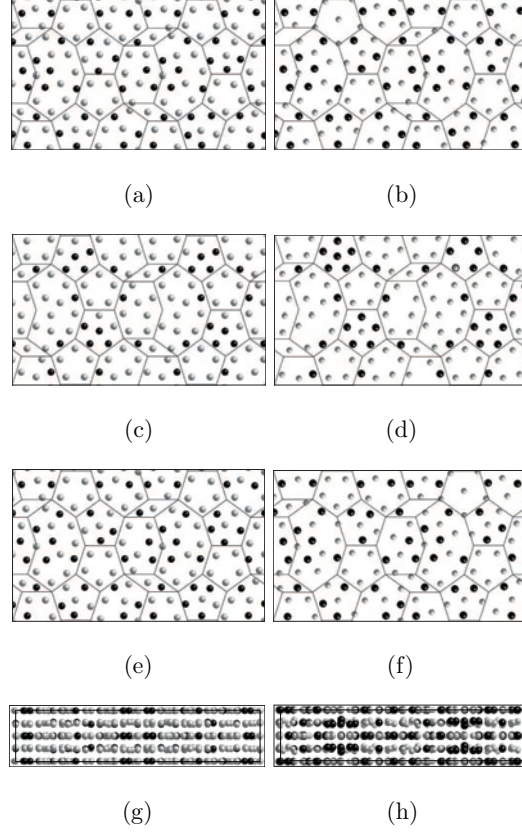


FIG. 4: Layers of the W-phase as derived from (a,c,e,g) basic Co-rich d-Al_{72.5}Co_{18.5}Ni₉ compared to its actual structure (b,d,f,h) [12]; (a, b) flat $x_3 = 3/8$, (c,d) puckered $x_3 = 1/8$, (e,f) flat $x_3 = -1/8$ and (g,h) the layer structure shown along x_3 . Grey and black circles correspond to Al and TM atoms, respectively.

-
- [1] A. Strutz, A. Yamamoto and W. Steurer, Phys. Rev. B **80**, 184102 (2009).
 - [2] W. Steurer, Z. Kristallogr. **219**, 319 (2004) and references therein.
 - [3] S. Katrych, W. Steurer, Z. Kristallogr. **219**, 606 (2004).
 - [4] W. Steurer, S. Deloudi, *Crystallography of Quasicrystals. Concepts, Methods and Structures*, Series in Materials Science vol.126, (Springer-Verlag, Berlin Heidelberg, 2009).
 - [5] S. Deloudi, F. Fleischer, W. Steurer, Acta Crystallogr. B (2010), submitted.
 - [6] K. Edagawa, M. Ichihara, K. Suzuki, S. Takeuchi, Philos. Mag. Lett. **66**, 19 (1992).

- [7] A. Yamamoto, H. Takakura, and E. Abe, Phys. Rev. B **72**, art. no. 144202 (2005).
- [8] A. Yamamoto, S. Weber Phys. Rev. Lett. **79**, 861 (1997).
- [9] A. Yamamoto, Sci. Technol. Adv. Mater. **9**, 13001 (2008).
- [10] W. Massa, *Crystal Structure Determination* (Springer-Verlag, Berlin Heidelberg, 2004) p. 117.
- [11] See EPAPS Document No. [number will be inserted by publisher] for an overview of OD and their subdomains as well as of the list of all parameters.
- [12] K. H. Hassdenteufel, A. R. Oganov, S. Katrych, W. Steurer, Phys. Rev. B **75**, art. no. 144115 (2007) and references cited therein.
- [13] where necessary, external (physical or parallel) and internal (perpendicular) space parameters are marked by superscripts e or i , respectively

5.2 Supplement - Article III

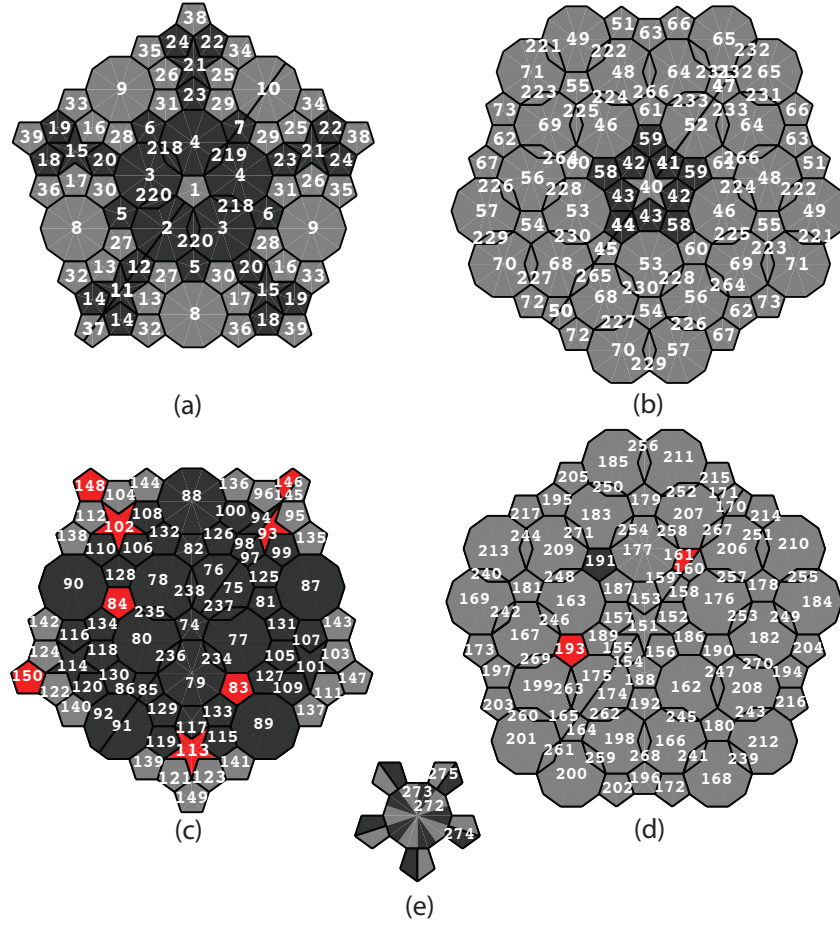


Fig. 1 Independent OD of the refined structure model of basic Co-rich d-Al-Co-Ni, located at (a) A $(0,2,-1,1,5/8)/5$, (b) B $(0,4,-2,2,5/8)/5$, (c) C $(0,-2,1,-1,-5/8)/5$, (d) D $(0,-4,2,-2,-5/8)/5$, and (e) E $(0,0,0,0,-5/8)/5$, $(1,1,1,1,-5/8)/5$, $(2,2,2,2,-5/8)/5$, $(-1,-1,-1,-1,-5/8)/5$, and $(-2,-2,-2,-2,-5/8)/5$. Note: since $(0,0,0,0,-1/8)$ is not a lattice point of the superstructure unit cell, the four additional, to E symmetrically equivalent, OD will not be generated by the 5D space group symmetry operators and have to be given explicitly. Subdomains with TM (Co or Ni), Al and mixed Al/TM occupancy are shaded dark, light and intermediate gray, respectively.

TABLE I: Refined parameters: the external space displacements u_1 , u_2 and u_3 (along the periodic direction); B_{\parallel} and B_{\perp} components of the ADP; total and partial occupancy factors p for TM and Al. esds of refined parameters are less or equal 0.01. Fixed parameters are indicated by *.

subdomain: \mathbf{x}^i	u_1 (Å)	u_2 (Å)	u_3 (Å)	B_{\parallel} (Å ²)	B_{\perp} (Å ²)	p	$p(\text{TM})$	$p(\text{Al})$
OD1: $\mathbf{x}_0 = (0.0, 0.4, -0.2, 0.2, 0.125)$				0.95	0.19			
1: $\tau^{-4}(0, 0, 0, 0, 0)^i$	0*	0*	0*			1*	0	1
2: $\tau^{-3}(0.001, 0.6, 0.2, -0.2, -0.6, 0)^i$	-0.02	0*	0.12			1*	1	0
3: $\tau^{-3}(-0.2, -0.6, 0, 0.6, 0.2, 0)^i$	-0.02	0*	0.15			1*	1	0
4: $\tau^{-3}(0.6, 0.2, -0.2, -0.6, 0, 0)^i$	-0.02	0*	0.12			1*	1	0
5: $\tau^{-4}(-0.2, 0, 0.2, 0.4, -0.4, 0)^i$	-0.07	0*	-0.29			1*	0.86	0.14
6: $\tau^{-4}(0.4, -0.4, -0.2, 0, 0.2, 0)^i$	-0.07	0*	0.31			1*	0.86	0.14
7: $\tau^{-4}(0.001, 0.2, 0.4, -0.4, -0.2, 0)^i$	-0.07	0*	-0.29			1*	0.86	0.14
8: $\tau^{-3}(0.4, 0, -0.4, 0.2, -0.2, 0)^i$	-0.12	0*	0.02			1*	0.22	0.78
9: $\tau^{-3}(0.2, -0.2, 0.4, 0, -0.4, 0)^i$	-0.12	0*	-0.11			1*	0.22	0.78
10: $\tau^{-3}(0.001, -0.4, 0.2, -0.2, 0.4, 0)^i$	-0.12	0*	0.02			1*	0.22	0.78
11: $\tau^{-4}(0.001, 0.4, -0.2, 0.2, -0.4, 0)^i$	-0.17	0*	-0.04			1*	1	0
12: $\tau^{-4}(0.001, 1.2, 0.4, -0.4, -1.2, 0)^i$	-0.1	0*	-0.17			1*	0.99	0.01
13: $\tau^{-4}(0.0876, 0.3124, -0.1708, 0.2, -0.4292, 0)^i$	-0.07	-0.37	0.02			1*	0	1
14: $\tau^{-4}(-0.8, 0.4, 0.6, 0.8, -1, 0)^i$	0.21	0.31	0.1			1*	0.32	0.68
15: $\tau^{-4}(0.2, -0.4, 0, 0.4, -0.2, 0)^i$	-0.17	0*	-0.07			1*	1	0
16: $\tau^{-4}(0.2, 0.4, 0.6, -0.2, -1, 0)^i$	-0.07	-0.37	0.14			1*	0	1
17: $\tau^{-4}(1, 0.2, -0.6, -0.4, -0.2, 0)^i$	-0.07	-0.37	0.14			1*	0	1
18: $\tau^{-4}(-0.6, -0.4, 0.8, 1, -0.8, 0)^i$	0.21	0.31	0.12			1*	0.32	0.68
19: $\tau^{-4}(0.8, -1, -0.8, 0.4, 0.6, 0)^i$	0.21	0.31	0.12			1*	0.32	0.68
20: $\tau^{-4}(-0.4, -1.2, 0, 1.2, 0.4, 0)^i$	-0.1	0*	0.13			1*	0.99	0.11
21: $\tau^{-4}(0.4, -0.2, 0.2, -0.4, 0, 0)^i$	-0.17	0*	-0.04			1*	1	0
22: $\tau^{-4}(0.4, 0.6, 0.8, -1, -0.8, 0)^i$	0.21	0.31	0.1			1*	0.32	0.68
23: $\tau^{-4}(1.2, 0.4, -0.4, -1.2, 0, 0)^i$	-0.1	0*	-0.17			1*	0.99	0.01
24: $\tau^{-4}(1, -0.8, -0.6, -0.4, 0.8, 0)^i$	0.21	0.31	0.1			1*	0.32	0.68
25: $\tau^{-4}(-0.2, -1, 0.2, 0.4, 0.6, 0)^i$	-0.07	-0.37	0.02			1*	0	1
26: $\tau^{-4}(-0.4, -0.2, 1, 0.2, -0.6, 0)^i$	-0.07	-0.37	0.02			1*	0	1
27: $\tau^{-4}(0.6, 0.6, -0.4, -0.4, -0.4, 0)^i$	0.01	0.07	-0.18			1*	0	1
28: $\tau^{-4}(-0.4, -0.4, 0.6, 0.6, -0.4, 0)^i$	0.01	0.07	0.17			1*	0	1
29: $\tau^{-4}(0.6, -0.4, -0.4, -0.4, 0.6, 0)^i$	0.01	0.07	-0.18			1*	0	1
30: $\tau^{-4}(0.4, -0.6, -0.6, 0.4, 0.4, 0)^i$	0.01	0.07	0.17			1*	0	1
31: $\tau^{-4}(0.4, 0.4, 0.4, -0.6, -0.6, 0)^i$	0.01	0.07	-0.18			1*	0	1
32: $\tau^{-4}(-0.2, -0.2, -0.2, 0.8, -0.2, 0)^i$	-0.03	-0.05	0.38			1*	0.29	0.71
33: $\tau^{-4}(0.8, -0.2, -0.2, -0.2, -0.2, 0)^i$	-0.03	-0.05	0.32			1*	0.29	0.71
34: $\tau^{-4}(-0.2, -0.2, 0.8, -0.2, -0.2, 0)^i$	-0.03	-0.05	0.38			1*	0.29	0.71
35: $\tau^{-4}(0.2, -0.8, 0.2, 0.2, 0.2, 0)^i$	-0.03	-0.05	0.38			1*	0.29	0.71
36: $\tau^{-4}(0.2, 0.2, 0.2, 0.2, -0.8, 0)^i$	-0.03	-0.05	0.32			1*	0.29	0.71
37: $\tau^{-4}(0.001, 1, 0, 0, -1, 0)^i$	-0.36	0*	-0.05			1*	0.3	0.7
38: $\tau^{-4}(1, 0, 0, -1, 0, 0)^i$	-0.36	0*	-0.05			1*	0.3	0.7
39: $\tau^{-4}(0, -1, 0, 1, 0, 0)^i$	-0.36	0*	0.05			1*	0.3	0.7
218: $\tau^{-4}(0.0292, -0.0292, 0.0584, 0, -0.0584, 0)^i$	-0.19	0*	0*			1*	1	0
219: $\tau^{-4}(0, -0.0584, 0.0292, -0.0292, 0.0584, 0)^i$	-0.19	0*	0*			1*	1	0
220: $\tau^{-4}(0.0584, 0, -0.0584, 0.0292, -0.0292, 0)^i$	-0.19	0*	0*			1*	1	0
OD2: $\mathbf{x}_0 = (0.0, 0.8, -0.4, 0.4, 0.125)$				1.22	1.6			
40: $\tau^{-4}(0, 0, 0, 0, 0, 0)^i$	0*	0*	0*			1*	0	1
41: $\tau^{-4}(0.001, 0.8, 0.6, -0.6, -0.8, 0)^i$	0.03	0*	0.43			1*	0.35	0.65
42: $\tau^{-4}(0.0876, -0.0876, 0.0292, 0, -0.0292, 0)^i$	0.03	0*	0.39			1*	0.35	0.65
43: $\tau^{-4}(-0.8, 0, 0.8, 0.6, -0.6, 0)^i$	0.03	0*	0.43			1*	0.35	0.65
44: $\tau^{-4}(0.001, 0.6, 0.2, -0.2, -0.6, 0)^i$	-0.07	0*	0.12			1*	1	0
45: $\tau^{-4}(0.001, -0.2, -0.4, 0.4, 0.2, 0)^i$	0.15	0*	0.12			1*	0	1
46: $\tau^{-3}(0.4, -0.4, -0.2, 0, 0.2, 0)^i$	-0.03	0*	-0.2			1*	0	1
47: $\tau^{-4}(0.001, -0.4, 0.2, -0.2, 0.4, 0)^i$	-0.05	0*	-0.48			1*	0	1
48: $\tau^{-3}(-0.4, -0.2, 1, 0.2, -0.6, 0)^i$	0.03	0*	-0.03			1*	0	1
49: $\tau^{-3}(0.8, 0, 0.2, -0.6, -0.4, 0)^i$	-0.01	-0.21	-0.12			1*	0	1
50: $\tau^{-4}(0.002, -0.4, -0.8, 0.8, 0.4, 0)^i$	-0.34	0*	0.09			1*	0	1

51: $\tau^{-4}(0.2, 0, 0.8, -0.4, -0.6, 0)^i$	-0.03	-0.97	0.05	1*	0	1
52: $\tau^{-3}(0.001, 0.2, 0.4, -0.4, -0.2, 0)^i$	-0.03	0*	-0.52	1*	0	1
53: $\tau^{-3}(-0.2, 0, 0.2, 0.4, -0.4, 0)^i$	-0.03	0*	-0.52	1*	0	1
54: $\tau^{-4}(0.4, 0, -0.4, 0.2, -0.2, 0)^i$	-0.05	0*	-0.48	1*	0	1
55: $\tau^{-4}(0.2, -0.2, 0.4, 0, -0.4, 0)^i$	-0.05	0*	0.48	1*	0	1
56: $\tau^{-3}(1, 0.2, -0.6, -0.4, -0.2, 0)^i$	0.03	0*	0.19	1*	0	1
57: $\tau^{-3}(0.2, -0.6, -0.4, 0.8, 0, 0)^i$	-0.01	-0.21	-0.05	1*	0	1
58: $\tau^{-4}(-0.2, -0.6, 0, 0.6, 0.2, 0)^i$	-0.07	0*	-0.08	1*	1	0
59: $\tau^{-4}(0.6, 0.2, -0.2, -0.6, 0, 0)^i$	-0.07	0*	0.12	1*	1	0
60: $\tau^{-4}(0.4, 0.2, 0, -0.2, -0.4, 0)^i$	0.15	0*	-0.12	1*	0	1
61: $\tau^{-4}(-0.2, -0.4, 0.4, 0.2, 0, 0)^i$	0.15	0*	0.12	1*	0	1
62: $\tau^{-4}(0.8, 0.4, 0, -0.4, -0.8, 0)^i$	-0.34	0*	0*	1*	0	1
63: $\tau^{-4}(-0.4, -0.8, 0.8, 0.4, 0, 0)^i$	-0.34	0*	0.09	1*	0	1
64: $\tau^{-3}(-0.2, -1, 0.2, 0.4, 0.6, 0)^i$	0.03	0*	-0.03	1*	0	1
65: $\tau^{-3}(0.6, -0.2, 0, -0.8, 0.4, 0)^i$	-0.01	-0.21	-0.12	1*	0	1
66: $\tau^{-4}(0.4, -0.8, 0, -0.2, 0.6, 0)^i$	-0.03	-0.97	0.05	1*	0	1
67: $\tau^{-4}(0.8, -0.4, -0.6, 0.2, 0, 0)^i$	-0.03	-0.97	-0.09	1*	0	1
68: $\tau^{-3}(0.6, -0.2, -1, 0.2, 0.4, 0)^i$	0.03	0*	0.19	1*	0	1
69: $\tau^{-3}(0.2, 0.4, 0.6, -0.2, -1, 0)^i$	0.03	0*	0.19	1*	0	1
70: $\tau^{-3}(0.4, 0.6, -0.2, 0, -0.8, 0)^i$	-0.01	-0.21	-0.12	1*	0	1
71: $\tau^{-3}(0, -0.8, 0.4, 0.6, -0.2, 0)^i$	-0.01	-0.21	-0.05	1*	0	1
72: $\tau^{-4}(0.6, 0.4, -0.8, 0, -0.2, 0)^i$	-0.03	-0.97	0.05	1*	0	1
73: $\tau^{-4}(0, -0.2, 0.6, 0.4, -0.8, 0)^i$	-0.03	-0.97	-0.09	1*	0	1
221: $\tau^{-4}(0.2292, -0.2292, 0.4584, 0, -0.4584, 0)^i$	-0.29	0*	0*	1*	0	1
222: $\tau^{-4}(0.2, -0.2584, 0.4292, -0.0229, -0.3416, 0)^i$	0.2	0.41	0*	1*	0.48	0.52
223: $\tau^{-4}(0.2584, -0.2, 0.3416, 0.0292, -0.4292, 0)^i$	0.2	0.41	0*	1*	0.48	0.52
224: $\tau^{-4}(0.1708, -0.1416, 0.4, -0.0584, -0.3708, 0)^i$	-0.42	0*	0*	1*	0	1
225: $\tau^{-4}(0.1416, -0.1708, 0.3708, 0.0584, -0.4, 0)^i$	-0.42	0*	0*	1*	0	1
226: $\tau^{-4}(0.4292, -0.0292, -0.3416, 0.2, -0.2584, 0)^i$	0.2	0.41	0*	1*	0.48	0.52
227: $\tau^{-4}(0.3416, 0.0292, -0.4292, 0.2584, -0.2, 0)^i$	0.2	0.41	0*	1*	0.48	0.52
228: $\tau^{-4}(0.4, -0.0584, -0.3708, 0.1708, -0.1416, 0)^i$	-0.42	0*	0*	1*	0	1
229: $\tau^{-4}(0.4584, 0, -0.4584, 0.2292, -0.2292, 0)^i$	-0.29	0*	0*	1*	0	1
230: $\tau^{-4}(0.3708, 0.0584, -0.4, 0.1416, -0.1708, 0)^i$	-0.42	0*	0*	1*	0	1
231: $\tau^{-4}(0.0292, -0.4292, 0.2584, -0.2, 0.3416, 0)^i$	0.2	0.41	0*	1*	0.48	0.52
232: $\tau^{-4}(0, -0.4584, 0.2292, -0.2292, 0.4584, 0)^i$	-0.29	0*	0*	1*	0	1
233: $\tau^{-4}(0.0584, -0.4, 0.1416, -0.1708, 0.3708, 0)^i$	-0.42	0*	0*	1*	0	1
264: $\tau^{-4}(0.4292, 0.1416, 0, -0.1416, -0.4292, 0)^i$	-0.98	0*	0*	1*	0.86	0.14
265: $\tau^{-4}(0, -0.1416, -0.4292, 0.4292, 0.1416, 0)^i$	-0.98	0*	0*	1*	0.86	0.14
266: $\tau^{-4}(-0.1416, -0.4292, 0.4292, 0.1416, 0, 0)^i$	-0.98	0*	0*	1*	0.86	0.14
OD3: $\mathbf{x}_0 = (0.0, -0.4, 0.2, -0.2, -0.125)$						
74: $\tau^{-4}(0, 0, 0, 0, 0, 0)^i$	0*	0*	0*	0.97	0.71	
75: $\tau^{-3}(-0, -0.6, -0.2, 0.2, 0.6, -0)^i$	0.03	0*	0*	1*	0.28	0.72
76: $\tau^{-3}(-0, -0.6, -0.2, 0.2, 0.6, -0)^i$	0.03	0*	0*	1*	0.95	0.05
77: $\tau^{-3}(0.2, 0.6, -0, -0.6, -0.2, -0)^i$	0.03	0*	0*	1*	0.9	0.1
78: $\tau^{-3}(-0.2, 0.2, 0.6, -0, -0.6, -0)^i$	0.03	0*	0*	1*	0.85	0.15
79: $\tau^{-3}(-0.6, -0.2, 0.2, 0.6, -0, -0)^i$	0.03	0*	0*	1*	1	0
80: $\tau^{-3}(0.6, -0, -0.6, -0.2, 0.2, -0)^i$	0.03	0*	0*	1*	0.95	0.05
81: $\tau^{-4}(0.2, -0, -0.2, -0.4, 0.4, -0)^i$	0.31	0*	0*	1*	0.9	0.1
82: $\tau^{-4}(-0.2, -0.4, 0.4, 0.2, -0, -0)^i$	0.31	0*	0*	1*	0	1
83: $\tau^{-4}(-0.4, 0.4, 0.2, -0, -0.2, -0)^i$	0.31	0*	0*	1*	0.85	0.15
84: $\tau^{-4}(0.4, 0.2, -0, -0.2, -0.4, -0)^i$	0.31	0*	0*	1*	0.41	0.59
85: $\tau^{-4}(-0, -0.2, -0.4, 0.4, 0.2, -0)^i$	0.31	0*	0*	1*	0.44	0.56
86: $\tau^{-4}(-0, -0.2, -0.4, 0.4, 0.2, -0)^i$	0.31	0*	0*	1*	0	1
87: $\tau^{-3}(-0.4, -0, 0.4, -0.2, 0.2, -0)^i$	0	0*	0*	1*	0.85	0.15
88: $\tau^{-3}(0.4, -0.2, 0.2, -0.4, -0, -0)^i$	0	0*	0*	1*	0.64	0.36
89: $\tau^{-3}(-0.2, 0.2, -0.4, -0, 0.4, -0)^i$	0	0*	0*	1*	0.7	0.3
90: $\tau^{-3}(0.2, -0.4, -0, 0.4, -0.2, -0)^i$	0	0*	0*	1*	0.78	0.22
91: $\tau^{-3}(-0, 0.4, -0.2, 0.2, -0.4, -0)^i$	0	0*	0*	1*	0.56	0.44
92: $\tau^{-3}(-0, 0.4, -0.2, 0.2, -0.4, -0)^i$	0	0*	0*	1*	0.64	0.36
93: $\tau^{-4}(-0, -0.4, 0.2, -0.2, 0.4, -0)^i$	-0.04	0*	0*	1*	0.7	0.3
					0.5	0.5

94: $\tau^{-4}(-0.4, 0.2, -0.2, 0.4, -0)^i$	-0.04	0*	0*	1*	0.65	0.35
95: $\tau^{-4}(-0.0292, -0.4, 0.2292, -0.2876, -0)^i$	-0.28	0.01	0*	1*	0	1
96: $\tau^{-4}(0.0292, -0.4876, 0.2876, -0.2292, 0.4, -0)^i$	0.2	-0.67	0*	1*	0.26	0.74
97: $\tau^{-4}(-0.3708, 0.1124, -0.1124, 0.3708, -0)^i$	-0.17	0*	0*	1*	0.88	0.12
98: $\tau^{-4}(-0.3708, 0.1124, -0.1124, 0.3708, -0)^i$	0.07	0*	0*	1*	0.97	0.03
99: $\tau^{-4}(-0.0876, -0.3124, 0.1708, -0.2, 0.4292, -0)^i$	-0.06	0.23	0*	1*	1	0
100: $\tau^{-4}(0.0876, -0.4292, 0.2, -0.1708, 0.3124, -0)^i$	0.21	0.02	0*	1*	1	0
101: $\tau^{-4}(-0.2, 0.4, -0.4, 0.2, -0)^i$	-0.04	0*	0*	1*	0.65	0.35
102: $\tau^{-4}(0.2, -0.2, 0.4, -0.4, -0)^i$	-0.04	0*	0*	1*	0.5	0.5
103: $\tau^{-4}(-0.2292, 0.4, 0.0292, -0.4876, 0.2876, -0)^i$	-0.28	0.01	0*	1*	0	1
104: $\tau^{-4}(0.2292, -0.2876, 0.4876, -0.0292, -0.4, -0)^i$	0.2	-0.67	0*	1*	0.26	0.74
105: $\tau^{-4}(-0.1124, 0.3708, -0.3708, 0.1124, -0)^i$	-0.17	0*	0*	1*	0.85	0.15
106: $\tau^{-4}(0.1124, -0.1124, 0.3708, -0.3708, -0)^i$	0.07	0*	0*	1*	1	0
107: $\tau^{-4}(-0.1708, 0.3124, 0.0876, -0.4292, 0.2, -0)^i$	-0.06	0.23	0*	1*	1	0
108: $\tau^{-4}(0.1708, -0.2, 0.4292, -0.0876, -0.3124, -0)^i$	0.21	0.02	0*	1*	1	0
109: $\tau^{-4}(-0.2, 0.4292, -0.0876, -0.3124, 0.1708, -0)^i$	-0.06	0.23	0*	1*	1	0
110: $\tau^{-4}(0.2, -0.1708, 0.3124, 0.0876, -0.4292, -0)^i$	0.21	0.02	0*	1*	1	0
111: $\tau^{-4}(-0.2876, 0.4876, -0.0292, -0.4, 0.2292, -0)^i$	-0.28	0.01	0*	1*	0	1
112: $\tau^{-4}(0.2876, -0.2292, 0.4, 0.0292, -0.4876, -0)^i$	0.2	-0.67	0*	1*	0.26	0.74
113: $\tau^{-4}(-0.4, 0.2, -0.2, 0.4, -0, -0)^i$	-0.04	0*	0*	1*	0.5	0.5
114: $\tau^{-4}(0.4, -0.4, 0.2, -0.2, -0)^i$	-0.04	0*	0*	1*	0.65	0.35
115: $\tau^{-4}(-0.4292, 0.2, -0.1708, 0.3124, 0.0876, -0)^i$	-0.05	0.1	0*	1*	1	0
116: $\tau^{-4}(0.4292, -0.0876, -0.3124, 0.1708, -0.2, -0)^i$	0.2	0.15	0*	1*	1	0
117: $\tau^{-4}(-0.3708, 0.1124, -0.1124, 0.3708, -0, -0)^i$	-0.08	0*	0*	1*	0.88	0.12
118: $\tau^{-4}(0.3708, -0.3708, 0.1124, -0.1124, -0)^i$	-0.02	0*	0*	1*	0.97	0.03
119: $\tau^{-4}(-0.3124, 0.1708, -0.2, 0.4292, -0.0876, -0)^i$	-0.05	0.1	0*	1*	1	0
120: $\tau^{-4}(0.3124, 0.0876, -0.4292, 0.2, -0.1708, -0)^i$	0.2	0.15	0*	1*	1	0
121: $\tau^{-4}(-0.4, 0.2292, -0.2876, 0.4876, -0.0292, -0)^i$	-0.24	-0.08	0*	1*	0	1
122: $\tau^{-4}(0.4, 0.0292, -0.4876, 0.2876, -0.2292, -0)^i$	0.15	-0.59	0*	1*	0.26	0.74
123: $\tau^{-4}(-0.4876, 0.2876, -0.2292, 0.4, 0.0292, -0)^i$	-0.24	-0.08	0*	1*	0	1
124: $\tau^{-4}(0.4876, -0.0292, -0.4, 0.2292, -0.2876, -0)^i$	0.15	-0.59	0*	1*	0.26	0.74
125: $\tau^{-4}(-0.6, -0.6, 0.4, 0.4, -0)^i$	-0.21	-0.1	0*	1*	1	0
126: $\tau^{-4}(0.6, -0.4, -0.4, -0.4, 0.6, -0)^i$	-0.12	-0.31	0*	1*	0.78	0.22
127: $\tau^{-4}(0.4, 0.4, -0.6, -0.6, 0.4, -0)^i$	-0.21	-0.1	0*	1*	1	0
128: $\tau^{-4}(-0.4, -0.4, 0.6, 0.6, -0.4, -0)^i$	-0.12	-0.31	0*	1*	0.78	0.22
129: $\tau^{-4}(-0.6, 0.4, 0.4, 0.4, -0.6, -0)^i$	-0.24	-0.16	0*	1*	1	0
130: $\tau^{-4}(0.6, 0.6, -0.4, -0.4, -0.4, -0)^i$	-0.09	-0.25	0*	1*	0.78	0.22
131: $\tau^{-4}(-0.4, 0.6, 0.6, -0.4, -0.4, -0)^i$	-0.21	-0.1	0*	1*	1	0
132: $\tau^{-4}(0.4, 0.4, 0.4, -0.6, -0.6, -0)^i$	-0.12	-0.31	0*	1*	0.78	0.22
133: $\tau^{-4}(-0.4, -0.4, -0.4, 0.6, 0.6, -0)^i$	-0.24	-0.16	0*	1*	1	0
134: $\tau^{-4}(0.4, -0.6, -0.6, 0.4, 0.4, -0)^i$	-0.09	-0.25	0*	1*	0.78	0.22
135: $\tau^{-4}(0.2, 0.2, 0.2, -0.8, 0.2, -0)^i$	-0.95	0.08	0*	0.5*	0.96	0.04
136: $\tau^{-4}(-0.2, -0.2, 0.8, -0.2, -0.2, -0)^i$	0.94	1.13	0*	0.5*	0.16	0.84
137: $\tau^{-4}(-0.8, 0.2, 0.2, 0.2, 0.2, -0)^i$	-0.95	0.08	0*	0.5*	0.81	0.19
138: $\tau^{-4}(0.8, -0.2, -0.2, -0.2, -0.2, -0)^i$	0.94	1.13	0*	0.5*	0.31	0.69
139: $\tau^{-4}(0.2, 0.2, -0.8, 0.2, 0.2, -0)^i$	0.1	1.34	0*	0.5*	0.96	0.04
140: $\tau^{-4}(-0.2, -0.2, -0.2, 0.8, -0.2, -0)^i$	-0.11	-0.14	0*	0.5*	0.16	0.84
141: $\tau^{-4}(-0.2, 0.8, -0.2, -0.2, -0.2, -0)^i$	0.1	1.34	0*	0.5*	0.96	0.04
142: $\tau^{-4}(0.2, 0.2, 0.2, 0.2, -0.8, -0)^i$	-0.11	-0.14	0*	0.5*	0.16	0.84
143: $\tau^{-4}(-0.2, -0.2, -0.2, -0.2, 0.8, -0)^i$	-0.95	0.08	0*	0.5*	0.81	0.19
144: $\tau^{-4}(0.2, -0.8, 0.2, 0.2, 0.2, -0)^i$	0.94	1.13	0*	0.5*	0.31	0.69
145: $\tau^{-4}(-0, -1, -0, -0, 1, -0)^i$	-1.14	0*	0*	0.5*	0.17	0.83
146: $\tau^{-4}(-0, -1, -0, -0, 1, -0)^i$	0.21	0*	0*	0.5*	0.45	0.55
147: $\tau^{-4}(-0, 1, -0, -1, -0, -0)^i$	-1.14	0*	0*	0.5*	0	1
148: $\tau^{-4}(-0, -0, 1, -0, -1, -0)^i$	0.21	0*	0*	0.5*	0.62	0.38
149: $\tau^{-4}(-1, -0, -0, 1, -0, -0)^i$	-1.14	0*	0*	0.5*	0.17	0.83
150: $\tau^{-4}(1, -0, -1, -0, -0, -0)^i$	0.21	0*	0*	0.5*	0.45	0.55
234: $\tau^{-4}(-0.0292, 0.0292, -0.0584, -0.0584, -0)^i$	0.14	0*	0*	1*	0.89	0.11
235: $\tau^{-4}(0.0292, -0.0584, -0.0584, -0.0292, -0)^i$	0.14	0*	0*	1*	0.89	0.11
236: $\tau^{-4}(-0.0584, -0.0292, 0.0292, -0.0584, -0)^i$	0.14	0*	0*	1*	0.89	0.11
237: $\tau^{-4}(-0.0584, -0.0584, -0.0292, 0.0292, -0)^i$	0.14	0*	0*	1*	0.89	0.11

238: $\tau^{-4}(0.0584, -0.0292, 0.0292, -0.0584, -0, -0)^i$	0.14	0*	0*			1*	0.89	0.11
OD4: $\mathbf{x}_0 = (0.0, -0.8, 0.4, -0.4, -0.125)$				0.5	1.28			
151: $\tau^{-4}(-0, -0, -0, -0, -0, -0)^i$	0*	0*	0*			1*	0	1
152: $\tau^{-4}(-0.0292, -0, 0.0292, -0.0876, 0.0876, -0)^i$	0.29	0*	0*			1*	0	1
153: $\tau^{-4}(0.0292, -0.0876, 0.0876, -0.0292, -0, -0)^i$	-0.33	0*	0*			1*	0.11	0.89
154: $\tau^{-4}(-0, 0.0292, -0.0876, 0.0876, -0.0292, -0)^i$	-0.14	0*	0*			1*	0	1
155: $\tau^{-4}(-0, 0.0292, -0.0876, 0.0876, -0.0292, -0)^i$	0.11	0*	0*			1*	0.11	0.89
156: $\tau^{-4}(-0.0876, 0.0876, -0.0292, -0, 0.0292, -0)^i$	-0.14	0*	0*			1*	0.11	0.89
157: $\tau^{-4}(0.0876, -0.0292, -0, 0.0292, -0.0876, -0)^i$	0.11	0*	0*			1*	0	1
158: $\tau^{-4}(-0, -0.6, -0.2, 0.2, 0.6, -0)^i$	-0.36	0*	0*			1*	0.36	0.64
159: $\tau^{-4}(-0, -0.6, -0.2, 0.2, 0.6, -0)^i$	0.54	0*	0*			1*	0	1
160: $\tau^{-4}(-0, 0.2, 0.4, -0.4, -0.2, -0)^i$	-0.16	0*	0*			1*	0.25	0.75
161: $\tau^{-4}(-0, 0.2, 0.4, -0.4, -0.2, -0)^i$	1.37	0*	0*			1*	0.75	0.25
162: $\tau^{-3}(-0.4, 0.4, 0.2, -0, -0.2, -0)^i$	-0.11	0*	0*			1*	0	1
163: $\tau^{-3}(0.4, 0.2, -0, -0.2, -0.4, -0)^i$	0.02	0*	0*			1*	0	1
164: $\tau^{-4}(-0, 0.4, -0.2, 0.2, -0.4, -0)^i$	0	0*	0*			1*	0	1
165: $\tau^{-4}(-0, 0.4, -0.2, 0.2, -0.4, -0)^i$	0.28	0*	0*			1*	0	1
166: $\tau^{-3}(0.4, 0.2, -1, -0.2, 0.6, -0)^i$	0.69	0.26	0*			1*	0	1
167: $\tau^{-3}(-0.4, -0.6, 0.2, 1, -0.2, -0)^i$	-0.45	-0.23	0*			1*	0	1
168: $\tau^{-3}(-0.8, -0, -0.2, 0.6, 0.4, -0)^i$	-0.82	-0.08	0*			0.5*	0	1
169: $\tau^{-3}(0.8, -0.4, -0.6, 0.2, -0, -0)^i$	-1.1	0.4	0*			0.5*	0.15	0.85
170: $\tau^{-4}(-0, 0.4, 0.8, -0.8, -0.4, -0)^i$	-0.08	0*	0*			1*	0	1
171: $\tau^{-4}(-0, 0.4, 0.8, -0.8, -0.4, -0)^i$	-0.7	0*	0*			1*	0	1
172: $\tau^{-4}(-0.2, -0, -0.8, 0.4, 0.6, -0)^i$	-0.06	0.06	0*			1*	0.02	0.98
173: $\tau^{-4}(0.2, -0.6, -0.4, 0.8, -0, -0)^i$	0.32	-0.35	0*			1*	0	1
174: $\tau^{-3}(-0, -0.2, -0.4, 0.4, 0.2, -0)^i$	-0.11	0*	0*			1*	0	1
175: $\tau^{-3}(-0, -0.2, -0.4, 0.4, 0.2, -0)^i$	0.02	0*	0*			1*	0	1
176: $\tau^{-3}(0.2, -0, -0.2, -0.4, 0.4, -0)^i$	-0.11	0*	0*			1*	0	1
177: $\tau^{-3}(-0.2, -0.4, 0.4, 0.2, -0, -0)^i$	0.02	0*	0*			1*	0	1
178: $\tau^{-4}(-0.4, -0, 0.4, -0.2, 0.2, -0)^i$	0.52	0*	0*			1*	0	1
179: $\tau^{-4}(0.4, -0.2, 0.2, -0.4, -0, -0)^i$	-0.24	0*	0*			1*	0	1
180: $\tau^{-4}(-0.2, 0.2, -0.4, -0, 0.4, -0)^i$	0	0*	0*			1*	0	1
181: $\tau^{-4}(0.2, -0.4, -0, 0.4, -0.2, -0)^i$	0.28	0*	0*			1*	0	1
182: $\tau^{-3}(-1, -0.2, 0.6, 0.4, 0.2, -0)^i$	0.13	0.08	0*			1*	0	1
183: $\tau^{-3}(1, -0.2, -0.4, -0.6, 0.2, -0)^i$	0.11	-0.05	0*			1*	0	1
184: $\tau^{-3}(-0.2, 0.6, 0.4, -0.8, -0, -0)^i$	-1.29	0.4	0*			0.5*	0.15	0.85
185: $\tau^{-3}(0.2, -0, 0.8, -0.4, -0.6, -0)^i$	-0.63	-0.08	0*			0.5*	0	1
186: $\tau^{-4}(0.2, 0.6, -0, -0.6, -0.2, -0)^i$	-0.36	0*	0*			1*	0	1
187: $\tau^{-4}(-0.2, 0.2, 0.6, -0, -0.6, -0)^i$	0.54	0*	0*			1*	0.36	0.64
188: $\tau^{-4}(-0.6, -0.2, 0.2, 0.6, -0, -0)^i$	-0.36	0*	0*			1*	0.36	0.64
189: $\tau^{-4}(0.6, -0, -0.6, -0.2, 0.2, -0)^i$	0.54	0*	0*			1*	0	1
190: $\tau^{-4}(-0.4, -0.2, -0, 0.2, 0.4, -0)^i$	-0.16	0*	0*			1*	0	1
191: $\tau^{-4}(0.4, -0.4, -0.2, -0, 0.2, -0)^i$	1.37	0*	0*			1*	1	0
192: $\tau^{-4}(0.2, 0.4, -0.4, -0.2, -0, -0)^i$	1.42	0*	0*			1*	0.25	0.75
193: $\tau^{-4}(-0.2, -0, 0.2, 0.4, -0.4, -0)^i$	-0.21	0*	0*			1*	0.75	0.25
194: $\tau^{-4}(-0.8, -0.4, -0, 0.4, 0.8, -0)^i$	-0.08	0*	0*			1*	0	1
195: $\tau^{-4}(0.8, -0.8, -0.4, -0, 0.4, -0)^i$	-0.7	0*	0*			1*	0	1
196: $\tau^{-4}(0.4, 0.8, -0.8, -0.4, -0, -0)^i$	-0.72	0*	0*			1*	0	1
197: $\tau^{-4}(-0.4, -0, 0.4, 0.8, -0.8, -0)^i$	-0.06	0*	0*			1*	0	1
198: $\tau^{-3}(0.2, 1, -0.2, -0.4, -0.6, -0)^i$	0.69	0.26	0*			1*	0	1
199: $\tau^{-3}(-0.2, 0.6, 0.4, 0.2, -1, -0)^i$	-0.45	-0.23	0*			1*	0	1
200: $\tau^{-3}(-0.6, 0.2, -0, 0.8, -0.4, -0)^i$	-0.82	-0.08	0*			0.5*	0	1
201: $\tau^{-3}(0.6, 0.4, -0.8, -0, -0.2, -0)^i$	-1.1	0.4	0*			0.5*	0.15	0.85
202: $\tau^{-4}(-0.4, 0.8, -0, 0.2, -0.6, -0)^i$	-0.06	0.06	0*			1*	0.02	0.98
203: $\tau^{-4}(0.4, 0.6, -0.2, -0, -0.8, -0)^i$	0.32	-0.35	0*			1*	0	1
204: $\tau^{-4}(-0.8, 0.4, 0.6, -0.2, -0, -0)^i$	-0.06	0.06	0*			1*	0.02	0.98
205: $\tau^{-4}(0.8, -0, 0.2, -0.6, -0.4, -0)^i$	0.32	-0.35	0*			1*	0	1
206: $\tau^{-3}(-0.6, 0.2, 1, -0.2, -0.4, -0)^i$	0.13	0.08	0*			1*	0	1
207: $\tau^{-3}(0.6, 0.4, 0.2, -1, -0.2, -0)^i$	0.11	-0.05	0*			1*	0	1
208: $\tau^{-3}(-0.2, -0.4, -0.6, 0.2, 1, -0)^i$	0.13	0.08	0*			1*	0	1

209: $\tau^{-3}(0.2, -1, -0.2, 0.6, 0.4, -0)^i$	0.11	-0.05	0*	1*	0	1
210: $\tau^{-3}(-0.4, -0.6, 0.2, -0, 0.8, -0)^i$	-1.29	0.4	0*	0.5*	0	1
211: $\tau^{-3}(0.4, -0.8, -0, -0.2, 0.6, -0)^i$	-0.63	-0.08	0*	0.5*	0.15	0.85
212: $\tau^{-3}(-0, 0.8, -0.4, -0.6, 0.2, -0)^i$	-1.29	0.4	0*	0.5*	0.15	0.85
213: $\tau^{-3}(-0, -0.2, 0.6, 0.4, -0.8, -0)^i$	-0.63	-0.08	0*	0.5*	0	1
214: $\tau^{-4}(-0.6, -0.4, 0.8, -0, 0.2, -0)^i$	-0.06	0.06	0*	1*	0.02	0.98
215: $\tau^{-4}(0.6, -0.2, -0, -0.8, 0.4, -0)^i$	0.32	-0.35	0*	1*	0	1
216: $\tau^{-4}(-0, 0.2, -0.6, -0.4, 0.8, -0)^i$	-0.06	0.06	0*	1*	0.02	0.98
217: $\tau^{-4}(-0, -0.8, 0.4, 0.6, -0.2, -0)^i$	0.32	-0.35	0*	1*	0	1
239: $\tau^{-4}(-0.2292, 0.2292, -0.4584, -0, 0.4584, -0)^i$	0.05	0*	0*	1*	1	0
240: $\tau^{-4}(0.2292, -0.4584, -0, 0.4584, -0.2292, -0)^i$	0.05	0*	0*	1*	1	0
241: $\tau^{-4}(-0.2, 0.2584, -0.4292, 0.0229, 0.3416, -0)^i$	0.08	0.06	0*	1*	0	1
242: $\tau^{-4}(0.2, -0.3416, -0.0229, 0.4292, -0.2584, -0)^i$	0.08	0.06	0*	1*	0	1
243: $\tau^{-4}(-0.2584, 0.2, -0.3416, -0.0292, 0.4292, -0)^i$	0.08	0.06	0*	1*	0	1
244: $\tau^{-4}(0.2584, -0.4292, 0.0292, 0.3416, -0.2, -0)^i$	0.08	0.06	0*	1*	0	1
245: $\tau^{-4}(-0.1708, 0.1416, -0.4, 0.0584, 0.3708, -0)^i$	0.2	0.21	0*	1*	0	1
246: $\tau^{-4}(0.1708, -0.3708, -0.0584, 0.4, -0.1416, -0)^i$	0.2	0.21	0*	1*	0	1
247: $\tau^{-4}(-0.1416, 0.1708, -0.3708, -0.0584, 0.4, -0)^i$	0.2	0.21	0*	1*	0	1
248: $\tau^{-4}(0.1416, -0.4, 0.0584, 0.3708, -0.1708, -0)^i$	0.2	0.21	0*	1*	0	1
249: $\tau^{-4}(-0.4292, 0.0292, 0.3416, -0.2, 0.2584, -0)^i$	0.08	0.06	0*	1*	0	1
250: $\tau^{-4}(0.4292, -0.2584, 0.2, -0.3416, -0.0292, -0)^i$	0.08	0.06	0*	1*	0	1
251: $\tau^{-4}(-0.3416, -0.0292, 0.4292, -0.2584, 0.2, -0)^i$	0.08	0.06	0*	1*	0	1
252: $\tau^{-4}(0.3416, -0.2, 0.2584, -0.4292, 0.0292, -0)^i$	0.08	0.06	0*	1*	0	1
253: $\tau^{-4}(-0.4, 0.0584, 0.3708, -0.1708, 0.1416, -0)^i$	0.2	0.21	0*	1*	0	1
254: $\tau^{-4}(0.4, -0.1416, 0.1708, -0.3708, -0.0584, -0)^i$	0.2	0.21	0*	1*	0	1
255: $\tau^{-4}(-0.4584, -0, 0.4584, -0.2292, 0.2292, -0)^i$	0.05	0*	0*	1*	1	0
256: $\tau^{-4}(0.4584, -0.2292, 0.2292, -0.4584, -0, -0)^i$	0.05	0*	0*	1*	1	0
257: $\tau^{-4}(-0.3708, -0.0584, 0.4, -0.1416, 0.1708, -0)^i$	0.2	0.21	0*	1*	0	1
258: $\tau^{-4}(0.3708, -0.1708, 0.1416, -0.4, 0.0584, -0)^i$	0.2	0.21	0*	1*	0	1
259: $\tau^{-4}(-0.0292, 0.4292, -0.2584, 0.2, -0.3416, -0)^i$	0.08	0.06	0*	1*	0	1
260: $\tau^{-4}(0.0292, 0.3416, -0.2, 0.2584, -0.4292, -0)^i$	0.08	0.06	0*	1*	0	1
261: $\tau^{-4}(-0, 0.4584, -0.2292, 0.2292, -0.4584, -0)^i$	0.05	0*	0*	1*	1	0
262: $\tau^{-4}(-0.0584, 0.4, -0.1416, 0.1708, -0.3708, -0)^i$	0.2	0.21	0*	1*	0	1
263: $\tau^{-4}(0.0584, 0.3708, -0.1708, 0.1416, -0.4, -0)^i$	0.2	0.21	0*	1*	0	1
267: $\tau^{-4}(-0, 0.1416, 0.4292, -0.4292, -0.1416, -0)^i$	-0.19	0*	0*	1*	0.07	0.93
268: $\tau^{-4}(0.1416, 0.4292, -0.4292, -0.1416, -0, -0)^i$	-0.19	0*	0*	1*	0.07	0.93
269: $\tau^{-4}(-0.1416, -0, 0.1416, 0.4292, -0.4292, -0)^i$	-0.19	0*	0*	1*	0.07	0.93
270: $\tau^{-4}(-0.4292, -0.1416, -0, 0.1416, 0.4292, -0)^i$	-0.19	0*	0*	1*	0.07	0.93
271: $\tau^{-4}(0.4292, -0.4292, -0.1416, -0, 0.1416, -0)^i$	-0.19	0*	0*	1*	0.07	0.93
OD5: $\mathbf{x}_0 = (0, 0, 0, 0, -0.125)$				1.32	3.5	
272: $\tau^{-3}(0, 0, 0, 0, 0, 0)^i$	0*	0*	0*			1*
273: $\tau^{-3}(0, 0, 0, 0, 0, 0)^i$	0*	0*	0*			1*
274: $\tau^{-4}(0, -0.6, -0.2, 0.2, 0.6, 0)^i$	0*	0*	0*			1*
275: $\tau^{-4}(0, -0.6, -0.2, 0.2, 0.6, 0)^i$	0*	0*	0*			1*
OD6: $\mathbf{x}_0 = (0.2, 0.2, 0.2, 0.2, -0.125)$				1.32	3.5	
276: $\tau^{-3}(0, 0, 0, 0, 0, 0)^i$	0*	0*	0*			1*
277: $\tau^{-3}(0, 0, 0, 0, 0, 0)^i$	0*	0*	0*			1*
278: $\tau^{-4}(0, -0.6, -0.2, 0.2, 0.6, 0)^i$	0*	0*	0*			1*
279: $\tau^{-4}(0, -0.6, -0.2, 0.2, 0.6, 0)^i$	0*	0*	0*			1*
OD7: $\mathbf{x}_0 = (0.4, 0.4, 0.4, 0.4, -0.125)$				1.32	3.5	
280: $\tau^{-3}(0, 0, 0, 0, 0, 0)^i$	0*	0*	0*			1*
281: $\tau^{-3}(0, 0, 0, 0, 0, 0)^i$	0*	0*	0*			1*
282: $\tau^{-4}(0, -0.6, -0.2, 0.2, 0.6, 0)^i$	0*	0*	0*			1*
283: $\tau^{-4}(0, -0.6, -0.2, 0.2, 0.6, 0)^i$	0*	0*	0*			1*
OD8: $\mathbf{x}_0 = (-0.2, -0.2, -0.2, -0.2, -0.125)$				1.32	3.5	
284: $\tau^{-3}(0, 0, 0, 0, 0, 0)^i$	0*	0*	0*			1*
285: $\tau^{-3}(0, 0, 0, 0, 0, 0)^i$	0*	0*	0*			1*

286: $\tau^{-4}(0, -0.6, -0.2, 0.2, 0.6, 0)^i$	0*	0*	0*			1*	1	0
287: $\tau^{-4}(0, -0.6, -0.2, 0.2, 0.6, 0)^i$	0*	0*	0*			1*	0	1
OD9: $\mathbf{x}_0 = (-0.4, -0.4, -0.4, -0.4, -0.125)$				1.32	3.5			
288: $\tau^{-3}(0, 0, 0, 0, 0, 0)^i$	0*	0*	0*			1*	0	1
289: $\tau^{-3}(0, 0, 0, 0, 0, 0)^i$	0*	0*	0*			1*	1	0
290: $\tau^{-4}(0, -0.6, -0.2, 0.2, 0.6, 0)^i$	0*	0*	0*			1*	1	0
291: $\tau^{-4}(0, -0.6, -0.2, 0.2, 0.6, 0)^i$	0*	0*	0*			1*	0	1

In Fig. 5.1, the developments of the R and wR values as a function of the refinement steps for all, main and super reflection data sets are presented. As an initial step, only three non-structural parameters (scaling, extinction and global phason displacement) have been refined. In the next step, 52 shift parameters related to an average structure have been introduced. In steps 4-6, different superstructure shift modulation parameters, related to a superstructure, have been refined. These parameter are shown in Fig. 1 in Article III. Next, 10 ADP parameters were included. After that, 19 puckering parameters (atomic shifts along the periodic direction) were considered. In the next two steps, mixing parameters that contribute to superstructure chemical modulations were refined. In the final step, the refinement parameter related to the small rhombic occupation domains were included. In total, the refinement was done with 250 parameters, where 133 and 117 parameters are respectively related to an average structure and superstructure.

In Fig. 5.2 a statistical analysis is presented. It was important to check the quality of the refinement and to understand whether the distribution of the weak superstructure reflections is consistent with the statistics of the main reflections. For this, two different idealized cases were considered. In the first case, sigmas (standard deviations) of the observed intensities were calculated using the Poisson distribution, Fig. 5.2 (c). These results show that the distribution of the weak reflections of our experimental data is indeed in agreement with the Poisson distribution and follows the distribution of the main reflections.

In Fig. 5.3, the atomic layers are given and their corresponding occupation domains are shown (numbered). The projection of the three atomic layers, given in Fig. 3 in Article III, is shown in Fig. 5.4. Al atoms in the atomic layers at $x_3 = -1/8$, $x_3 = 1/8$ and $x_3 = 3/8$ are indicated by green, pink and gray colors, respectively. Co atoms at atomic layers at $x_3 = -1/8$, $x_3 = 1/8$ and $x_3 = 3/8$ are indicated by blue, violet and black colors, respectively. The inner part of the columnar cluster, defined by a decagonal cage in Fig. 5.4, is shown in Fig. 5.5. Al atoms in the puckered layers are indicated by pink and in the flat layers by light blue. Co atoms are indicated by dark blue. Two partially occupied Al atom positions with very short interatomic distances, so called *split positions*, are present (Fig. 5.5 (a)).

A comparison of the 20 Å clusters of the average structure and of the superstructure is shown in Fig. 5.6. In Fig. 5.6 (a) the 20 Å cluster is a fragment of the MEM map calculated using the refined average structure. The presented atomic layer of the 20 Å cluster is a superposition of the two layers of the four-layer superstructure. In Fig. 5.6 (b), a projection of the two layers resulting from the refined model of the four-layer superstructure is shown; the individual layers are presented in Fig. 5.6 (c-d). This comparison shows very good agreement and clarifies the origin of the strange electron density distribution observed in the MEM maps of the average structure.

The resulting Fourier maps after the MEM improvement in external space are shown in

Fig. 5.7. The electron density distributions for the five different occupation domains are compared for the cases where all (Fig. 5.8 (b, e, h, k, n)) and only main (Fig. 5.8 (c, f, i, l, o)) reflections are taken into account. The main differences are observed in the occupation domains C and D. In these occupation domains, the five-fold symmetry is clearly broken. One should keep in mind, that the projected structure (average structure) should preserve the five-fold symmetry. The occupation domains C and D are related by c -glide occupation domains C' and D' located at $x_3 = 3/8$. Hence, the projection of the occupation domains C with C' as well as D with D' should possess five-fold symmetry.

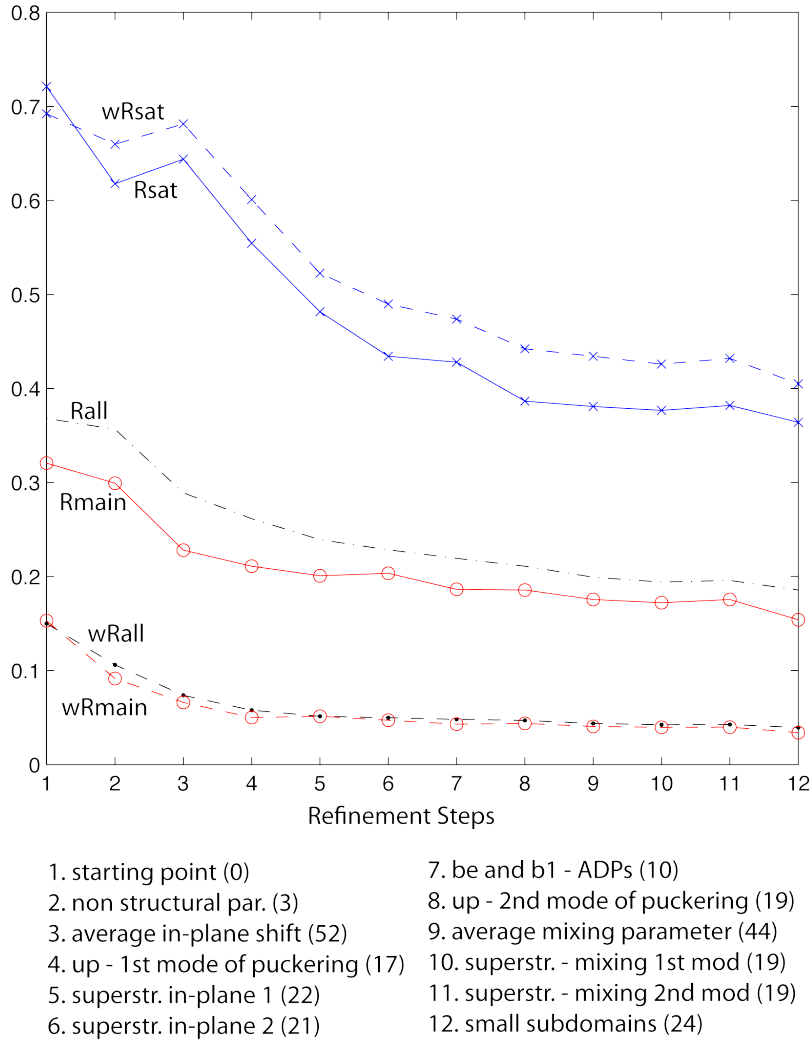


Figure 5.1: Development of the R and wR values as a function of the refinement steps for all, main and superstructure reflections. The refinement steps are given with the corresponding number of the refined parameters in the brackets.

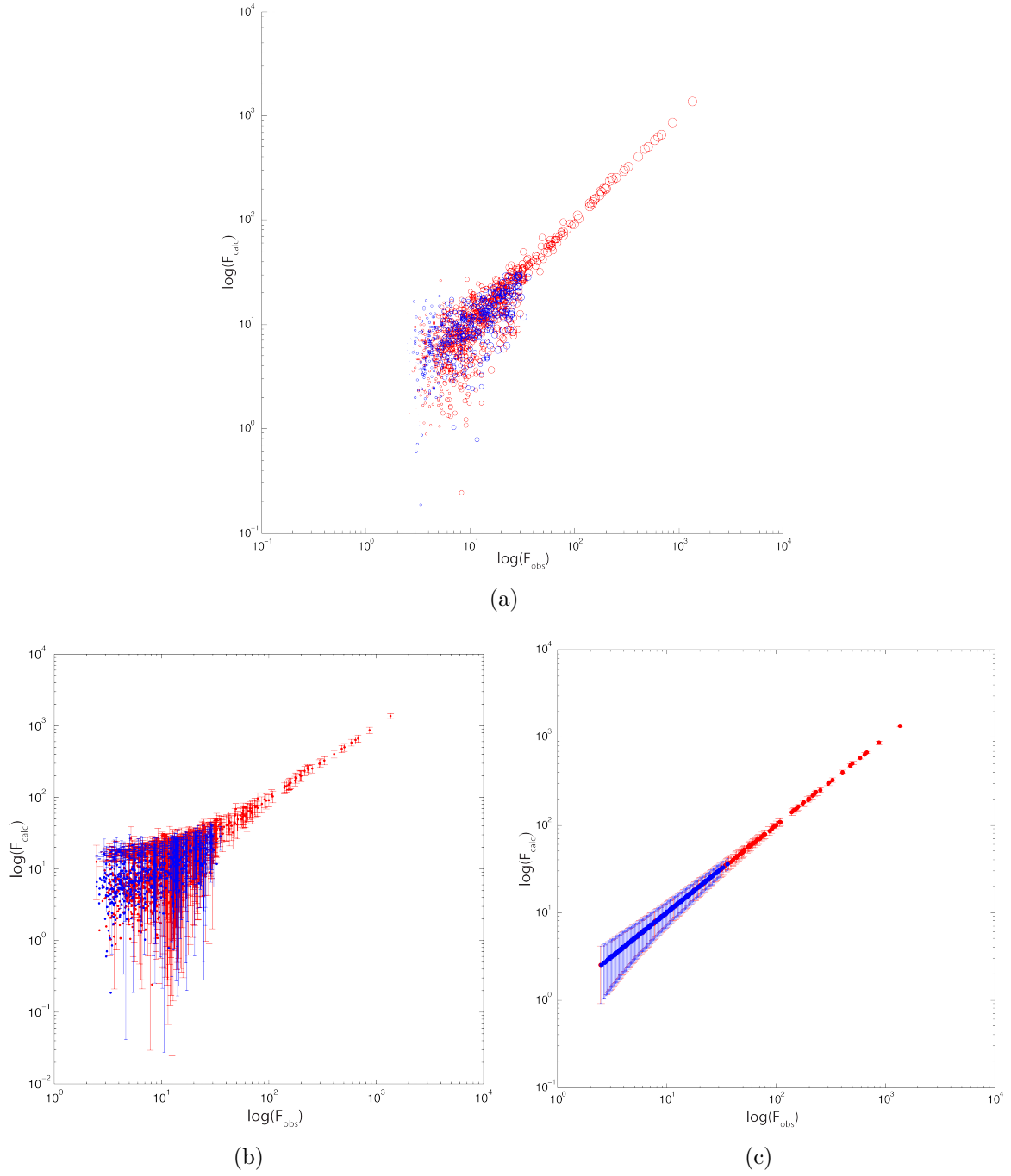
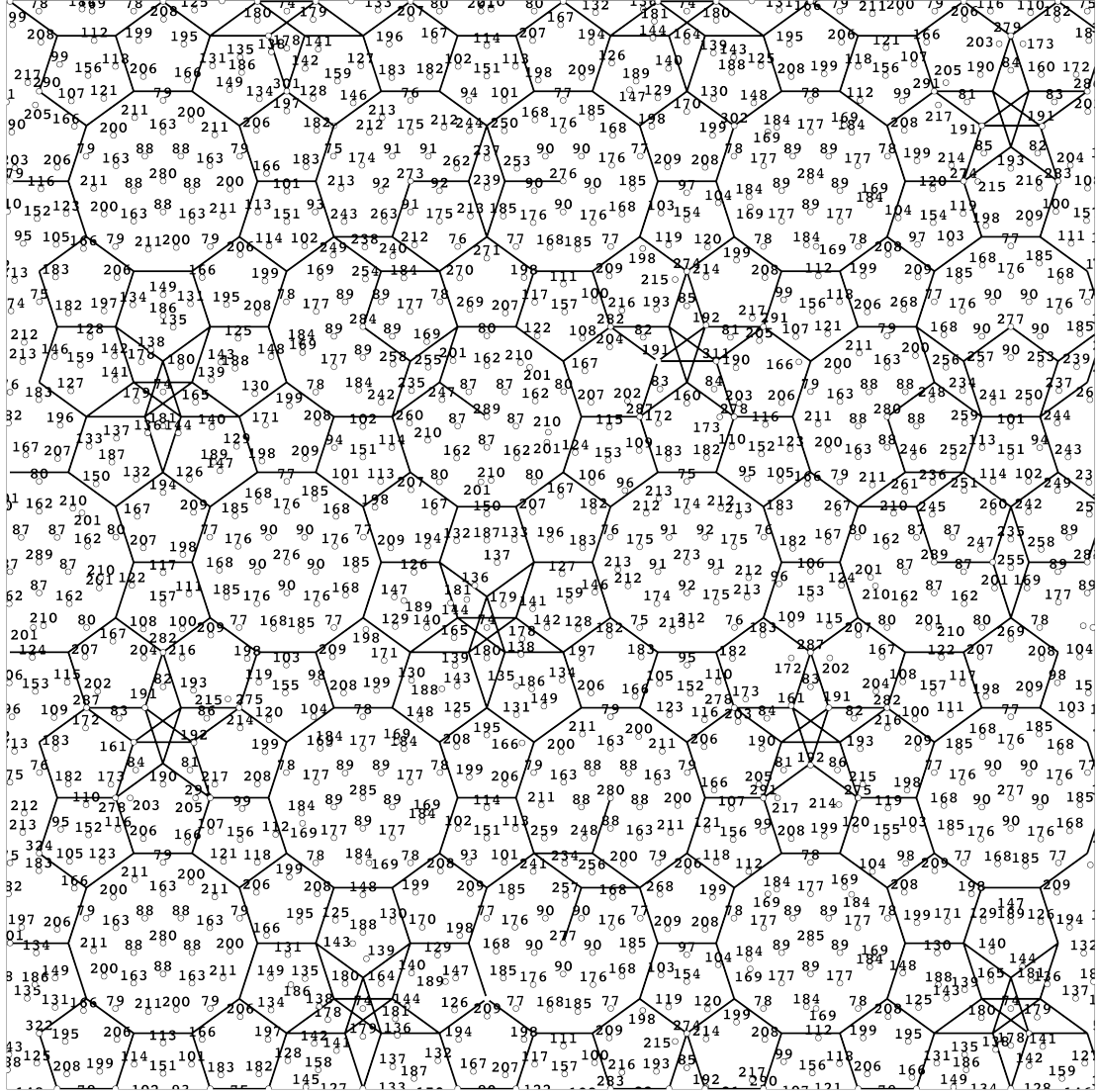
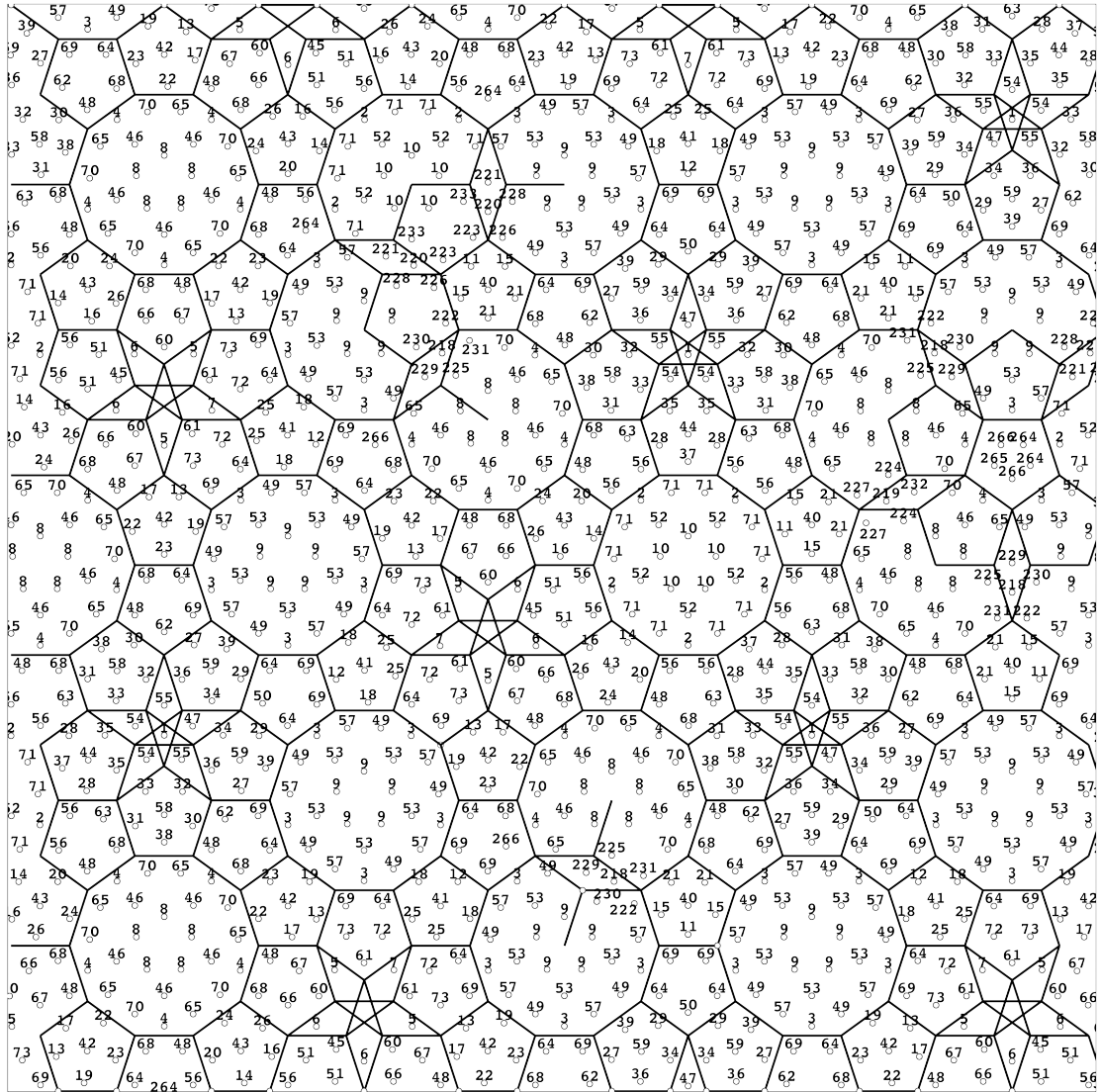


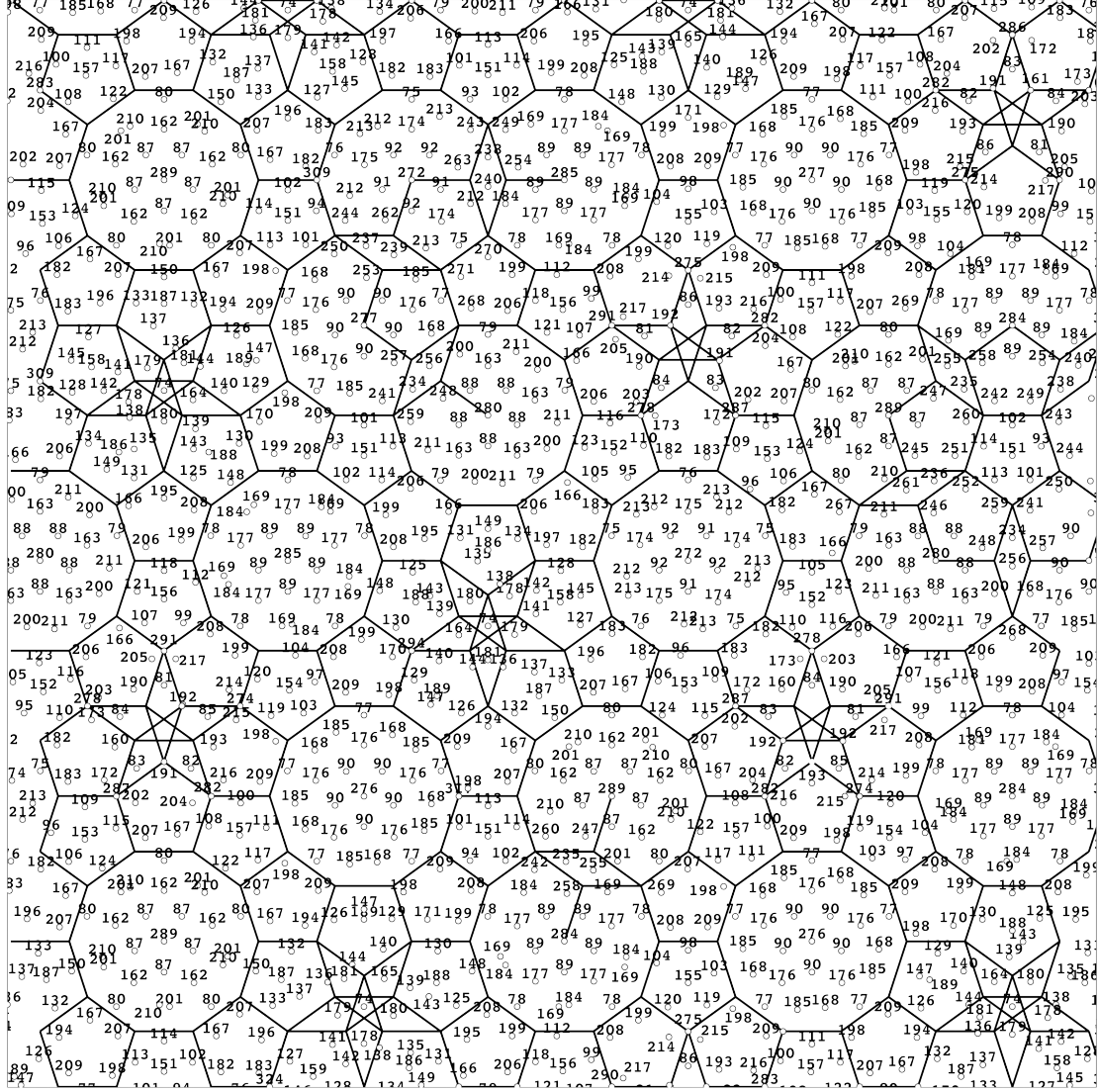
Figure 5.2: Study of $F_{\text{obs}}/F_{\text{calc}}$ on the logarithmic scale and the corresponding sigma values influence. Black and gray dots correspond to main and satellite reflections, respectively. (a) the circle sizes correspond to F_{obs}/σ_F ; (b) the bar sizes correspond to the sigma values. (c) F_{obs} with the calculated sigmas following Poisson distribution.



(a)



(b)



(c)

Figure 5.3: $90 \times 90 \text{ \AA}^2$ sections of the atomic layers at (a) $x_3 = -1/8$ (flat), (b) $x_3 = 1/8$ (puckered) and (c) $x_3 = 3/8$ (flat) of the four-layer superstructure of decagonal $\text{Al}_{72.5}\text{Co}_{18.5}\text{Ni}_9$ related to Fig. 3 in Article III with an indicated number for each atom.

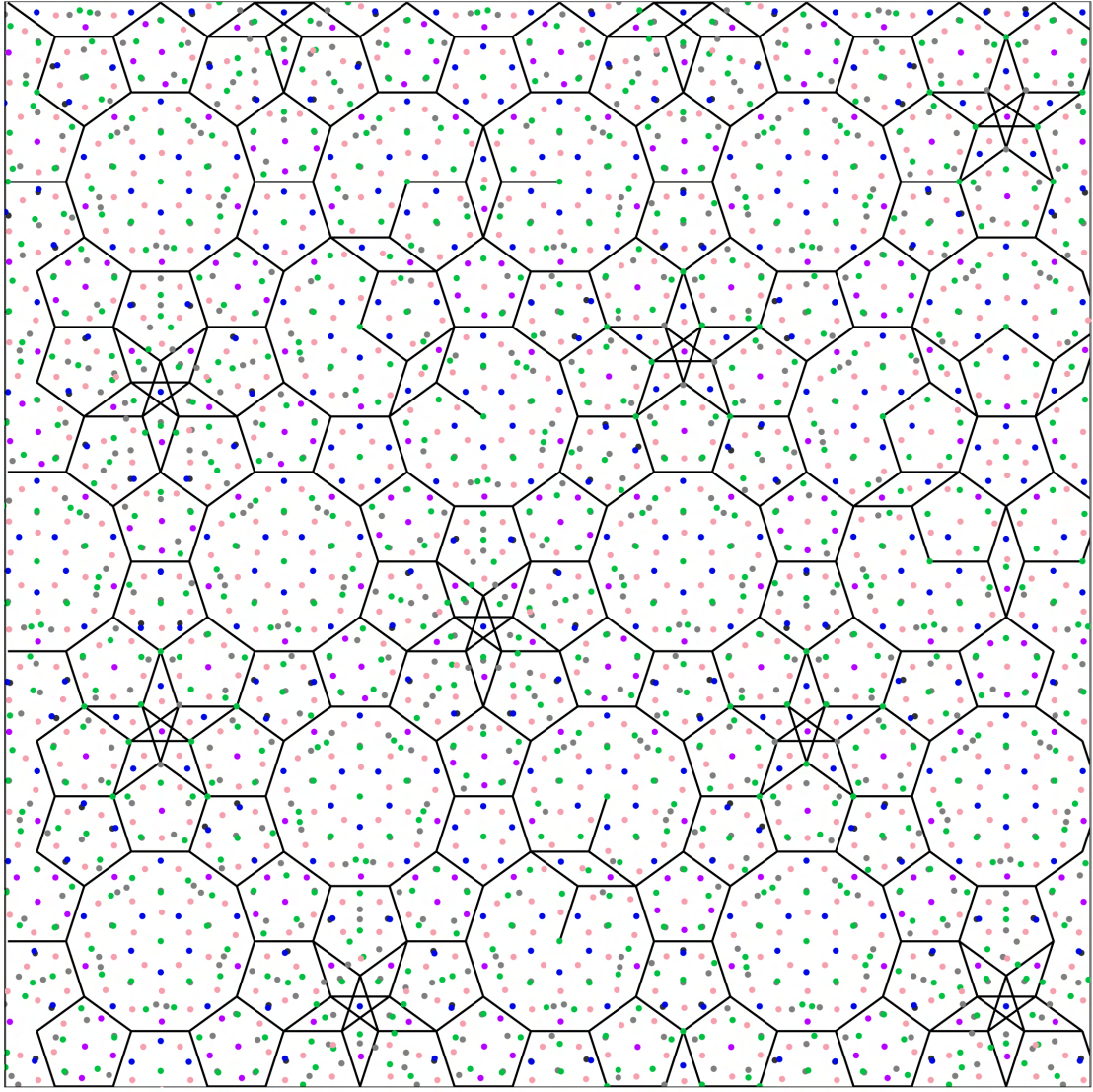


Figure 5.4: $90 \times 90 \text{ \AA}^2$ projection of the three atomic structure layers of decagonal $\text{Al}_{72.5}\text{Co}_{18.5}\text{Ni}_9$ given in Fig. 3 in Article III.

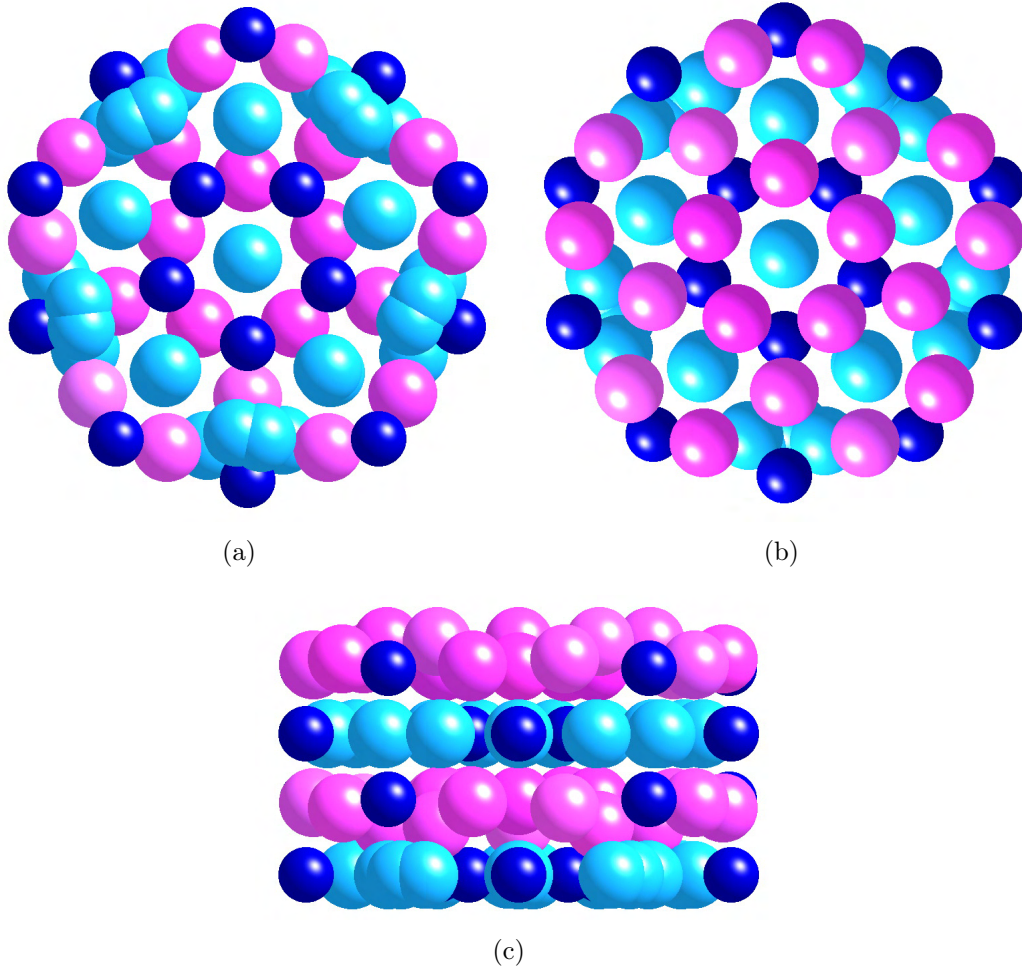


Figure 5.5: The inner part of the columnar cluster, defined by a decagonal cage in Fig. 5.4. The cluster is shown in a top view along the (a) $[00100]$, (b) $[00-100]$ and (c) side view.

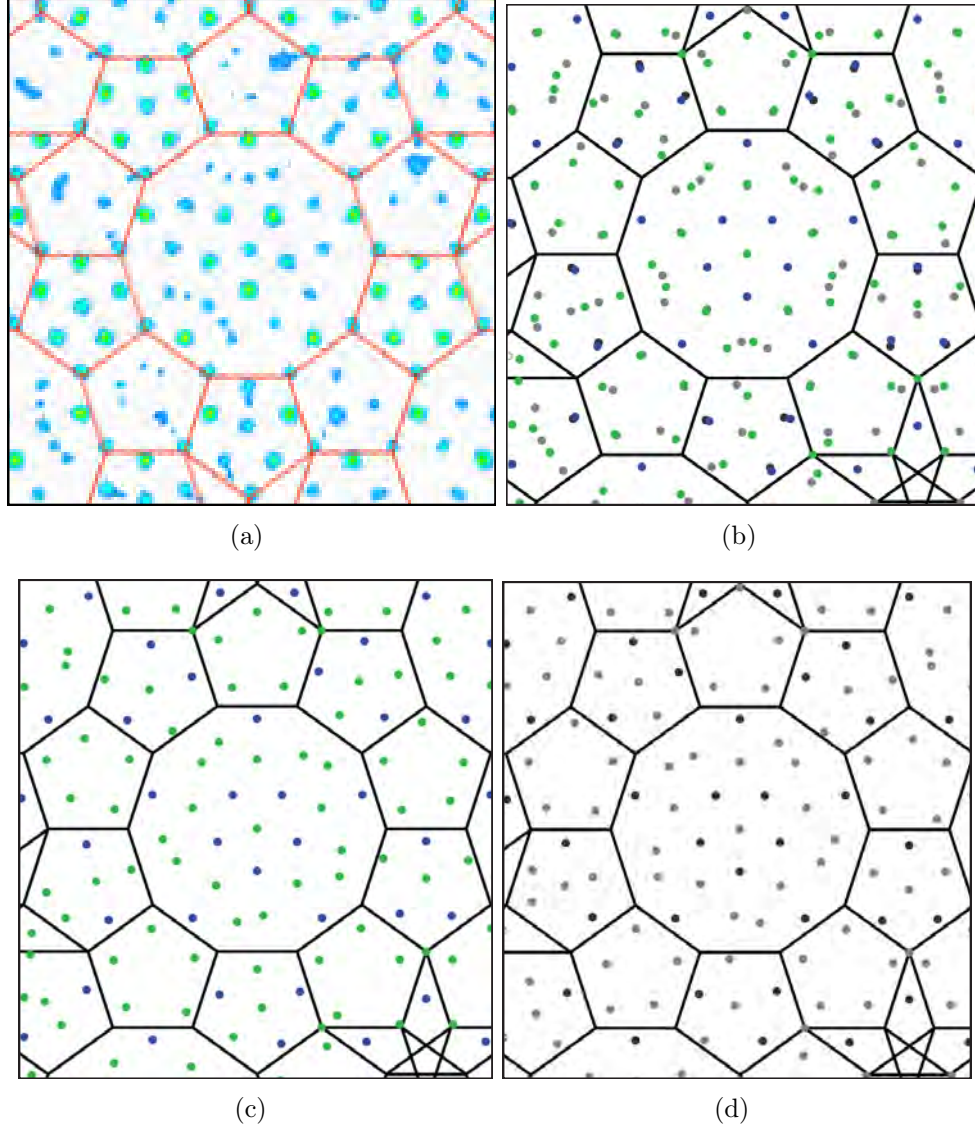
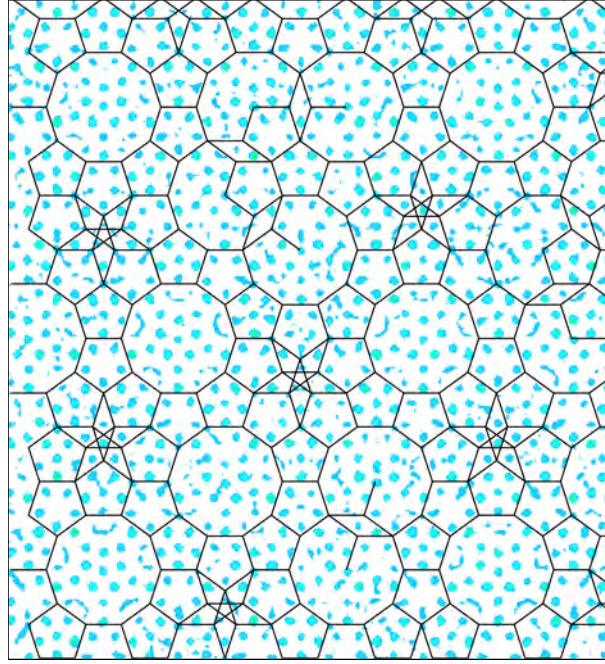
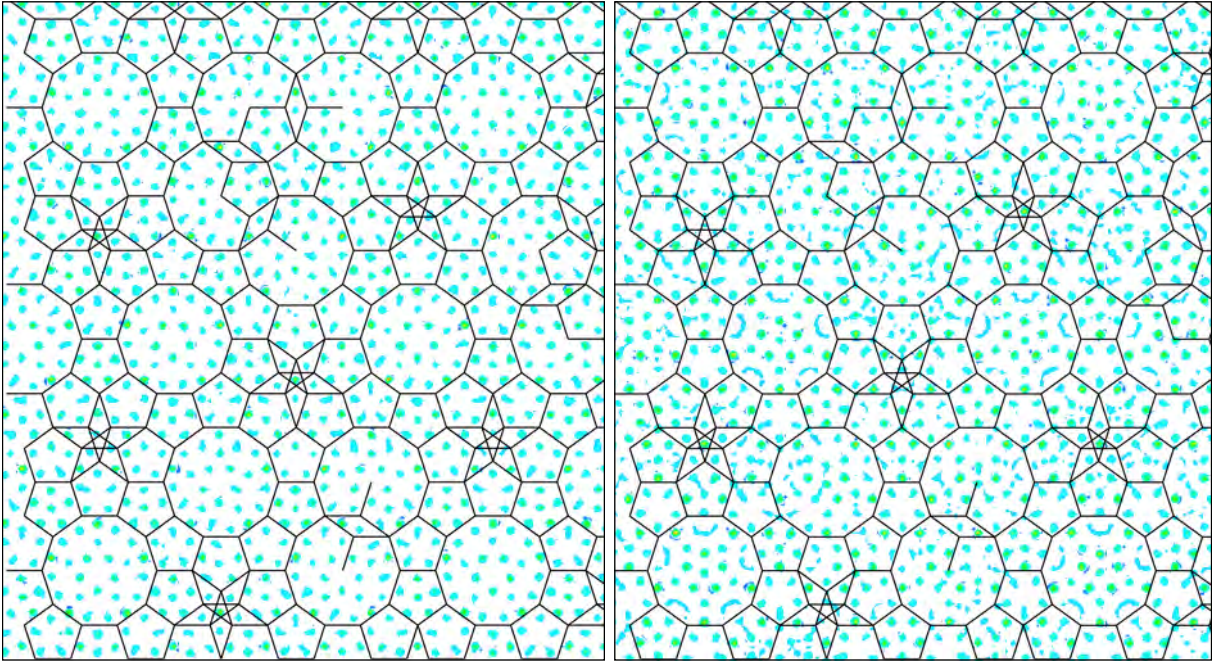


Figure 5.6: Comparison between clusters (a) obtained by MEM calculations after an average structure refinement; (b) a projection from two layers that are shown in (c) and (d) obtained from a refined superstructure model; individual atomic layers at (c) $x_3 = -1/8$ and (d) $x_3 = 3/8$. Al atoms in the atomic layers at $x_3 = -1/8$ and $x_3 = 3/8$ are indicated by green and gray colors, respectively. Co atoms at atomic layers at $x_3 = -1/8$ and $x_3 = 3/8$ are indicated by blue and black colors, respectively.



(a)



(b)

(c)

Figure 5.7: Electron density distribution in external space after refinement and MEM calculations at (a) $x_3 = -1/8$, (b) $x_3 = 1/8$ and (c) $x_3 = 3/8$.

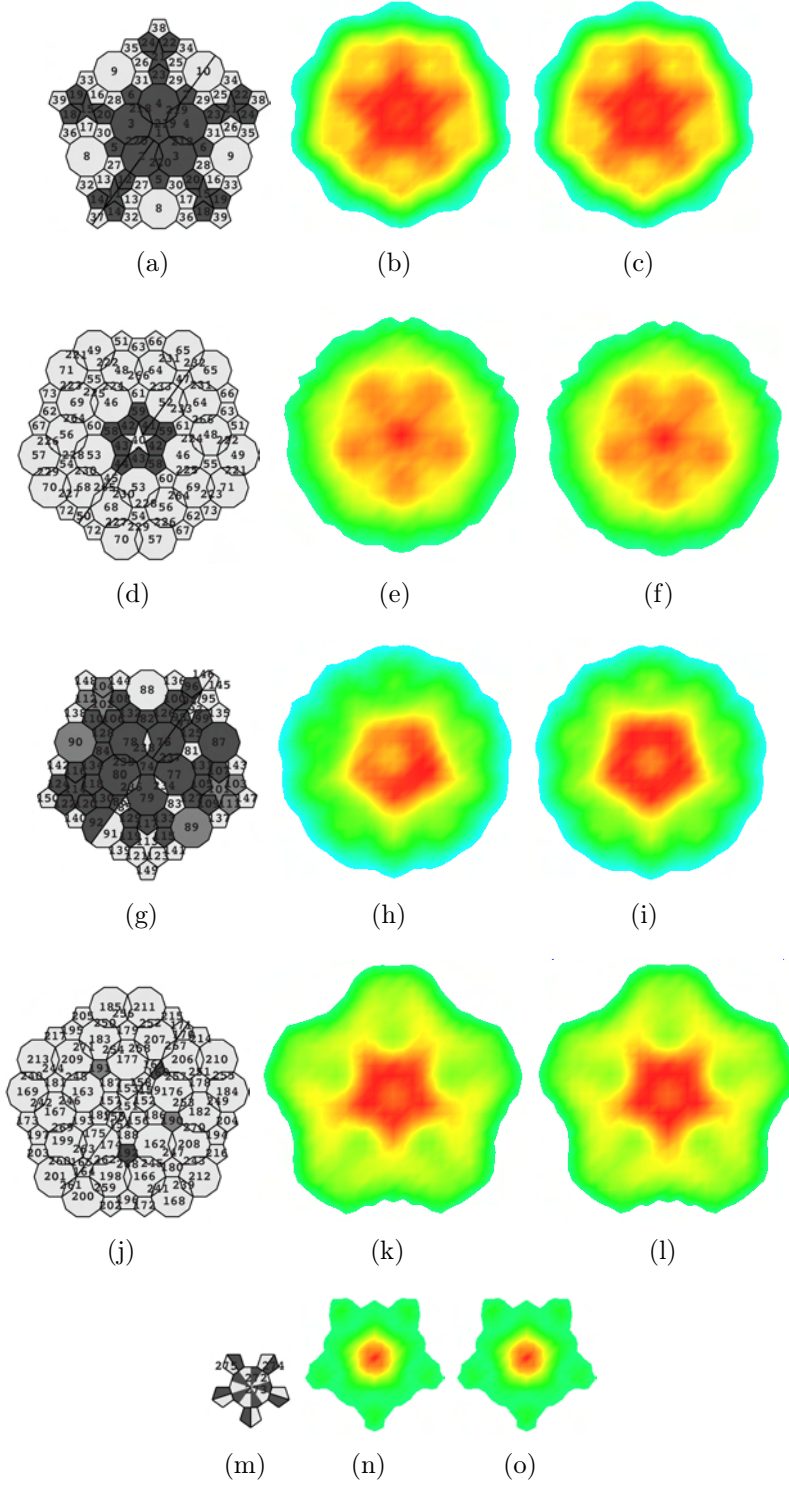


Figure 5.8: Occupation domains at (a-c) A $(0,2,-1,1,5/8)/5$, (d-f) B $(0,4,-2,2,5/8)/5$, (g-i) C $(0,-2,1,-1,-5/8)/5$, (j-l) D $(0,-4,2,-2,-5/8)/5$, and (m-o) E $(0,0,0,0,-5/8)/5$ (also $(1,1,1,1,-5/8)/5$, $(2,2,2,2,-5/8)/5$, $(-1,-1,-1,-1,-5/8)/5$, and $(-2,-2,-2,-2,-5/8)/5$), as obtained from the refined five-dimensional structure model (a, d, g, j, m) and from Fourier transform for all (b, e, h, k, n) and for main (c, f, i, l, o) reflection data sets.

Chapter 6

Concluding Remarks

The diffraction patterns of decagonal quasicrystals show ten-fold symmetry and have one periodic direction. Decagonal phases in the Al-Co-Ni system show a wide variety of structural modifications. More precisely, there are several superstructures formed which can be recognized by the presence of satellite reflections as well as by their period along the periodic direction. The diffraction pattern of the basic-Ni rich modification consists only of main reflections and can be regarded as a basic structure. Until now it has not been clear which structural modulations contribute to satellite reflections. Although several models that can mimic the observed diffraction patterns have been proposed, their reliability has to be checked by qualitative analysis.

A critical success factor for the current work was that a high-quality single-crystal of the decagonal phase was grown. Moreover, its X-ray diffraction pattern shows sharp Bragg peaks in the main layers and also in intermediate layers. This indicates the presence of a well-ordered four-layer superstructure with a period of ≈ 8 Å along the periodic direction and hence, serves as a key compound in the decagonal Al-Co-Ni system. This fact provided a unique opportunity to make a full structure solution of a four-layer superstructure of basic Co-rich decagonal Al-Co-Ni.

As is well known, a superstructure of the decagonal phase cannot be determined directly and has to be obtained based on the average structure solution. In an attempt to solve the average structure, LDE/CF methods were first applied to obtain a rough electron density distribution. This resulted in information about the average structure with a period of ≈ 4 Å along the periodic direction. Based on these results, when combined with the higher-dimensional model for Al-Fe-Ni proposed by A. Yamamoto, a model for an average structure of $\text{Al}_{72.5}\text{Co}_{18.5}\text{Ni}_9$ has been constructed. Subsequently, this model has been improved by a refinement process resulting in wR and R factors of 0.123 and 0.156, respectively.

The average structure solution served as a valuable starting point in the search for a superstructure model. In contrast to the average structure, the superstructure could

not be solved using LDE/CF methods. One of the reasons is that LDE/CF methods are inefficient in assigning correct phases to weak reflections. Hence, only by providing a good initial superstructure model and improving it by a refinement process, can superstructure modulations be validated. A crucial factor was to find a superstructure model that will reproduce the observed satellite reflections with their peculiar extinction conditions. It has been revealed that chemical modulations alone cannot explain the intensity distribution of the satellite reflections; it was highly important to account for displacement modulations (puckering and in-plane atomic displacements) to obtain a realistic picture. Finally, we succeeded in constructing a five-dimensional structure model that explains the origin of the satellite reflections. By an irrational cut of the five-dimensional structure, a three-dimensional structure model can be generated. For the present case, the convergence of R factors is shown in Fig. 5.1. For the satellite reflections, wR and R -values dropped from 70% to values below 40%. In spite of this significant drop, there is still room for improvement. In the present superstructure analysis, it was not possible to obtain better refinement results for several reasons. Some of the difficulties stem from the nature of the superstructure of decagonal quasicrystals, others are caused by experimental limitations. Hence, the reliability of the measured intensities is unsatisfying and as a consequence the quality of the integrated data is questionable. On top of this, the construction of a superstructure model for a decagonal quasicrystal that will be able to explain experimentally acquired results is a very demanding task. This is because satellite reflections are weak and extremely sensitive to small variations in the structure model. In addition, the existing extinction conditions cannot be explained by the superspace group. Hence, to explain the rigorous extinction conditions of the superstructure, additional constraints have to be used in the refinement.

To vindicate the validity of the refined superstructure, a known approximant structure, the W-phase, was generated by introducing appropriate linear phason strains to the five-dimensional quasicrystal model and by cutting it through an appropriate origin. An important result of this thesis is that the structures of the generated and the actual W-phase approximants show a good agreement. Moreover, it was proven that the W-phase is a $\langle 3/2, 2/1 \rangle$ -approximant of the four-layer superstructure of decagonal Al-Co-Ni. This is an excellent foundation for modeling all different modifications of Al-based decagonal phases with a four-layer period, since the clusters identified in the W-phase can be used as fundamental clusters for this purpose.

This superstructure solution defines new frontiers in the field of quasicrystal structure analysis and provides a good starting point for further investigations. For future work, I would propose to collect a higher quality X-ray diffraction data set corrected for multiple diffraction which is omnipresent in quasicrystals. In addition, neutron experiments could be performed in order to determine the distribution of Co and Ni in the structure.

Bibliography

Bibliography

- [BLVA08] A. Bahabad, R. Lifshitz, N. Voloch, A. Arie. *Phil. Mag.* **88**, 2285 (2008).
- [B86] P. Bak, *Phys. Rev. Lett.* **56**, 861 (1986).
- [B85] L. Bendersky, *Phys. Rev. Lett.* **55**, 1461 (1985).
- [BS09] L. Bindi, P. J. Steinhardt, N. Yao, P. J. Lu, *Science* **324**, 1306 (2009).
- [BBNWZ78] H. Brown, R. Bülow, J. Neubüser, H. Wondratschek, H. Zassenhaus, *Crystallographic groups of four-dimensional space*, John Wiley & Sons, New-York, (1978).
- [dB81] N. de Bruijn, *Nedert. Akad. Wetensch. Proc. Ser. A* **43**, 39. 53 (1981).
- [BNW71] R. Bülow, J. Neubüser, H. Wondratschek, *Acta Crystallogr. A* **27**, 520 (1971).
- [CGM88a] J. W. Chan, D. Gratias, B. Mozer, *Journal de Physique (Paris)* **49**, 1225 (1988).
- [CGM88b] J. W. Chan, D. Gratias, B. Mozer, *Phys. Rev. B* **38**, 1638 (1988).
- [CRST85] K. Chattopadhyay, S. Ranganathan, G. N. Subbanna, N. Thangaraj, *Scripta Metall.* **19**, 767 (1985).
- [DK85] M. Duneau, A. Katz, *Phys. Rev. Lett.* **54**, 2688 (1985).
- [EIST92] K. Edagawa, M. Ichihara, K. Suzuki, S. Takeuchi, *Philos. Mag. Lett.* **66**, 19 (1992).
- [ETYST94] K. Edagawa, H. Tamaru, S. Yamaguchi, K. Suzuki, S. Takeuchi, *Phys. Rev. B* **50**, 12413 (1994).
- [E85a] V. Elser, *Phys. Rev. Lett.* **54**, 1730 (1985).

- [E85b] V. Elser, Phys. Rev. B **32**, 4892 (1985).
- [E86] V. Elser, Acta Crystallogr. A **42**, 36 (1986).
- [EH85] V. Elser, C. Henley, Phys. Rev. Lett. **55**, 2883 (1985).
- [FLFS07] B. Freedman, R. Lifshitz, J. W. Fleischer, M. Segev, Nature Materials **6**, 776 (2007).
- [GS85] B. Grünbaum, G. C. Sheppard, Tilings and Patterns, edited by W. H. Freeman and Company (New York, 1986).
- [GU94] B. Grushko, K. Urban, Philos. Mag. B **70**, 1063 (1994).
- [GH96a] B. Grushko, D. Holland-Moritz, J. Alloys Comp. **236**, 243 (1996).
- [GH96b] B. Grushko, D. Holland-Moritz, Scr. Mater. **356**, 1141 (1996).
- [GH98] B. Grushko, D. Holland-Moritz, J. Alloys Comp. **280**, 215 (1998).
- [GD04] B. Grushko, M. Döblinger, Z. Kristallogr. B **219**, 447 (2004).
- [G96] P. Gummelt, Geometriae Dedicata, **62**, 1 (1996).
- [HDT07] K. Hayashida, T. Dotera, A. Tanako, Phys. Rev. Lett. **98**, 195502 (2007).
- [H85] C. Henley, J. Non-Cryst. Solids **75**, 91 (1985).
- [HON01] K. Hiraga, T. Ohsuna, S. Nishimura, J. Alloys Comp. **325**, 145 (2001).
- [HOSS01] K. Hiraga, T. Ohsuna, W. Sun, K. Sugiyama, Mater. Trans. JIM **42**, 2354 (2001).
- [HOSS02] K. Hiraga, T. Ohsuna, W. Sun, K. Sugiyama, J. Alloys Comp. **342**, 110 (2002).
- [I89] Y. Ishii, Phys. Rev. B **39**, 11862 (1989).
- [JJ77] A. Janner, T. Janssen, Phys. Rev. B **15**, 643 (1977).
- [JJ79] A. Janner, T. Janssen, Physica A **99**, 47 (1979).
- [JJ80] A. Janner, T. Janssen, Acta Cryst. A **36**, 399 (1980).
- [J86] T. Janssen, Acta Cryst. A **42**, 261 (1986).
- [J88] T. Janssen, Acta Cryst. A **168**, 55 (1988).
- [K91] S. Kek, Doctoral thesis, Univ. Stuttgart, Germany (1991).

- [KN84] P. Kramer, R. Neri, *Acta Cryst. A* **40**, 580 (1984).
- [KKL85] P. A. Kalugin, A. Kitaev, L. Levitov, *Journal de Physique (Paris)* **46**, L601 (1985).
- [LS84] D. Levine, P.J. Steinhardt, *Phys. Rev. Lett.* **53**, 2477 (1984).
- [L95] R. Lifshitz, Ph.D. thesis Cornell University (1995).
- [LAB05] R. Lifshitz, A. Arie, A. Bahabad, *Phys. Rev. Lett.* **95**, 133901 (2005).
- [M82] A. L. Mackay, *Physica*, **114** A, 609 (1982).
- [ML83] D. Mercier, J. C. S. Levy, *Phys. Rev. B* **27**, 77 (1983).
- [MRHB08] J. Mikhael, J. Roth, L. Helden, C. Bechinger, *Nature*. **454**, 501 (2008).
- [N91] K. Niizeki, *J. Phys. A: Math Gen* **24**, 3641 (1991).
- [NWB71] J. Neubüser, H. Wondratschek, R. Bülow, *Acta Cryst. A* **27**, 517 (1971).
- [OS04] G. Oszlányi, A. Süto, *Acta Cryst. A* **60**, 134 (2004).
- [OS05] G. Oszlányi, A. Süto, *Acta Cryst. A* **61**, 147 (2005).
- [P04] L. Palatinus, *Acta Cryst. A* **60**, 604 (2004).
- [P74] R. Penrose, *Bull. Inst. Math. Appl.* **10**, 266 (1974).
- [RBNL95] S. Ritsch, C. Beeli, H. Nissen, R. Lück, *Philos. Mag. A* **71**, 671 (1995).
- [RBNGSL98] S. Ritsch, C. Beeli, H. U. Nissen, T. Gödecke, M. Scheffer, R. Lück, *Philos. Mag. Lett.* **78**, 67 (1998).
- [RWM88a] D. S. Rokhsar, D. C. Wright, N. D. Mermin, *Acta Cryst. A* **44**, 197 (1988).
- [RWM88b] D. S. Rokhsar, D. C. Wright, and N. D. Mermin, *Phys. Rev. B* **37**, 8145 (1988) .
- [SS90] M. Sakata, M. Sato, *Acta Cryst. A* **46**, 263 (1990).
- [S80] R. L. E. Schwarzenberger, *N-dimensional crystallography*, Pitman, London (1980).
- [SBG84] D. Shechtman, I. Blech, D. Gratias, J. W. Cahn, *Phys. Rev. Lett.* **53**, 1951 (1984).
- [SSL85] J. E. S. Socolar, P. J. Steinhardt, D. Levine, *Phys. Rev. B* **32**, 5547 (1985).

- [S04] W. Steurer, Z. Kristallogr. **219**, 319 (2004).
- [SD08] W. Steurer, S. Deloudi, Acta Cryst. A **64**, 1 (2008).
- [SD09] W. Steurer, S. Deloudi, Crystallography of Quasicrystals - Concepts, Methods and Structures, Springer Series in Materials Science, (2009), ISBN: 978-3-642-01898-5.
- [SYS10] A. Strutz, A. Yamamoto and W. Steurer, accepted to Phys. Rev. B (2010).
- [TYSST02] H. Takakura, A. Yamamoto, M. Shiono, T.J. Sato, A.P. Tsai, J. Alloys Comp. **342**, 72 (2002).
- [TSBCM09] D. V. Talapin, E. V. Shevchenko, M. I. Bodnarchuk, X. Ye, J. Chen, C. B. Murray, Nature. **461**, 964 (2009).
- [TTT94] M. Tanaka, M. Terauchi, K. Tsuda, Convergent-Beam Electron Diffraction III, JEOL Ltd., Tokyo Japan (1994).
- [TIM89] A. P. Tsai, A. Inoue, T. Masumoto, Mater. Trans. JIM **30**, 150 (1989).
- [W97] S. Weber, PhD thesis No. 945587, University of Tsukuba, Japan (1997).
- [WW88] J. W. Whittaker, R. M. Whittaker, Acta Cryst. A **44**, 105 (1988).
- [dW74] P. M. de Wolff, Acta Cryst. A **30**, 777 (1974).
- [dW77] P. M. de Wolff, Acta Cryst. A **33**, 493 (1977).
- [WBN71] H. Wondratschek, R. Bülow, J. Neubüser, Acta Cryst. A **27**, 523 (1971).
- [Y96] A. Yamamoto, Acta Cryst. A **52**, 509 (1996).
- [YW97a] A. Yamamoto, S. Weber, Phys. Rev. Lett. **78**, 4430 (1997).
- [YW97b] A. Yamamoto, S. Weber, Phys. Rev. Lett. **79**, 861 (1997).
- [YTA05] A. Yamamoto, H. Takakura, and E. Abe, Phys. Rev. B **72**, art. no. 144202 (2005).
- [Y08] A. Yamamoto, Sci. Technol. Adv. Mater. **9**, 13001 (2008).
- [ZULPDH08] X. Zeng, G. Ungar, Y. Liu, V. Percec, A. E. Dulcey, J. Hobbs, Nature. **428**, 157 (2004).

Appendix

A - Program Package QUASI07_08_f90

The results reported in Chapters 4 and 5 have been carried out by the programs developed by Dr. Akiji Yamamoto and included in a program package QUASI07_08_f90 [Y08]. Although a good help file with detailed descriptions for each program included in the package is already given, here additional comments will be given.

All related LDE, MEM and Fourier calculations as well as structure refinement presented in this thesis have been carried out using programs developed by Dr. Akiji Yamamoto. These programs are based on a symmetry operator in a higher dimension, thus simplifying a structure analysis of aperiodic structures. Main convince of these programs is the reach possibility to check your results after each step. This can be done by graphical visualization and by detailed information listed in output files after each step of calculations. I will try to give some more hints and explanations using as an example case the analyzed structure in this thesis. All the calculations were implemented on MAC system with intel processor.

All programs are executed from X-terminal:

program_name < file name (including its extension)

1. QCDIFF is a least-squares refinement program for quasicrystals.
2. QCMEM is a higher-dimensional Fourier, Patterson and maximum entropy methods.
3. QCSTRC generates and plots structure projections in all subspaces using the section method.
4. LODEM is a program for a direct method structure determination based on a Low Density Elimination algorithm
5. LPHASON is calculating linear phason strains. (After determination of the cut plane, use QCSTRT to plot the approximant structure)
6. POLYGN generates and plots ODs based on the model input file.

Here the input files for the refinement of the average model as an example.

```
.atm file
1 'co(a)' 2 2 2 1. 0. 0. 0.0902 1. 0. 0. (smaller pentagon)
x= 0.2 0.2 0.2 0.2 0.25 0.0
xe1= 0.0 0.0 0.0 0.0 0.0 0.0 u1=0.0
xe2= 0.0 0.0 0.0 0.0 0.0 0.0 u2=0.0
xe3= 0.0 0.0 0.0 0.0 0.0 0.0 u3=0.0
xi= 0.0 0.0 0.0 0.0 0.0 0.0 v=0.0
isyd=1
2 'co(a)' 2 30 7 1. 0. 0. 0.1459 1. 0. 0. (larger decagon)
x= 0.2 0.2 0.2 0.2 0.25 0.0
xe1= 0.0 -1.0 0.0 0.0 0.0 0.0 u1=0.0
xe2= 0.0 0.0 0.0 0.0 0.0 0.0 u2=0.0
xe3= 0.0 0.0 0.0 0.0 0.0 0.0 u3=0.0
xi= 0.4 0.4 0.4 -0.6 -0.6 0.0 v=0.618
isyd=2
3 'co(a)' 2 3 4 1. 0. 0. 0.0902 0.5 0. 0. (smaller pentagon)
x= 0.2 0.2 0.2 0.2 0.25 0.0
xe1= 1.0 0.0 0.0 0.0 0.0 0.0 u1=0.0
xe2= 0.0 0.0 0.0 0.0 0.0 0.0 u2=0.0
xe3= 0.0 0.0 0.0 0.0 0.0 0.0 u3=0.0
xi= 0.8 -0.2 -0.2 -0.2 -0.2 0.0 v=0.618
isyd=1
4 'al(a)' 1 1 7 1. 0. 0. 0.1459 1. 0. 0. (larger decagon)
x= 0.2 0.2 0.2 0.2 0.25 0.0
xe1= 1.0 0.0 0.0 0.0 0.0 0.0 u1=0.0
xe2= 0.0 0.0 0.0 0.0 0.0 0.0 u2=0.0
xe3= 0.0 0.0 0.0 0.0 0.0 0.0 u3=0.0
xi= 0.4 -0.6 0.4 0.4 -0.6 0.0 v=0.618
isyd=1
5 'co(a)' 2 14 9 1. 0. 0. 0.0902 1. 0. 0. (small star)
x= 0.2 0.2 0.2 0.2 0.25 0.0
xe1= 0.0 -1.0 0.0 0.0 0.0 0.0 u1=0.0
xe2= 0.0 0.0 0.0 0.0 0.0 0.0 u2=0.0
xe3= 0.0 0.0 0.0 0.0 0.0 0.0 u3=0.0
xi= 0.6 -0.4 0.6 -0.4 -0.4 0.0 v=0.618
isyd=1
6 'al(a)' 1 3 9 1. 0. 0. 0.0902 1. 0. 0. (small pentagon)
x= 0.2 0.2 0.2 0.2 0.25 0.0
xe1= 0.0 -1.0 0.0 0.0 0.0 0.0 u1=0.0
xe2= 1.0 0.0 0.0 0.0 0.0 0.0 u2=0.0
xe3= 0.0 0.0 0.0 0.0 0.0 0.0 u3=0.0
xi= -0.2 -1.2 0.8 0.8 -0.2 0.0 v=0.618
isyd=1
7 'co(a)' 1 3 9 1. 0. 0. 0.0902 1. 0. 0. (small pentagon)
x= 0.2 0.2 0.2 0.2 0.25 0.0
xe1= 0.0 -1.0 0.0 0.0 0.0 0.0 u1=0.0
xe2= 0.0 0.0 0.0 0.0 0.0 0.0 u2=0.0
xe3= 0.0 0.0 0.0 0.0 0.0 0.0 u3=0.0
xi= 0.8 0.8 0.8 -1.2 -1.2 0.0 v=0.618
isyd=1
8 'al(a)' 2 3 9 1. 0. 0. 0.0902 1.0 0. 0. (small pentagon)
x= 0.2 0.2 0.2 0.2 0.25 0.0
xe1= 0.0 -1.0 0.0 0.0 0.0 0.0 u1=0.0
xe2= 1.0 0.0 0.0 0.0 0.0 0.0 u2=0.0
xe3= 0.0 0.0 0.0 0.0 0.0 0.0 u3=0.0
xi= 1.8 -0.2 -0.2 -1.2 -0.2 0.0 v=0.618
isyd=1
9 'al(a)' 1 2 6 1. 0. 0. 0.0902 1. 0. 0. (smaller pentagon)
x= 0.2 0.2 0.2 0.2 0.25 0.0
xe1= 0.0 -1.0 0.0 0.0 0.0 0.0 u1=0.0
xe2= 1.0 0.0 0.0 0.0 0.0 0.0 u2=0.0
xe3= 0.0 0.0 0.0 0.0 0.0 0.0 u3=0.0
xi= 0.0 0.0 1.0 0.0 -1.0 0.0 v=0.618
isyd=1
10 'al(a)' 1 2 6 1. 0. 0. 0.0902 1. 0. 0. (smaller pentagon)
x= 0.2 0.2 0.2 0.2 0.25 0.0
xe1= 0.0 -1.0 0.0 0.0 0.0 0.0 u1=0.0
xe2= 1.0 0.0 0.0 0.0 0.0 0.0 u2=0.0
xe3= 0.0 0.0 0.0 0.0 0.0 0.0 u3=0.0
xi= 1.0 -1.0 0.0 0.0 0.0 0.0 v=0.618
isyd=1
11 'al(a)' 1 2 4 1. 0. 0. 0.0902 0.3 0. 0. (smaller pentagon)
x= 0.2 0.2 0.2 0.2 0.25 0.0
xe1= 0.0 -1.0 0.0 0.0 0.0 0.0 u1=0.0
xe2= 0.0 0.0 0.0 0.0 0.0 0.0 u2=0.0
xe3= 0.0 0.0 0.0 0.0 0.0 0.0 u3=0.0
xi= 1.0 0.0 1.0 -1.0 -1.0 0.0 v=0.618
isyd=1
12 'co(a)' 2 11 4 1. 0. 0. 0.0902 1. 0. 0. (rhombus)
x= 0.2 0.2 0.2 0.2 0.25 0.0
xe1= 1.0 0.0 0.0 0.0 0.0 0.0 u1=0.0
xe2= 0.0 0.0 0.0 0.0 0.0 0.0 u2=0.0
xe3= 0.0 0.0 0.0 0.0 0.0 0.0 u3=0.0
xi= 0.4 -0.6 0.4 0.4 -0.6 0.0 v=0.0902
isyd=1
13 'al(a)' 1 14 9 1. 0. 0. 0.0902 0.7 0. 0. (small star)
x= 0.4 0.4 0.4 0.4 0.25 0.0
xe1= 0.0 0.0 0.0 0.0 0.0 0.0 u1=0.0
xe2= 0.0 0.0 0.0 0.0 0.0 0.0 u2=0.0
xe3= 0.0 0.0 0.0 0.0 0.0 0.0 u3=0.0
xi= 0.0 0.0 0.0 0.0 0.0 0.0 v=0.618
isyd=1
14 'al(a)' 2 3 9 1. 0. 0. 0.0902 1. 0. 0. (small pentagon)
x= 0.4 0.4 0.4 0.4 0.25 0.0
xe1= 1.0 0.0 0.0 0.0 0.0 0.0 u1=0.0
xe2= 0.0 0.0 0.0 0.0 0.0 0.0 u2=0.0
xe3= 0.0 0.0 0.0 0.0 0.0 0.0 u3=0.0
xi= 0.8 -0.2 -0.2 -0.2 -0.2 0.0 v=0.618
isyd=1
15 'al(b)' 1 30 7 1. 0. 0. 0.1459 1. 0. 0. (larger decagon)
x= 0.4 0.4 0.4 0.4 0.25 0.0
xe1= 1.0 0.0 0.0 0.0 0.0 0.0 u1=0.0
xe2= 0.0 0.0 0.0 0.0 0.0 0.0 u2=0.0
xe3= 0.0 0.0 0.0 0.0 0.0 0.0 u3=0.0
xi= 0.8 -0.2 -0.2 -0.2 -0.2 0.0 v=0.618
isyd=4
16 'al(b)' 1 31 11 1. 0. 0. 0.1459 1. 0. 0. (larger decagon)
x= 0.4 0.4 0.4 0.4 0.25 0.0
xe1= 1.0 0.0 0.0 0.0 0.0 0.0 u1=0.0
xe2= 0.0 -1.0 0.0 0.0 0.0 0.0 u2=0.0
xe3= 0.0 0.0 0.0 0.0 0.0 0.0 u3=0.0
xi= -0.2 -1.2 0.8 0.8 -0.2 0.0 v=0.618
isyd=4
17 'al(b)' 1 30 11 1. 0. 0. 0.1459 1.0 0. 0. (larger decagon)
x= 0.4 0.4 0.4 0.4 0.25 0.0
xe1= 1.0 0.0 0.0 0.0 0.0 0.0 u1=0.0
xe2= 0.0 -1.0 0.0 0.0 0.0 0.0 u2=0.0
xe3= 0.0 0.0 0.0 0.0 0.0 0.0 u3=0.0
xi= 0.8 -0.2 0.8 -0.2 -1.2 0.0 v=0.618
isyd=2
18 'al(b)' 1 3 6 1. 0. 0. 0.0902 1.0 0. 0. (smaller pentagon)
x= 0.4 0.4 0.4 0.4 0.25 0.0
xe1= 1.0 0.0 0.0 0.0 0.0 0.0 u1=0.0
xe2= 0.0 -1.0 0.0 0.0 0.0 0.0 u2=0.0
xe3= 0.0 0.0 0.0 0.0 0.0 0.0 u3=0.0
xi= 0.2 -0.8 1.2 0.2 -0.8 0.0 v=0.618
isyd=1
19 'al(b)' 1 2 4 1. 0. 0. 0.0902 1. 0. 0. (smaller pentagon)
x= 0.4 0.4 0.4 0.4 0.25 0.0
xe1= 1.0 0.0 0.0 0.0 0.0 0.0 u1=0.0
xe2= 0.0 0.0 0.0 0.0 0.0 0.0 u2=0.0
xe3= 0.0 0.0 0.0 0.0 0.0 0.0 u3=0.0
xi= 0.4 -0.6 0.4 0.4 -0.6 0.0 v=0.618
isyd=1
20 'al(b)' 1 2 4 1. 0. 0. 0.0902 1. 0. 0. (smaller pentagon)
x= 0.4 0.4 0.4 0.4 0.25 0.0
xe1= 0.0 -1.0 0.0 0.0 0.0 0.0 u1=0.0
xe2= 0.0 0.0 0.0 0.0 0.0 0.0 u2=0.0
xe3= 0.0 0.0 0.0 0.0 0.0 0.0 u3=0.0
xi= 0.4 0.4 0.4 -0.6 -0.6 0.0 v=0.618
isyd=1
21 'al(b)' 1 3 4 1. 0. 0. 0.0902 1.0 0. 0. (smaller pentagon)
x= 0.4 0.4 0.4 0.4 0.25 0.0
xe1= 0.0 -1.0 0.0 0.0 0.0 0.0 u1=0.0
xe2= 0.0 0.0 0.0 0.0 0.0 0.0 u2=0.0
xe3= 0.0 0.0 0.0 0.0 0.0 0.0 u3=0.0
xi= 0.2 -0.8 0.2 0.2 0.2 0.0 v=0.618
isyd=1
22 'al(b)' 1 2 6 1. 0. 0. 0.0902 1. 0. 0. (smaller pentagon)
x= 0.4 0.4 0.4 0.4 0.25 0.0
xe1= 0.0 -1.0 0.0 0.0 0.0 0.0 u1=0.0
xe2= 0.0 0.0 0.0 0.0 0.0 0.0 u2=0.0
xe3= 0.0 0.0 0.0 0.0 0.0 0.0 u3=0.0
xi= 0.2 -0.8 0.2 0.2 0.2 0.0 v=1.236
isyd=1
23 'co(a)' 1 11 4 1. 0. 0. 0.0902 1. 0. 0. (rhombus)
x= 0.4 0.4 0.4 0.4 0.25 0.0
xe1= 1.0 0.0 0.0 0.0 0.0 0.0 u1=0.0
xe2= 0.0 0.0 0.0 0.0 0.0 0.0 u2=0.0
xe3= 0.0 0.0 0.0 0.0 0.0 0.0 u3=0.0
xi= 0.4584 -0.6876 0.4584 0.4584 -0.6876 0.0 v=0.618
isyd=1
24 'co(a)' 1 11 4 1. 0. 0. 0.0902 1. 0. 0. (rhombus)
x= 0.4 0.4 0.4 0.4 0.25 0.0
xe1= 0.0 -1.0 0.0 0.0 0.0 0.0 u1=0.0
xe2= 1.0 0.0 0.0 0.0 0.0 0.0 u2=0.0
xe3= 0.0 0.0 0.0 0.0 0.0 0.0 u3=0.0
xi= 0.4584 -0.6876 0.452120 0.318680 -0.541600 0.0 v=0.618
isyd=7
25 'al(a)' 1 11 4 1. 0. 0. 0.0902 1. 0. 0. (rhombus)
x= 0.4 0.4 0.4 0.4 0.25 0.0
xe1= 0.0 -1.0 0.0 0.0 0.0 0.0 u1=0.0
xe2= 1.0 0.0 0.0 0.0 0.0 0.0 u2=0.0
xe3= 0.0 0.0 0.0 0.0 0.0 0.0 u3=0.0
xi= 0.312400 -0.541600 0.4584 0.312400 -0.541600 0.0 v=0.618
isyd=3
26 'al(a)' 1 25 4 1. 0. 0. 0.0902 1. 0. 0. (rhombus)
x= 0.4 0.4 0.4 0.4 0.25 0.0
xe1= 0.0 -1.0 0.0 0.0 0.0 0.0 u1=0.0
xe2= 0.0 0.0 0.0 0.0 0.0 0.0 u2=0.0
xe3= 0.0 0.0 0.0 0.0 0.0 0.0 u3=0.0
xi= 0.2876 -0.8584 0.2876 0.1416 0.1416 0.0 v=0.618
isyd=7
27 'co(a)' 2 16 2 1. 0. 0. 0.0902 1. 0. 0. (smaller pentagon)
x= -0.2 -0.2 -0.2 -0.2 -0.2500 0.0
xe1= 0.0 0.0 0.0 0.0 0.0 0.0 u1=0.0
xe2= 0.0 0.0 0.0 0.0 0.0 0.0 u2=0.0
```

```

xe3= 0.0 0.0 0.0 0.0 0.0 0.0 u3=0.0
xi= 0.0 0.0 0.0 0.0 0.0 0.0 v=0.0
isyd=1
28 'co(a)' 2 32 7 1. 0. 0. 0.1459 1. 0. 0. (larger decagon)
x= -0.2 -0.2 -0.2 -0.2 -0.25 0.0
xe1= 1.0 0.0 0.0 0.0 0.0 0.0 u1=0.0
xe2= 0.0 0.0 0.0 0.0 0.0 0.0 u2=0.0
xe3= 0.0 0.0 0.0 0.0 0.0 0.0 u3=0.0
xi= 0.4 0.4 -0.6 -0.6 0.4 0.0 v=-0.618
isyd=2
29 'co(a)' 2 17 4 1. 0. 0. 0.0902 1. 0. 0. (smaller pentagon)
x= -0.2 -0.2 -0.2 -0.2 -0.25 0.0
xe1= 0.0 0.0 0.0 0.0 -1.0 0.0 u1=0.0
xe2= 0.0 0.0 0.0 0.0 0.0 0.0 u2=0.0
xe3= 0.0 0.0 0.0 0.0 0.0 0.0 u3=0.0
xi= -0.2 -0.2 -0.2 -0.2 0.8 0.0 v=-0.618
isyd=1
30 'co(a)' 2 15 7 1. 0. 0. 0.1459 1. 0. 0. (larger decagon)
x= -0.2 -0.2 -0.2 -0.2 -0.25 0.0
xe1= 0.0 0.0 0.0 0.0 -1.0 0.0 u1=0.0
xe2= 0.0 0.0 0.0 0.0 0.0 0.0 u2=0.0
xe3= 0.0 0.0 0.0 0.0 0.0 0.0 u3=0.0
xi= -0.6 0.4 0.4 -0.6 0.4 0.0 v=-0.618
isyd=1
31 'co(a)' 2 28 9 1. 0. 0. 0.0902 1. 0. 0. (small star)
x= -0.2 -0.2 -0.2 -0.2 -0.25 0.0
xe1= 1.0 0.0 0.0 0.0 0.0 0.0 u1=0.0
xe2= 0.0 0.0 0.0 0.0 0.0 0.0 u2=0.0
xe3= 0.0 0.0 0.0 0.0 0.0 0.0 u3=0.0
xi= -0.4 0.6 -0.4 -0.4 0.0 0.0 v=-0.618
isyd=1
32 'co(a)' 2 17 9 1. 0. 0. 0.0902 1. 0. 0. (small pentagon)
x= -0.2 -0.2 -0.2 -0.2 -0.25 0.0
xe1= 1.0 0.0 0.0 0.0 0.0 0.0 u1=0.0
xe2= 0.0 0.0 0.0 0.0 -1.0 0.0 u2=0.0
xe3= 0.0 0.0 0.0 0.0 0.0 0.0 u3=0.0
xi= -1.2 0.8 0.8 -0.2 -0.2 0.0 v=-0.618
isyd=1
33 'co(a)' 2 17 9 1. 0. 0. 0.0902 1. 0. 0. (small pentagon)
x= -0.2 -0.2 -0.2 -0.2 -0.25 0.0
xe1= 1.0 0.0 0.0 0.0 0.0 0.0 u1=0.0
xe2= 0.0 0.0 0.0 0.0 0.0 0.0 u2=0.0
xe3= 0.0 0.0 0.0 0.0 0.0 0.0 u3=0.0
xi= 0.8 0.8 -1.2 -1.2 0.8 0.0 v=-0.618
isyd=1
34 'al(a)' 1 17 9 1. 0. 0. 0.0902 0.4 0. 0. (small pentagon)
x= -0.2 -0.2 -0.2 -0.2 -0.25 0.0
xe1= 1.0 0.0 0.0 0.0 0.0 0.0 u1=0.0
xe2= 0.0 0.0 0.0 0.0 -1.0 0.0 u2=0.0
xe3= 0.0 0.0 0.0 0.0 0.0 0.0 u3=0.0
xi= -0.2 -0.2 -1.2 -0.2 1.8 0.0 v=-0.618
isyd=1
35 'co(a)' 2 16 6 1. 0. 0. 0.0902 1. 0. 0. (smaller pentagon)
x= -0.2 -0.2 -0.2 -0.2 -0.25 0.0
xe1= 1.0 0.0 0.0 0.0 0.0 0.0 u1=0.0
xe2= 0.0 0.0 0.0 0.0 -1.0 0.0 u2=0.0
xe3= 0.0 0.0 0.0 0.0 0.0 0.0 u3=0.0
xi= 0.0 1.0 0.0 -1.0 0.0 0.0 v=-0.618
isyd=1
36 'al(a)' 1 16 6 1. 0. 0. 0.0902 0.4 0. 0. (smaller pentagon)
x= -0.2 -0.2 -0.2 -0.2 -0.25 0.0
xe1= 1.0 0.0 0.0 0.0 0.0 0.0 u1=0.0
xe2= 0.0 0.0 0.0 0.0 -1.0 0.0 u2=0.0
xe3= 0.0 0.0 0.0 0.0 0.0 0.0 u3=0.0
xi= -1.0 0.0 0.0 0.0 1.0 0.0 v=-0.618
isyd=1
37 'al(a)' 1 16 4 1. 0. 0. 0.0902 1.0 0. 0. (smaller pentagon)
x= -0.2 -0.2 -0.2 -0.2 -0.25 0.0
xe1= 1.0 0.0 0.0 0.0 0.0 0.0 u1=0.0
xe2= 0.0 0.0 0.0 0.0 0.0 0.0 u2=0.0
xe3= 0.0 0.0 0.0 0.0 0.0 0.0 u3=0.0
xi= 0.0 1.0 -1.0 -1.0 1.0 0.0 v=-0.618
isyd=1
38 'co(a)' 2 25 4 1. 0. 0. 0.0902 1. 0. 0. (rhombus)
x= -0.2 -0.2 -0.2 -0.2 -0.25 0.0
xe1= 0.0 0.0 0.0 0.0 -1.0 0.0 u1=0.0
xe2= 0.0 0.0 0.0 0.0 0.0 0.0 u2=0.0
xe3= 0.0 0.0 0.0 0.0 0.0 0.0 u3=0.0
xi= -0.6 0.4 0.4 -0.6 0.4 0.0 v=-0.0902
isyd=1
39 'co(a)' 1 28 9 1. 0. 0. 0.0902 0.4 0. 0. (small star)
x= -0.4 -0.4 -0.4 -0.4 -0.25 0.0
xe1= 1.0 0.0 0.0 0.0 0.0 0.0 u1=0.0
xe2= 0.0 0.0 0.0 0.0 0.0 0.0 u2=0.0
xe3= 0.0 0.0 0.0 0.0 0.0 0.0 u3=0.0
xi= 0.0 0.0 0.0 0.0 0.0 0.0 v=-0.618

isyd=1
40 'al(a)' 1 17 9 1. 0. 0. 0.0902 1.0 0. 0. (small pentagon)
x= -0.4 -0.4 -0.4 -0.4 -0.25 0.0
xe1= 0.0 0.0 0.0 0.0 -1.0 0.0 u1=0.0
xe2= 0.0 0.0 0.0 0.0 0.0 0.0 u2=0.0
xe3= 0.0 0.0 0.0 0.0 0.0 0.0 u3=0.0
xi= 0.2 -0.8 -0.8 0.2 1.2 0.0 v=-0.618
isyd=1
41 'al(b)' 1 32 7 1. 0. 0. 0.1459 1. 0. 0. (larger decagon)
x= -0.4 -0.4 -0.4 -0.4 -0.25 0.0
xe1= 0.0 0.0 0.0 0.0 -1.0 0.0 u1=0.0
xe2= 0.0 0.0 0.0 0.0 0.0 0.0 u2=0.0
xe3= 0.0 0.0 0.0 0.0 0.0 0.0 u3=0.0
xi= -0.2 -0.2 -0.2 -0.2 0.8 0.0 v=-0.618
isyd=4
42 'al(b)' 1 29 11 1. 0. 0. 0.1459 1. 0. 0. (larger decagon)
x= -0.4 -0.4 -0.4 -0.4 -0.25 0.0
xe1= 1.0 0.0 0.0 0.0 0.0 0.0 u1=0.0
xe2= 0.0 0.0 0.0 0.0 -1.0 0.0 u2=0.0
xe3= 0.0 0.0 0.0 0.0 0.0 0.0 u3=0.0
xi= -1.2 0.8 0.8 -0.2 -0.2 0.0 v=-0.618
isyd=1
43 'al(b)' 1 33 11 1. 0. 0. 0.1459 0.5 0. 0. (larger decagon)
x= -0.4 -0.4 -0.4 -0.4 -0.25 0.0
xe1= 1.0 0.0 0.0 0.0 0.0 0.0 u1=0.0
xe2= 0.0 0.0 0.0 0.0 -1.0 0.0 u2=0.0
xe3= 0.0 0.0 0.0 0.0 0.0 0.0 u3=0.0
xi= -0.2 0.8 -0.2 -1.2 0.8 0.0 v=-0.618
isyd=2
44 'al(b)' 1 17 6 1. 0. 0. 0.0902 1. 0. 0. (smaller pentagon)
x= -0.4 -0.4 -0.4 -0.4 -0.25 0.0
xe1= 1.0 0.0 0.0 0.0 0.0 0.0 u1=0.0
xe2= 0.0 0.0 0.0 0.0 -1.0 0.0 u2=0.0
xe3= 0.0 0.0 0.0 0.0 0.0 0.0 u3=0.0
xi= -0.8 1.2 0.2 -0.8 0.2 0.0 v=-0.618
isyd=1
45 'al(b)' 1 16 4 1. 0. 0. 0.0902 1. 0. 0. (smaller pentagon)
x= -0.4 -0.4 -0.4 -0.4 -0.25 0.0
xe1= 0.0 0.0 0.0 0.0 -1.0 0.0 u1=0.0
xe2= 0.0 0.0 0.0 0.0 0.0 0.0 u2=0.0
xe3= 0.0 0.0 0.0 0.0 0.0 0.0 u3=0.0
xi= -0.6 0.4 0.4 -0.6 0.4 0.0 v=-0.618
isyd=1
46 'al(b)' 1 16 4 1. 0. 0. 0.0902 0.6 0. 0. (smaller pentagon)
x= -0.4 -0.4 -0.4 -0.4 -0.25 0.0
xe1= 1.0 0.0 0.0 0.0 0.0 0.0 u1=0.0
xe2= 0.0 0.0 0.0 0.0 0.0 0.0 u2=0.0
xe3= 0.0 0.0 0.0 0.0 0.0 0.0 u3=0.0
xi= 0.4 0.4 -0.6 -0.6 0.4 0.0 v=-0.618
isyd=1
47 'al(b)' 1 17 4 1. 0. 0. 0.0902 1. 0. 0. (smaller pentagon)
x= -0.4 -0.4 -0.4 -0.4 -0.25 0.0
xe1= 1.0 0.0 0.0 0.0 0.0 0.0 u1=0.0
xe2= 0.0 0.0 0.0 0.0 0.0 0.0 u2=0.0
xe3= 0.0 0.0 0.0 0.0 0.0 0.0 u3=0.0
xi= -0.8 0.2 0.2 0.2 0.2 0.0 v=-0.618
isyd=1
48 'al(b)' 1 16 6 1. 0. 0. 0.0902 1.0 0. 0. (smaller pentagon)
x= -0.4 -0.4 -0.4 -0.4 -0.25 0.0
xe1= 1.0 0.0 0.0 0.0 0.0 0.0 u1=0.0
xe2= 0.0 0.0 0.0 0.0 0.0 0.0 u2=0.0
xe3= 0.0 0.0 0.0 0.0 0.0 0.0 u3=0.0
xi= -0.8 0.2 0.2 0.2 0.2 0.0 v=-1.236
isyd=1
49 'al(a)' 1 25 4 1. 0. 0. 0.0902 0.7 0. 0. (rhombus)
x= -0.4 -0.4 -0.4 -0.4 -0.25 0.0
xe1= 0.0 0.0 0.0 0.0 -1.0 0.0 u1=0.0
xe2= 0.0 0.0 0.0 0.0 0.0 0.0 u2=0.0
xe3= 0.0 0.0 0.0 0.0 0.0 0.0 u3=0.0
xi= -0.6876 0.4584 0.4584 -0.6876 0.4584 0.0 v=-0.618
isyd=1
50 'co(a)' 1 25 4 1. 0. 0. 0.0902 1.0 0. 0. (rhombus)
x= -0.4 -0.4 -0.4 -0.4 -0.25 0.0
xe1= 1.0 0.0 0.0 0.0 0.0 0.0 u1=0.0
xe2= 0.0 0.0 0.0 0.0 -1.0 0.0 u2=0.0
xe3= 0.0 0.0 0.0 0.0 0.0 0.0 u3=0.0
xi= -0.541600 0.4584 0.312400 -0.541600 0.312400 0.0 v=-0.618
isyd=3
51 'al(a)' 1 11 4 1. 0. 0. 0.0902 1. 0. 0. (rhombus)
x= -0.4 -0.4 -0.4 -0.4 -0.25 0.0
xe1= 1.0 0.0 0.0 0.0 0.0 0.0 u1=0.0
xe2= 0.0 0.0 0.0 0.0 0.0 0.0 u2=0.0
xe3= 0.0 0.0 0.0 0.0 0.0 0.0 u3=0.0
xi= -0.8584 0.2876 0.1416 0.1416 0.2876 0.0 v=-0.618
isyd=1

```

```

.pod file
nsymo=2 icent=0 brv='p'
symmetry operator
t,-x-y-z-t,x,y,-u+1/2,v 10bar
t,z,y,x,u,-v m'(m')
1 3 1 'decagon'
ej= 0.0 1.0 -1.0 0.0 0.0 0.0
ej= -1.0 1.0 0.0 0.0 0.0 0.0
ej= -1.0 0.0 0.0 0.0 1.0 0.0
nth=2 1 2 2 3
101010101000000000000
2 5 2 'pentagon' ej= 0.000 0.1 -0.3 0.3 -0.1 0.
ej= 0.4 0.4 -0.6 0.4 -0.6 0.0
ej= -0.6 0.4 -0.6 0.4 0.4 0.0
ej= -0.6 0.4 0.4 -0.6 0.4 0.0
ej= 0.4 -0.6 0.4 -0.6 0.4 0.0
ej= 0.4 -0.6 0.4 0.4 -0.6 0.0
nth=5 1 2 2 3 3 4 4 5 5 1
100000000000000000000
3 5 2 'pentagon' ej= 0.000 0.1 -0.3 0.3 -0.1 0.
ej= -0.4 -0.4 0.6 -0.4 0.6 0.0
ej= 0.6 -0.4 0.6 -0.4 -0.4 0.0
ej= 0.6 -0.4 -0.4 0.6 -0.4 0.0
ej= -0.4 0.6 -0.4 0.6 -0.4 0.0
ej= -0.4 0.6 -0.4 -0.4 0.6 0.0
nth=5 1 2 2 3 3 4 4 5 5 1
100000000000000000000
4 4 2 'truncated star A5'
ej= -0.2 0.8 -1.2 0.8 -0.2 0.0
ej= -0.2 0.8 -1.2 1.8 -1.2 0.0
ej= 0.8 -0.2 -1.2 1.8 -1.2 0.0
ej= 0.8 -0.2 -0.2 0.8 -1.2 0.0
nth=3 1 2 2 3 3 4
101010101000000000000
5 4 2 'truncated star A5'
ej= 0.2 -0.8 1.2 -0.8 0.2 0.0
ej= 0.2 -0.8 1.2 -1.8 1.2 0.0
ej= -0.8 0.2 1.2 -1.8 1.2 0.0
ej= -0.8 0.2 0.2 -0.8 1.2 0.0
nth=3 1 2 2 3 3 4
101010101000000000000
6 5 2 'pentagon' ej= 0.000 0.1 -0.3 0.3 -0.1 0.
ej= -0.4 -0.4 0.6 -0.4 0.6 0.0
ej= 0.6 -0.4 0.6 -0.4 -0.4 0.0
ej= 0.6 -0.4 -0.4 0.6 -0.4 0.0
ej= -0.4 0.6 -0.4 0.6 -0.4 0.0
ej= -0.4 0.6 -0.4 -0.4 0.6 0.0
nth=5 1 2 2 3 3 4 4 5 5 1
100000000000000000000
7 4 2 'truncated star A5'
ej= 0.2 -0.8 1.2 -0.8 0.2 0.0
ej= 0.2 -0.8 1.2 -1.8 1.2 0.0
ej= -0.8 0.2 1.2 -1.8 1.2 0.0
ej= -0.8 0.2 0.2 -0.8 1.2 0.0
nth=3 1 2 2 3 3 4
101010101000000000000
8 3 1 '1/10 decagon left -> pinwheel '
ej= 0.0 -0.5 1.0 -0.5 0.0 0.0
ej= 0.0 -1.0 1.0 0.0 0.0 0.0
ej= 0.5 -1.0 0.5 0.0 0.0 0.0
nth=2 1 2 2 3
101010101000000000000
9 7 1 'half decagon right '
ej= 0.0 -0.5 1.0 -0.5 0.0 0.0
ej= 0.0 0.0 1.0 -1.0 0.0 0.0
ej= 0.0 0.0 0.0 -1.0 1.0 0.0
ej= -1.0 0.0 0.0 0.0 1.0 0.0
ej= -1.0 1.0 0.0 0.0 0.0 0.0
ej= 0.0 1.0 -1.0 0.0 0.0 0.0
ej= 0.0 0.5 -1.0 0.5 0.0 0.0
nth=7 1 2 2 3 3 4 4 5 5 6 6 7 7 1
100000000000000000000
10 4 2 'rhombus for overlapped domain'
ej= -1.0 1.0 0.0 0.0 0.0 0.0
ej= -2.0 1.0 0.0 0.0 1.0 0.0
ej= -1.0 0.0 0.0 0.0 1.0 0.0
ej= -0.0002 0.0001 0.0 0.0 0.0001 0.0
nth=4 4 1 1 2 2 3 3 4
100000000000000000000
11 4 2 'rhombus for overlapped domain'
ej= 1.0 -1.0 0.0 0.0 0.0 0.0
ej= 2.000000 -1.0 0.0 0.0 -1.0 0.0
ej= 1.0 0.0 0.0 0.0 -1.0 0.0
ej= 0.0002 -0.0001 0.0 0.0 -0.0001 0.0
nth=4 4 1 1 2 2 3 3 4
100000000000000000000
12 2 2 '1/10 decagon'
ej= 0.0 0.0 1.0 -1.0 0.0 0.0
ej= 0.0 0.0 0.0 -1.0 1.0 0.0
nth=1 1 2
101010101000000000000
13 2 2 '1/10 decagon'
ej= 0.0 0.0 0.0 -1.0 1.0 0.0
ej= -1.0 0.0 0.0 0.0 1.0 0.0
nth=1 1 2
101010101000000000000
14 3 2 'pentagon A5'
ej= -0.2 0.8 -1.2 0.8 -0.2 0.0
ej= 0.43 0.43 -0.43 0.0 -0.43 0.0

ej= 0.8 -0.2 -0.2 0.8 -1.2 0.0
nth=2 1 2 2 3
101010101000000000000
15 3 1 'decagon'
ej=-1.0 1.0 0.0 0.0 0.0 0.0
ej= -1.0 0.0 0.0 0.0 1.0 0.0
ej= 0.0 0.0 0.0 -1.0 1.0 0.0
nth=2 1 2 2 3
101010101000000000000
16 5 2 'pentagon' ej= -0.1 0.3 -0.3 0.1 0.0 0.
ej=-0.4 0.6 -0.4 0.6 -0.4 0.0
ej= -0.4 0.6 -0.4 -0.4 0.6 0.0
ej= -0.4 -0.4 0.6 -0.4 0.6 0.0
ej=0.6 -0.4 0.6 -0.4 -0.4 0.0
ej=0.6 -0.4 -0.4 0.6 -0.4 0.0
nth=5 1 2 2 3 3 4 4 5 5 1
100000000000000000000
17 5 2 'pentagon' ej= 0.000 0.1 -0.3 0.3 -0.1 0.
ej= 0.4 -0.6 0.4 -0.6 0.4 0.0
ej=0.4 -0.6 0.4 0.4 -0.6 0.0
ej=0.4 0.4 -0.6 0.4 -0.6 0.0
ej= -0.6 0.4 -0.6 0.4 0.4 0.0
ej= -0.6 0.4 0.4 -0.6 0.4 0.0
nth=5 1 2 2 3 3 4 4 5 5 1
100000000000000000000
18 4 2 'truncated star A5'
ej= -0.8 1.2 -0.8 0.2 0.2 0.0
ej= -0.8 1.2 -1.8 1.2 0.2 0.0
ej=0.2 1.2 -1.8 1.2 -0.8 0.0
ej=0.2 0.2 -0.8 1.2 -0.8 0.0
nth=3 1 2 2 3 3 4
101010101000000000000
19 4 2 'truncated star A5'
ej=0.8 -1.2 0.8 -0.2 -0.2 0.0
ej=0.8 -1.2 1.8 -1.2 -0.2 0.0
ej= 0.2 -1.2 1.8 -1.2 0.8 0.0
ej= 0.2 -0.2 0.8 -1.2 0.8 0.0
nth=3 1 2 2 3 3 4
101010101000000000000
20 5 2 'pentagon' ej= 0.000 0.1 -0.3 0.3 -0.1 0.
ej= 0.4 -0.6 0.4 0.6 0.4 0.0
ej=0.4 -0.6 0.4 0.4 0.6 0.0
ej=0.4 0.4 -0.6 0.4 0.6 0.0
ej= -0.6 0.4 -0.6 0.4 0.4 0.0
ej= -0.6 0.4 0.4 0.6 0.4 0.0
nth=5 1 2 2 3 3 4 4 5 5 1
100000000000000000000
21 4 2 'truncated star A5'
ej=0.8 -1.2 0.8 -0.2 -0.2 0.0
ej=0.8 -1.2 1.8 -1.2 -0.2 0.0
ej= -0.2 -1.2 1.8 -1.2 0.8 0.0
ej= -0.2 -0.2 0.8 -1.2 0.8 0.0
nth=3 1 2 2 3 3 4
101010101000000000000
22 3 1 '1/10 decagon left -> pinwheel '
ej= 0.5 -1.0 0.5 0.0 0.0 0.0
ej= 1.0 -1.0 0.0 0.0 0.0 0.0
ej= 1.0 -0.5 0.0 0.0 -0.5 0.0
nth=2 1 2 2 3
101010101000000000000
23 7 1 'half decagon right '
ej=0.5 -1.0 0.5 0.0 0.0 0.0
ej=0.0 -1.0 1.0 0.0 0.0 0.0
ej=0.0 0.0 1.0 -1.0 0.0 0.0
ej= 0.0 0.0 0.0 -1.0 1.0 0.0
ej= -1.0 0.0 0.0 0.0 1.0 0.0
ej= -1.0 1.0 -0.0 0.0 0.0 0.0
ej= -0.5 1.0 -0.5 0.0 0.0 0.0
nth=7 1 2 2 3 3 4 4 5 5 6 6 7 7 1
100000000000000000000
24 4 2 'rhombus for overlapped domain'
ej= -1.0 0.0 0.0 0.0 1.0 0.0
ej= -1.0 0.0 0.0 -1.0 2.0 0.0
ej= 0.0 0.0 0.0 -1.0 1.0 0.0
ej= -0.0001 0.0 0.0 -0.0001 0.0002 0.0
nth=4 4 1 1 2 2 3 3 4
100000000000000000000
25 4 2 'rhombus for overlapped domain'
ej= 1.0 0.0 0.0 0.0 -1.0 0.0
ej= 1.0 0.0 0.0 1.00 -2.0 0.0
ej= 0.0 0.0 0.0 1.0 -1.0 0.0
ej= 0.0001 0.0 0.0 0.0001 0.0002 0.0
nth=4 4 1 1 2 2 3 3 4
100000000000000000000
26 2 2 '1/10 decagon'
ej= 0.0 -1.0 1.0 0.0 0.0 0.0
ej= 0.0 0.0 1.0 -1.0 0.0 0.0
nth=1 1 2
101010101000000000000
27 2 2 '1/10 decagon'
ej=0.0 0.0 1.0 -1.0 0.0 0.0
ej= 0.0 0.0 0.0 -1.0 1.0 0.0
nth=1 1 2
101010101000000000000
28 3 2 'pentagon A5'
ej= -0.8 1.2 -0.8 0.2 0.2 0.0
ej=-0.43 0.43 -0.0 0.43 -0.43 0.0
ej=0.2 0.2 -0.8 1.2 -0.8 0.0
nth=2 1 2 2 3

```

```

10101010100000000000
29 10 2 'decagon minus three rhombus'
ej= 1.0 -1.0 0.0 0.0 0.0 0.0
ej= 1.0 0.0 0.0 0.0 -1.0 0.0
ej= 1.0 0.0 -1.0 0.0 0.0 0.0
ej= 0.0 0.0 -1.0 1.0 0.0 0.0
ej= 0.0 1.0 -1.0 0.0 0.0 0.0
ej= 0.0 0.0 -1.0 0.0 1.0 0.0
ej= -1.0 0.0 0.0 0.0 1.0 0.0
ej= 0.0 0.0 0.0 -1.0 1.0 0.0
ej= 0.0 -1.0 0.0 0.0 1.0 0.00
ej= 0.0 -1.0 1.0 0.0 0.0 0.0
nth=10 1 2 2 3 3 4 4 5 5 6 6 7 7 8 8 9 9 10 10 1
10000000000000000000
30 10 2 'decagon minus two rhombus'
ej= 1.0 -1.0 0.0 0.0 0.0 0.0
ej= 1.0 0.0 0.0 0.0 -1.0 0.0
ej= 0.0 0.0 0.0 1.0 -1.0 0.0
ej= 0.0 0.0 -1.0 1.0 0.0 0.0
ej= 0.0 1.0 -1.0 0.0 0.0 0.0
ej= 0.0 0.0 -1.0 0.0 1.0 0.0
ej= -1.0 0.0 0.0 0.0 1.0 0.0
ej= 0.0 0.0 0.0 -1.0 1.0 0.0
ej= 0.0 -1.0 0.0 0.0 1.0 0.00
ej= 0.0 -1.0 1.0 0.0 0.0 0.0
nth=10 1 2 2 3 3 4 4 5 5 6 6 7 7 8 8 9 9 10 10 1
10000000000000000000
31 10 2 'decagon minus three rhombus'
ej= -1.0 1.0 0.0 0.0 0.0 0.0
ej= -1.0 0.0 0.0 0.0 1.0 0.0
ej= -1.0 0.0 1.0 0.0 0.0 0.0
ej= 0.0 0.0 1.0 -1.0 0.0 0.0
ej= 0.0 -1.0 1.0 0.0 0.0 0.0
ej= 0.0 0.0 1.0 0.0 -1.0 0.0
ej= 1.0 0.0 0.0 0.0 -1.0 0.0
ej= 0.0 0.0 0.0 1.0 -1.0 0.0
ej= 0.0 1.0 0.0 0.0 -1.0 0.00
ej= 0.0 1.0 -1.0 0.0 0.0 0.0
nth=10 1 2 2 3 3 4 4 5 5 6 6 7 7 8 8 9 9 10 10 1
10000000000000000000
32 10 2 'decagon minus two rhombus'
ej=1.0 0.0 0.0 0.0 -1.0 0.0
ej=0.0 0.0 0.0 1.0 -1.0 0.0
ej=0.0 0.0 -1.0 1.0 0.0 0.0
ej=0.0 1.0 -1.0 0.0 0.0 0.0
ej=-1.0 1.0 0.0 0.0 0.0 0.0
ej=0.0 1.0 0.0 -1.0 0.0 0.0
ej= 0.0 0.0 0.0 -1.0 1.0 0.0
ej=0.0 0.0 1.0 -1.0 0.0 0.0
ej=1.0 0.0 0.0 -1.0 0.0 0.00
ej=1.0 -1.0 0.0 0.0 0.0 0.0
nth=10 1 2 2 3 3 4 4 5 5 6 6 7 7 8 8 9 9 10 10 1
10000000000000000000
33 10 2 'decagon minus one rhombus'
ej=1.0 0.0 0.0 0.0 -1.0 0.0
ej=0.0 0.0 0.0 1.0 -1.0 0.0
ej=0.0 0.0 -1.0 1.0 0.0 0.0
ej=0.0 1.0 -1.0 0.0 0.0 0.0
ej=-1.0 1.0 0.0 0.0 0.0 0.0
ej=0.0 1.0 0.0 -1.0 0.0 0.0
ej= 0.0 0.0 0.0 -1.0 1.0 0.0
ej=0.0 0.0 1.0 -1.0 0.0 0.0
ej=0.0 -1.0 1.0 0.0 0.0 0.0
ej=1.0 -1.0 0.0 0.0 0.0 0.0
nth=10 1 2 2 3 3 4 4 5 5 6 6 7 7 8 8 9 9 10 10 1
10000000000000000000

```

B - Core Glossary

ADP	Atomic Displacement Parameter(s)
CBED	Convergent-Beam Electron Diffraction
CF	Charge Flipping
DM	Dual Method
GDM	Generalized Dual Method
HAADF-STEM	High Angle Annular Dark Field Scanning Transmission Electron Microscopy
HRTEM	High Resolution Electron Microscope
IDM	Inflation/Deflation Method
LDE	Low Density Elimination
MEM	Maximum Entropy Method
PM	Projection Method
SM	Section Method
PF	Patterson Function

Acknowledgements

It is a pleasure to thank those who made this thesis possible:

I am heartily thankful to my advisor Prof. Walter Steurer for his support, guidance, patience, trust and for the freedom he granted me in the course of my Ph.D. I had perfect conditions to advance and to develop my knowledge - both in physical and complementary spaces.

山本昭二先生 博士論文を書き上げるにあたり、先生からご指導いただきましたことを心より感謝申し上げます。先生にはNIMSへの訪問を温かく歓迎していただき、一緒に研究を行う機会を与えていただきました。昼食時や休憩中には楽しく有意義な議論を交わすことができ、NIMSにおいて過ごした時間は、博士課程の生活の中でも最高の一時でした。先生からは、準結晶について多くのことを教えて頂きました。そして何よりも、先生との交わりを通して、科学への熱い思いが再び沸いてきました。

Prof. Uwe Grimm, thank you for revising my thesis and for your helpful comments. Dear Prof. Cesar Pay Gómez, I would like to thank you for the support and uncountable number of fruitful scientific discussions.

I would like to thank the members of the Laboratory of Crystallography for all the support, the scientific discussions and the cakes.

I am indebted to my family and my friends for enriching my life by making it so diverse, intense and sportive. I am especially obliged to Mehmet Erbudak, Andrew Pratt and Arkadiy Simonov for their many helpful suggestions.

Very special thanks go to my dearest Manuel whose everlasting support and patient love enabled me to complete this work.

So Long and Thanks for All the Fish.

This work was partially financially supported by the Swiss National Science Foundation(SNF).